

Development of particle-based high-density peptide arrays for application in antibody assays

Dissertation

submitted to the

Combined Faculties for the Natural Sciences and Mathematics

of the Ruperto-Carola University of Heidelberg, Germany

for the degree of

Doctor of Natural Sciences

Presented by

Dipl. Phys. Felix Löffler

born in Göttingen

March 2012

Dissertation
submitted to the
Combined Faculties for the Natural Sciences and Mathematics
of the Ruperto-Carola University of Heidelberg, Germany
for the degree of
Doctor of Natural Sciences

Presented by
Dipl. Phys. Felix Löffler
born in Göttingen

Date of oral examination: April 18th 2012

Development of particle-based high-density peptide arrays for application in antibody assays

Referees: **Prof. Dr. Michael Hausmann**

Prof. Dr. Reiner Dahint

Abstract

Over the last few years, peptide libraries gained in importance, but the market is still lacking low cost high-throughput methods. By means of a new method for the production of peptide microarrays with amino acid bioparticles, developed at the German Cancer Research Center and the Kirchhoff Institute of Physics in Heidelberg, the spot resolution was drastically increased, whereas the combinatorial procedure was simplified. With increasing complexity, these techniques require high precision, thus, deposition of bioparticles without contamination is essential, to meet the high standards of modern diagnostics.

Focusing on full combinatorial peptide synthesis, the deposition of bioparticles was thoroughly analyzed, regarding two related techniques. On the one hand, the laser printing technique was improved, by theoretically and experimentally elucidating different substrate properties, resulting in an optimized printing pattern quality. On the other hand, the CMOS chip-based particle pattern generation was theoretically and experimentally analyzed. This yielded a significant improvement of the particle deposition precision and at the same time a reduction of the contamination, leading for the first time to a successful combinatorial peptide synthesis on a CMOS chip.

Kurzfassung

Peptidbibliotheken sind für vielfältige Untersuchungen in den Lebenswissenschaften von Bedeutung. Es existieren zwar bereits Möglichkeiten diese herzustellen, jedoch mangelt es an kostengünstigen Hochdurchsatzverfahren. Mit Hilfe einer neuen Technik zur Herstellung von Peptid-Microarrays, basierend auf der ortsgenauen Ablagerung von Aminosäure-Biopartikeln, entwickelt am Deutschen Krebsforschungszentrum und dem Kirchhoff-Institut für Physik, konnte die Spotdichte drastisch gesteigert und die Syntheseschritte vereinfacht werden. Mit steigender Komplexität erfordern diese Verfahren aber eine hohe Präzision, d.h. eine kontaminationsfreie Ablagerung der Biopartikel wird unumgänglich.

Für die vollkombinatorische Peptidsynthese wurden zwei verwandte Techniken zur Ablagerung von Partikeln analysiert. Zum einen wurde die Laserdruck-Methode theoretisch und experimentell untersucht, was zu einer Optimierung des Druckbildes und des Substrates geführt hat. Zum anderen wurde die CMOS-Chip Technik mit Hilfe von theoretischen Modellen, numerischen Verfahren und experimentellen Erweiterungen entscheidend verbessert. Die Kontamination wurde signifikant verringert und zum ersten Mal wurde somit eine vollkombinatorische Peptidsynthese auf einem CMOS-Chip erfolgreich durchgeführt.

Table of contents

1	Introduction.....	1
1.1	Microarray technology.....	4
1.2	Peptides and proteins.....	5
1.3	Peptide synthesis.....	7
1.3.1	<i>Merrifield peptide synthesis</i>	7
1.3.2	<i>SPOT and lithographic peptide synthesis</i>	10
1.4	Particle-based peptide synthesis.....	11
1.4.1	<i>Peptide laser printer</i>	12
1.4.2	<i>CMOS chip</i>	13
1.4.2.1	<i>Aerosol generation</i>	16
1.4.3	<i>CMOS chip printer</i>	17
1.4.4	<i>Amino acid particles</i>	18
1.5	Motivation and underlying problems.....	20
2	Principles of measurement.....	23
2.1	Measuring q/m values.....	24
2.1.1	<i>Particle-flow tribo-electrometer</i>	25
2.1.2	<i>Particle charge electrometer</i>	27

3	Theory and simulations.....	29
3.1	Simulation of the laser printing process.....	29
3.2	Simulation of the CMOS chip.....	32
3.2.1	<i>Forces and boundary conditions</i>	32
3.2.1.1	<i>Fluid related forces</i>	32
3.2.1.2	<i>Electric forces</i>	36
3.2.1.3	<i>Overview and estimations of forces</i>	38
3.2.2	<i>Geometry and boundary simulation</i>	40
3.2.3	<i>Particle deposition concept and simulation</i>	41
3.2.4	<i>Effect of the particle diameter on deposition</i>	43
3.2.5	<i>Long-range electrical fields</i>	46
3.2.6	<i>Field superposition</i>	47
3.2.7	<i>Restriction of deposition layer thickness</i>	48
3.2.8	<i>Estimated range of selective electric forces</i>	49
3.3	Simulation of miniaturized chip pixels.....	50
3.3.1	<i>Simulation setup</i>	50
3.3.2	<i>Influence of particle size</i>	51
3.3.3	<i>Influence of particle charge</i>	52
3.3.4	<i>Influence of grid voltage</i>	53
3.3.5	<i>Influence of grid width</i>	54
3.3.6	<i>Influence of the sieve voltage</i>	55
3.3.7	<i>Conclusion from miniaturization simulations</i>	56

4	Materials and Methods.....	57
4.1	Amino acid particle composition.....	57
4.2	Aerosol generator and particles.....	57
4.3	Design of the HA/Flag array for the chip.....	59
4.4	Surface coatings for peptide synthesis	61
4.4.1	<i>Silanization</i>	<i>63</i>
4.4.2	<i>PEGMA/MMA coating</i>	<i>63</i>
4.4.3	<i>AEG₃ coating.....</i>	<i>65</i>
4.5	Peptide synthesis protocol	66
4.6	Staining protocol and image acquisition	67
4.6.1	<i>CMOS chip based arrays.....</i>	<i>67</i>
4.6.2	<i>Laser printed arrays.....</i>	<i>68</i>
5	Experimental results and discussion	71
5.1	Analyzing the gap phenomenon	71
5.1.1	<i>Surface conductivity.....</i>	<i>73</i>
5.1.2	<i>Improved printing results</i>	<i>76</i>
5.2	CMOS chip deposition improvement	77
5.2.1	<i>Implementation of a sieve in the aerosol flow</i>	<i>77</i>
5.2.2	<i>Development and construction of an aerosol generation system.....</i>	<i>79</i>
5.2.3	<i>Improved experimental particle deposition on the chip.....</i>	<i>83</i>
5.2.4	<i>Deposition reproducibility.....</i>	<i>89</i>
5.2.5	<i>Pixel miniaturization</i>	<i>95</i>

5.2.6	<i>CMOS chip printing</i>	98
5.3	Peptide synthesis on a CMOS chip	99
5.3.1	<i>Synthesis on AEG₃ coated CMOS chips</i>	100
5.3.2	<i>Synthesis on PEGMA/MMA coated CMOS chips</i>	102
5.3.2.1	<i>Analysis of the HA-epitope</i>	102
5.3.2.2	<i>Analysis of the Flag-epitope</i>	106
5.3.2.3	<i>Intensity variations of fluorescence staining</i>	111
5.3.3	<i>Deposition quality on CMOS chips during synthesis</i>	111
5.4	Epitope mapping using laser printed arrays.....	114
5.4.1	<i>Tetanus toxin/toxoid mapping</i>	114
6	Conclusion and outlook	119
	Appendix	125
	Acknowledgments	135
	References	137

Parts of this thesis have already been published:

- A. Nesterov, **F. Löffler**, K. König, U. Trunk, K. Leibe, T. Felgenhauer, V. Stadler, F.R. Bischoff, F. Breitling, V. Lindenstruth, and M. Hausmann. Noncontact charge measurement of moving microparticles contacting dielectric surfaces. *Rev Sci Instrum*, 78:075-111 (2007)
 - A. Nesterov, **F. Löffler**, K. König, U. Trunk, K. Leibe, T. Felgenhauer, F.R. Bischoff, F. Breitling, V. Lindenstruth, V. Stadler, and M. Hausmann. Measurement of triboelectric charging of moving micro particles by means of an inductive cylindrical probe. *J Phys D: Appl Phys*, 40:6115–6120 (2007)
 - A. Nesterov, **F. Löffler**, Y.-C. Cheng, G. Torralba, K. König, M. Hausmann, V. Lindenstruth, V. Stadler, F. R. Bischoff, and F. Breitling. Characterization of triboelectrically charged particles deposited on dielectric surfaces, *J Phys D: Appl Phys*, 43:165301 (2010)
 - K. König, I. Block, A. Nesterov, G. Torralba, S. Fernandez, T. Felgenhauer, K. Leibe, C. Schirwitz, **F. Löffler**, F. Painke, J. Wagner, U. Trunk, F.R. Bischoff, F. Breitling, V. Stadler, M. Hausmann, and V. Lindenstruth. Programmable high voltage CMOS chips for particle-based high-density combinatorial peptide synthesis. *Sensor Actuat B-Chemical* 147:418-427 (2010)
 - Y.C. Cheng, **F. Löffler**, K. König, A. Nesterov, E. Dörsam, and F. Breitling. Chip Printer. Proceedings of the 2nd WSEAS International Conference on Nanotechnology. ISSN: 1790-5117, 19-22. (2010)
 - **F. Löffler**, J. Wagner, K. Koenig, C. Schirwitz, F. Märkle, S. Fernandez, T. Felgenhauer, K. Leibe, G. Torralba, V. Lindenstruth, M. Hausmann, V. Stadler, F. R. Bischoff, A. Nesterov, and F. Breitling. Particle-based CMOS-chip arrays for antibody screening. Poster presentation, Systems biology of human disease 2010, Boston, Harvard Medical School (2010).
 - J. Wagner, **F. Löffler**, K. König, S. Fernandez, A. Nesterov-Müller, F. Breitling, F. R. Bischoff, V. Stadler, M. Hausmann, and V. Lindenstruth. Quality analysis of selective microparticle deposition on electrically programmable surfaces. *Rev Sci Instrum*, 81:073703 (2010)
 - A. Nesterov, E. Dörsam, Y.C. Cheng, C. Schirwitz, F. Märkle, **F. Löffler**, K. König, V. Stadler, R. Bischoff, and F. Breitling. Peptide Arrays with a Chip. *Methods in Molecular Biology, Volume on Small Molecule Arrays* (2010)
 - **F. Löffler**, J. Wagner, K. König, F. Märkle, S. Fernandez, C. Schirwitz, G. Torralba, M. Hausmann, V. Lindenstruth, F. R. Bischoff, F. Breitling, and A. Nesterov. High-precision combinatorial deposition of micro particle patterns on a microelectronic chip. *Aerosol Sci Tech*, 45:65-74 (2011)
 - **F. Löffler**, Y.-C. Cheng, T. Förtsch, E. Dörsam, R. Bischoff, F. Breitling, and A. Nesterov-Müller. Biofunctional Xerography, *Biotechnology of Biopolymers*, Magdy Elnashar (Ed.), ISBN: 978-953-307-179-4, InTech (2011)
 - J. Wagner, K. Koenig, T. Foertsch, **F. Loeffler***, S. Fernandez, T. Felgenhauer, F. Painke, G. Torralba, V. Lindenstruth, V. Stadler, F.R. Bischoff, F. Breitling, M. Hausmann*, and A. Nesterov-Mueller* (***shared corresponding author**). Microparticle transfer onto pixel electrodes of 45 μm pitch on HV-CMOS chips – Simulation and experiment. *Sensor Actuat A-Physical*, 172:533-545 (2011)
 - **F. Loeffler**, C. Schirwitz, J. Wagner, K. Koenig, F. Maerkle, G. Torralba, M. Hausmann, F.R. Bischoff, A. Nesterov-Mueller, and F. Breitling. Biomolecule arrays using functional combinatorial particle patterning on microchips. *Adv Funct Mater*, *submitted* (2012)
-

1 Introduction

The human genome comprises about 23,000 genes ([1]), which are in turn estimated to code for roughly one million different proteins ([2]). Proteins are the executive forces in the human body and take part in virtually every process in a cell. They fulfill widely diverse functions, amongst others, serving as scaffolds, receptors, or means of transportation, as well as performing signaling and enzymatic tasks.

In this context, specific protein binding is the key to these complex tasks: A match in a spatial

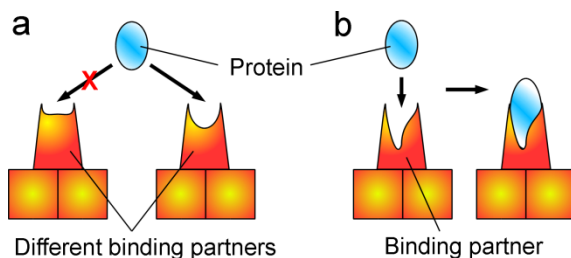


Figure 1.1: The key-lock principle (a) and the induced-fit-concept (b). The protein either matches the binding partner (a) or a spatial modification can be induced (b) to fit the binding partner.

complementary way (lock-and-key principle, Figure 1.1a) is required or the matching is induced by conformational flexibility of the chemical bonds (induced-fit-concept, Figure 1.1b). Several forces play an important role in these binding interactions: van-der-Waals, ionic, and hydrogen bonds, as well as hydrophobic forces.

Proteins are composed of one or more polypeptides ([3]), which are folded in a three-dimensional manner (Figure 1.2). A polypeptide is a linear chain, composed of different building blocks, called amino acids. In the human body, 20 different amino acids are typically available, forming very complex molecules: Supposing that one wants to acquire a library of all such peptides with a length of 10 amino acids (10meric peptides), one would have to generate 20^{10} different species of peptides. Extending these calculations to polypeptides with about one hundred amino acids, one can anticipate the tremendous diversity of proteins. However, nature seems to exploit only a small fraction of this diversity, several proteins or protein domains and their functions are conserved throughout different species with only minimal modifications.

The length of a polypeptide chain is usually less than a few hundred amino acids, however, no exact length definition can be found in the literature. Shorter polypeptide chains (less than about 50 amino acids) are called peptides.

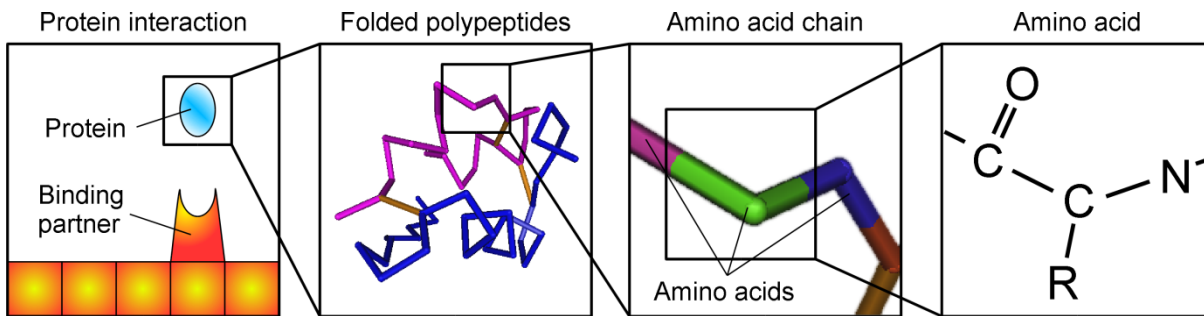


Figure 1.2: Schematic constitution of a protein. A protein is composed of one (or more) folded polypeptides (shown: porcine insulin from [4], [5]; two polypeptides: pink, blue; side chain residues were neglected). A polypeptide is an amino acid chain, which is composed of different monomers, called the amino acids.

Focusing on protein interactions, even the substitution of a single amino acid in a polypeptide may have a decisive effect upon binding efficiency and might highly amplify or completely inhibit binding. Hence, from a scientific point of view, all variations (even non-natural) may be of interest. Yet, it turned out that a theoretical prediction of such complex molecules is very difficult, not only due to the multitude of building blocks, interacting forces, and the conformational diversity, but also due to the lack of experimental knowledge.

To acquire a deeper insight into a scientific question, it is advisable to confine the problem to a certain extent. Regarding protein interactions, one way to such an approach is to restrict the protein interactions to protein-peptide interactions.

Protein-peptide interactions are very common in various biological reactions e.g. in the immune system. Antibodies are proteins, produced by the immune system to identify and neutralize pathogens ([6]). All pathogens are possible antigens (originally from: *antibody generating*), which are today defined as the interaction (or binding) partners for antibodies. Antigens are commonly proteins, peptides, or membrane fragments on the surface of a pathogen, but can also include carbohydrates, lipids, nucleic acids, or other chemical compounds. In many cases, however, the antigens are proteins. The specific structure, which is recognized by an antibody, can consist of small regions of the antigen, called epitopes. An epitope ultimately determines the antibody-antigen binding (see Figure 1.3) and can be a continuous epitope (coherent region, usually 6 – 12 amino acids long) or a discontinuous epitope (two or more regions, adjacent through three-dimensional folding).

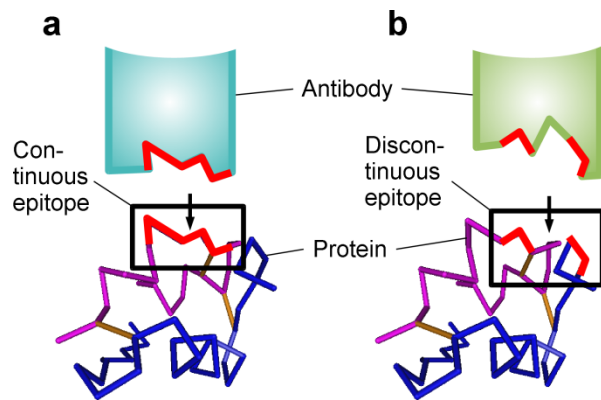


Figure 1.3: Scheme of a specific antibody binding to a continuous epitope (a) and to a discontinuous epitope (b). In this example, the depicted protein is insulin; the antibody is only a schematic drawing.

For reasons of simplicity, in the scope of this thesis, all mentioned epitopes will be restricted to continuous short protein fragments, the peptides. This restriction is not excessively limiting, because e.g. antibodies are known to be rather promiscuous binders. Thus, many protein-protein interactions may be investigated and mimicked with continuous epitopes, i.e. peptides.

An important role of peptides in the immune system is their presentation on the major histocompatibility complex (MHC) molecule. There are two types of MHC molecules, class I and class II ([6]). The MHC class I molecules can be found on the outer surface of every nucleated cell (i.e. possessing a cell nucleus) in the body and report to the immune system, whether a cell is healthy. MHC-I is constantly expressed and loaded with native protein fragments (i.e. peptides) from the cytosol. If a cell is infected with e.g. a virus, the foreign virus fragments are also presented on the MHC-I and are recognized, a cytotoxic T cell initiates apoptosis (programmed cell death) of the infected cell.

The MHC-II molecules are only located on specialized immune cells (e.g. dendritic cells, macrophages, B cells) and present fragments from digested extracellular proteins. If an MHC-II bound peptide is recognized by a T helper cell as foreign and a B cell also recognized this foreign antigen, the T helper cell mediates the differentiation of the B cell to an antibody producing plasma B cell, with antibodies directed against this antigen.

A more detailed description of the immune system and immunobiology can be found in the literature ([6]). Concluding, in the immune system, a specific binding of epitopes is required for an efficient adaptive immune response.

As one can see, a profound understanding of these peptide-based interactions would be very valuable for immunology and medicine, possibly giving rise to new drugs, vaccines, or therapies ([7]).

With today's knowledge, deeper insights into protein-peptide interactions require a versatile, fast, and cost-efficient experimental system, which can display a multitude of peptide interaction partners. One possible experimental solution to the investigation of protein-peptide interactions would be to offer a defined library of peptides to a specific type of protein. Indeed, this can be accomplished with peptide microarrays if the restriction to continuous binding regions is tolerable. Yet, the enormous complexity of short peptides entails the need for an experimental approach with peptide microarrays, which can help to solve numerous unsettled questions in life sciences.

However, using conventional tools and techniques, larger diagnostic peptide assays are practically impossible, due to unaffordable costs and time-consumption. In respect to this task, a new technique has been invented in a cooperation of the German Cancer Research Center and the Kirchhoff Institute of Physics in Heidelberg, which allows for the rapid production of cost-efficient high-density peptide microarrays with frugal consumption of expensive chemicals and analyte.

1.1 Microarray technology

Microarrays are in general solid supports, often in the size of a microscope glass slide, offering a multitude of different biological or biochemical compounds on a small area. Such molecule libraries in a microarray format allow for massively parallel high-throughput assays with frugal consumption of analyte. Each spot of the array features only one specific type of molecule. Thus, a small amount of analyte can be probed for a reaction with all library members simultaneously.

In Figure 1.4, the principle of a microarray application is shown: An array of oligomeric biomolecules (Figure 1.4a), which can be e.g. DNA, RNA, polysaccharides, peptides, proteins, or other molecules, is incubated with a small amount of analyte (Figure 1.4b). The analytic molecules (e.g. single-stranded DNA, RNA, proteins, viruses, or even complete cells) can bind to the different biomolecule spots with specific strength. Fluorescence molecules are either coupled directly to the analytic molecules before incubation or have to be "stained" in a subsequent step. Afterwards, the array is scanned with a fluorescence scanner, resulting in a characteristic intensity pattern for the array. Each spot represents a different experiment, testing the binding quality of the analytic molecules to all library members at once.

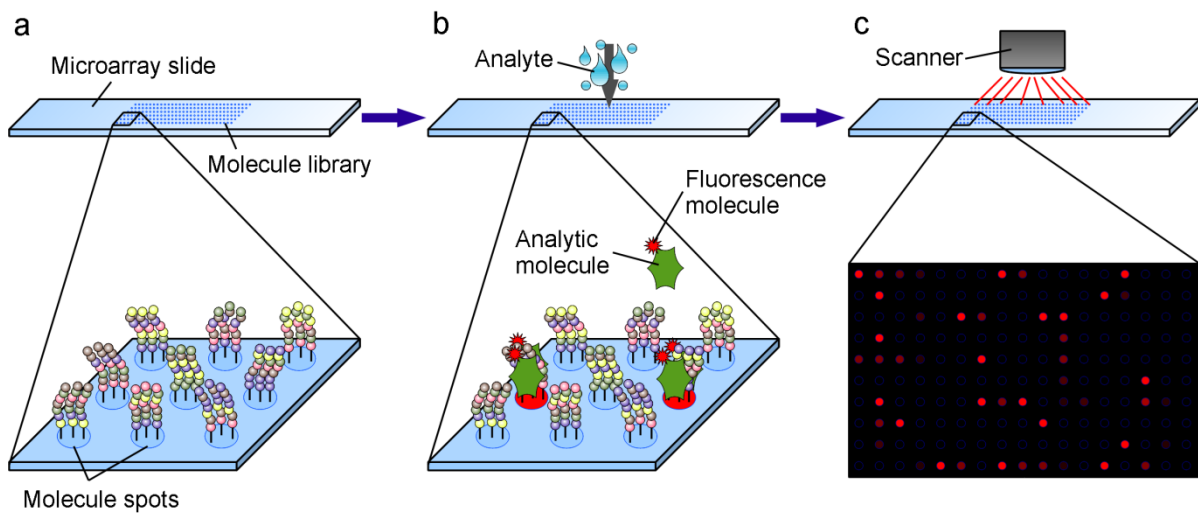


Figure 1.4: Principle of microarray application. The microarray slide with the molecule library (a) is incubated with a small amount of analyte (b). The analytic molecules bind to the surface with different strength, which is visible in the fluorescence image of the microarray (c).

Yet, it requires sophisticated technologies to facilitate such high-density arrays. The smaller the spots and the higher the spot density, the more experiments can be conducted at the same instance.

In the fields of genomics and transcriptomics, microarrays have already revolutionized assay applications ([8], [9]), nevertheless, significant research effort is invested into technological improvements (e.g. [10], [11]).

While the synthesis of DNA or RNA arrays only requires four different building blocks, highly versatile methods for combinatorial synthesis are required to generate e.g. peptides ([12]) or polysaccharides ([13]). In the case of “natural” peptides, 20 different building blocks (amino acid monomers) need to be processed in a fully combinatorial manner, yielding the possibility to assemble any desired amino acid sequence.

1.2 Peptides and proteins

The DNA sequence of a gene of a living cell is transcribed into RNA, which is then translated at the ribosome into the required protein. Hence, the DNA is the blueprint for the different proteins.

Proteins are composed of one or more (poly-)peptides which are folded into a three-dimensional structure. Peptides play an important role in biology and science ([7]). Amongst others, they have tasks like protein interaction mediators, signal transduction (e.g. endorphins, insulin), anti- or pro-inflammatory, and antibiotic or antiviral effects.

A “natural” peptide is a single polymer chain. Each chain member is composed of one of the 20 different proteinogenic building blocks, called amino acids (Figure 1.5). The 20 types of amino acids only differ in their side chain residue (**R**), the amino acid group itself is conserved (red rectangle). These building blocks can be assembled into any arbitrary sequence, connected with a peptide bond. For more information on the side chain residues (**R**), a list of the 20 amino acids, structures, and residues is shown in the Appendix (p. 125). Further references can be found in the literature ([3]).

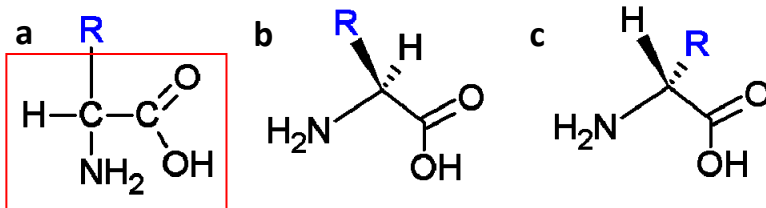


Figure 1.5: Chemical structure of an alpha-amino acid. The amino acid (red rectangle) and the side chain residue (**R**) in simplified form (a). Stereochemistry of the amino acids: L-amino acid (b) and D-amino acid (c)

In Figure 1.5b and c, the two (chemically different) isomers of an amino acid are shown: the L-amino acid and the D-amino acid form. Almost all of the 20 proteinogenic amino acids are L-amino acids, except for glycine, which has no

sterical preference, because the residue is only one hydrogen atom. The “natural” form is always the L-form; D-amino acids are also called synthetic amino acids, because they are not used in standard biological peptide or protein synthesis.

Figure 1.6 shows the chemical reaction of two amino acids, forming a di-peptide under dehydration. The elongation of a peptide always occurs at the amino (N-terminus) or carboxyl group (C-terminus) of the amino acid.

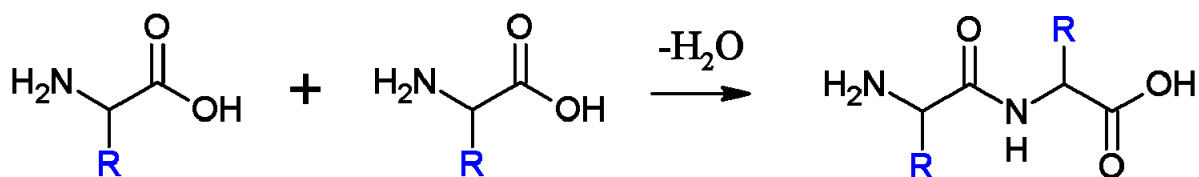


Figure 1.6: Two amino acids form a peptide bond. The carboxyl group of the first amino acid reacts with the amino group of the second amino acid and forms under dehydration a carboxamide group.

1.3 Peptide synthesis

The biological synthesis of peptides takes place at the ribosomes in the cytoplasm of a cell. There, an RNA template is translated into an amino acid chain (for further information, see [3]).

In contrast to this, all recent chemical peptide syntheses are based on the Nobel Prize awarded technique of solid phase peptide synthesis developed by Merrifield in the early 1960s ([14-16]).

The Merrifield synthesis was further advanced by Frank ([17]), who invented the SPOT-synthesis. This principle allows for an automated production of peptides, using a robotic system for the printing liquefied amino acids.

1.3.1 Merrifield peptide synthesis

Merrifield's solid phase peptide synthesis allows to synthesize peptides on a solid support (e.g. glass substrate). Before, peptides were synthesized in a solution, which entailed several complex protection steps, making it almost impossible to synthesize longer peptides.

Our group has slightly adjusted Merrifield's synthesis principle to new requirements. Before a peptide can be synthesized onto a solid support, the solid substrate has to be chemically altered: a 40 - 50 nm thin copolymer film of poly(ethylene glycol) methacrylate (PEGMA) and methyl methacrylate (MMA) with mole fractions of 10 % PEGMA and 90 % MMA is polymerized onto the substrate ([18], [19]). The coating provides for the functional hydroxyl groups which are subsequently modified with a spacer of three β -alanine residues according to standard protocols to render the amino groups required for the peptide synthesis ([20]).

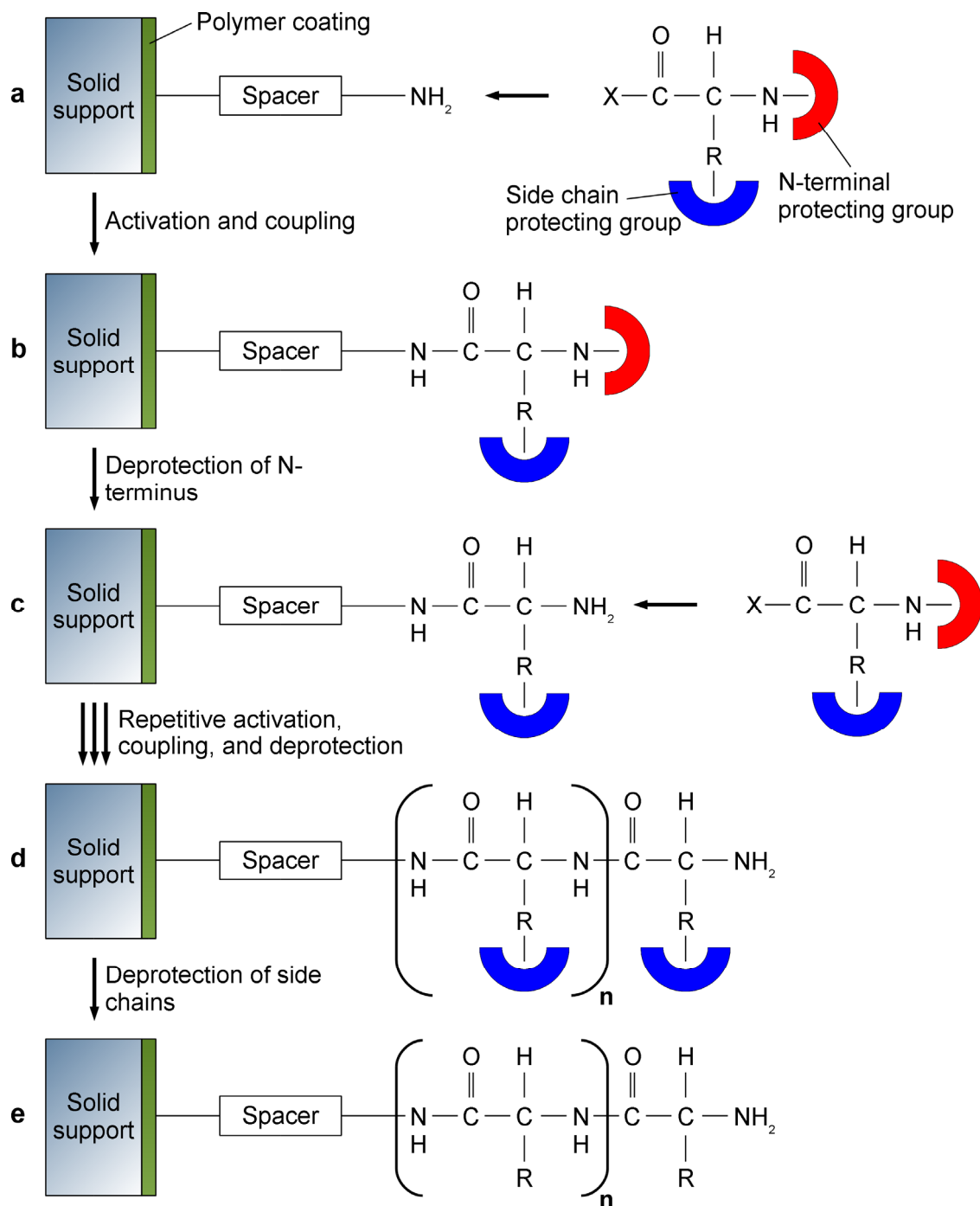


Figure 1.7: Solid phase peptide synthesis based on Merrifield. The polymer coated solid support displays the spacer with an amino group (a). The N-terminal and side chain protected amino acid is C-terminally activated (X represents the OPfp ester) and coupled to the amino group (b). The newly coupled amino acid is deprotected at the N-terminus whereas the side chain protecting group stays unaffected (c). The coupling steps are repeated layer by layer, until the desired peptide chain length ($n + 1$) is reached (d). Finally, the peptide is side chain deprotected (e).

Measurement of the starting density of amino groups upon fluorenylmethyloxycarbonyl (Fmoc) protecting group cleavage resulted in about 1 nmol/cm^2 . Differently designed spacers offer the possibility for either better peptide accessibility (due to length extension and/or

hydrophilic/-phobic residues) or cleavage of the peptides from the solid support, using a cleavable linker.

In Figure 1.7, the principle of the synthesis is shown. The polymer coated solid support displays the spacer with a terminal amino group (Figure 1.7a). All amino acids used in the synthesis bear an N-terminal Fmoc protecting group and (if necessary) acid labile side chain protecting groups. The C-terminal end is pre-activated as pentafluorophenyl (Opfp) ester, represented as an X, (Figure 1.7b) which enables direct coupling of the compound. After each coupling reaction, unreacted amino groups on the support are capped by acetylation with acetic anhydride and diisopropylethylamine ($\text{Ac}_2\text{O}/\text{DIPEA}$). Then, the Fmoc protecting groups are cleaved from the terminal amino acid which makes new amino groups accessible. The Fmoc deblocking is routinely conducted with a base (piperidine) which leaves the acid-labile side chain protecting groups unaffected (Figure 1.7c). This coupling cycle is repeated for each combinatorial layer, until the desired peptide length ($n + 1$) is reached (Figure 1.7d). Finally, all peptides are simultaneously side chain deprotected with trifluoroacetic acid (TFA) (Figure 1.7e). If the spacer was designed to be cleavable under e.g. acidic conditions, the peptides are side chain deprotected and cleaved from the solid support at the same time. In the end, peptides are in a dissolved state.

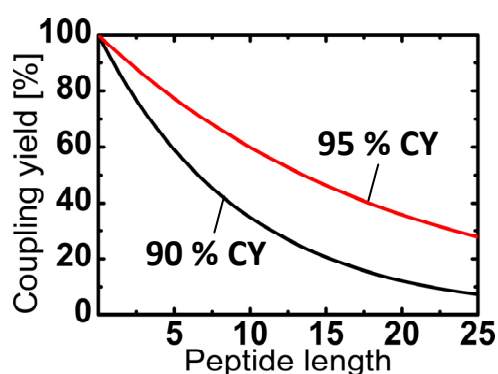


Figure 1.8: Relative coupling yield in dependence of the peptide length (in amino acids) with coupling yields (CY) of 90 % (black) and 95 % (red).

A C-terminal OPfp-ester is needed for the coupling reaction of the peptide bond, but, due to better comprehensibility, the activation group (OPfp-ester) is depicted as an X (for further information, see [21]). In general, the particle based peptide synthesis reaches coupling yields of 90 – 95 %. Every unreacted amino group on the surface has to be capped prior to Fmoc-deprotection to avoid formation of incorrect amino acid sequences. Since the capping (acetylation reaction) described before is very effective, the peptide synthesis produces only truncated peptides among the full-length molecules. However, the consequence of imperfect coupling yields is that the amount of correctly assembled peptides decreases exponentially with increasing peptide length.

Therefore, this peptide synthesis technique is limited to a total number of about 20 amino acids per peptide if a peptide density of at least 0.1 nmol/cm^2 is required.

In Figure 1.8, the total percentage of correctly (fully) synthesized peptides is graphically shown, depending on the total peptide length. The longer the peptide, the less peptides are correctly synthesized, the rest remain truncated.

1.3.2 SPOT and lithographic peptide synthesis

The SPOT peptide synthesis, developed by Ronald Frank ([17]), is based on a hollow needle, which spots liquefied amino acids onto a nitrocellulose substrate. In Figure 1.9a, the principle of the SPOT synthesis is shown: A print head with a hollow needle is positioned relative to the substrate. Drops of liquefied amino acids are deposited onto the substrate, the synthesis reaction starts as soon as the drop contacts the surface. The peptide yield rate of this synthesis technique is quite high, due to the possibility of pre-swelling the substrate. Yet, a spot density of only 25 different peptides per cm^2 limits the application range of this method: Smaller spots require smaller droplets, which tend to evaporate or spread on the substrate, prohibiting a higher spot density.

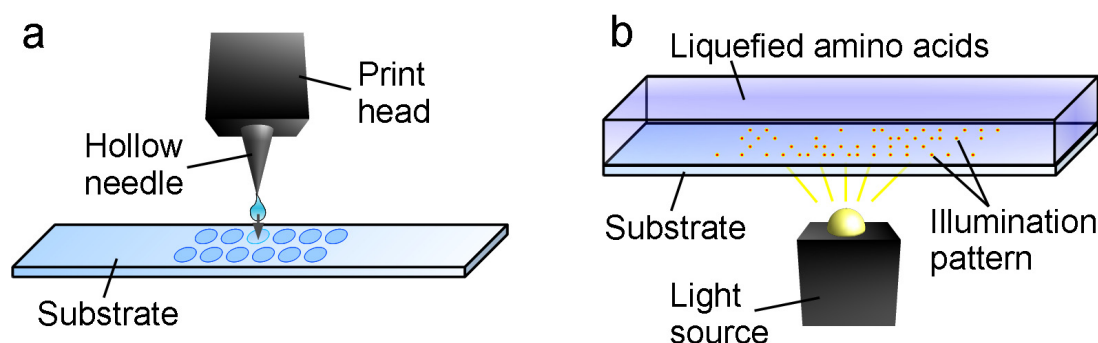


Figure 1.9: The SPOT synthesis (a) and the lithographic method (b).

Figure 1.9b shows the lithographic peptide synthesis method, which was devised by Fodor in 1991 ([22]). The substrate, which is covered with a liquid of one type of dissolved amino acid, is illuminated in a spatially defined manner. The liquefied amino acids possess a photolabile protection group, which is cleaved by the illumination and, thus, the amino acid can couple to the substrate. This method provides for high spot densities, however, the chemistry with photolabile protection groups is rather complicated and, therefore, the peptide yield rate seems to prohibit broad application of lithographic methods.

These drawbacks evoked the development of another synthesis method, which was devised in the DKFZ by Frank Breitling and will be discussed in the following section.

1.4 Particle-based peptide synthesis

The particle-based combinatorial synthesis of a peptide array is shown in Figure 1.10. First, particles are deposited onto the functionalized substrate exhibiting the reactive amino groups (black dots) (Figure 1.10a). Each particle type imbeds a different amino acid type inside of the particle matrix (in gray). The amino acids are illustrated by the differently colored spheres. When the particle matrix is melted, the OPfp pre-activated amino acids diffuse and couple to the amino groups on the surface (Figure 1.10b). Afterwards, excess particles (gray matrix) and uncoupled monomers are washed away (Figure 1.10c), using a mixture of dimethylformamide, acetic anhydride, and diisopropylethylamine (DMF/Ac₂O/DIPEA) which at the same time acetylates (i.e. caps) unreacted amino groups. Finally, the Fmoc-protecting groups (green triangles) are removed from the coupled monomers (Figure 1.10d), using a solution of 20 % piperidine in DMF.

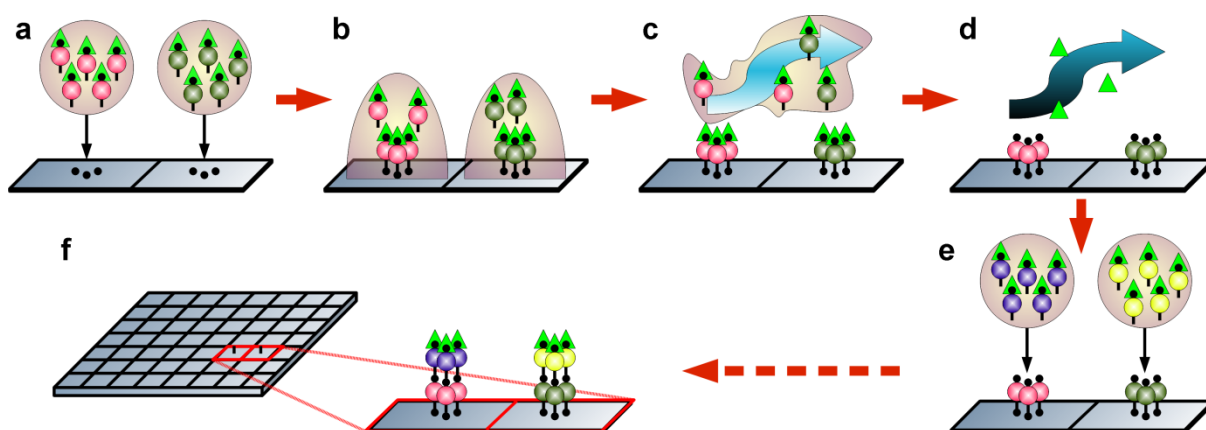


Figure 1.10: Combinatorial synthesis of a (peptide) molecule array. First, the particles are transferred to a substrate (a). Each particle type contains a different (amino acid) building block, represented as colored spheres. Afterwards, the particles are melted and the monomeric building blocks couple to the surface (b). Then, the melted matrix and uncoupled monomers are washed away (c) and finally, the protective groups (green triangles) are removed (d). These steps are repeated with different particle patterns (e, f), until the desired array is completed.

Hence, new amino groups are presented on the surface for the next coupling cycle. This procedure is repeated with layers of different particle patterns (Figure 1.10e, f), until the desired combinatorial array is completed.

Using this technique, it is easily possible to generate a variety of biologically or chemically different molecules, provided that the building blocks are compatible with the synthesis reaction. The maximum achievable peptide length depends on the amino acid coupling yield, which is about 90 %. Since the signal to noise ratio (peptides to truncated peptides) might become increasingly relevant, a total peptide yield of at least 10 % is set as a limit. In this case, the maximum peptide length is about 20 amino acids with a density of 0.1 nmol/cm², the rest of the peptides are truncated.

The main advantage of this method imposes the amino acids in solid particle form. This allows for the temporal separation of the amino acid positioning and the synthesis reaction. Another advantage of the solid form is that the particles do not evaporate or spread, because of their high viscosity even in melted form. This allows for the possibility to facilitate arrays with a very high resolution, a rapid production process, and a good coupling yield.

A selection of different methods to generate a particle pattern will be discussed in the following subsection.

1.4.1 Peptide laser printer

The most prominent method for spatial defined particle deposition is laser printing. The central component of the laser printer is the organic photoconductor (OPC) drum. An organic photoconductor is a material, which has insulating properties in the dark. If the organic photoconductor is exposed to light, it becomes conductive.

The OPC drum is composed of a metal drum, which is covered with a thin layer of organic photoconductor. Figure 1.11 shows the scheme of the laser printing principle: The OPC drum is uniformly negatively charged by a corona or a charge roller. Afterwards, light-emitting diodes (LEDs) selectively illuminate the organic photoconductor and create the “latent” image on the drum surface. Due to the friction between the charging drum and the transfer drum, the toner particles are charged and uniformly cover the transfer drum because of the adhesion forces. By means of electrical fields, the particles are selectively transferred from the transfer drum to the illuminated regions of the OPC drum, thus, the image is “developed”. Finally, the image is transferred to the substrate, again, by using adhesion

forces and an electric field between the OPC drum and the opposing drum electrode. Particles, which have not been transferred (by mistake), are removed by a cleaning unit.

For further information on the laser printing process and the underlying principles, see [23].

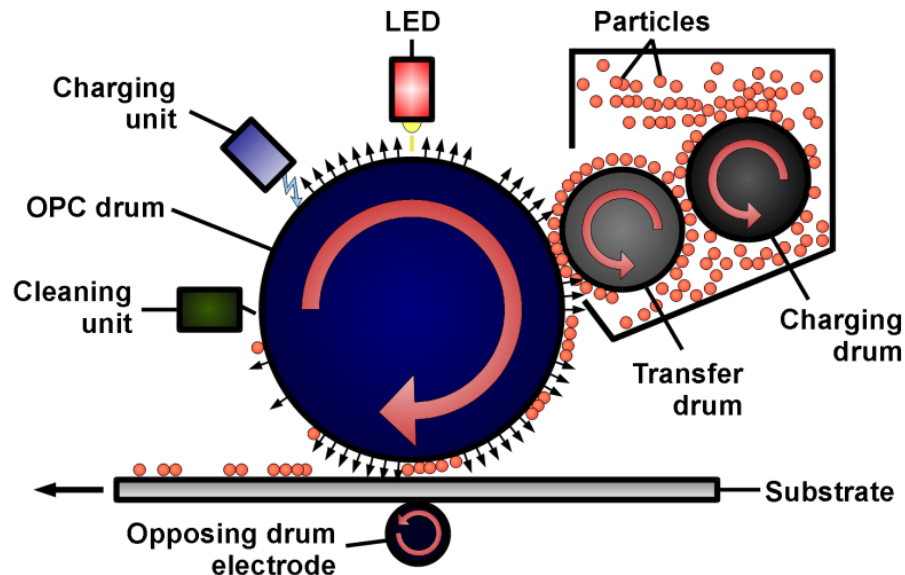


Figure 1.11: Principle of the laser printer. The OPC drum is uniformly negatively charged by a corona or a charge roller. Afterwards, light-emitting diodes (LEDs) selectively illuminate the organic photoconductor and create the “latent” image on the drum surface. Due to the friction between the charging drum and the transfer drum, the toner particles are charged and uniformly cover the transfer drum. By means of electrical fields, the particles are transferred from the transfer drum to the illuminated regions of the OPC drum, thus, the image is “developed”. Finally, the image is transferred to the substrate, again, by using adhesion forces and an electric field between the OPC drum and the opposing drum electrode. Particles, which have not been transferred, are removed by a cleaning unit.

Exploiting this technique, our research group, together with the Fraunhofer Institute for Manufacturing, Engineering, and Automation (IPA, Stuttgart), has developed the peptide laser printer ([24]), which is composed of 20 consecutive printing units (one unit is shown in Figure 1.11). Each unit deposits one type of particles consecutively onto a substrate, each particle type has imbedded only one kind of the 20 amino acids. Thus, 20 different self-made particle types had to be produced, which will be introduced in subsection 1.4.4. A spin-off company was founded, making these arrays commercially available ([25]).

1.4.2 CMOS chip

In a different approach, a CMOS (complementary metal oxide semiconductor) chip has been designed for defined spatial particle deposition ([26], [27], [28]). The idea is to use strong

local electric fields of programmable single pixel electrodes ($100\ \mu\text{m} \times 100\ \mu\text{m}$) and charged particles in order to realize selective particle deposition. By addressing each pixel individually, any high voltage pattern can be programmed. The electric field attracts negatively charged micro particles, which will be deposited according to the voltage pattern. Currently, the chip features 10,000 pixels per cm^2 with a pixel pitch of $100\ \mu\text{m}$, resulting in a total of 16,384 pixels on $1.28 \times 1.28\ \text{cm}^2$ as an active pixel area. The chip (Figure 1.12 left), with a total size of about $2.0 \times 1.9\ \text{cm}^2$, is glued and bonded to a (green) printed circuit board (PCB) which is designed in the size of a standard microscope slide of $2.5 \times 7.6\ \text{cm}^2$.

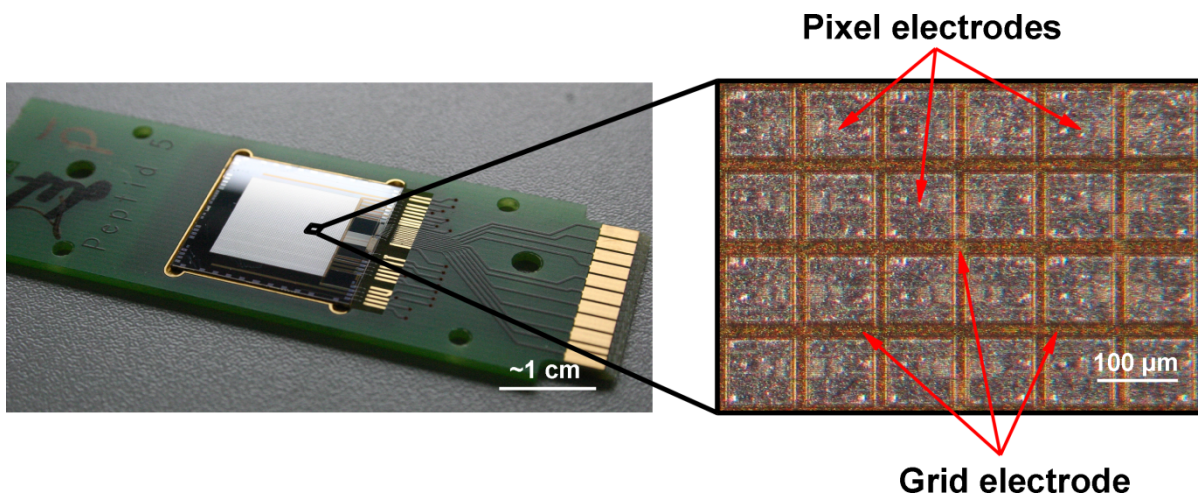


Figure 1.12: The CMOS chip. (left) The chip ($2.0 \times 1.9\ \text{cm}^2$) is glued and bonded to a (green) printed circuit board ($2.5 \times 7.6\ \text{cm}^2$). (right) The microscopic magnification of a detail of the chip surface shows the aluminum pixels (gray) which are surrounded and thereby separated by the grid electrode (brown).

Figure 1.12 right shows a magnification of the chip surface: The pixels have an aluminum surface (gray) and are surrounded, and thereby separated, by the grid electrode (brown). The grid electrode and the pixels are located in the topmost metal layer of the chip and are insulated from each other by silicon dioxide. The grid is (in contrast to the pixels) covered by a silicon nitrite insulator to prevent electrical breakdown. In the experiments performed, the voltages applied to each of the pixels were either 0 V or 100 V, the grid electrode was grounded or set to a constant voltage of 30 V. Further details will be discussed in the simulation section (section 3.2).

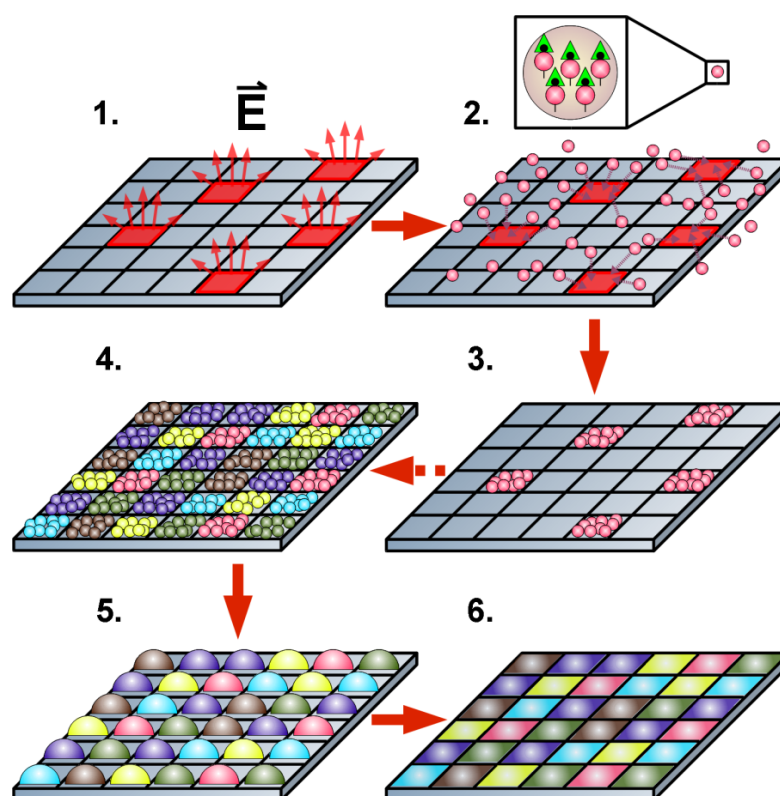


Figure 1.13: Microelectronic CMOS chip principle. Schematic deposition process: The chip is programmed to exhibit a voltage pattern on its surface (1). Then, the chip is exposed to an aerosol; the particles are attracted by the resulting electric field and are deposited according to the desired pattern (2-3). The magnification of a particle (2) shows that each particle type incorporates only one kind of monomeric building block. After application of a first particle type, the chip is reprogrammed to a different voltage pattern. Due to the adhesion forces of the particles, the already deposited pattern remains on the surface without distortion. Next, the particle deposition is repeated with different particle types consecutively (4), each type comprising a different monomer. These deposition steps can be repeated until the final deposition layer is completed. Afterwards, the chip is heated and, thus, the gel-like particle matrix releases the monomers for the coupling reaction (5). Finally, the chip is subjected to several washing steps (6) and the complete process is repeated layer by layer until the terminal molecule length is reached.

For combinatorial synthesis, the chip is programmed to exhibit a voltage pattern on its surface (Figure 1.13, step 1). Then, the chip is exposed to an aerosol of micro particles: Particles are only attracted and deposited onto those pixel electrodes which exhibit an electric field E . Thus, the voltage pattern is transformed into the according particle pattern (Figure 1.13, step 2-3). The magnification of a single particle (Figure 1.13, step 2) shows that each particle type incorporates only one kind of monomeric building block. After application of a first particle type, the chip is reprogrammed to a different voltage pattern. Due to the adhesion forces of the particles, the already deposited pattern remains on the surface without distortion. Next, the particle deposition is repeated with different particle types consecutively (Figure 1.13, step 4), each type comprising a different monomer.

These deposition steps can be repeated, until the final deposition layer is completed. Afterwards, the chip is heated and the particle matrix becomes a highly viscous fluid, forming distinct gel-like reaction spheres. Similar to Merrifield's solid phase peptide synthesis, the particle matrix releases the monomers, which now couple to the surface bound amino groups, without losing the spatial resolution of the deposition pattern (Figure 1.13, step 5). Then, the chip is allowed to cool to room temperature, which causes the reaction spheres to solidify, "freezing" the coupling reaction. Finally, the chip is subjected to several washing steps, removing excess monomers and the particle matrix. Yet, the different monomers remain coupled to the pixels (Figure 1.13, step 6). The complete process cycle has to be repeated layer by layer until the terminal molecule length is reached (see Figure 1.10 for further information on the coupling and synthesis cycle).

The process and especially the quality of particle deposition on the CMOS chip will be one of the central points of interest in this thesis.

1.4.2.1 Aerosol generation

In this subsection the former aerosol generation method is only briefly introduced, because, in the scope of this thesis, a new, more compact, and automated aerosol generation system was devised and assembled. The former aerosol generator (called aerosol chamber) was manufactured of poly(methyl methacrylate) (PMMA). In Figure 1.14 left, the principle of the aerosol generation and flow in the aerosol chamber is shown: In (1), the pressurized air enters the aerosol chamber and drives the air injector. The particles are siphoned into the injector geometry in (2) and are guided through a hose (3) to the cyclone (4). In the cyclone, the particles are charged due to the friction with the PMMA surface. Afterwards, the charged aerosol is either deflected into the outlet direction (5), where the CMOS chip is located, or, the particles slowly settle (6) at the bottom of the chamber (2), where they can be reintroduced into the cycle.

Figure 1.14 right shows the aerosol chamber with the (black) lever to manually activate the pressurized air valve which starts the aerosol generation.

Although several fundamental and successful experiments have been conducted with this aerosol chamber ([26], [28]), in the scope of this thesis, it turned out that the most

prominent drawbacks of this method were the hardly adjustable stability of the aerosol density, the clogging of bottlenecks in the chamber, and the massive consumption of particles. Thus, it was necessary to devise a completely new aerosol generation system.

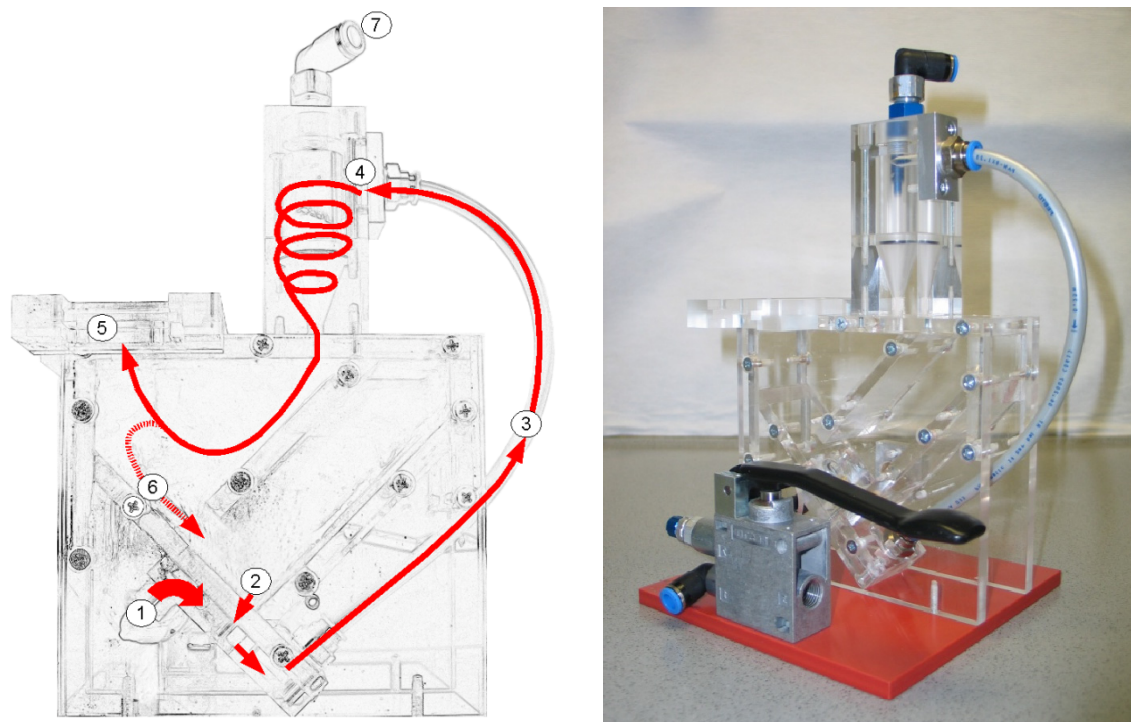


Figure 1.14: State-of-the-art aerosol system. (left) (from [28], reprinted with permission) The principle of the aerosol generation and flow in the aerosol chamber (for explanation see text). (right) The aerosol chamber with the (black) lever to manually activate the pressurized air valve which starts the aerosol generation.

1.4.3 CMOS chip printer

Another possible application for the CMOS chip is the CMOS chip printer. The idea was first mentioned in [29] and will be subject of further research ([30]).

The CMOS chip is used to generate the particle pattern (Figure 1.15a, b), as mentioned before in the CMOS chip deposition technique. Now, the chip is positioned parallel, about 40 μm apart from a glass slide with an electrode located beneath it (Figure 1.15c). An electric potential between the chip and the electrode results in a force which transfers the particles from the chip to the glass slide (Figure 1.15d).

This technique allows for the transfer of the particle pattern to a glass slide, which makes the chip reusable, yet the problem of positioning and parallelization of the chip has to be solved [31].

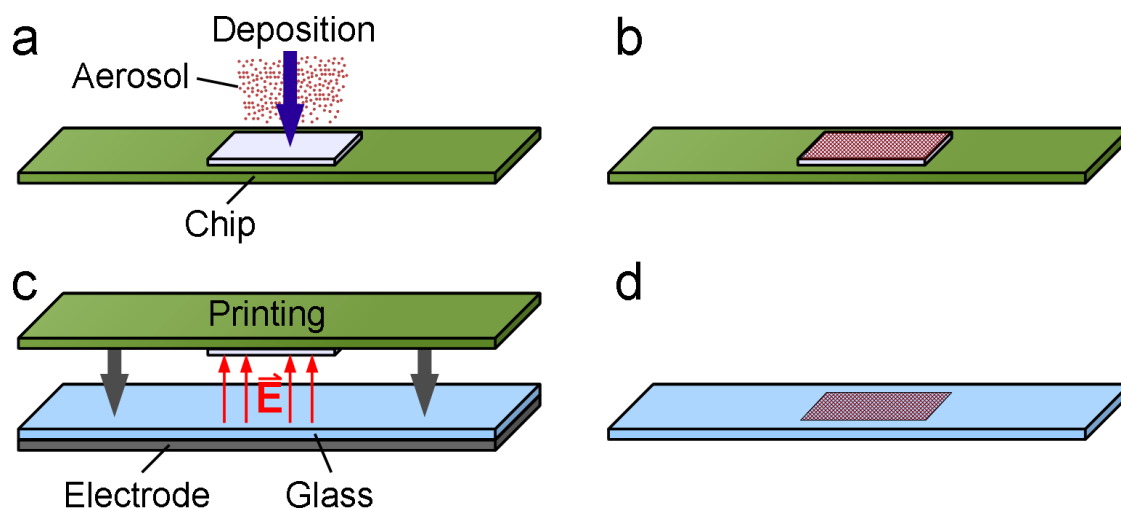


Figure 1.15: CMOS chip printer. The scheme shows the particle deposition (a, b) as in the before mentioned CMOS chip deposition technique. The chip is then positioned parallel to a glass slide with an electrode beneath (c). An electric potential between the chip and the electrode results in a force which transfers the particles from the chip to the slide (d).

1.4.4 Amino acid particles

The micro particles, designed to meet the requirements of particle-based synthesis, mainly consist of a styrene acrylic copolymer (SAC), together with the amino acid. The particle matrix components are augmented with two additives: a charge control agent (CCA) and a colorant. The colorant is used for a better visibility of the particles, the CCA has the property to provide for a uniform triboelectric charging of the particles. For further information on the particle matrix and the components, see [24] (Supporting information).

In Figure 1.16, the process of particle matrix production is shown: The components for the amino acid particles (amino acid and matrix components) are dissolved in a solvent (Figure 1.16a) and the mixture is stirred (Figure 1.16b). Afterwards, the distillation is started and the solvent evaporates (Figure 1.16c). The dried amino acid particle matrix remains in the flask (Figure 1.16d).

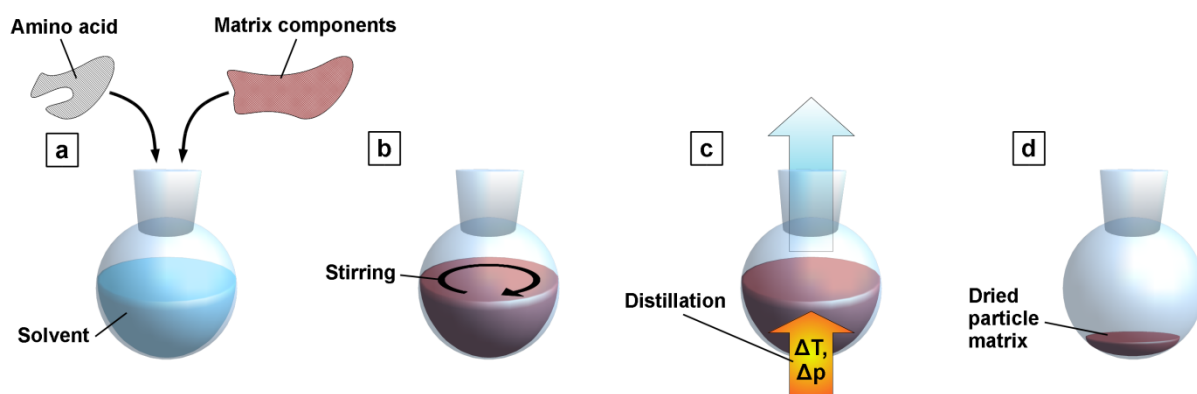


Figure 1.16: Production of the particle compound. The components for the amino acid particles (amino acid and matrix components) are dissolved in a solvent (a). The mixture is stirred (b), and afterwards distilled. The solvent evaporates (c) and the dried amino acid particle matrix remains in the flask (d).

The dry coarse matrix is milled in a blade granulator (IKA GmbH & Co. KG, Germany) (Figure 1.17a), to achieve a preliminary particle granularity. The granulate material is then milled in a Hosokawa Alpine AS 100 air jet mill (Figure 1.17b) and subsequently sieved in an analytical sieve. These particles are finally separated in a Hosokawa Alpine winnower (Figure 1.17c) into two different fractions, the fine and the coarse fraction. The winnower separates the two fractions at about 7 μm . However, the separation process is not perfectly accurate; one can rather speak of a blurred separation threshold.



Figure 1.17: The blade granulator (a), the AS 100 air jet mill (b), and the winnower (c).

The density of the major component (SAC) is about $1,100 \text{ kg/m}^3$, thus, it is assumed that the particle density is similar. The size analysis of the particles is performed with a Malvern Mastersizer (Malvern Instruments Ltd.), measuring the laser diffraction and refraction. The analysis gives a volume fraction (% v/v) based size distribution (Figure 1.18).

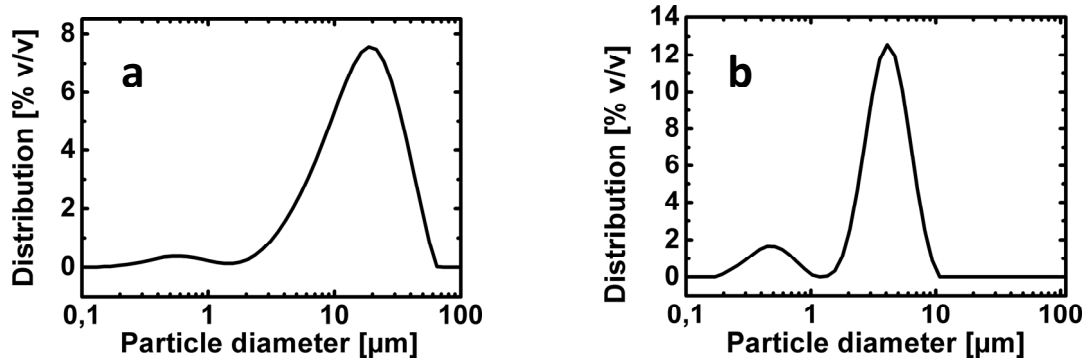


Figure 1.18: Particle size distribution in % v/v. The distribution of the coarse particle fraction (a) and the of the fine particle fraction (b).

To prevent particle agglomeration and to improve particle fluidity, silica nano particles are added after the process (Aerosil, 812, Degussa, Germany).

For the laser printer, only the coarse particle fraction can be used (Figure 1.18a), the fine particle fraction (Figure 1.18b) causes contaminations in the printed image, and therefore, cannot be used in the context. The correct particle type for the on-chip deposition will be evaluated in this thesis.

1.5 Motivation and underlying problems

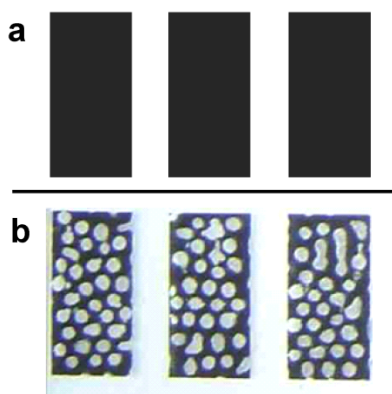


Figure 1.19: (a) expected printing pattern of three solid black rectangles printed with commercial OKI black toner (drawing); **(b)** resulting pattern at about 4.2 kV with many empty circular gaps inside of the solid rectangles

This thesis was conducted in the scope of analyzing and improving two generally related particle patterning methods for combinatorial peptide synthesis.

On the one hand, the **laser printing** technique seems to be a well-developed method. Yet, the underlying principle was devised for printing on paper and has some difficulties with glass substrates: To improve the quality of the particle pattern, which is transferred from the image drum onto the glass substrate, the voltage between the image drum and the substrate was increased, in order to maximize the amount of transferred particles. However, this resulted in a yet unknown effect: The expected pattern of three solid black rectangles printed with commercial OKI black toner

(computer drawing) is shown in Figure 1.19a. In Figure 1.19b, the experimentally obtained black rectangles show an effect, which prohibits a homogenous particle deposition on the substrate: Many empty circular gaps (without any deposited particles) appear in a supposedly homogeneously printed solid pattern of three rectangles. These problems are related to the transfer voltage: At lower voltages, often, the particle layer was too thin. At higher voltages the circular gaps occurred, which could not be reasonably explained yet. A course of simulations and experiments was performed to elucidate this phenomenon.

Secondly, the already mentioned **CMOS chip** technique was investigated and analyzed in more detail. The objective of this technique is to produce patterns with high complexity and arbitrary configuration, which should allow for a full combinatorial peptide synthesis. Although arbitrary voltage patterns were already achievable with microelectronic chips, until recently, it was observed that the contamination rate in any other pattern, other than the chess-board pattern (which allows for only two different peptides) was still so high that combinatorial peptide synthesis was practically impossible. In Figure 1.20 (left), the chess board pattern (1 of 2 pixels switched on) shows a still acceptable quality of the deposition pattern, less dense particle patterns (Figure 1.20 right), with e.g. 1 of 16 pixels switched on, show a high background contamination.

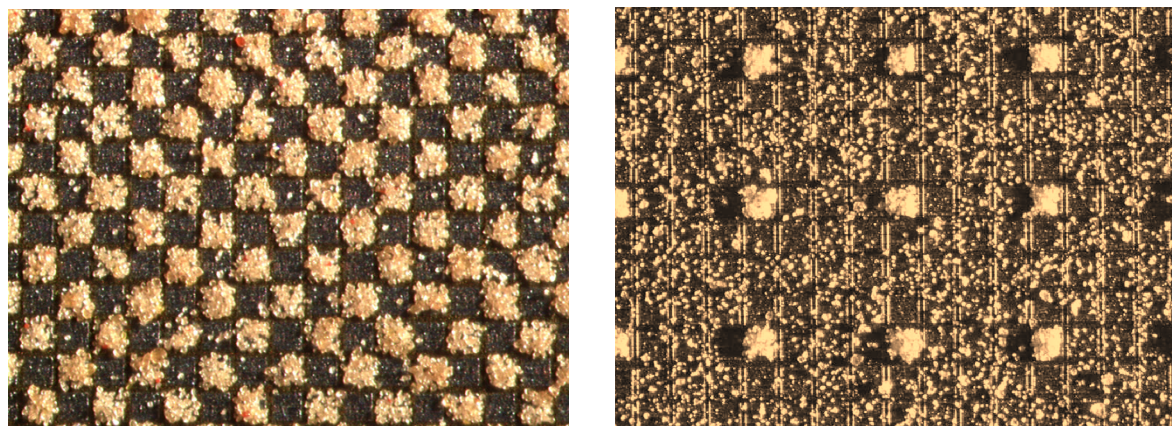


Figure 1.20: Magnification of the CMOS chip surface with deposited particles. The chess board pattern (left) shows an acceptable quality of the deposition pattern, less dense particle patterns (right), like 1 of 16, show a high background contamination.

Regarding this problem, a theoretical and numerical analysis of particle dynamics was performed, with the objective to significantly reduce the contamination in particle deposition and to thereby realize for the first time a truly combinatorial peptide synthesis. In the course of this thesis, the simulation results made it necessary to devise new particles,

which in turn led to the requirement of a new and especially designed aerosol generator and a new deposition geometry.

2 Principles of measurement

This chapter will begin with a discussion of the most important particle characteristics which have a major impact on selective particle deposition using electric fields.

Due to the underlying principle of using electric fields for selective particle deposition, one can assume that the driving force in the mentioned particle patterning methods (laser printer and CMOS chip) is defined by the electric field \mathbf{E} (other forces will be discussed in chapter 3). Thus, the force acting on a micro particle with the charge q is defined by the equation:

$$\mathbf{F} = q\mathbf{E} . \quad (2.1)$$

Using Newton's second law of motion ($\mathbf{F} = m\mathbf{a}$), the acceleration acting on a particle depends on the electric field \mathbf{E} and on the ratio of charge and mass (q/m) of the particle:

$$\mathbf{a} = \frac{q}{m} \mathbf{E} . \quad (2.2)$$

The intrinsic limits of the particle patterning methods only allow certain maximum electric fields \mathbf{E} , to prevent damage due to electric air breakdown or leakage currents. Therefore, when describing the particle trajectory using the acceleration \mathbf{a} , the q/m value intuitively gives the most important particle characteristic in selective deposition: Assuming that, the higher the ratio of q and m , the higher the acceleration \mathbf{a} is, and hence, the more precisely one can deposit the particles. Consequential, one can either increase the particle charge q or decrease the particle mass m , which is proportional to the particle size.

However, it turned out, that it was not sufficient to only increase the particle charge. Especially when considering the friction which occurs during deposition of particles in a fluid (e.g. air), the particle size or respectively the size distribution of a particle ensemble also has to be considered (see chapter 3, subsection 3.2.1).

Yet, the following sections will focus on different methods for measuring the particle charge and try to gain an insight into the particle charging process.

2.1 Measuring q/m values

Measuring q/m values of particles is connected with using an electric probe which is based on the Faraday cup principle. The basic principle of the Faraday cup is a metal cup, which is supposed to surround the charge completely (in 4π solid angle). If a charge is completely surrounded by a metal surface, a charge q induces a charge displacement in the metal due to the image force. This displacement can be measured if the metal cup is connected to an oscilloscope: The measured charge transfer, which is necessary to compensate the displacement, is equal to the charge $-q$. Thus, it is a rather direct method to measure a charge. The solid angle for an adequate cup geometry can be assumed to be almost 4π .



Figure 2.1: Charge to mass ratio test system from TREK (TREK, INC., USA)

The measurement was previously performed with a “charge to mass ratio test system” from TREK (TREK, INC., USA). The system (see Figure 2.1) is based on the “draw off” toner transfer method: Toner particles are mixed and stirred in a flask with a coarse fraction of iron oxide particles, the particle-particle friction causes triboelectric charging of the particles. Afterwards, the finer toner particles are siphoned off through a sieve into a Faraday cup, the coarse iron oxide particles remain in the flask. The charge can be evaluated by integration of the electric current over time.

However, this method has several drawbacks for our purposes. Because the triboelectric charging is based on a very complex principle, the toner charging using iron oxide particles does not represent the charging process in our case. Moreover, the particles are transported into a cup and cannot be used in a subsequent particle deposition process.

Therefore, new methods were devised, which allow measuring the particle charge during particle movement and, on the other hand, to observe the particle charging and discharging process.

2.1.1 Particle-flow tribo-electrometer

In this context, a method, which possesses the described advantages, was devised. The basics of the method were published in [33] and [34]. The setup is illustrated in Figure 2.2a:

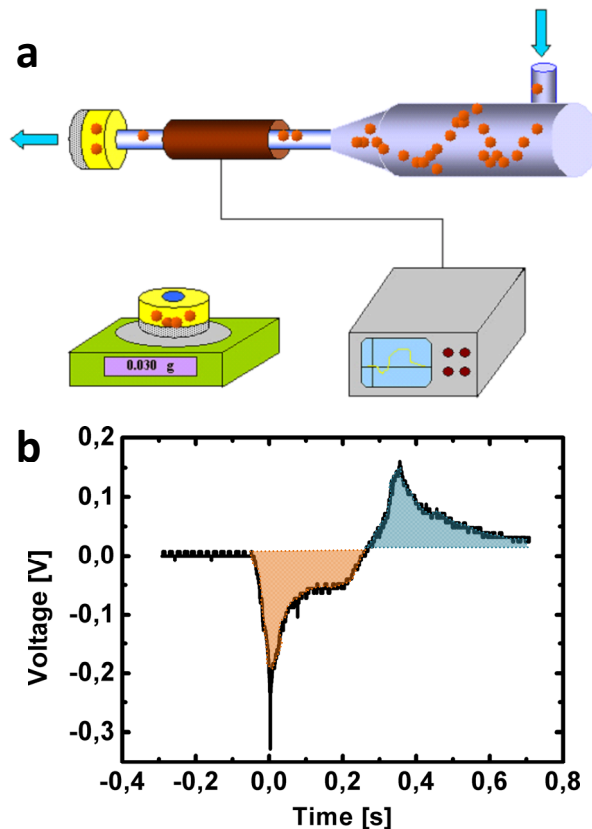


Figure 2.2: (a) Measurement of the q/m -value with the inductive cylindrical probe (from [32]) (b) example measurement with cylindrical probe. Each colored area in the measurement graph represents the two peaks (see text).

Particles are introduced into a tube with a spatula. Pressurized air is connected to the tube and the particles are accelerated, entering a cyclone structure. The particles are accelerated due to the centripetal force and the occurring friction causes the triboelectric charging of the particles. Leaving the cyclone structure, the particles are guided through a 3 – 5 m long tube, which is completely covered with a cylindrical metal tube (e.g. aluminum foil). Finally, the particles are collected in a filter, which has to be weighed. The charge, which is induced in this metal probe, is measured with an oscilloscope and the resulting q/m value is determined by calculating (using Ohm's law) the total charge from the oscilloscope signal and dividing it by the mass difference of the filter.

The measurement is dependent on the dimension of the particle cloud, which varies with the geometry and the air pressure: The particles are accelerated and a particle cloud with a certain dimension (length) is created in the tube. If the cloud has reached a certain length in the tube, the cylindrical metal probe has to be even longer, in order to measure the complete charge of the cloud (which is a basic requirement for the Faraday cup principle). This length can be evaluated with the point-shaped probes described in [33]. Figure 2.2b shows a typical measurement: The particle cloud moves into the probe, resulting in the first peak (colored in orange). The second peak (highlighted in blue) is a result of the cloud, leaving the probe geometry. The integral of each peak (equal to the colored areas) gives the

important information on the total charge. If the integrals of the peaks over time are equal, then the charge of the particle cloud is unchanged. However, due to the friction with the tube wall and the resulting triboelectric charging of the particles, in most cases, the charge did increase and, thus, the integral of the first peak was smaller than the second.

The calculation using Ohm's law, $I(t) = U(t) / R$, with the resistance R of the oscilloscope being $1 \text{ M}\Omega$, gives the possibility to evaluate the total charge Q by integrating the current $I(t)$ over time. Finally, dividing the total charge with the weighed particle mass results in the desired q/m -value. For further information on the method, see [33], [34], [32].

Exploiting this technique, an amino acid particle characterization was performed in [35], which pinpointed to a certain correlation: The charge to mass ratio (q/m value) of the particles is mainly dependent on their mean diameter, the different amino acids in different particle types seem to have a neglectable impact on the final particle charge. Measuring the q/m value of two fractions of the same particle type, the fine particle fraction with a mean diameter of $2.3 \text{ }\mu\text{m}$ yielded a ratio of up to $-8 \cdot 10^{-3} \text{ C/kg}$, in contrast to the coarse fraction with a mean diameter of $15.6 \text{ }\mu\text{m}$, possessing a charge to mass ratio of about $-3 \cdot 10^{-3} \text{ C/kg}$. This is partly explained by the fact that the surface to volume ratio is increased when the particle diameter is decreased. However, due to the measurement technique, the obtained q/m value specifies only a mean charge value for the particle sample under consideration, thus, single particle charges can differ widely due to different microscopic charging processes ([36], [37], [38]).

All amino acid particles have negative q/m -values and average surface charge densities of $-0.5 \cdot 10^{-5}$ to $-2 \cdot 10^{-5} \text{ C/m}^2$ were achieved. Thus, an activated particle has several thousand elementary charges. It is a rather effective charging process, compared to the critical air breakdown charge density of $\sigma = -2.6 \cdot 10^{-5} \text{ C/m}^2$ ([39]), at which air breakdown occurs on a conductive surface.

Using this method, one can also observe a certain increase or decrease in charge at two different points in time if comparing the charge of the particles when entering and leaving the cylindrical probe geometry. Yet, this method could not provide the possibility to measure the particle charge over time. Therefore, another method was devised, which will be discussed in the following subsection.

2.1.2 Particle charge electrometer

Here, a particle electrometer method is presented, which was published in [40]. The basic principle is shown in Figure 2.3a: A rotating particle support, which in our case is a microscope glass slide with deposited particles, is moved repeatedly into a probe. The principle of the probe is again similar to the Faraday cup. The probe is connected to an integrator unit, which is connected to an oscilloscope. The output signal is proportional to the registered charge, located inside the probe. Thus, from the oscilloscope signal, one can directly calculate the total electric charge without integrating the signal over time. If the charge is now inserted into the probe repeatedly by rotation, the charge decay over time can be tracked directly. Figure 2.3b illustrates a typical measurement: Each maximum peak value corresponds to the total charge, which is located inside the probe at that time. Additionally, the decay of the charge can be observed. The calculation of the total charge $Q(t)$ at time t ,

induced in the Faraday cup, is based on the formula:

$$Q(t) = -CU(t) . \quad (2.3)$$

C is the capacitance of the capacitor, in our case C was 100 nF, and $U(t)$ is the measured voltage at a time point t . For further information, also see [40].

The main idea of the rotation was, to prevent the occurrence of a bias, i.e. current leakage can cause small errors. However, for our purposes, it is sufficient to obtain qualitative results, without the repeated rotation. An error of less than 10 % over 50 seconds allowed keeping the particle support statically inside the probe.

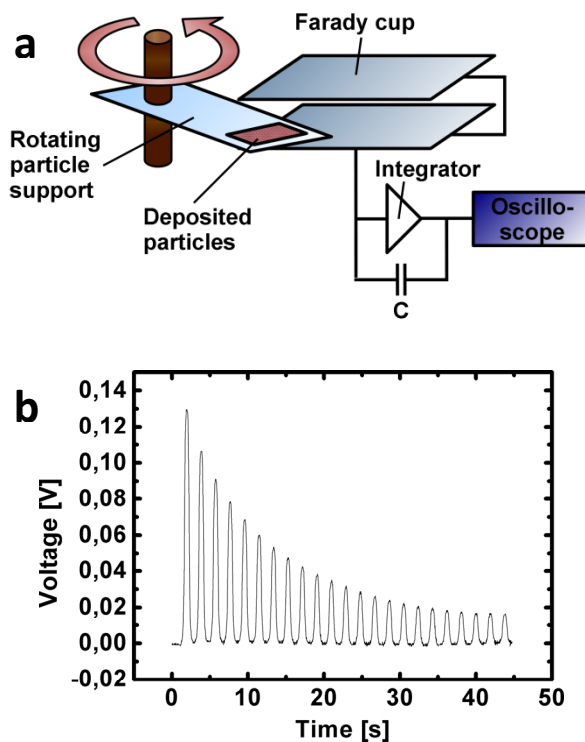


Figure 2.3: (a) The rotating particle electrometer principle, (b) typical measurement results.

The most remarkable result is that it is possible to observe the charge decay over time. Moreover, the decay of the charge is dependent on the particle support: Different glass

types yield different decay rates ([40]), which can be explained by different glass conductivities.

Exploring this phenomenon, the results in the context of the laser printer will be discussed in chapter 5, subsection 5.1.1.

3 Theory and simulations

This chapter describes the theoretical background and simulation of the laser printer and the chip-based method. First, the simulations of the laser printing process will be discussed (section 3.1). Secondly, the simulations of particle deposition on the CMOS chip will be elaborated in more detail (section 3.2), which can be considered as the main objective in this thesis. In a third approach, the simulations of a miniaturized CMOS chip pixel pitch will be evaluated (section 3.3), which allows for a higher spot density and, thus, for a higher peptide spot density, significantly increasing the efficiency.

Using the commercially available program COMSOL Multiphysics (COMSOL, Inc., USA), a finite element analysis solver and simulation software, several qualitative simulation results could be obtained, which can explain the underlying problems, stated in section 1.5.

3.1 Simulation of the laser printing process

The principle of the laser printer is based on the generation of a latent image on the organic photoconductor (OPC) drum, subsequent development of the image with toner particles, and finally, the transfer to the substrate (see subsection 1.4.1).

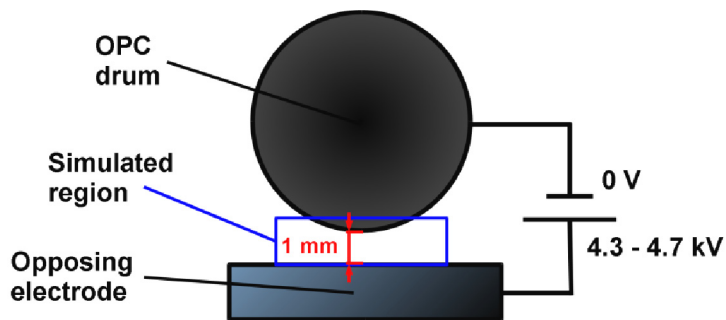


Figure 3.1: Laser printer simulation model. The OPC drum is located at a distance of 1 mm from a solid opposing electrode. All surfaces are assumed to be conductive, the OPC drum is grounded, the electric potential of the opposing electrode is varied between 4.3 and 4.7 kV.

and finally, the transfer to the substrate (see subsection 1.4.1).

Because the peptide laser printer has to transfer the pattern onto a glass substrate instead of a paper substrate, the rigidity and the greater thickness (1 mm instead of about 100 μm) of the substrate requires a small change in the printer setup: The opposing

electrode drum is replaced by a solid opposing electrode, which is moved together with the substrate. Additionally, due to the greater thickness of the substrate, the opposing electrode is located further away from the OPC drum.

On the one hand, the rigidity of the glass substrate has the advantage that the substrate can be reproducibly positioned. On the other hand, the rigidity decreases the particle adhesion forces to the substrate and fewer particles are transferred. Due to the positioning problems, softer substrate materials were discarded.

In Figure 3.1, a simplified model of the printing process is shown: The OPC drum (3 cm in diameter) is located in a distance of 1 mm from a solid opposing electrode. All surfaces are assumed to be conductive; the organic photoconductive layer is neglected. Furthermore, in this simple model, one can also neglect the dielectric glass substrate between the

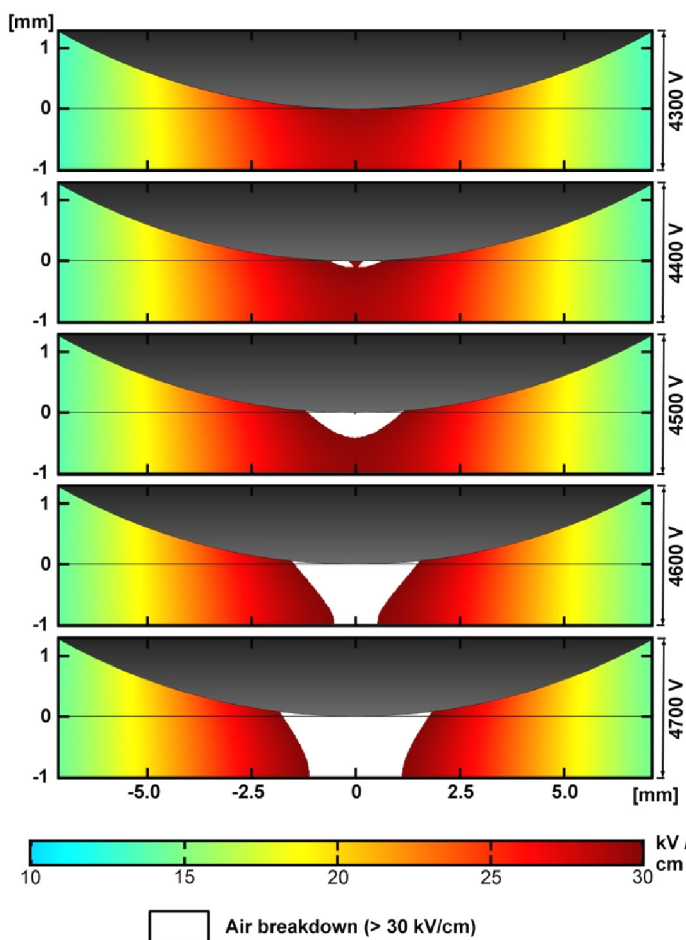


Figure 3.2: Simulation of the deposition region. The region is illustrated in Figure 3.1, different opposing electrode potentials are tested (4.3 – 4.7 kV). The area of air breakdown is shown in white.

about 30 kV/cm. This value is only an estimate, but seems to be valid for two opposing planar conductive surfaces. However, the critical value differs depending on the electrode geometry: If one of the plate electrodes is replaced by a spherical electrode, the critical value decreases with decreasing sphere radius ([41]). Yet, our estimate seems to offer a

electrodes. The OPC drum is grounded, the electric potential of the opposing electrode is varied between 4.3 and 4.7 kV. In COMSOL, this geometry was introduced and the Poisson equation was numerically solved with the relevant boundary conditions (OPC drum 0 V, opposing electrode 4.3 – 4.7 kV):

$$\Delta\varphi = \frac{\rho}{\varepsilon}.$$

The Poisson equation within charge-free space ($\rho = 0$) reduces to the Laplace equation.

Derived from the work of Hermstein from 1960 ([41]), an estimation of the critical electrical field for air breakdown resulted in

good qualitative approach to our problem, because the air breakdown field can be set to an arbitrary level, according to our requirements.

In Figure 3.2, the simulation of the region illustrated in Figure 3.1 for different opposing electrode potentials is shown. The electric air breakdown is depicted in white, which occurs at fields equal or greater to 30 kV/cm. At 4.3 kV, the phenomenon of air breakdown is not present. Gradually increasing the electrode voltage in 100 V steps, the region of assumed air breakdown grows.

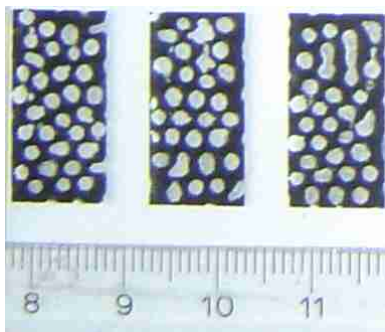


Figure 3.3: Gap phenomenon. OKI black particles transferred onto glass, resulting pattern with 4.3 kV transfer voltage.

These simulations can explain the phenomenon, which was observed during printing OKI black particles with 4.3 kV (see Figure 3.3). The gaps occur due to the high electrical fields, causing electrical breakdown of the air. The air breakdown will result in the discharge of particles, which are located between the OPC drum and the opposing electrode. This will cause the particles to remain on the OPC drum, instead of being transferred to the substrate.

Furthermore, one can now derive simple predictions from this model: If a certain critical voltage between the OPC drum and the opposing electrode is reached in the experimental setup, the phenomenon of air breakdown is possible. Another simple prediction is that with increasing voltage, the more particles will remain on the OPC drum, the gaps will grow in diameter.

These qualitative results have to be integrated into a more realistic picture of the experiments. Certain variations in the critical voltage were observed, it was dependent on the particle type, the substrate and other yet unknown factors. E.g., the “influence of absolute humidity on the electrical breakdown in air” ([42]) has to be taken into account, as well as the dielectric properties of the substrate, which is completely omitted in our simulations. Thus, these considerations will be further analyzed in the experimental section 5.1.

3.2 Simulation of the CMOS chip

In this section, the particle deposition on the CMOS chip will be theoretically analyzed. The

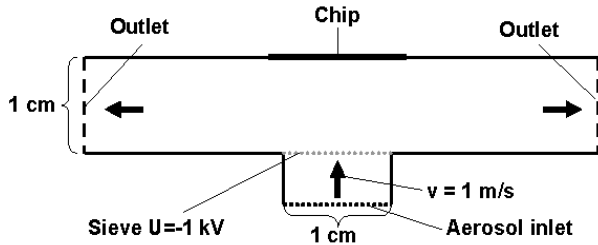


Figure 3.4: Schematic geometry of aerosol outlet and CMOS chip position above the air stream for particle deposition (from [43])

detailed geometry for the particle deposition is outlined in Figure 3.4. The aerosol, generated as described in the introduction (subsection 1.4.2.1), enters the geometry through the aerosol inlet. Afterwards, particles and possible agglomerates have to pass a sieve with negative voltage of 1 kV. The

implementation of the sieve is an anticipation of the experimental results (subsection 5.2.1): Due to the mesh size of about $25 \mu\text{m}$, only particles with a smaller diameter can pass the sieve, agglomerates are held back. Moreover, the sieve voltage acts as a particle sorter, separating particles by charge: Negatively charged particles, located between chip and sieve, are accelerated towards the chip; positively charged particles are decelerated and cannot reach the chip surface. Hence, positively charged particles are excluded from the aerosol stream. This reduces contaminations by restraining positively charged particles and particle agglomerations from entering the deposition region.

3.2.1 Forces and boundary conditions

The process of particle deposition comprises various different forces interacting with the particles. According to Newton's second law, all forces \mathbf{F} interacting with a single particle with mass m and acceleration \mathbf{a} will add up to $m\mathbf{a} = \sum \mathbf{F}$. First, one has to consider the geometry and the boundary conditions, which on the one hand leads to the fluid related forces and on the other hand to the electric forces. The latter are the most important forces, yet, other forces will be discussed and compared in the following subsections as well.

3.2.1.1 Fluid related forces

Because aerosols are particles suspended in a fluid (i.e. air), the Navier-Stokes equation, describing the fluid motion in our geometry, is essential for the simulations (also see [44],

[45]). However, due to its complexity, several presumptions are possible, simplifying the Navier-Stokes equation before implementation: First, one can assume that particle movement does not influence the surrounding air flow and that particle-particle interaction (e.g. collision) is small due to a low aerosol density and can therefore be neglected. In order to apply the (simplified) static incompressible Navier-Stokes equation with laminar flows, two parameters have to be considered: the Mach number Ma and the Reynolds number Re . For a thorough introduction to this field, see [45].

The *Mach number* ([45]) describes whether a compressibility of the fluid is relevant in the calculations of a specific problem. It is defined as:

$$Ma = \frac{v}{v_{\text{sound}}} \approx \frac{1}{343} \quad (3.1)$$

In our case, the sound velocity in air is 343 m/s (at 20 °C, 1 bar) and the velocity of our fluid is about 1 m/s. The fluid flow can be assumed as incompressible if $Ma \ll 1$. Thus, in our case the fluid flow is in fact incompressible.

The *Reynolds number* ([44]) is also defined as a dimensionless number, in our case describing the flow conditions of the air, predicting whether the flow is turbulent or laminar:

$$Re = \frac{\rho_{\text{air}} v L}{\eta_{\text{air}}} \approx 656 \quad (3.2)$$

$\eta_{\text{air}} = 18.36 \cdot 10^{-6}$ Pa·s (at 20 °C) is the dynamic viscosity of air, $\rho_{\text{air}} = 1.2$ kg/m³ (at sea level, 20 °C) is the density of air, $v = 1$ m/s is the velocity of the air, and $L = 0.01$ m is the diameter of the tube in our geometry (Figure 3.4). The critical Reynolds number, where the flow in a tube is assumed to be still laminar is about $Re_{\text{crit}} \approx 1000$, thus, the flow in our case can be assumed as laminar.

Concluding from these results and expecting that the fluid flow can be described as static, the solution of the static incompressible Navier-Stokes equation is sufficient for a complete description of a laminar air flow in our geometry. The incompressible Navier-Stokes equation (without external forces) can be written as:

$$\rho_{\text{air}} \left(\frac{\partial \mathbf{v}}{\partial t} + (\mathbf{v} \cdot \nabla) \mathbf{v} \right) = -\nabla p + \eta_{\text{air}} \Delta \mathbf{v} \quad (3.3)$$

with $\nabla \cdot \mathbf{v} = 0$

These equations are dependent on the dynamic viscosity η_{air} of air and the air density ρ_{air} , as well as the air velocity field \mathbf{v} and the scalar pressure field p . In our geometry (Figure 3.4), the velocity at the inlet is 1 m/s, the pressure at the outlets is 1 bar (laboratory atmosphere), and all other boundaries were set to the no-slip condition (i.e. fluid velocity is zero at the boundary).

Considering a particle in the air flow, one has to calculate the particle Reynolds number, to determine if the flow around the particle is laminar:

$$\text{Re}_{\text{part}} = \frac{\rho_{\text{air}} |\mathbf{v}_{\text{air}} - \mathbf{v}_{\text{part}}| d_{\text{part}}}{\eta_{\text{air}}} \leq 0.07 \quad (3.4)$$

It is dependent on the dynamic viscosity of the fluid η_{air} , the air density ρ_{air} , the particle diameter d_{part} ($\leq 10 \mu\text{m}$), and the relative velocity of the particle to the flow ($\leq 1 \text{ m/s}$). Because the particle Reynolds number is smaller than 0.1, the flow around the particle can be considered as laminar and the Stokes' law is applicable.

Thus, the Stokes' law sufficiently describes the drag force \mathbf{F}_{drag} exerted on a particle, due to the friction of the particle with the fluid. It depends on the particle diameter d , the dynamic viscosity of the air η_{air} , the air velocity field \mathbf{v}_{air} in our geometry (Figure 3.4), and the particle velocity \mathbf{v}_{part} . Hence, the Stokes' drag force is defined as:

$$\mathbf{F}_{\text{drag}} = 3\pi d \eta_{\text{air}} (\mathbf{v}_{\text{air}} - \mathbf{v}_{\text{part}}) \quad (3.5)$$

However, the Stokes' drag force is only valid if the surrounding fluid can be considered as a continuum: With decreasing particle diameter, Brownian motion becomes relevant. The importance of the latter can be estimated with the particle Knudsen number K_n ([45]):

$$K_n = \frac{\lambda_{\text{air}}}{d_{\text{part}}/2} \quad (3.6)$$

The particle Knudsen number is calculated by the ratio of mean free path length of air λ_{air} ($\sim 68 \text{ nm}$) and the particle radius $d_{\text{part}}/2$. If $K_n \ll 1$, the surrounding fluid can be assumed as a continuum. In our case, the drag force for smaller particles needs to be

corrected with the Cunningham slip correction factor C_C , a phenomenological factor which can be approximated as $C_C = 1 + 1.14 \cdot K_n$ for particle diameters greater than or equal to $1 \mu\text{m}$:

$$\mathbf{F}_{\text{corr,drag}} = \frac{\mathbf{F}_{\text{drag}}}{C_C} \quad (3.7)$$

The influence of the particle diameter on particle dynamics can be qualitatively demonstrated by the stopping distance S

Table 3.1: Stopping distance S for different particle diameters d with corresponding Knudsen number K_n and Cunningham correction factor C_C ; initial velocity is $v = 1\text{m/s}$

d [μm]	K_n	C_C	τ [s]	$S_{v=1\text{ m/s}}$ [μm]
3	0.04	1.05	$28 \cdot 10^{-06}$	28
5	0.03	1.03	$77 \cdot 10^{-06}$	77
10	0.01	1.01	$305 \cdot 10^{-06}$	305

of a particle, which is defined as the product of initial particle velocity v_0 and the relaxation time τ of a particle, which in turn is the time needed, until a particle with no initial velocity, released into a moving fluid, reaches $(1 - 1/e) \approx 63.2\%$ of its final velocity v_f . Hence, the relaxation

time is defined as ([44]):

$$\tau = \frac{\rho_{\text{part}} d_{\text{part}}^2 C_C}{18 \eta_{\text{air}}}, \quad (3.8)$$

whereas ρ_{part} is the density of the particle matrix and d_{part} the particle diameter, η_{air} is the dynamic viscosity of the air. As shown in Table 3.1, the stopping distance decreases quickly with the particle diameter, resulting in a lower deviation of the particle trajectories from the fluid flow with decreasing diameter.

In contrast to the previously introduced drag force equations (3.5 and 3.7), for the COMSOL simulations, instead of using the Stokes' drag force \mathbf{F}_{drag} with complex corrections, a generalized force \mathbf{F}_{KR} , called Khan Richardson force, was used ([46]). The Khan Richardson force is partly based on experimental results and is applicable for a wide range of particle Reynolds numbers Re_{part} (see equation 3.4). The Khan Richardson force affecting a spherical particle with the diameter d in a surrounding fluid is defined as:

$$\mathbf{F}_{\text{KR}} = \frac{\pi}{4} d^2 \rho_{\text{air}} \left| \mathbf{v}_{\text{air}} - \mathbf{v}_{\text{part}} \right| \left(\mathbf{v}_{\text{air}} - \mathbf{v}_{\text{part}} \right) \left(1.84 Re_{\text{part}}^{-0.31} + 0.293 Re_{\text{part}}^{0.06} \right)^{3.45}, \quad (3.9)$$

\mathbf{v}_{part} and \mathbf{v}_{air} are the corresponding velocities of the particle and the surrounding air that can be assumed as a laminar fluid with the dynamic viscosity η_{air} and the density ρ_{air} . For an accurate air flow simulation, the specific geometry (Figure 3.4) has to be taken into account. The initial aerosol stream velocity at the inlet is 1 m/s, the sieve was not taken into consideration for air stream deceleration, because the experimentally determined aerosol velocity was measured after passing the sieve. One can assume that local air turbulences at the sieve, due to the small mesh size, can be neglected, as the distance between chip and sieve is much larger than the mesh size.

The gravitational force F_g will be discussed and compared in the overview subsection, the buoyancy force F_b of the air can be neglected, being about three orders of magnitude smaller than the gravitational force.

Although assumed in [27] and [47], the centripetal force, in fact, is already included in the force calculation of the drag force. Thus, the centripetal force is an intrinsic part of the drag force, which fully describes the particle movement in a fluid due to fluid friction.

3.2.1.2 Electric forces

Defining the electric properties of the boundaries of our geometry (Figure 3.4), the sieve was set to an electric potential of -1 kV, the chip electrodes were set to either 0 or +100 V, and all other boundaries were defined as insulators. Assuming that the particles do not significantly disturb the electric potential of the boundaries, the electric field \mathbf{E} inside of the geometry can be calculated solving the Poisson equation with the charge density ρ_f inside of the geometry being zero:

$$\Delta\varphi = 0 \quad (3.10)$$

Consequently, the following electric forces acting on a moving particle have to be considered: The electric force \mathbf{F}_{el} , the dielectrophoretic force \mathbf{F}_{dep} , and the electric image force \mathbf{F}_{img} . These electric forces occur due to the electric charge of the particles, their dielectric properties, and the electric fields emanating from the metal electrodes of the CMOS chip.

Using the presented particle charge measurement techniques, the mean particle charge to mass ratio was about $q/m = -3 \cdot 10^{-3}$ C/kg (see subsection 2.1.1).

The electric force \mathbf{F}_{el} results from the particle charge q_{part} and the electric field \mathbf{E} , due to applied voltages on charged surfaces, in our case the chip and the sieve:

$$\mathbf{F}_{el} = \mathbf{E} q_{part} \quad (3.11)$$

The dielectrophoretic force, resulting from the polarization of the dielectric particle material is defined as:

$$\mathbf{F}_{dep} = 2\pi \left(\frac{d_{part}}{2}\right)^3 \varepsilon_0 \varepsilon_1 \frac{(\varepsilon_2 - \varepsilon_1)}{(\varepsilon_2 + 2\varepsilon_1)} \text{grad}(|\mathbf{E}|^2) \quad (3.12)$$

It features the vacuum permittivity ε_0 and relative permittivities of air $\varepsilon_1 = 1$ and of the particle $\varepsilon_2 = 4$ (see [48]).

Anticipating some results from the coming simulations, the dielectrophoretic force $F_{dep,y}$ in chip direction at 50 μm distance from the chip surface could be estimated and compared with the electric force F_{el} in the same location:

$$\text{with } \varepsilon_0 = 8.85 \cdot 10^{-12} \frac{\text{F}}{\text{m}}; \varepsilon_1 = 1; \varepsilon_2 = 4; \frac{d}{2} = 10 \mu\text{m}; \frac{\partial}{\partial y} |\mathbf{E}|^2 \approx 10^{14} \frac{\text{V}^2}{\text{m}} \quad (3.13)$$

$$\text{results to } F_{dep,y} \approx 2.8 \cdot 10^{-12} \text{ N}; F_{el} \approx 1.4 \cdot 10^{-9} \text{ N}$$

Because the dielectrophoretic force is about 3 orders of magnitude smaller than the mean electric forces, the dielectrophoretic force plays a negligible role in static electric fields, as in our CMOS chip-based application.

The image force is defined as:

$$\mathbf{F}_{img} = \frac{q_{part}^2}{4\pi\varepsilon_0 a_{p,S}^2} \quad (3.14)$$

It depends on the particle charge q_{part} , and the distance of the particle to the metal surface $a_{p,S}$. The resulting interaction with the metallic chip surface in a distance of 50 μm can be calculated as $F_{img} = 2.3 \cdot 10^{-12}$ N and is therefore also negligible.

3.2.1.3 Overview and estimations of forces

To give an overview and estimations of the occurring forces acting on a particle in our geometry, all mentioned relevant forces are summarized in Table 3.2.

All estimations were calculated for particle diameters of 2 and 20 μm . The drag force was estimated with a maximum particle velocity of 1 m/s relative to the air. For the dielectrophoretic force and the image force the forces were estimated in 50 μm distance of the chip surface.

In a more complete picture, the adhesion force F_{adh} also needs to be mentioned, which plays an important role after particles were deposited. According to [49], the adhesion force can be simulated using the van-der-Waals force, the capillary force, and electric forces. The estimations for the adhesion force were derived from the simulations in [49]. Hence, deposited particle patterns will keep their spatial position, even when depositing additional different particle patterns onto the chip subsequently, because the adhesion force is much higher than the corresponding drag force.

Table 3.2: Formulas and estimations of the relevant forces acting on a particle in the geometry.

Force	Formula	Estimation [N]
Adhesion force	see text ([49])	$10^{-6} - 10^{-8}$
Drag force	$\mathbf{F}_{\text{drag}} = 3\pi d_p \eta_{\text{air}} (\mathbf{v}_{\text{air}} - \mathbf{v}_p)$	$10^{-8} - 10^{-12}$
Electric force	$\mathbf{F}_{\text{el}} = \mathbf{E} q_p$	$10^{-8} - 10^{-12}$
Gravitational force	$\mathbf{F}_g = mg$	$10^{-11} - 10^{-14}$
Dielectrophoretic force	$\mathbf{F}_{\text{dep}} = 2\pi \left(\frac{d_p}{2}\right)^3 \epsilon_0 \epsilon_1 \frac{(\epsilon_2 - \epsilon_1)}{(\epsilon_2 + 2\epsilon_1)} \text{grad}(\mathbf{E} ^2)$	$10^{-12} - 10^{-15}$
Electric image force	$\mathbf{F}_{\text{img}} = \frac{q_p^2}{4\pi\epsilon_0 a_{p,S}^2}$	$10^{-10} - 10^{-16}$

Concluding from these estimations, one can certainly neglect the gravitational force for micro particles with a diameter of about 20 μm or less. Considering a micro particle with a diameter of 20 μm and a charge per mass ratio $q/m = -3 \cdot 10^{-3} \text{ C/kg}$, located 50 μm beneath the chip surface, the estimations reveal that the dielectrophoretic force F_{dep} is at least three orders of magnitude smaller than the electrical force. The image force, resulting from the particle charge interacting with the metallic chip surface in a distance of 50 μm can be calculated as $F_{\text{img}} = 2.3 \cdot 10^{-12} \text{ N}$. Both $(F_{\text{dep}}, F_{\text{img}})$ are therefore negligible.

Thus, for our simulations, only two forces are necessary to describe the particle dynamics and deposition on the CMOS chip: the electrostatic force F_{el} and the drag force F_{drag} . Hence, electrical and drag force add up to the total force F_{part} , affecting a single particle:

$$\mathbf{F}_{\text{part}} = \mathbf{F}_{\text{el}} + \mathbf{F}_{\text{drag}} \quad (3.15)$$

In Figure 3.5, these relevant forces were evaluated for two different relative particle velocities: the drag force is compared with the electric forces of two different voltages. Figure 3.5 left shows the forces acting on a particle with 20 μm diameter, Figure 3.5 right shows the forces acting on a particle with 2 μm diameter. The drag force clearly dominates in the case of small particles. The electric field E was estimated with $E = U/L$, where U is the voltage (100 V or 30 V) and L is the pixel pitch (100 μm). The 30 V electrodes will be introduced in the following subsections in respect to the grid electrode voltage.

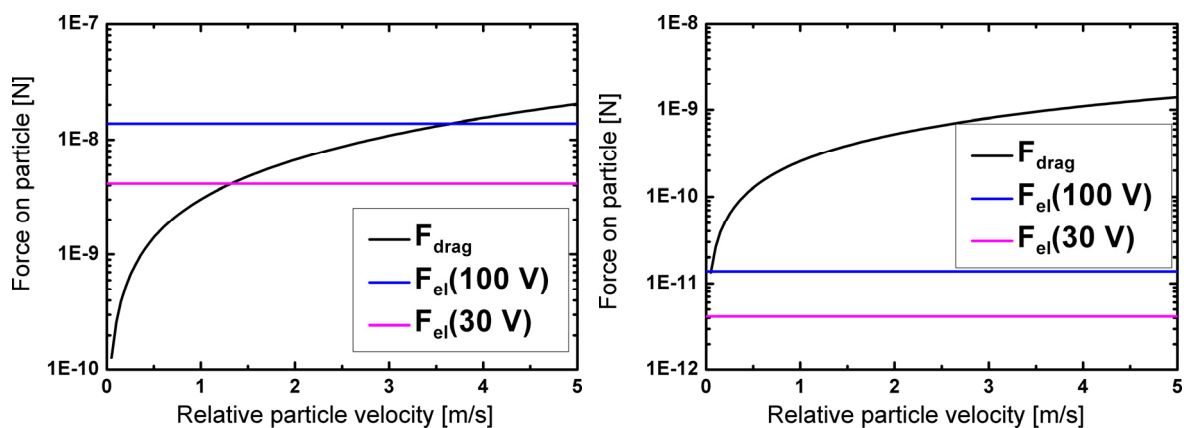


Figure 3.5: Relevant forces on a particle. (left) Particle with diameter 20 μm and (right) 2 μm diameter. The drag force dominates in the case of small particles.

Naively considered, these estimations might lead to the following conclusion: The movement of smaller particles is dominated by the drag force, which seems to be unfavorable. In contrast, bigger particles are mainly controlled by the electric forces.

However, the following subsections will identify a different interpretation of this relation: In fact, the drag force has not only negative effects on particle deposition, but also decelerates particles in proximity of the chip surface (also see stopping distance), providing more time and precision for a selective deposition mediated by the electric fields.

3.2.2 Geometry and boundary simulation

Previously, the problem was approached with MATLAB (MathWorks, Inc., USA), a commercially available numerical computing environment and programming language, together with the partial differential equation toolbox. It was possible to obtain first results for single particle simulations. However, MATLAB was experienced to be computationally intensive and, thus, time consumption was high. The comfortable geometry editor and the easy implementation of the Navier-Stokes equation in COMSOL made the application of MATLAB unnecessary.

Therefore, the following simulations for particle deposition analysis were obtained with the commercially available program COMSOL Multiphysics (COMSOL, Inc., USA), a finite element analysis solver, and simulation software.

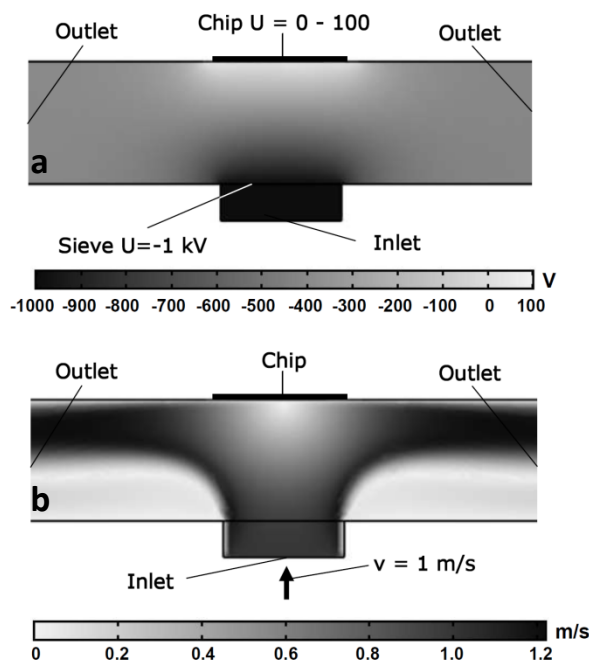


Figure 3.6: Simulation for the specific geometry as shown in Figure 3.4. (a) air velocity field; (b) electrostatic potential (from [43])

First, the stationary Navier-Stokes equation for the incompressible air flow was solved: The geometry shown in Figure 3.4 was discretized by means of Lagrange finite elements with an average area ratio of $2.6 \cdot 10^{-5}$ each compared to the total area. This fine triangulation guarantees a good numerical solution to the incompressible Navier-Stokes equation, which was linearized and solved up to a relative uncertainty of 10^{-6} by the standard solver for stationary, non-linear differential equations. Second, the Poisson equation for the electrical field on the chip surface

was solved on the same triangulation up to a relative uncertainty of 10^{-6} using the standard solver for electrostatic problems. Finally, particle trajectories were simulated, established on the solutions for the air velocity field and the electrical field in our geometry. The relative error tolerance of the solver basing on the Runge-Kutta methods of order four and five was also set to 10^{-6} .

In Figure 3.6a, the air velocity field is shown. The boundaries were assumed to exhibit the no slip condition, the inlet air velocity was 1 m/s, and the outlets were both set to comprise a pressure of 10^5 Pa. The density and the dynamic viscosity of the fluid were set to the coefficients $\rho_{\text{air}} = 1.293 \text{ kg/m}^3$ and $\eta_{\text{air}} = 17.1 \text{ } \mu\text{Pa} \cdot \text{s}$. In Figure 3.6b, the simulated electrostatic potential is shown for the geometry outlined in Figure 3.4. All boundaries, except for the chip and the sieve, were assumed to have no charge.

Based on the calculated spatial distribution of forces, particle trajectories can be simulated.

3.2.3 Particle deposition concept and simulation

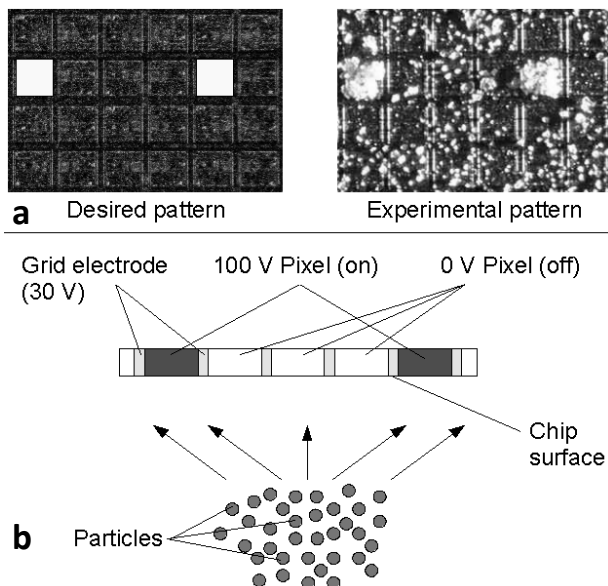


Figure 3.7: Desired particle deposition pattern (a, left, scheme) and experimentally achieved pattern (a, right); (b) schematic of particle deposition on a chip. Particles move towards the chip and are manipulated by electrical fields resulting from the voltage pattern on the chip surface to enable spatial defined particle deposition (from [43])

Particles, passing the sieve, enter the deposition region where the electrical fields between chip and sieve selectively guide the aerosol particles to the active deposition areas. Comparing the desired deposition pattern in Figure 3.7a (left) with the one obtained in a deposition experiment (Figure 3.7a right), contaminations can be observed, indicating that the deposition conditions in practice still have to be improved. It was experimentally verified that the more pixels are switched off in a voltage pattern on the chip surface, the more contaminations on these pixels could be observed after deposition.

To investigate the causes of contamination, a two-dimensional simulation model has been designed, as detailed in Figure 3.7b: Particles with a predefined size and negative charge are attracted by the electrical field of the chip. The latter is modeled by two active pixels set at 100 V separated by three inactive pixels at 0 V each. Taking into account that the average particle diameter is about 5 – 10 % of the size of one pixel, nine pixels are a sufficient chip detail to investigate the effects observed in experiments: Therefore, the entire chip does not have to be modeled for the simulation. Motivated by experiments, another pattern was modeled which consisted of two active pixels separated by seven inactive pixels as this combination showed a high probability of contamination.

Particles were injected into the air stream (see Figure 3.4 and Figure 3.6) in a distance of about 1 cm away from the chip surface (near the sieve) with an initial particle and air stream velocity of $v_0 = 1$ m/s in chip direction. Larger initial velocities up to 5 m/s were also simulated, but, the velocity variation in this range does not lead to a significant change in particle deposition and is therefore not considered in this article. The exponential decrease of electrical field intensity emanating from the chip thereby confines the region of interest, where the selective effect of the chip dominates particle manipulation. Simulations showed

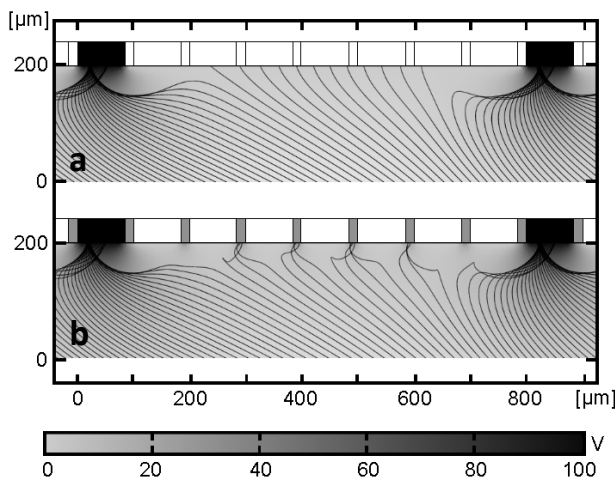


Figure 3.8: Grid electrode. Simulation detail of particle deposition on a chip; particles are 10 μm in diameter and feature a q/m value of $-3 \cdot 10^{-3}$ C/kg; (a) the voltage of the grid electrode is 0 V, several particles are deposited as contaminations on deactivated pixels; (b) voltage of the grid electrode is 30 V, excess particles are solely deposited on the grid electrode (from [43])

that this region extends only 200 μm from the chip surface, as subsequently demonstrated.

In the simulations, the charge per mass ratio (q/m value) of the particles and the particle diameter were systematically varied. The sieve voltage was set to -1 kV, high enough to have an abundant selective effect on particles, and low enough not to risk destroying the chip by electrical breakdown and arc-over between sieve and chip. Pixel voltages on the chip were set to 100 V, the technical limit of the microchip used, and 0 V to obtain the greatest possible selective effect. The

voltage of the grid electrode was set to 0 V (Figure 3.8a) or 30 V (Figure 3.8b).

The effect of the grid electrode on particle deposition is illustrated in Figure 3.8. Particle trajectories are represented as black lines; the electrical potential in V is shown in gray scale. Above the trajectories, the voltage pattern on the chip surface is indicated: Two pixels are switched to high voltage, in between 7 grounded pixels are located.

Particles with a diameter of 10 μm and a q/m value of $-3 \cdot 10^{-3}$ C/kg are deposited on the chip. In Figure 3.8a, the grid electrode is grounded, just like the switched off pixels. Excess particles will reach the chip surface and will be deposited not only on the grid electrode, but also on the grounded pixels, causing contaminations. In comparison to this, Figure 3.8b shows the same particle deposition with the grid electrode set to 30 V. Particles, which are not deposited on the desired pixels, are solely deposited on the grid electrode. This allows using the grid electrode as an adsorber for excess particles, as long as not too many particles are deposited on the grid electrode. Thus, the described effect of the grid electrode is important for contamination free particle deposition. In all further simulations, the grid electrode is switched to 30 V.

3.2.4 Effect of the particle diameter on deposition

In the simulation shown in Figure 3.9, the particle size was altered between 3 and 10 μm ((a) 3 μm ; (b) 5 μm ; (c) 10 μm) and the charge per mass ratio (q/m value) of the particles was defined as $-3 \cdot 10^{-3}$ C/kg in all three cases.

The particle deposition in Figure 3.9a features very few deposition events on the chip surface. In Figure 3.9b and c, the number of deposition events rises with particle diameter. In this simulation, all particles are deposited either on the 100 V pixels or on the grid electrode, which resembles the ideal and desired deposition pattern.

In contrast to this simulation, experiments exhibit a crucial difference: Particles with a mean diameter of 10 μm or greater tend to be deposited on both active and grounded pixels and hence cause contaminations.

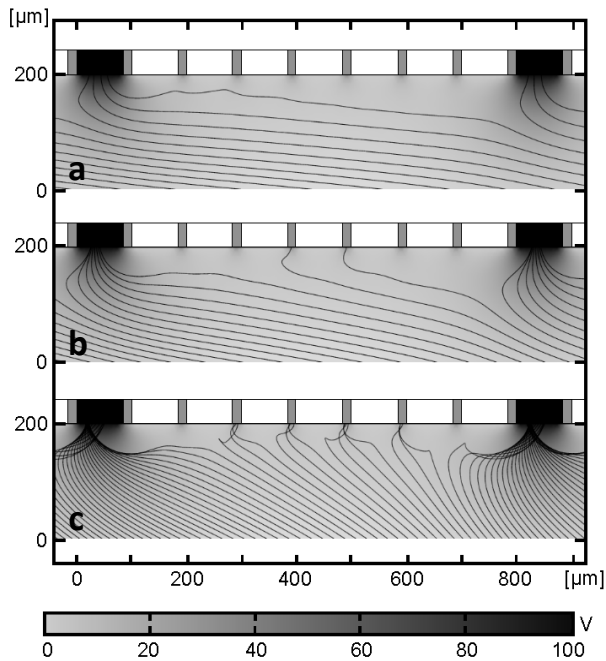


Figure 3.9: Simulation of particle deposition on a chip. Particle trajectories are represented as black lines, grayscale represents the electrical potential [V]; particle diameters are (a) 3 μm , (b) 5 μm , (c) 10 μm ; with q/m value of $-3 \cdot 10^{-3}$ C/kg; in all cases no contamination on grounded pixels occurs (from [43])

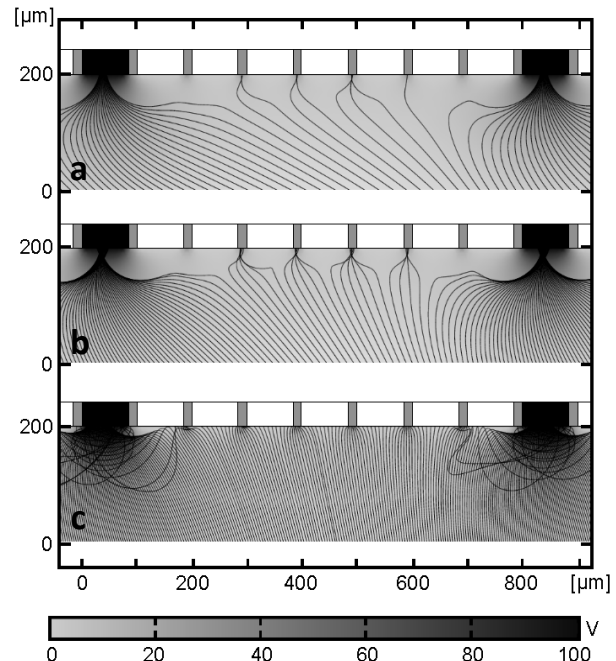


Figure 3.10: Simulation of particle deposition on a chip. Particle trajectories are represented as black lines, grayscale represents the electrical potential [V]; particle diameters are (a) 3 μm , (b) 5 μm , (c) 10 μm ; with q/m value of $-3 \cdot 10^{-2}$ C/kg; in (a, b) no contamination on grounded pixels occurs in contrast to (c) (from [43])

Now, the q/m value was altered in one order of magnitude. In Figure 3.10, a value of $-3 \cdot 10^{-2}$ C/kg was used. In Figure 3.9 and Figure 3.10, the same number of starting particles was simulated, but the overall number of deposition events on the chip surface has risen. In Figure 3.10a and b the particle deposition is still as desired, without contamination. In Figure 3.10c many particle trajectories end on grounded pixels, indicating contamination. Some trajectories near the 100 V pixels are incorrect due to the lack of adhesion forces, making odd bends near the chip surface.

Intuitively, one would expect, that particles with a higher q/m value are easier to manipulate by electrical fields and therefore should yield a better deposition quality. However, this is not the case in the given configuration. A higher q/m value combined with a larger inert mass will cause particles to divert from their appointed path, determined by the electrical field configuration. Due to the electrical potential between chip and sieve, particles with a higher charge are accelerated more intensely towards the chip. Hence, the efficiency of the selective local fields of the chip declines and the deposition quality decreases. Moreover,

this also entails, that more particles will reach the chip surface, visible in the simulations as a higher overall number of deposition events.

These results imply that highly charged particles are an intrinsic characteristic of the aerosol created in our experiments. As stated in [40], highly triboelectrically charged particles with a surface charge density two orders higher than the critical surface charge density in air were observed. This seemingly paradox value was documented to be a common result for particles ([50], [51]). In fact, the critical surface charge density, defined as the value where electrical breakdown between two parallel metal plates occurs, is invalid for dielectric particles. Due to the curvature of a particle surface and their dielectric character, higher electrical surface fields are possible without electrical breakdown, allowing microscopic particles to maintain higher charges than macroscopically planar metal surfaces.

Concluding, a greater particle diameter yields higher particle inertia. On the other side, bigger particles possess a higher total charge. This leads to the result that a larger particle diameter causes contaminations in this case of spatial defined particle deposition by means of an aerosol.

3.2.5 Long-range electrical fields

Another interesting effect, connected with the sieve voltage, is delineated in Figure 3.11.

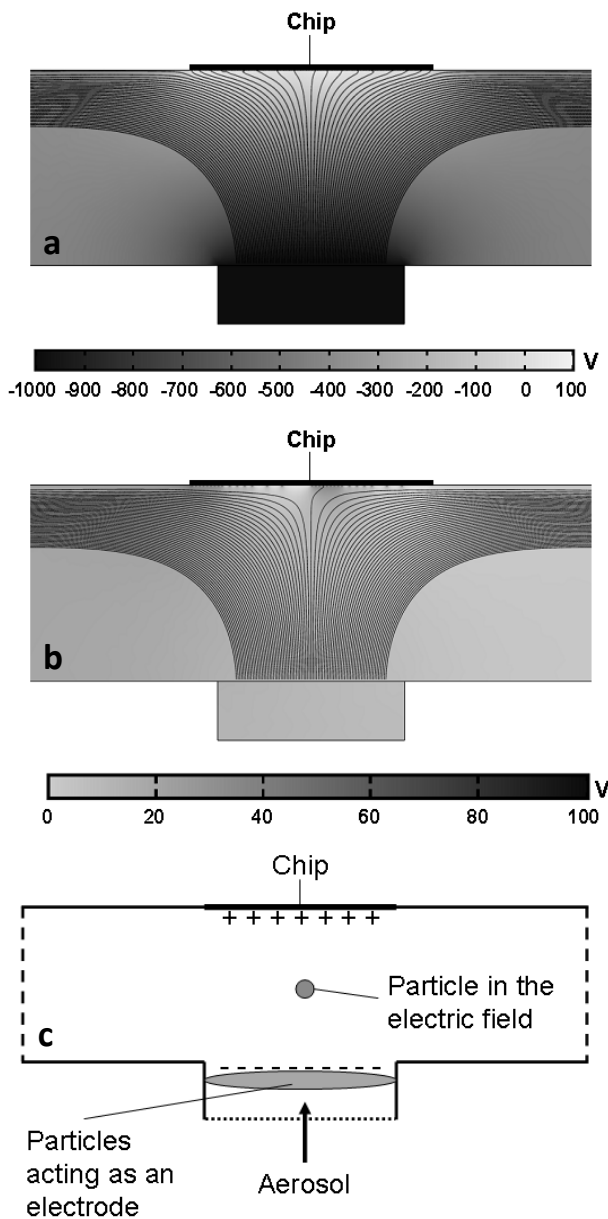


Figure 3.11: Simulation of particle deposition on a chip. The electrostatic potential [V] is shown in grayscale, particle trajectories are shown as black lines; particles are $10\ \mu\text{m}$ in diameter and possess a q/m value of $-3 \cdot 10^{-3}\ \text{C/kg}$; (a) the voltage of the sieve is $-1\ \text{kV}$, several particle trajectories end on the chip surface; (b) the voltage of the sieve is $0\ \text{V}$, only one single particle trajectory ends on the chip surface; (c) schematic of a particle in the electrical field resulting from the charge of the aerosol and the chip surface, acting as opposing electrodes (from [43])

Grayscale represents the electrostatic potential between the chip surface and the sieve. Particle trajectories are shown starting at the sieve and ending at the outlets or on the chip surface. The simulations were started with 80 particles with a diameter of $10\ \mu\text{m}$; the q/m value was set to $-3 \cdot 10^{-3}\ \text{C/kg}$. In Figure 3.11a, 17 out of 80 particles are deposited on the chip, the remaining particles move past the chip without being deposited and leave the deposition region through one of the outlets. In Figure 3.11b, the voltage of the sieve was set to $0\ \text{V}$ instead of $-1\ \text{kV}$. In this case, all 80 particles, except for one, move past the chip without being deposited. Only one single trajectory ends on the chip surface. The significant discrepancy in the number of deposited particles evolves in (a) due to the attracting force in chip direction, generated by the electrostatic potential between chip and sieve and in (b) due to the non-existing force, because the sieve is grounded.

This effect can also be observed when the number of particles in the simulation is increased by a factor of 10: Beginning with 800 instead of 80 particles, the simulation with no sieve voltage yielded only 7

deposited particles, whereas in the simulation with activated sieve voltage, 178 particles were deposited on the chip.

The experiment, in comparison, offers a completely different picture: Applying no voltage to the sieve, a lot of particles are deposited on the chip surface, which could not even be reproduced in simulations by altering the q/m value of the particles.

It was proposed that the charged aerosol particles in the experiment have an effect similar to the sieve with a voltage of -1 kV on particles, located between the outlet and the chip. In Figure 3.11c therefore, the total charge of a particle cloud acts as a negative electrode. If a uniform distribution of 0.1 mg of particles with 10 μm in diameter is assumed (about $1.7 \cdot 10^5$ particles) and a q/m value of $-3 \cdot 10^{-3}$ C/kg over a surface area of 1 cm^2 , one can substitute the sieve voltage in the simulation with a constant area charge density of $\delta = -2.7 \cdot 10^{-6}$ C/m², representing the charge of 0.1 mg particles. This resulted in an electrostatic potential of

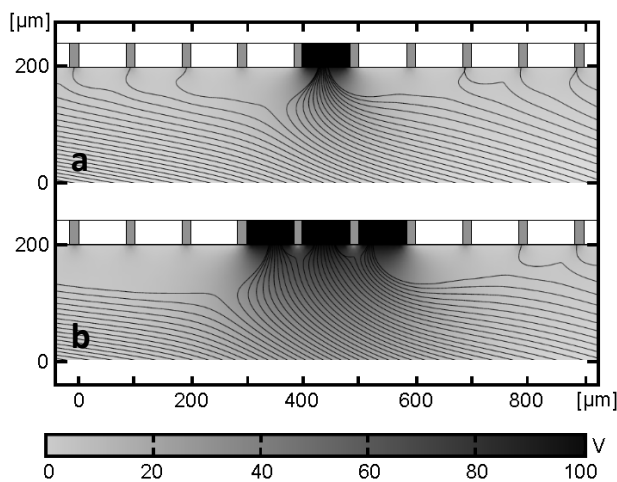


Figure 3.12: Simulation of particle deposition on a chip. The electrostatic potential [V] is shown in gray scale, particle trajectories are shown as black lines; particles are 5 μm in diameter and possess a q/m value of $-3 \cdot 10^{-3}$ C/kg; (a) one pixel with 100 V is neighbored by 0 V pixels; particles tend to be deposited on the middle of the 100 V pixel; (b) three adjacent pixels with 100 V are neighbored by 0 V pixels; particles are deposited equally distributed on the 100 V pixel in the center, particles deposited on the left and right 100 V pixel tend to be deposited on the side of the pixel, into direction of the center pixel (from [43])

about -2 kV in proximity of this simulated particle layer, which then yielded the effects obtained in experiments, explaining the discrepancy between simulation and practical observations.

Thus, the sieve and the applied voltage provide an important tool in particle manipulation, due to long-range electrical fields comparable to a particle cloud. Additionally, the sieve provides for the possibility to sustain reproducible and constant electrical fields.

3.2.6 Field superposition

Another noticeable result using the fine particle fraction is shown in Figure 3.12:

Particles with a diameter of 5 μm and a

q/m value of $-3 \cdot 10^{-3}$ C/kg were simulated. The electrical charge pattern on the chip (Figure

3.12a) comprised one single 100 V pixel. Here, particles tend to be deposited only at the center of the active pixel. In Figure 3.12b, a similar effect was observed with three adjacent 100 V pixels, neighbored by 0 V pixels. In this case, particles are uniformly deposited on the central 100 V pixel, while the active pixels to the left and right of the central one are only half covered at the side adjacent to the central pixel. This simulated effect coincides with observations in experiments (Figure 5.18) and can be explained by the superposition of electrical fields. When attracting and repelling fields of direct adjacent 0 V and 100 V pixels unite, electrical fields are altered, such that particles will be deposited as observed in Figure 3.12 and Figure 5.18.

While the effect in Figure 3.12a is still acceptable for particle deposition, the result shown in Figure 3.12b is insufficient for combinatorial peptide syntheses.

3.2.7 Restriction of deposition layer thickness

An important restrictive effect in the selective particle deposition is illustrated in Figure 3.13: A simulation of particles with a diameter of 5 μm ($q/m = -3 \cdot 10^{-3} \text{ C/kg}$) is shown. In Figure 3.13a and c, a 10 μm thick pre-deposited particle layer is shown, represented by a black rectangle with a surface charge of $2.7 \cdot 10^{-5} \text{ C/m}^2$ (a) and $5.4 \cdot 10^{-5} \text{ C/m}^2$ (c), which represents

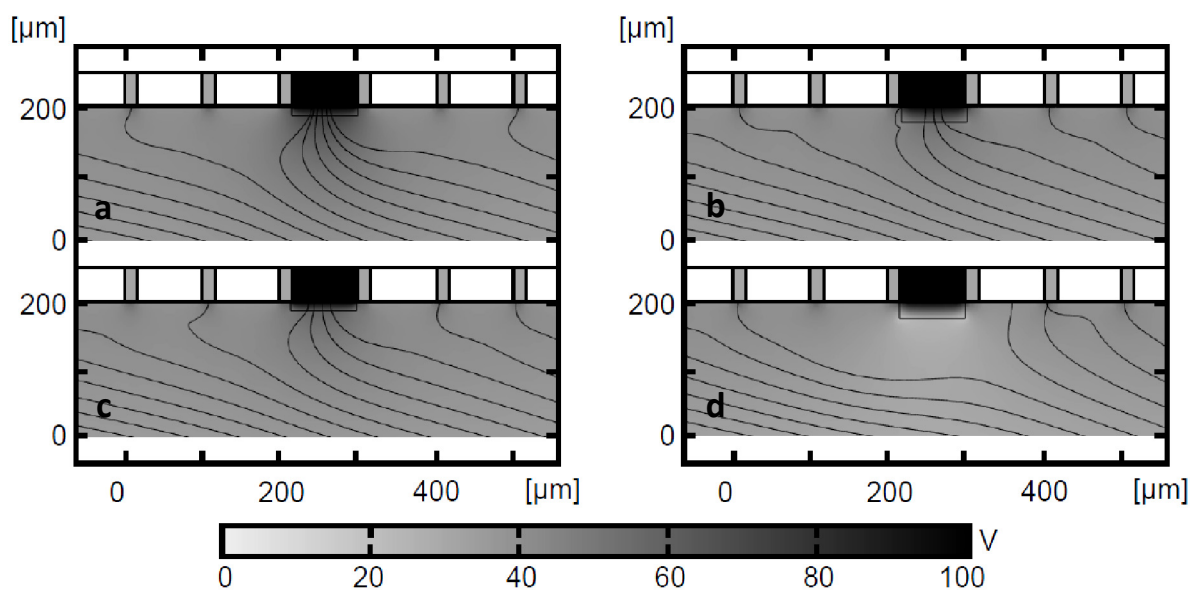


Figure 3.13: Simulation of particles with a diameter of 5 μm , deposited onto a chip. (a, c) show a 10 μm particle layer (black rectangle), surface charge is $2.7 \cdot 10^{-5} \text{ C/m}^2$ (a) and $5.4 \cdot 10^{-5} \text{ C/m}^2$ (c); (b, d) show a 20 μm particle layer, surface charge is $2.7 \cdot 10^{-5} \text{ C/m}^2$ (b) and $5.4 \cdot 10^{-5} \text{ C/m}^2$ (d). (from [32])

the possible surface charge range of a deposited particle layer. Fewer particles are deposited on the 100 V pixel in the bottom left picture, because of the increased repulsive force of the particle layer. In Figure 3.13b and d, a 20 μm thick pre-deposited particle layer is shown, again represented by a black rectangle with a surface charge of $2.7 \cdot 10^{-5} \text{ C/m}^2$ (b) and $5.4 \cdot 10^{-5} \text{ C/m}^2$ (d). Here, the effect of the particle layer becomes more dominant (b) and eventually prevents any further particle deposition on the 100 V pixel. Moreover, in (d), one particle trajectory ends on an adjacent 0 V pixel, causing contamination.

These simulations imply that it is not only important to study the selective effect on single particles: Especially the effect of already deposited particles on afterwards following particles is not yet fully investigated. Experiments suggest that the selectivity of the CMOS chip slowly declines with increasing particle load on the chip surface or more precisely the grid electrode. Thus, each pattern has a critical limit of maximum particle load, where further particle deposition will lead to contaminations on the chip surface. Hence, this topic was further investigated in experiments (see subsection 5.2.4).

3.2.8 Estimated range of selective electric forces

To gain an impression of the range of the selective electric forces from the chip, the electric potential together with the equipotential lines with a 5 V stepping were simulated (Figure 3.14). From this simulation, one can see that the highest selective forces act on the particles in the range of 100 – 0 μm distance from the chip surface.

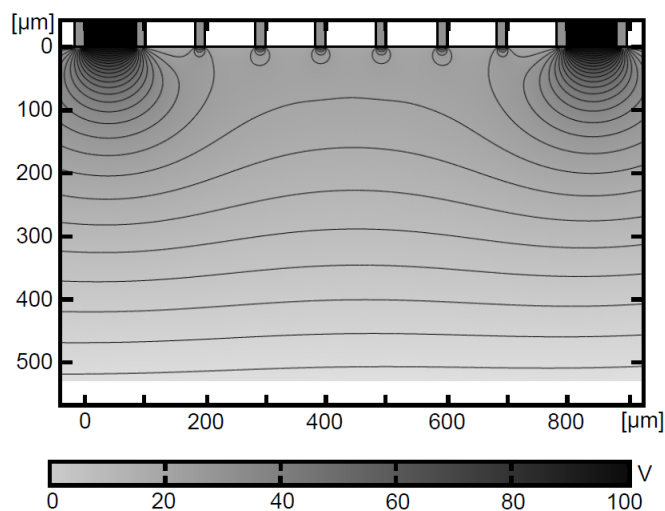


Figure 3.14: Simulation of electric potential and equipotential lines with 5 V stepping; the highest selective forces are acting between 100 – 0 μm distance of the chip surface

3.3 Simulation of miniaturized chip pixels

The previous section, discussing the simulations of particle deposition on the CMOS chip, was devised in the scope of a chip with a fixed pixel pitch of 100 μm .

In order to increase the spot density of an array, a smaller pixel pitch of 45 μm was simulated, which is leading to a roughly four times higher pixel density. The following simulations were conducted in accordance to the previously shown simulations in the scope of a bachelor thesis by T. Förtsch ([52]), initiated and supervised by myself, and were published in [53].

The most important change to the previous simulations in the boundary conditions, besides the pixel size, is the lower pixel voltage of only 30 V: Due to restrictions of the used high-voltage CMOS process, each pixel electrode requires its own high-voltage transistor, which is located beneath the pixel electrode in a lower (hidden) layer of the chip. The capability of the transistor to switch a certain maximum voltage correlates with the size of the transistor and, thus, with the pixel area. A pixel pitch of 100 μm allows for a maximum of about 120 V. A pitch of 45 μm , which is about a quarter of the 100 x 100 μm^2 area, only allows for a maximum pixel voltage of 30 V. Therefore, only a pixel voltage of 30 V is considered in the subsequent simulations.

3.3.1 Simulation setup

The geometry in the following simulations has been adapted to match the conditions in the aerosol generation system, which will be introduced later in subsection 5.2.2. The inlet width was increased to 3 cm, the geometry was cut off beneath the inlet (compare Figure 3.4), because it is irrelevant for the simulation.

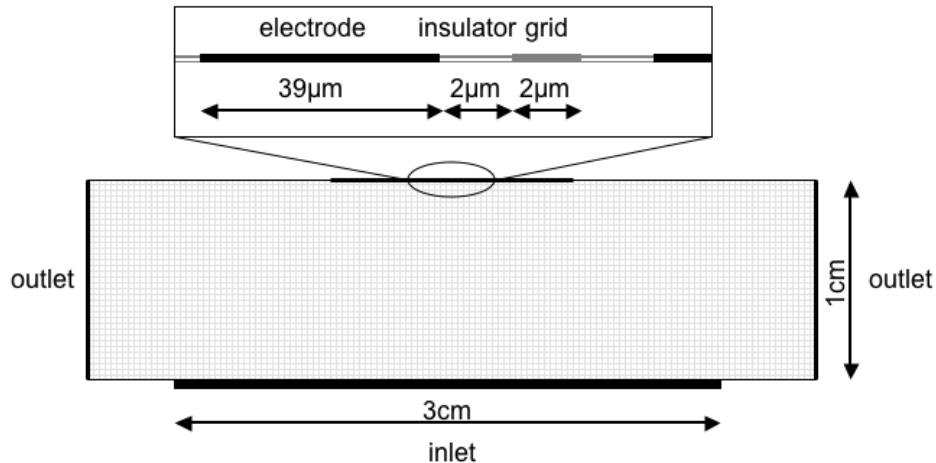


Figure 3.15: Simulated region, showing inlet, outlets, and the chip surface. The chip surface consists of the pixel electrode ($39\ \mu\text{m}$), the grid electrode ($2\ \mu\text{m}$) and the insulator ($2\ \mu\text{m}$) located between two electrodes. The pixel pitch is $45\ \mu\text{m}$ (from [53]).

The simulated region is shown in Figure 3.15. The boundaries of the simulated rectangle comprise the inlet, the outlets, and the chip surface. The chip surface is simulated with the prerequisites that the pixel electrode is $39\ \mu\text{m}$ and the grid electrode is $2\ \mu\text{m}$ in length. Between two electrodes, an insulator of $2\ \mu\text{m}$ separates the grid from the pixel in both directions. Thus, the pixel to pixel distance is $45\ \mu\text{m}$. Similar to previous simulations, a metal sieve is placed at the inlet, which is assumed not to interfere with the air flow (see subsection 3.2.1.1), but allows for applying an electric potential.

Simulating this geometry with COMSOL in analogy to the previous section, different parameters for particle deposition were evaluated: particle size, particle charge, grid voltage, grid size, and sieve voltage.

3.3.2 Influence of particle size

The influence of particle size on the deposition quality is investigated in Figure 3.16. The pixel voltage is either set to 30 or 0 V and the chosen pattern consists of two switched on pixels with seven switched off pixels in between (equivalent to previous simulations). The grid voltage is set to 25 V and the sieve voltage is set to -1000 V. A q/m value of the particles of $-3 \cdot 10^{-3}\ \text{C/kg}$ is assigned.

Figure 3.16 shows from top to bottom the influence of increasing particle diameter ((a) 2 μm , (b) 3 μm , (c) 5 μm , (d) 7 μm , (e) 10 μm). Similar to the simulations in the previous section, the amount of contamination increases with particle diameter.

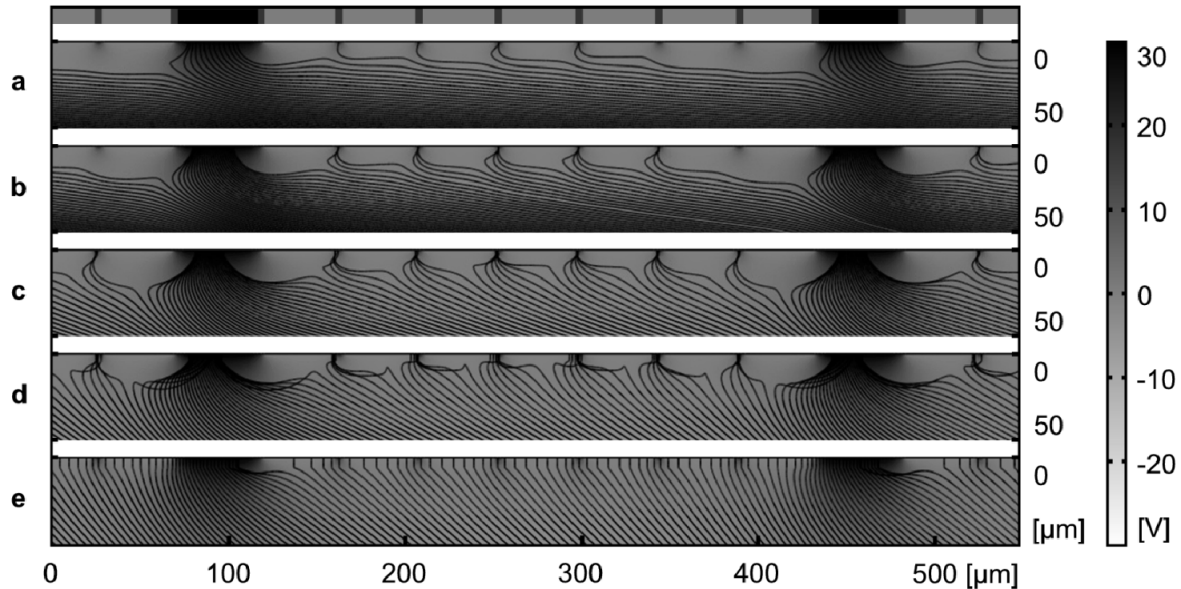


Figure 3.16: Simulation of particle deposition with a q/m of $-3 \cdot 10^{-3}$ C/kg and different particle diameters. Top to bottom: (a) 2 μm , (b) 3 μm , (c) 5 μm , (d) 7 μm , (e) 10 μm particle deposition onto a chip with 45 μm pixel pitch, 2 μm insulator, and 2 μm grid width. Two pixels are set to 30 V, separated by 7 pixels at 0 V with the grid electrode at 25 V (from [53]).

3.3.3 Influence of particle charge

In this section, the influence of the q/m value of the particles is discussed. In Figure 3.17, the particle diameter was defined to 5 μm (closest matching to the experimental particle diameter), the pixels were set to 0 or 30 V, and the grid was set to 25 V. The q/m values were set to: (a) 0, (b) $-0.1 \cdot 10^{-3}$, (c) $-1 \cdot 10^{-3}$, (d) $-3 \cdot 10^{-3}$, (e) $-15 \cdot 10^{-3}$, (f) $-30 \cdot 10^{-3}$ C/kg.

Again, similar to previous simulations, a small q/m value yields scarce deposition patterns, the influence of the air friction dominates the deposition. A too high q/m value leads to contaminations on the chip, because the deposition is dominated by the electrical fields. Only in the instance, when the electric forces and the fluid frictions are balanced, the deposition features a good deposition quality (i.e. no contamination).

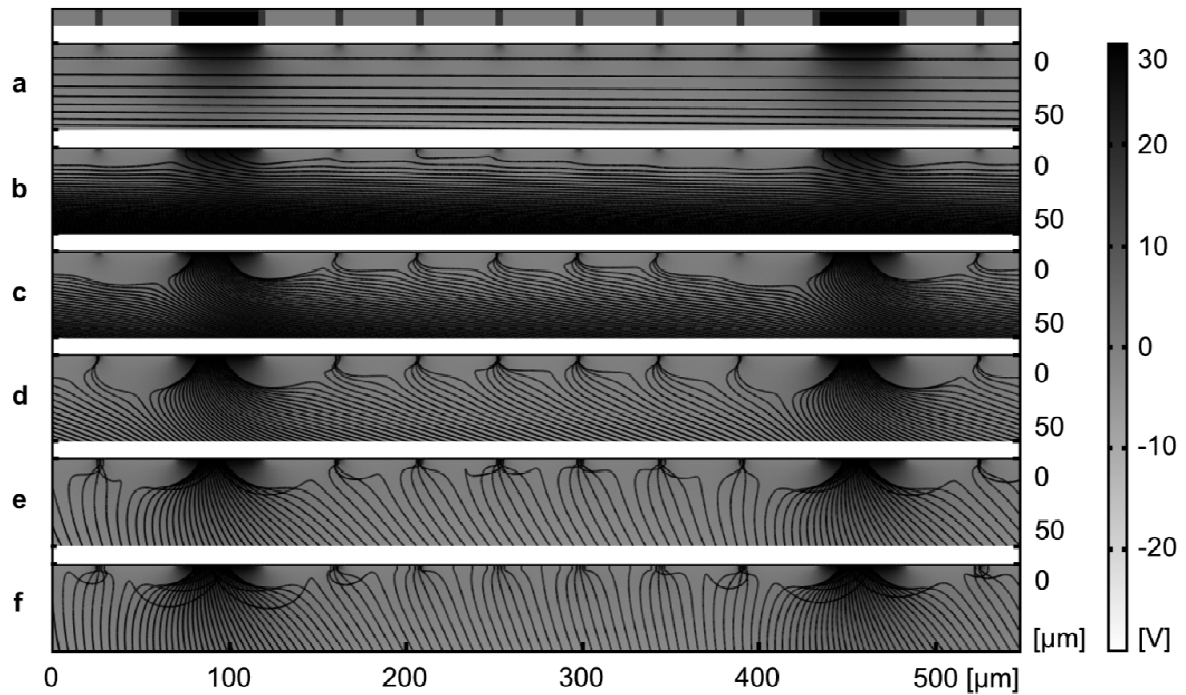


Figure 3.17: Simulation of particle deposition with a particle diameter of 5 μm and different particle q/m values. Top to bottom: (a) 0, (b) $-0.1 \cdot 10^{-3}$, (c) $-1 \cdot 10^{-3}$, (d) $-3 \cdot 10^{-3}$, (e) $-15 \cdot 10^{-3}$, (f) $-30 \cdot 10^{-3}$ C/kg particle deposition onto a chip with 45 μm pixel pitch, 2 μm insulator, and 2 μm grid width. Two pixels are set to 30 V, separated by 7 pixels at 0 V with the grid electrode at 25 V (from [53]).

3.3.4 Influence of grid voltage

The influence of different grid voltages on the deposition quality was investigated. Choosing particles with a diameter of 5 μm and a q/m value of $-30 \cdot 10^{-3}$ C/kg, the grid voltage was altered in Figure 3.18 from top to bottom: (a) 0 V, (b) 15 V, (c) 20 V, and (d) 25 V. The grid width, which will be investigated in the next subsection, was set to 6 μm instead of 2 μm . The grid voltage is tuned to a value, which will minimize the amount of contaminations on switched off pixel, but at the same instance should minimize the amount of particles deposited on the grid, as it serves as an adsorber for excess particles. The best results are achieved between 15 and 25 V.

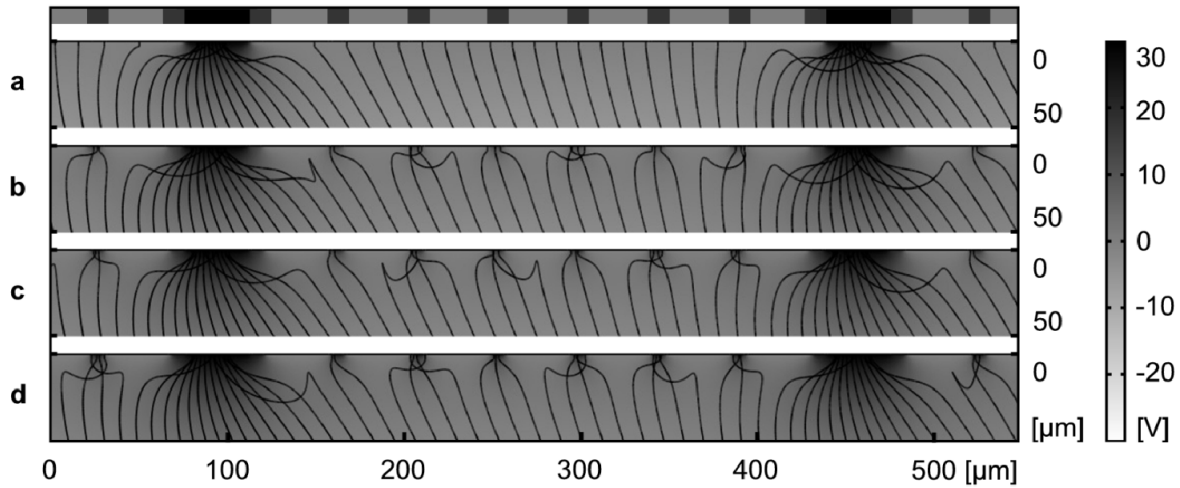


Figure 3.18: Simulation of particle deposition with a particle diameter of $5\ \mu\text{m}$, a q/m value of $-30 \cdot 10^{-3}\ \text{C/kg}$, and different grid voltages. Top to bottom (a) 0 V, (b) 15 V, (c) 20 V, (d) 25 V (from [53]).

3.3.5 Influence of grid width

Besides the grid voltage, another parameter of the grid is important: the grid width. At a fixed pixel to pixel distance ($45\ \mu\text{m}$), the electrode size together with the grid size was altered. The insulator is fixed at a width of $2\ \mu\text{m}$, due to CMOS design rules ([27]); the grid electrode is enlarged from 2 to $12\ \mu\text{m}$ and therefore, the electrode width is decreased from 39 to $29\ \mu\text{m}$. Figure 3.19 shows the different particle depositions for: (a) pixel electrode size of $39\ \mu\text{m}$ and grid width of $2\ \mu\text{m}$, (b) $35\ \mu\text{m}$ pixel electrode and $6\ \mu\text{m}$ grid width, (c) $32\ \mu\text{m}$ pixel electrode and $9\ \mu\text{m}$ grid size, and (d) $29\ \mu\text{m}$ pixel electrode and $12\ \mu\text{m}$ grid width.

Using particles with a diameter of $5\ \mu\text{m}$ and a q/m value of $-30 \cdot 10^{-3}\ \text{C/kg}$, one can observe that the degree of contamination decreases with increasing grid width. However, a grid width of more than $6\ \mu\text{m}$ does not significantly improve the deposition quality.

In the case of smaller particles with a smaller q/m value, a grid width of $2\ \mu\text{m}$ suffices for a good particle deposition quality.

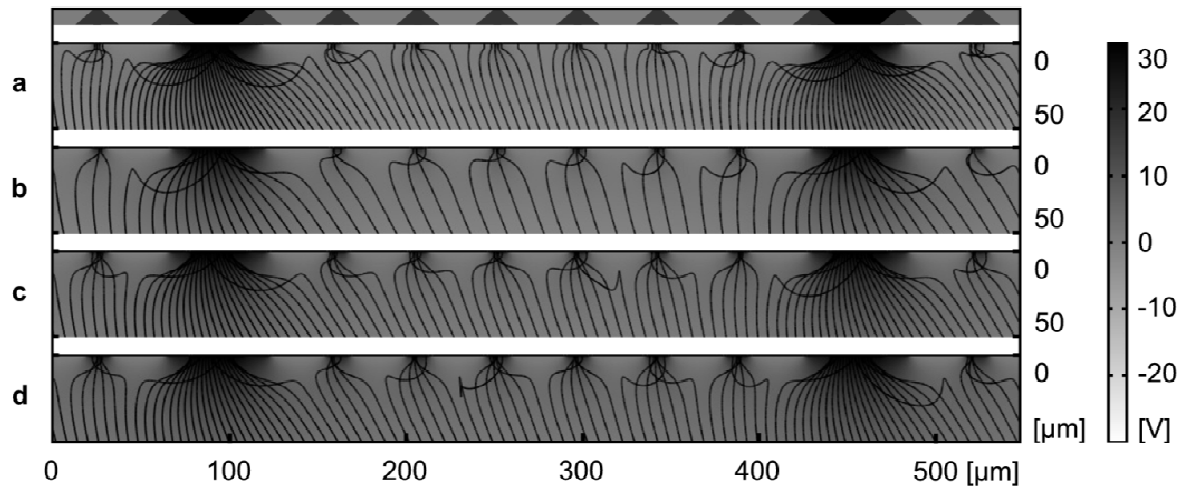


Figure 3.19: Simulation of particle deposition with a particle diameter of $5\ \mu\text{m}$, a q/m value of $-30\cdot 10^{-3}\ \text{C/kg}$, and different grid widths. Top to bottom: (a) pixel electrode size of $39\ \mu\text{m}$ and grid width of $2\ \mu\text{m}$, (b) $35\ \mu\text{m}$ pixel electrode and $6\ \mu\text{m}$ grid width, (c) $32\ \mu\text{m}$ pixel electrode and $9\ \mu\text{m}$ grid size, (d) $29\ \mu\text{m}$ pixel electrode and $12\ \mu\text{m}$ grid width (from [53]).

3.3.6 Influence of the sieve voltage

Finally, different sieve voltages at the inlet of the deposition geometry were simulated. Again, the particles were set to a diameter of $5\ \mu\text{m}$ and a q/m value of $-30\cdot 10^{-3}\ \text{C/kg}$. The pixel electrode size is $35\ \mu\text{m}$ and the grid width is $6\ \mu\text{m}$.

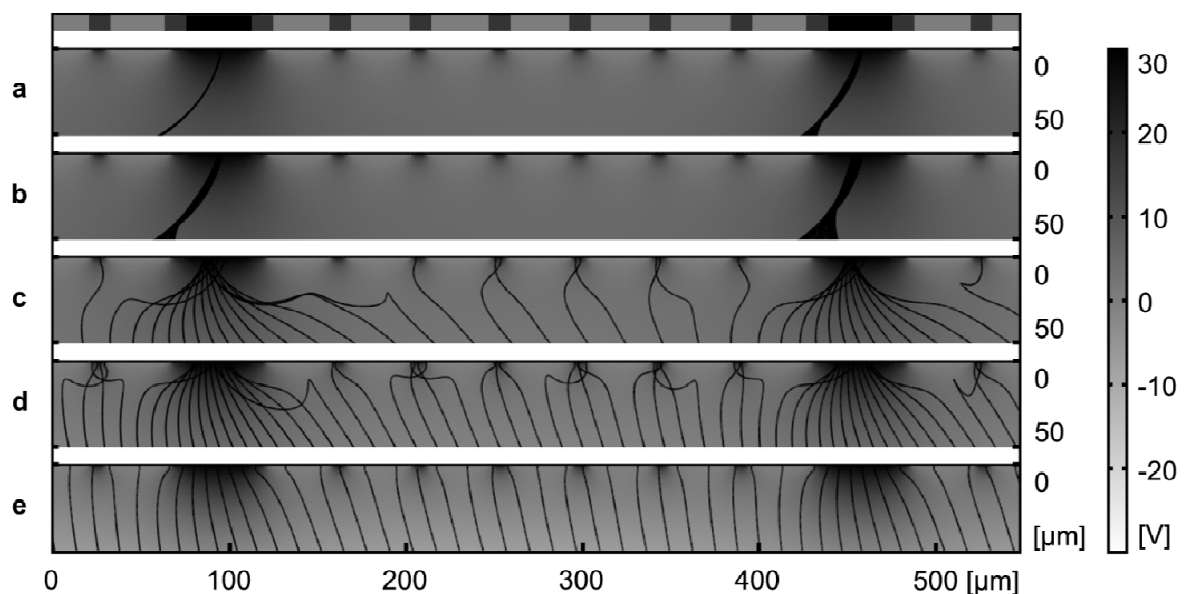


Figure 3.20: Simulation of particle deposition with a particle diameter of $5\ \mu\text{m}$, a q/m value of $-30\cdot 10^{-3}\ \text{C/kg}$, and different sieve voltages. Top to bottom: (a) $0\ \text{V}$, (b) $-30\ \text{V}$, (c) $-500\ \text{V}$, (d) $-1000\ \text{V}$, (e) $-2000\ \text{V}$ sieve voltage. The pixel electrode size is $35\ \mu\text{m}$ and the grid width is $6\ \mu\text{m}$ (from [53]).

In Figure 3.20, the sieve voltage is altered between: (a) 0 V, (b) -30 V, (c) -500 V, (d) -1000 V, and (e) -2000 V.

Similar to the particle charge (q/m) simulations in subsection 3.3.3, small sieve voltages result in scarce but high quality deposition patterns. On the other hand, a too high sieve voltage leads to contaminations on the chip, because the trajectories come closer to the chip surface, due to the increasing far field force and, therefore, highly charged particles contaminate the surface.

The theoretical optimum sieve voltage would be 0 V if the aerosol density would be high enough for an efficient long-range field effect (subsection 3.2.5) and no positively charged particles were existent. However, positively charged particles are a common characteristic in aerosols, and, thus, a sieve voltage of about -1000 V is a realistic parameter.

3.3.7 Conclusion from miniaturization simulations

Derived from the preceding simulations ([53]), several optimized parameters could be evaluated for a good particle deposition quality on a miniaturized CMOS chip with a sufficient particle deposition density and a low amount of contamination. Table 3.3 shows the optimum parameters for the particles (diameter, charge) and the optimum chip parameters for the grid width and the grid voltage. The optimum sieve voltage can only partly be derived from simulations, because the experiments deliver important results, which are very difficult to simulate (e.g. particle-particle interactions of particle ensembles).

Table 3.3: Optimized parameters for good particle deposition quality on a miniaturized CMOS chip with a sufficient particle deposition density and a low amount of contamination (derived from [53]).

Feature	Test range	Optimum parameter
Particle diameter	2 to 10 μm	2 μm
Particle charge (q/m)	0 to $-30 \cdot 10^{-3}$ C/kg	$-3 \cdot 10^{-3}$ C/kg
Grid width	2 to 12 μm	6 μm
Grid voltage	0 to 25 V	20 V
Sieve voltage	0 to -2000V	$-500 \text{ V} \geq U \geq -1000 \text{ V}$

4 Materials and Methods

4.1 Amino acid particle composition

The particles (also see subsection 1.4.4 and supporting information in [24]), used in the process, are composed of 84.5 % w/w polymer matrix (e.g. SLEC PLT 7552, Sekisui, Japan), 10 % w/w of 9-fluorenylmethoxycarbonyl (Fmoc) protected amino acid monomer (Novabiochem, Germany; Bachem, Switzerland; Sigma, USA) pre-activated as pentafluorophenyl (OPfp) ester, 4.5 % w/w pyrazolone orange (ABCR GmbH, Germany), and 1.0 % w/w of Fe(naphthol)₂ complex ([54]), acting as a charge control agent. The components for the amino acid particles are dissolved in a solvent (Figure 1.16a) and the mixture is stirred (Figure 1.16b). Afterwards, the distillation is started and the solvent evaporates (Figure 1.16c). The dried amino acid particle matrix remains in the flask (Figure 1.16d).

The dry coarse matrix is milled in a blade granulator (IKA, Germany) (Figure 1.17a), to achieve a preliminary particle granularity. The granulate material is then milled in a Hosokawa Alpine (Japan) AS 100 air jet mill (Figure 1.17b) and subsequently sieved in an analytical sieve. These particles are finally separated in a winnower (Hosokawa Alpine, Japan, see Figure 1.17c) into two different fractions, the fine and the coarse fraction. The winnower separates the two fractions at about 7 µm. However, the separation process is not perfectly accurate; one can rather speak of a blurred separation threshold.

Finally, 0.05 % w/w silica nano particles (Aerosil 812, Degussa, Germany) are added to improve flow properties and to prevent agglomeration. The particle production and development was conducted by S. Fernandez and D. Rambow.

According to the simulations, only the fine particle fraction was applied for the on-chip deposition.

4.2 Aerosol generator and particles

The new aerosol generator (see subsection 5.2.2) was calibrated to produce the best possible aerosol densities and stabilities. Thus, the pressures were optimized and adjusted

to the following parameters: initial pressure 4.5 bar; dosage air 1.0 bar; transport air 4.0 bar; vibration air 1.0 bar. Dosage air, transport air, and vibration air are all connected to the initial pressure valve. The transport air had to be additionally adjusted with a manually controlled needle valve for each particle type to ensure a certain aerosol density, which is rather subjective depending on the experimenter. Usually, a pattern is successfully deposited on the CMOS chip within one to three seconds of activated aerosol generation (i.e. once or twice activation of the automated aerosol generation).

In Table 4.1, all particle types, which were used in the aerosol generator, are listed together with the production date and the mean diameter. In some cases, the mean diameter was not measured. However, an appropriate estimation is about $5 \pm 2 \mu\text{m}$.

Table 4.1: A list of all particle types which were used in the aerosol generator, together with the control number in the generator, the production date, and the mean diameter.

# in generator	Type	Production date	Mean diameter [μm]
1	Lys	15.02.2011	3,3
2	Asp	14.04.2009	3,7
3	Pro	14.08.2006	4,0
4	Tyr	21.11.2006	3,7
5	Val	15.08.2006	4,0
6	Phe	10.07.2006	~5
7	Asn	27.07.2006	~5
8	Ser	27.02.2006	~5
9	Thr	24.10.2006	4,0
10	Trp	21.09.2006	~5
11	Ala	26.07.2006	3,7
12	Cys	06.07.2006	3,7
13	Gln	07.03.2006/16.11.2006	~5
14	Gly	19.06.2006	4,6
15	Arg	24.07.2006	4,5
16	Met	25.01.2006	~5
17	His	15.01.2009	4,3
18	Glu	21.05.2007	3,7
19	Ile	01.08.2007	4,5
20	Leu	27.11.2007	3,7

4.3 Design of the HA/Flag array for the chip

For a proof of principle experiment, the idea was to test the CMOS chip system with two well known peptides and to stain with their corresponding antibodies: the Flag and the HA epitope (see Table 4.2). The HA epitope is derived from the glycoprotein hemagglutinin, Flag is a synthetically designed epitope. For a full combinatorial approach, the amino acid sequences for these epitopes should be varied, to achieve distinct binding efficiencies of the corresponding antibodies (anti-Flag and anti-HA) towards the native and the variant peptides. Thus, for the synthesized peptides, the following design rules were presumed: It is favorable to produce as many different peptides as possible, however, due to the still semi-automated and, thus, time-consuming deposition process, it was refrained from applying all 20 amino acid types in every layer. A compromise was to reduce the complexity to a certain amount. In addition to the two epitopes, a third test epitope was designed, with the requirement that in each position to be only composed of one of the two amino acids of the Flag or the HA epitope (e.g. in position 9 either Lys or Ala, in position 8 either Asp or Tyr). The second requirement was, that it should differ sufficiently from the Flag and HA sequence, in order to function as a negative control, i.e. neither the anti-Flag nor the anti-HA antibody should bind to this test epitope (this was in fact not entirely achieved for the polyclonal anti-HA antibody, which still bound with low efficiency to the test epitope). In Table 4.2, the three epitope sequences are shown.

Table 4.2: Flag, HA, and the test epitope.

	1	2	3	4	5	6	7	8	9
Flag epitope	Tyr	Asp	Tyr	Lys	Asp	Asp	Asp	Asp	Lys
HA epitope	Tyr	Pro	Tyr	Asp	Val	Pro	Asp	Tyr	Ala
Test epitope	-	Asp	Ala	Asp	Asp	Pro	Asp	Asp	Ala

In two different array approaches, two different types of variations were realized. An overview of the chip layout and a complete list of all peptides can be found in the Appendix.

Reducing the complexity to an acceptable extent, in the first (bigger) type of array (see Table 4.3), except for position 1, all positions were subjected to small variations by interchanging the two amino acids of the Flag and the HA sequence, achieving a slight variation of the sequences. In addition, in position 4, Glu was also included in the possible substitutions, which is due to its acidic (carboxyl) residue similar to Asp and therefore might have a similar biological effect on binding. In position 7, Asp was substituted with Glu, Asn, and Gln. Again,

Glu was used, because of its acidic character. Asn and Gln are, except missing the carboxyl group, chemically identical to Asp and Glu, which is interesting from the point of view, whether the antibody binding depends on the acidic residue or only depends on conformational alignment. Furthermore, in position 8, Tyr was substituted with Trp, because both possess an aromatic group and are rather heavy amino acids, but still differ strongly in their configuration. Finally, also in position 8, Asp was substituted with Asn, again because of the acidic residue. All realized peptide variants of this array are listed in Table 4.3.

Table 4.3: The first (bigger) array offering 1,536 different peptide variants of the HA and Flag epitope.

	1	2	3	4	5	6	7	8	9
Synthesized peptide variants	Tyr	Pro	Tyr	Lys	Val	Pro	Asp	Tyr	Ala
		Asp	Ala	Asp	Asp	Asp	Glu	Trp	Lys
				Glu			Asn	Asp	
							Gln	Asn	

In a second (smaller) array, the two epitope sequences were kept completely static, no interchange of the two amino acids from the Flag and HA epitope was performed. Yet, on position 3 and 4, all 20 amino acids were used in every combination, thus, rendering 400 (20 x 20) variants of the Flag epitope and 400 variants of the HA epitope. All variants of this array are summarized in Table 4.4.

Table 4.4: The second (smaller) array offering 400 different peptide variants of the HA epitope and 400 variants of the Flag epitope.

	1	2	3	4	5	6	7	8	9
Flag epitope	Tyr	Asp	Tyr	Lys	Asp	Asp	Asp	Asp	Lys
HA epitope	Tyr	Pro	Tyr	Asp	Val	Pro	Asp	Tyr	Ala
Substitutions			Xxx	Xxx					

In Figure 4.1, the layout of the chip is shown. The chip pattern is divided into four repetitive regions (1 – 4, also see Supplementary Figure 1 left in the Appendix). Except for the control peptides (HA, Flag, Test) at the borders, which might differ slightly in the arrangement, all 4 regions resemble each other in terms of the amino acid sequences (except for region 1).

One region consists of three arrays (a, b, c): the two smaller arrays (a: upper left, b: lower left) and one bigger array (c: right). The two smaller arrays (a, b) possess the same sequences, except for region 1, where the lower left array (b) is cut off by the letters “DKFZ” and “KIP”.

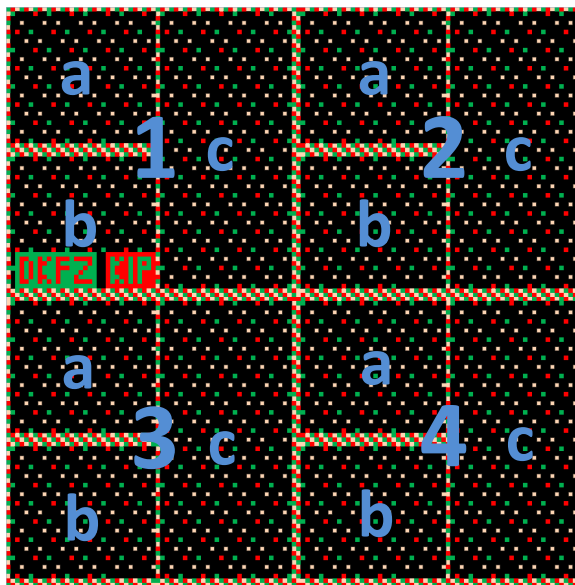


Figure 4.1: Layout of the peptide array on the CMOS chip (drawing). Expected staining: the HA epitope pixels in green, the Flag epitope pixels in red, and the control peptide pixels in pink. The black pixels correspond to modified Flag or HA epitope spots, which might possibly be stained.

Here, it is again noted that the complete layout of the array (showing all realized amino acid sequences), the amino acids, and their residues are depicted in the Appendix (p. 125).

4.4 Surface coatings for peptide synthesis

Before starting the actual peptide synthesis, the surface of the CMOS chip has to be modified with a functional coating. This provides for the surface-bound amino groups, which are required to covalently anchor the peptides on the solid support. In this work, two functional coatings were applied, which will be described in the following: a graft polymer of poly(ethylene glycol) methacrylate (PEGMA) and methyl methacrylate (MMA) (mole fractions 10 % PEGMA, 90 % MMA), called **PEGMA/MMA** coating, and an amino-terminated self-assembled monolayer (SAM) bearing an (ethylene glycol)₃ spacer, called **AEG₃ SAM**.

Protocols for the graft polymer coatings have already been published ([19]), however, an enhanced protocol for the graft polymer coating and a newly developed AEG₃ SAM were applied in the context of this work. Parts of the surface coating process are still subject to present research and are conducted in the scope of another thesis ([55]). Thus, the following will only briefly introduce and discuss the surface coating production and the protocols. For a more detailed approach, see [55]. A synthesis protocol for the polymer surface and the peptide synthesis can be also found in [56].

All subsequent steps, required for the surface coating, were conducted by C. Schirwitz or D. Rambow.

The standard surface coating for our peptide synthesis is an about 50 nm thin copolymer film of PEGMA/MMA with mole fractions of 10 % PEGMA and 90 % MMA ([19], [55]). The development of these graft polymer coatings was driven by the objective to render a high yield of starting groups (coupling sites) for the peptide synthesis together with the benefit of intrinsic protein resistance ([18], [19]). Polymers containing PEGMA are known for their resistance to unspecific protein adsorption, which is favorable for a background-free study of specific protein-protein interactions. Furthermore, the hydroxy-terminated side chains of the polymer can be modified to offer amino groups which are good starting points for the peptide synthesis ([21]).

Another approach to render amino groups for a peptide synthesis is the self-assembly of silane monolayers. In fact, the self-assembly of molecules is a versatile and widespread technique for the coating of metal and metal-oxide surfaces with functional layers ([57], [58]). In this work, the chip surfaces were functionalized with an amino-terminated SAM, bearing a short ethylene glycol₃ (EG₃) spacer. Even short EG sequences, starting from 2 EG units, can provide for protein resistance and, thus, prevent unspecific protein adsorption on the surface ([59]). Compared to the “three-dimensional” polymer surface, the “two-dimensional” SAM was assumed to provide better accessibility of the peptides for the analytic molecules.

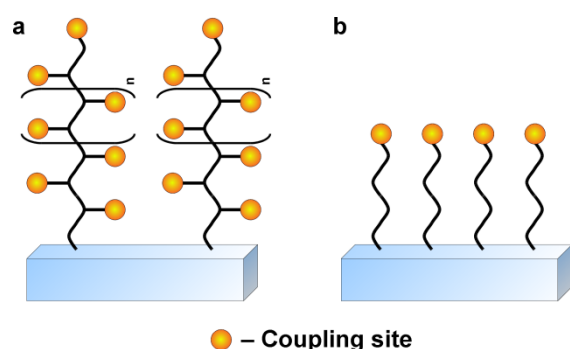


Figure 4.2: Schematic of a multilayer (a) and a self-assembled monolayer (b) on a substrate, with the coupling sites (amino groups) for the peptide synthesis.

Due to its polymeric character, the peptides coupled to the PEGMA/MMA surface may be inaccessible to protein interaction, because they are hidden inside the protein-resistant polymer layer (Figure 4.2a). Thus, the peptide synthesis was also conducted on the presumably less sterically hindering AEG₃ SAMs (Figure 4.2b), in order to determine whether peptides attached to these coatings possess a better accessibility for analytic

molecules.

4.4.1 Silanization

Starting point of each surface coating on the CMOS chip is a silanization, which covalently anchors an organic molecule to the aluminum oxide or silicon nitride ([28]). In this reaction, an ethoxysilane residue is covalently bound to the hydroxyl residues of the surface (Figure

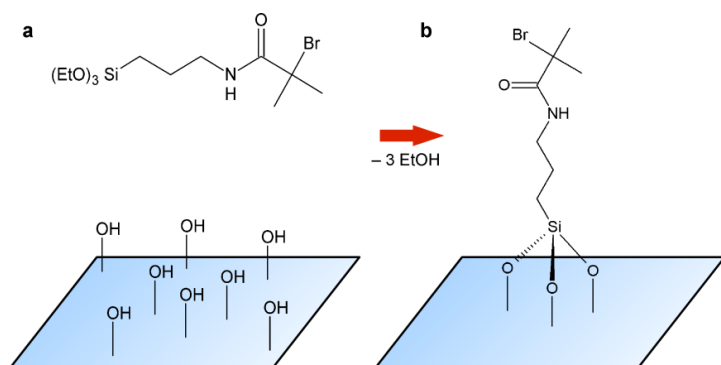


Figure 4.3: Bromine silane and the chip surface, exhibiting hydroxyl residues (a). The bromine silane couples to the surface, releasing ethanol (b).

4.3). The silane serves as the initiator for the subsequent polymerization reaction. First, the chip is irradiated with UV light for 2 h under atmospheric conditions, using a mercury vapor lamp (TQ 150, Heraeus Noblelight). This treatment removes contaminations and activates the oxide layer by generating surface-

bound hydroxyl groups. Then, the chip is incubated in a solution of 2 mM 2-bromo-N-(3-triethoxysilyl)propyl isobutyramide (bromine silane) and 8 mM N-propyltriethoxysilane (PTES) in anhydrous dichloromethane (DCM) overnight. Subsequently, the DCM is gradually replaced with ethanol (p.a.). The surfaces are washed three times for 5 min each with ethanol, twice for 2 min each with acetone, and then dried in a stream of compressed air. Finally, the chip is placed in a pre-heated oven at 110 °C for 2 h to achieve full condensation of the bromine silane with the surface. After cooling to room temperature, the chip is directly coated with the polymer or stored at 4 °C under argon atmosphere.

4.4.2 PEGMA/MMA coating

The bromine silane is now used as a linker for a surface-initiated atom transfer radical polymerization (ATRP), yielding the poly(ethylene glycol) methacrylate and methyl methacrylate (PEGMA/MMA; 10:90) surface coating.

Therefore, 2.88 ml PEGMA (8.75 mM; Sigma, USA), 8.38 ml MMA (78.75 mM, Merck Schuchardt, Germany), 91 µl pentamethyl-diethylenetriamine (PMDETA 0.44 mM, ≥ 98 %,

Merck Schuchardt), 620 μl triethylene glycol monomethyl ether (TEGMME, 3.96 mM, $\geq 97\%$, Merck Schuchardt) are mixed in 37 ml dimethyl sulfoxide (DMSO, $\geq 99.8\%$, Carl Roth GmbH, Germany) under argon atmosphere. Then, 44 mg CuCl (0.44 mM, $\geq 99\%$, Sigma, USA) are added and the solution is stirred, until the copper chloride is completely solved. The silanized chip is placed in a petri dish and covered with the mixture, inside of a desiccator. The desiccator is evacuated three times and brought to argon atmosphere. The polymerization step is allowed to proceed for 20 h.

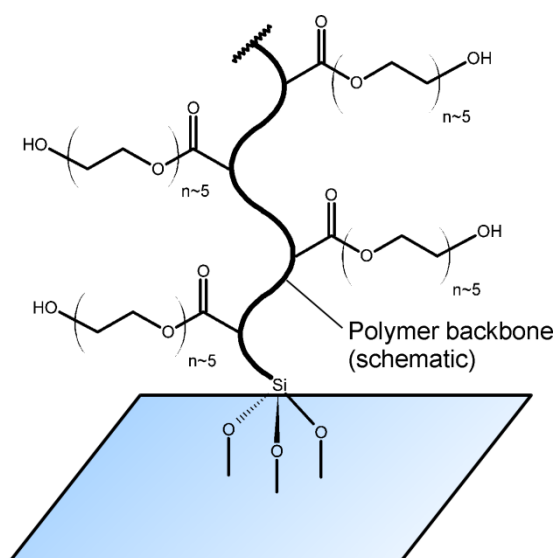


Figure 4.4: PEGMA/MMA surface coating. The polyethylene glycol side chains are connected to the polymer backbone (shown schematically). Subsequently, the hydroxyl groups are esterified with three β -alanine residues, to render the amino groups for the peptide synthesis (not shown).

After successful polymerization, the chip is thoroughly washed five times for 5 min each with DMSO, then, the chip is washed twice for 5 min with methanol (p.a.) and twice for 10 min with Milli-Q (Millipore, USA) water. After rinsing with acetone, the chip is dried in an air stream. In Figure 4.4, the schematic polymer backbone is shown, with the polyethylene glycol side chains, offering the hydroxyl groups.

To render the amino groups for the peptide synthesis and to introduce a short spacer between the surface and the peptides, the hydroxyl groups of PEGMA are consecutively modified with three β -alanine residues. A solution of 62.26 mg Fmoc- β -alanine (99.4%,

Iris BioTechnology GmbH, Germany) and 37.2 μl N,N'-diisopropylcarbodiimide (DIC, purum, Sigma) per ml anhydrous N,N-dimethylformamide (DMF, peptide grade) is prepared. After 5 min of stirring, 37.2 ml N-methylimidazole (NMI, analytical grade, Sigma) are added. The chip is incubated in this solution overnight under nitrogen atmosphere. Afterwards, the chip is washed three times in DMF for 5 min each. In order to block residual hydroxyl groups, the chip is incubated overnight in a solution of 10 % v/v acetic anhydride, 20 % v/v diisopropylethylamine, and 70 % v/v DMF. Then, the chip is washed five times with DMF for 5 min each, twice with methanol for 2 min each, and dried with compressed air. To cleave the Fmoc protecting groups from the β -alanine, the chip is incubated in 20 % v/v of

piperidine in DMF for 30 min. Finally, the chip is washed three times in DMF for 5 min each and twice in methanol for 3 min each. To couple the next β -alanine, the previous steps are repeated, until three successive β -alanine residues are coupled. At the terminal amino residue, the subsequent peptide synthesis can be initiated. Measurement of the starting density of amino groups upon Fmoc cleavage from the third Fmoc- β -alanine resulted in about 1 nmol/cm².

4.4.3 AEG₃ coating

The development of the SAM as a functional coating for the peptide synthesis is described in [55] in more detail.

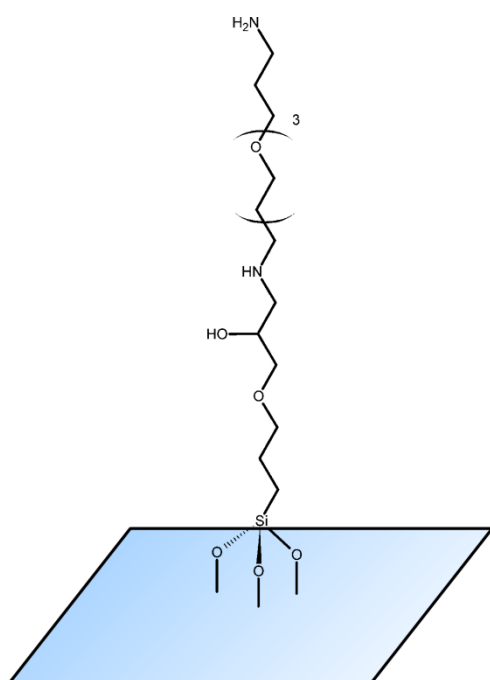


Figure 4.5: Single unit of the self-assembled monolayer structure with the amino terminus and three ethylene glycol units (AEG₃). The amino group eventually functions as the coupling site for the peptide synthesis.

A Solution of 30 mM 3-glycidylpropyl trimethoxy silane (3-GPS) in anhydrous DCM was prepared and added to the activated (UV irradiation) dry chips. The chips were left to react overnight in a desiccator under argon atmosphere. Subsequently, the surfaces were washed three times for 2 min each with DCM. A solution of 20 % (v/v) 1,13-diamino-4,7,10-trioxa tridecan (DATT) in anhydrous DMF was directly added to the surfaces without drying. The surfaces were allowed to react for 24 h. The samples were washed five times for 5 min each with DMF, twice with methanol for 3 min each, rinsed with acetone, and then dried in a stream of compressed air. AEG₃-coated surfaces were stored at 4 °C under argon atmosphere.

Figure 4.5 shows a single unit of the self-assembled monolayer structure with the amino terminus and three ethylene glycol subunits (AEG₃). The terminal amino group eventually functions as the coupling site for the peptide synthesis.

4.5 Peptide synthesis protocol

After the coating of the CMOS chip, the particle deposition was performed according to the principle illustrated in Figure 1.13. In Table 4.5, the different amino acid particle types for each layer are listed.

After one particle deposition layer is finished, the CMOS chip was heated under nitrogen atmosphere for 90 min to 90 °C. Afterwards, the chip is allowed to cool to room temperature. The chip was then inserted into a washing chamber (see [27] for further details), thus, only the active chip area is subjected to the subsequent chemical washing steps. Each washing chamber, equipped with one chip, requires about 12 ml of liquid for one washing step. A magnetic stir bar provides for the required turnover of the liquid and is used throughout all washing steps (at about 300 rpm).

Table 4.5: Deposited amino acid particle types in the different layers. Except for layer 6 and 7, where Xxx represents all 20 amino acid types, only one to four different types were deposited. Note: The deposition sequence is in reverse order, because a peptide is typically displayed from the N to the C-terminus. However, peptide synthesis in our case is performed starting from the C-terminus.

	9	8	7	6	5	4	3	2	1
Deposited amino acid particle types	Tyr	Pro	Xxx	Xxx	Val	Pro	Asp	Tyr	Ala
		Asp			Asp	Asp	Asn	Trp	Lys
							Gln	Asp	
							Glu	Asn	

Initiating the washing, the chip is subjected to a mixture of 12 ml acetic anhydride, N,N-diisopropylethylamine, and N,N-dimethylformamide (Ac₂O/DIPEA/DMF), with the volume ratios 10 % Ac₂O, 20 % DIPEA, and 70 % DMF, for five minutes while stirring and afterwards replaced with a fresh mixture and stirred again for 20 min (removal of toner matrix and uncoupled amino acids, capping of uncoupled surface amino residues).

Then, the chip is washed with DMF twice for 5 min, and subsequently 5 min with acetone. Afterwards it is washed again with DMF for 15 min (removal of Ac₂O/DIPEA remains and silica nano particles, pre-swelling of the surface with DMF). Now, a mixture of 20 % piperidine in DMF is applied for 30 min, which cleaves the Fmoc amino terminal protecting group from the coupled amino acids. Finally, the chips are washed three times for 5 min with DMF and afterwards twice with methanol (MeOH) for 3 min each.

After coupling and washing of the final amino acid layer, the peptides have to be side chain deprotected. Therefore, the chip is incubated with dichloromethane (DCM) for 30 min. Then, to cleave the side chain protecting groups from the amino acids, the chip is washed three times for 30 min each in a mixture of 51 % v/v trifluoroacetic acid (TFA), 3 % v/v triisobutylsilane (TiBS, ultrapure, Sigma, USA), 44 % v/v DCM, and 2 % v/v H₂O. Each of these three washing steps has to be performed with a fresh mixture. Afterwards, the chip is washed twice with DCM for 5 min, to remove any residuals from the previous washing steps. Now, the chip is washed with DMF for 5 min and then incubated for 30 min with 5 % v/v DIPEA in DMF, to neutralize any acidic residues due to the TFA step. Finally, the chip is washed twice for 5 min each in DMF and subsequently in methanol twice, again for 5 min each. The chip is dried in an air flow and is then ready for biological application. The protocols can be also found in [20] and [55].

4.6 Staining protocol and image acquisition

Phosphate buffer saline

The phosphate buffer saline (PBS) was prepared, dissolving 8.0 g NaCl (0.137 M), 0.2 g KCl (0.0027 M), 1.44 g Na₂HPO₄ · 2H₂O (0.0081 M), and 0.2 g KH₂PO₄ (0.15 M) in 1 l of Milli-Q (Millipore, USA) water. The solution naturally possesses a pH of 7.4. Generally, it is supplemented with 500 µl (0.05 % v/v) polysorbate 20 (Tween 20, Sigma, USA), which is then called PBS-T.

4.6.1 CMOS chip based arrays

After successful peptide synthesis and side chain deprotection, the peptide arrays were incubated for 30 min in PBS-T and afterwards blocked for 1 h in blocking buffer for fluorescent western blotting (Rockland Immunochemicals, Inc., USA), to prevent unspecific antibody binding. After one short washing step (10 s) with PBS-T, the arrays were then incubated with monoclonal mouse-Anti-HA 12CA5 IgG antibodies (provided by Dr. G. Moldenhauer, DKFZ) and polyclonal rabbit-Anti-Flag IgG antibodies (Sigma, USA), diluted (1:500) in PBS-T with 1:10 blocking buffer. Following two short washing steps with PBS-T, the binding was detected with the corresponding secondary antibodies goat-Anti-mouse

(Molecular Probes/Invitrogen, USA) conjugated with the fluorescent dye Alexa Fluor 546 and goat-Anti-rabbit (Molecular Probes/Invitrogen, USA) conjugated with Alexa Fluor 647 (diluted 1:1000 in: PBS-T + 1:10 blocking buffer). After 30 min of incubation, the arrays were washed shortly in PBS-T and then washed with Milli-Q water to remove salts and ions.

Monoclonal antibodies are generally derived from one B-cell clone and are identical and monospecific. Polyclonal antibodies are a mixture of antibodies, all directed against one antigen, but non-monospecific.

The reflected-light microscopy images of the chip surface were acquired with a Zeiss Axiovert 35 with a 5x magnification objective, using a Progres C5 from Zeiss as microscope camera.

The fluorescence images of the CMOS chip-based arrays were obtained with a Molecular Devices GenePix 4000B microarray scanner with two lasers of the excitation wavelengths of 532 nm and 635 nm and filters optimized for the emission wavelengths 570 nm and 670 nm. The scanning resolution was set to 5 μm . The shown images were only adjusted in brightness and contrast. The scanner was set to 33% laser power, in the case of AEG₃ surfaces the photomultiplier (PMT) sensitivities were set to 730 for the red channel and 900 for the green channel, in the case of PEGMA/MMA to 550 for the red channel and 480 for the green channel. Additionally, the focal plane was adjusted to acquire the best possible results.

4.6.2 Laser printed arrays

Similar to the chip-based arrays, the laser printed peptide arrays were produced and finalized completely by the company Pepperprint GmbH (Heidelberg, [25]). In the scope of this thesis, they were then incubated for 30 min in PBS-T and afterwards blocked for 1 h in blocking buffer, to prevent unspecific antibody binding. After one short washing step (10 s) with PBS-T, the arrays were then incubated for 1 h with the corresponding serum (diluted 1:100 in PBS-T + 1:10 blocking buffer). Following two short washing steps with PBS-T, the binding was detected either with the corresponding secondary antibodies F(ab')₂ goat-Anti-human conjugated with the fluorescent dye DyLight 680 (Thermo Scientific, USA) or with the secondary antibodies IgG goat-Anti-mouse conjugated with DyLight 680 (KPL, Inc., USA), depending on the type of primary antibodies (human or mouse). After 30 min of incubation,

the arrays were washed shortly in PBS-T and then washed with Milli-Q water to remove salts and ions.

In a similar staining step, the HA-epitope spots and the Flag-epitope spots were stained directly by incubation for 30 min with the monoclonal mouse-Anti-Flag M2 IgG1 (Sigma, USA) conjugated with FluoProbes 752 (Lightning-Link FluoProbes 752, Innova Biosciences Ltd., UK) and the monoclonal mouse-Anti-HA 12CA5 IgG antibodies (provided by Dr. G. Moldenhauer, DKFZ) conjugated with Atto 680 (Lightning-Link Atto680; Innova Biosciences Ltd., UK). Both antibodies were diluted 1:1000 in PBS-T + 1:10 blocking buffer.

The fluorescence images were obtained with an Odyssey scanner (LI-COR, Inc. USA) with two lasers of the excitation wavelengths of 685 nm and 785 nm and filters optimized for the emission wavelengths 700 nm and 800 nm. The scanner sensitivities were set to 7.0 for the 700 and 800 nm channels, the focal plane was set to 0.8 mm. Note: in the acquired images, the red channel represents the 700 nm channel and the green channel represents the 800 nm channel (false-color).

5 Experimental results and discussion

In this chapter experiments will be discussed, which were devised in respect to the results of chapter 3, “Theory and simulations”. The following sections will cover the experimental improvements of the laser printing process (section 5.1) and the on-chip particle deposition (section 5.2), as well as a proof-of-principle combinatorial peptide synthesis on the CMOS chip (section 5.3) and biological relevant epitope mappings (section 5.4) using laser printed arrays.

5.1 Analyzing the gap phenomenon

To improve the homogeneity of the printing pattern (see Figure 5.1), the transfer voltage was increased, which resulted in a yet unknown phenomenon.

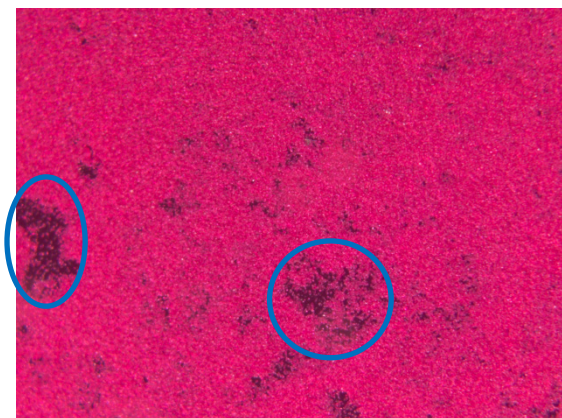


Figure 5.1: Inhomogenous laser printing of OKI magenta onto a glass slide (inhomogenities highlighted with blue circles).

The simulation of the laser printing process in section 3.1 provides for an explanation of the underlying problem, as described in the introduction (section 1.5, Figure 1.19): The higher the voltage between the image drum and the opposing electrode, the higher is the probability for electric breakdown of the air, which results in the described circular gaps in the deposited pattern.

The simulations in section 3.1 predict that the gaps occur at a critical voltage and the gap size increases with rising voltage. These predictions could be confirmed with experiments, which were conducted by Prof. Dr. Stefan Güttler and Ilja Fedoseev at the Fraunhofer Institute for manufacturing engineering and automation (IPA) in Stuttgart. Using a specially designed test laser printer (similar to the peptide laser printer) loaded with commercially available OKI toner particles, they could show that this phenomenon emerges with increasing voltage. In Figure 5.2, the repetitive printing of a homogenous area of OKI blue toner particles onto a glass substrate with various

voltages is shown. The phenomenon does not occur at lower voltages, but appears at around 3800 V. The gap size increases with increasing voltage, as predicted in the simulations.

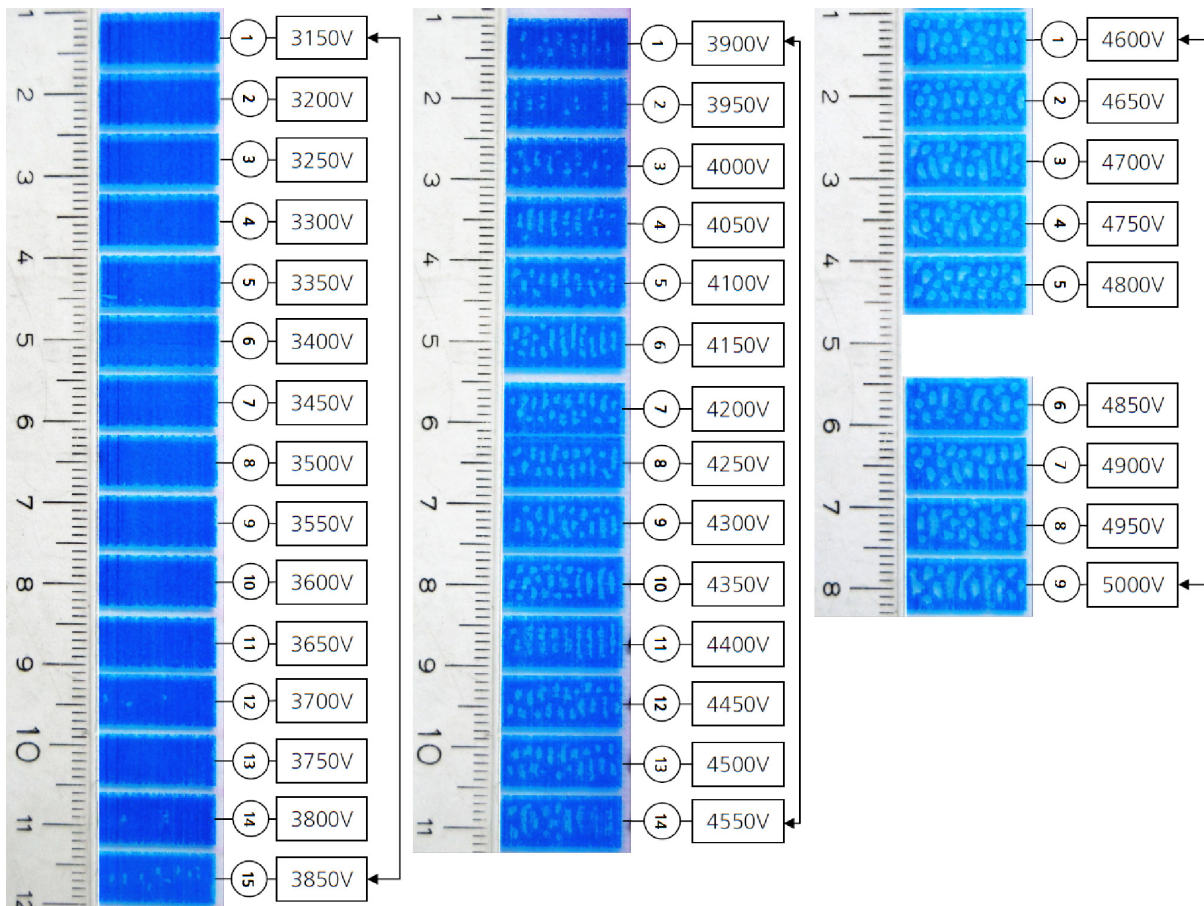


Figure 5.2: Repetitive printing of a homogenous area onto a glass substrate with various voltages. The phenomenon does not occur at lower voltages, but appears at around 3800 V. The gap size increases with increasing voltage. (By courtesy of Prof. Dr. Güttler/IPA Stuttgart)

In Figure 5.3, the effect can be observed on the image drum, when the printing process is interrupted: The gaps on the glass (Figure 5.3a) are visible as a negative image on the image drum (Figure 5.3b). The particles seem to have lost their charge, so that they remain on the image drum. Thus, the particles are probably discharged by the air ions as a result of the air breakdown.

This effect also appears on other surface materials which were glued on top of the glass substrate, such as paper or polypropylene (PP) foil. However, on these surfaces, the critical voltage was much higher than on the plain glass substrate. The increase in the height of the substrate of about 10 % (glass about 1 mm; paper or PP-foil about 0.1 mm thick glued onto

the glass) could not explain the required increase in the voltage of about 1000 V (paper) or 4000 V (PP foil). If approximated with the formula $E = U / d$, the voltage increase accounts for at least 20 % in the case of paper, which cannot be explained by the height difference. In the case of PP foil, it accounts for an increase of 100 %.

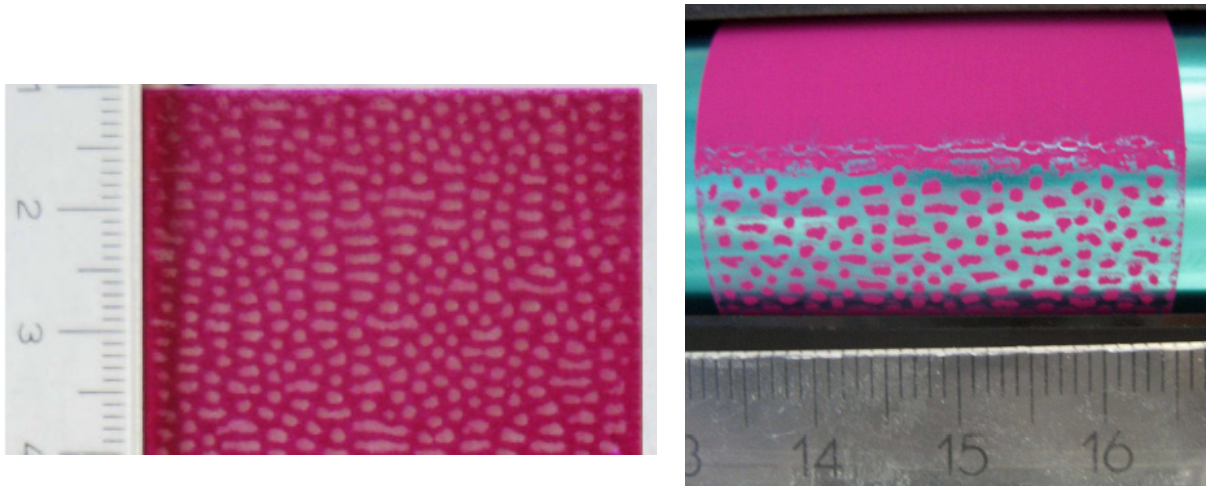


Figure 5.3: Interrupted printing process. The effect can be observed on the image drum, when the printing process is interrupted: The gaps on the glass (left) are visible as a negative image on the image drum (right). (By courtesy of Prof. Dr. Güttler/IPA Stuttgart)

The surface material seems to play a key role in the particle deposition with the laser printer. Thus, this problem was tackled with a different approach.

5.1.1 Surface conductivity

As introduced in subsection 2.1.2, the particle charge electrometer was used to measure the surface conductivity of different glass substrates. The following measurements were performed at 54 % relative humidity (rh), three different glass types were compared: one substrate from the company Langenbrinck (R. Langenbrinck, Germany) called **LB**, one (green substrate) from the company Marienfeld (Paul Marienfeld GmbH & Co. KG, Germany) called

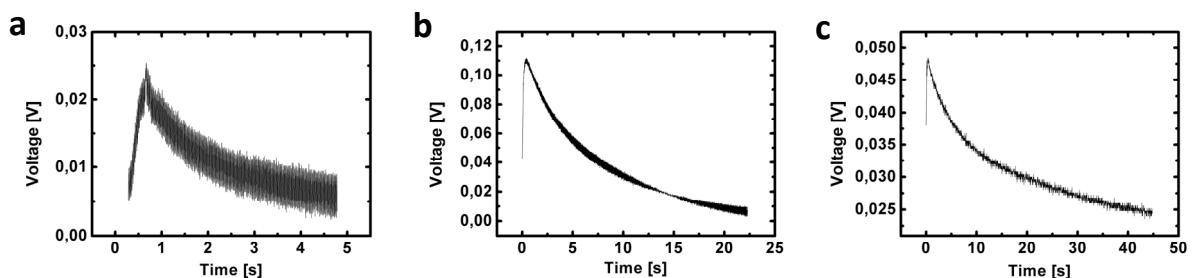


Figure 5.4: Measurement of glass surface conductivity with the particle charge electrometer (see subsection 2.1.2). The average half life of a charge induced on the glass slide is: MFg $\tau_a = 0.8$ s (a), LB $\tau_b = 4.2$ s (b), MFw $\tau_c = 6.2$ s (c)

MFg, and another (white substrate) from the company Marienfeld called **MFw**.

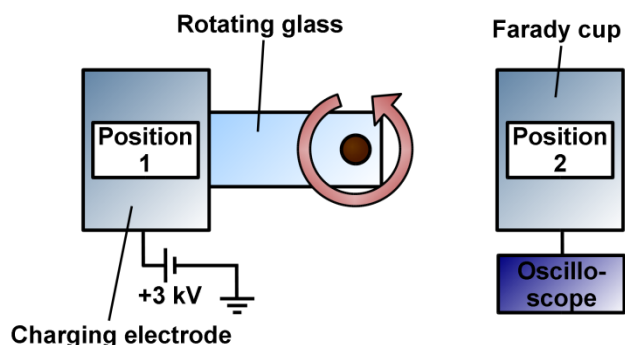


Figure 5.5: Measuring the surface conductivity of different glass slide types. In position 1, the electrode induces a polarization of the surface charge distribution in the glass slide. In position 2, the charge decay is measured until the equilibrium of charge distribution is reached.

Figure 5.4 shows the different measurements for the glass surface conductivities. The experimental setup is shown in Figure 5.5. The charge on the glass substrate was induced by an electrode, which was switched to +3 kV: Due to the possibility of rotating the glass slide, the glass slide was parked in position 1 near the +3 kV electrode (see Figure 5.5). After a charging time of about 30 s, the glass slide was moved into the Faraday cup (position 2) for the actual

measurement and the exponential decay of charge was observed.

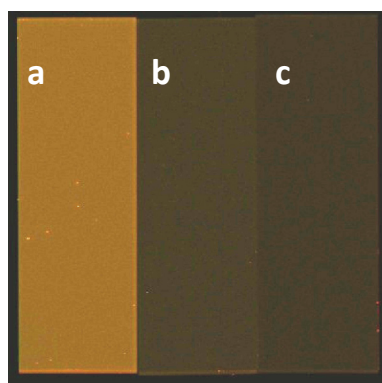


Figure 5.6: Autofluorescence in yellow (700 nm red + 800 nm green), resulting from the different glass materials. Glass types: MFg (a), MFw (b), LB (c).

The half lives of the different glass substrates gave reproducible results: MFg $\tau_a = 0.8$ s (a), LB $\tau_b = 4.2$ s (b), MFw $\tau_c = 6.2$ s (c). These values are only qualitative, but yet, they lead to an intriguing result. The surface conductivity is on the one hand dependent on the relative air humidity, which is already known and can be found in the literature ([42]). On the other hand, the surface conductivity of glass is essentially dependent on the glass ingredients. Especially the amount of iron oxide (Fe_2O_3) in the glass seems to play the key role, as shown in Table 5.1. The iron oxide is the only glass component which correlates to the measured half life.

The property of Fe_2O_3 being conductive, is also known, yet, its conductivity is much lower than compared to plain iron.

The rather low amount of iron oxide in the MFw glass type results in two different effects: on the one hand, one can see a very low fluorescence signal

Table 5.1: Amount of iron oxide in different glass types.

Glass type	Fe_2O_3 [% v/v]	τ [s]
Marienfeld green (MFg)	0.045	0.8
Marienfeld white (MFw)	0.015	6.2
Langenbrinck (LB)	0.03	4.2

resulting from the glass material, which gives a low (and desirable) background signal. In Figure 5.6, the fluorescence of the different glass types is shown at about 700 nm (shown in red) and 800 nm (shown in green, false-color). The MFg slide has the highest amount of iron oxide and the highest background signal. MFw and LB slides, both, show a quite low background signal which is acceptable for our needs.

Yet, the low conductivity causes charge to stay on the surface, which causes problems in particle deposition. Using the aerosol generator which will be introduced in the next section (section 4.2), it was possible to deposit particles onto different substrate materials, by placing an electrode behind the substrate, causing an electric field between the sieve and the electrode.

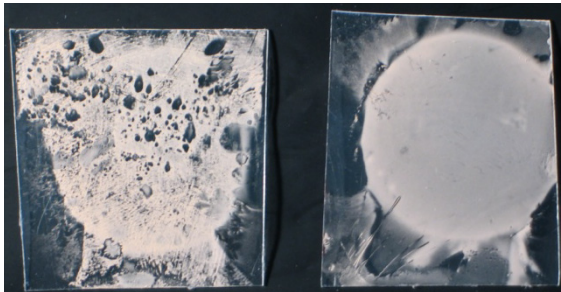


Figure 5.7: Particle deposition on two polypropylene foil pieces. The particle deposition is interfered by the surface charge, causing gaps in the pattern (left), or can be deposited homogenously if no surface charge persists (right).

First, particles were deposited on two polypropylene foil pieces. This material is known to have insulating properties and can be easily charged triboelectrically by contacting and rubbing with a glove of natural rubber latex. One of the pieces was triboelectrically charged and the second was only washed with methanol. Methanol has shown to neutralize any surface charge on the polypropylene foil.

In Figure 5.7, the deposition shows the two different results: on the left, the particle deposition shows several gaps, the charge seems to interfere with the homogenous deposition. On the right, a homogenous particle deposition was achieved and the deposition pattern has the shape of the electrode which was located behind the foil. The surface charge conductivity of the polypropylene foil could not be measured in the particle charge electrometer, because it has to be placed on top of a glass substrate, which makes the measurement useless due to the dominating glass surface conductivity. However, it could be observed that the charge was persistent over longer periods of time compared to glass surfaces, which lead to the assumption that the surface conductivity of polypropylene is rather low.

This effect has been observed recently on PDMS surfaces in a microscopic scale [60], showing that the triboelectric charging is not based on macro- but microscopic charging effects.

Similar to Figure 5.7, the depicted effect was also observed on MFw glass surfaces. Figure 5.8

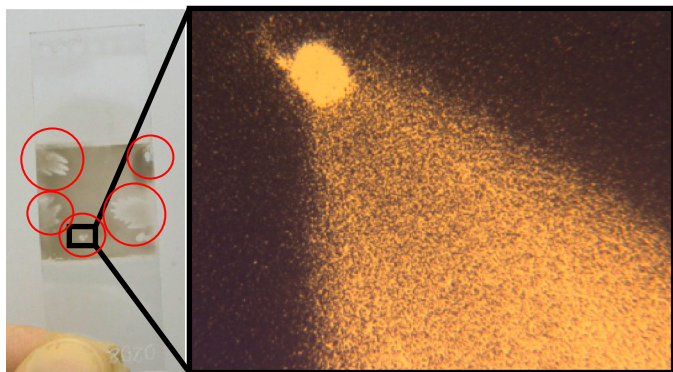


Figure 5.8: Particle deposition onto MFw glass. Surface charges interfere with homogenous particle deposition; red circles highlight scarce deposition areas.

shows a supposedly homogenous particle deposition with several gaps using the aerosol generator. This effect was only observed on the MFw glass type, the other two glass types did not appear to be susceptible to this effect. One can suppose that this is due to their higher surface conductivity.

Concluding from these results, one would intuitively propose, that a thorough cleaning of an MFw glass slide with methanol should render the best printing results with the peptide laser printer. However, in our case, the opposite turned out to be valid.

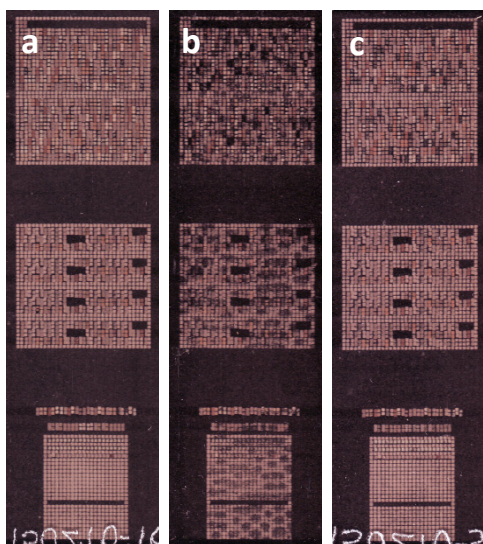


Figure 5.9: Laser printing results on different glass types. Glass types: MFg (a), MFw (b), LB (c). The best results are achieved with MFg and LB glasses, the MFw glass shows the gap phenomenon.

5.1.2 Improved printing results

Comparing the three different glass types in the printing process (see Figure 5.9), it could be observed that the best printing results are achieved on the MFg glass, the LB glass has almost the same quality. In comparison, the MFw glass showed the most prominent case of the gap phenomenon.

This was still the case after thorough cleaning with methanol, thus, one can explain this effect with the following hypothesis: Before the transfer of the pattern, the surface of the LB and the MFg glass is depleted of the surface charge by air breakdown, as

soon as the OPC drum comes into the proximity of the glass edge. During printing, the surface is already homogeneously depleted of the charge, which improves the printing result. In the case of the MFw glass type, the charge cannot be depleted at once, because the conductivity is low. This causes the charge to be confined to the surface, increasing the local electric fields between the OPC drum and the glass surface, causing the air breakdown and resulting in the gaps.

For the sake of completeness, it shall not be concealed that this is only a working hypothesis. Due to the very high electric fields, non-linear effects may change the dielectric properties of glass, resulting in very complex interactions. Yet, for our printing process, this hypothesis is applicable and helped to improve the pattern quality by using the LB glass type. This type has the best properties in terms of autofluorescence and pattern quality. However, in future works, the impact of air humidity on the printing quality should be further analyzed, because this parameter seems to have a decisive effect on the printing quality.

5.2 CMOS chip deposition improvement

In this section, the advances in aerosol controlling and the new aerosol generation system will be introduced. The subsequent sections will then show the improvements achieved exploiting the simulations and the new aerosol generator.

5.2.1 Implementation of a sieve in the aerosol flow

The results from the particle-flow tribo-electrometer (subsection 2.1.1) gave the impression, that the quality of the particle deposition pattern might be improved by increasing the q/m value of the particles. Derived from the charge measurements, this can be achieved by using particle fractions with a smaller mean diameter, because fine particle fractions can obtain higher q/m values. However, the simulations proved this statement to be wrong: The most important characteristic for a qualitatively good deposition pattern is in fact the particle size and its impact on fluid friction.

Yet, besides a small particle diameter, another important factor was found for high quality deposition of particles on the CMOS chip. Figure 5.10 shows two different effects observed

after particle deposition: In Figure 5.10a, the deposited pattern was completely inverted, due to an undesired inverse charging of the particles. This effect was caused by particles sticking to the walls of the cyclone of the (outdated) aerosol chamber (see Figure 1.14) and thus, particles were rubbing against particles, resulting in a positive instead of a negative particle charge. The second effect, displayed in Figure 5.10b, was caused by big particle agglomerates, contaminating the chip surface.

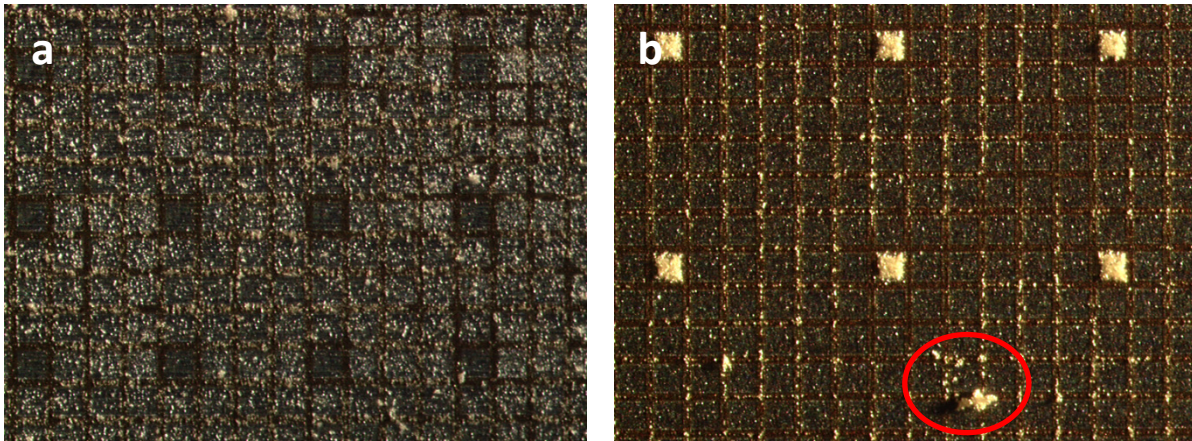


Figure 5.10: Different aspects of particle deposition on the chip surface. In (a), the deposition pattern was inverted due to an inverse charging of the particles. In (b), the pattern exhibits undesired particle agglomerates, contaminating switched off pixels.

Concluding from these results and other simple experiments (see [29]), where it could be observed that particles can be manipulated during movement in electric fields of about 1000 V/cm, a metal sieve (by Haver & Boecker, Germany) was introduced into the particle flow. Particles and possible agglomerates have to pass a sieve with negative voltage of 1 kV, before reaching the chip. Due to the small mesh size, only particles with a small diameter can pass the sieve, agglomerates are unable to reach the chip surface, because they are held back or are destroyed. Additionally, the sieve voltage acts as a particle sorter, separating particles by charge: Negatively charged particles, located between chip (about +100 V) and sieve (-1 kV), are accelerated towards the chip; positively charged particles are decelerated and cannot reach the chip surface. The sieve therefore allows the selection of particles smaller than the mesh size and, furthermore, the selection of particles with equal charge signs. This reduces contaminations by restraining positively charged particles and particle agglomerations from entering the deposition region. A reduction of the mesh size of the sieve to about 10 μm further improved the deposition quality.

5.2.2 Development and construction of an aerosol generation system

After the successful implementation of the sieve, the main objective was to create a new aerosol generation system, to evade the drawbacks of the former method: Especially, when using finer particle fractions in the aerosol chamber (see subsection 1.4.2.1), one generally obtained unstable aerosol conditions, clogging of bottlenecks in the chamber, and a massive consumption of particles due to the uncontrollable aerosol density.

Thus, a machine was developed, which allows for a stable aerosol generation and in the same instance is much more compact. The principle is based on an air ejector, which was especially designed by R.O.T (R.O.T GmbH Recycling- und Oberflächentechnik, Germany) for our needs. Therefore, a standard ejector from powder coating processes was redesigned by R.O.T to allow for very small amounts of aerosol to be ejected. A compact system was built, consisting of 20 different particle containers, mounted on a vibrating plate (also by R.O.T) to prevent undesired clogging and particle agglomeration. In Figure 5.11, the schematic of the ejector principle is shown: To generate an aerosol with reproducible quality and constant aerosol densities, the particles are siphoned out of their reservoir through an ejector by a pressurized air flow called *transport air*. The density of the aerosol can be controlled by an additional pressurized air flow, called *dosage air*: The dosage air forms a compound with the aerosol, rendered by the transport air, and thereby decreases the aerosol density and increases the flow velocity. This allows for a better aerosol transport and reduces clogging risks.

Subsequently, the automation, the calibration, and especially the design of the deposition geometry were devised solely in the scope of this thesis.

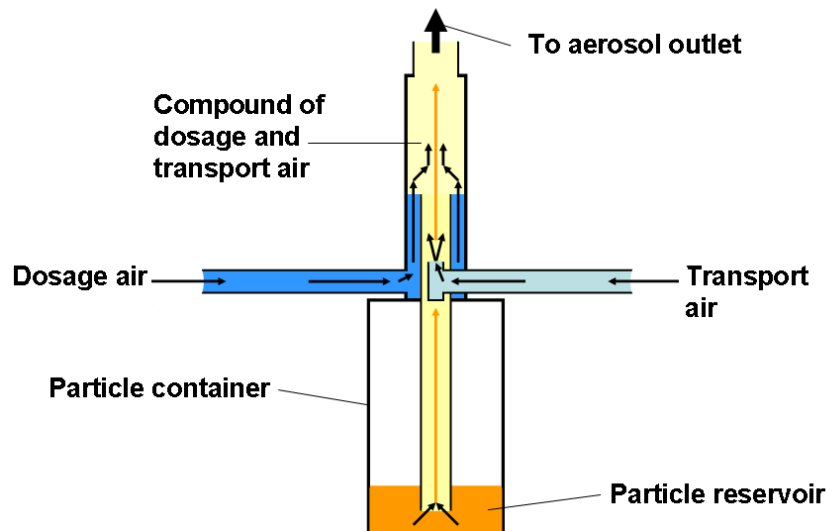


Figure 5.11: Principle of air ejector for aerosol generation. Particles are siphoned out of their reservoir by a pressurized air flow called *transport air*. The aerosol density can be controlled by another pressurized air flow, called *dosage air*: the more *dosage air* is added, the thinner is the aerosol.

Figure 5.12 shows the schematic setup for the particle deposition process: A polytetrafluoroethylene (PTFE) tube connects the ejector, mounted onto the particle reservoir, with an outlet where the CMOS chip for particle deposition is brought into contact with the aerosol. To obtain triboelectrically charged micro particles, the particles are guided

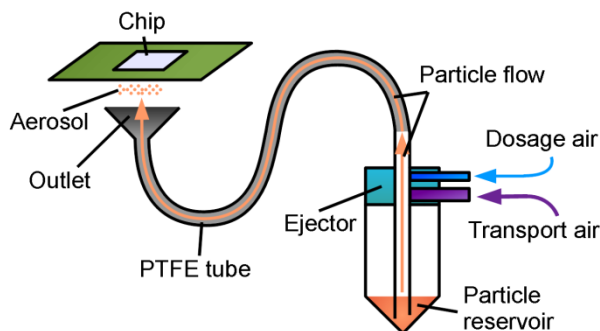


Figure 5.12: Principle of aerosol generation. Particles are siphoned out of a reservoir through an ejector, the aerosol is guided through a PTFE tube to the outlet, where the aerosol is brought into contact with the chip surface

through the PTFE tube. Due to the turbulent flow in the tube, particles contact the inner surface of the tube, resulting in triboelectric charge of the particles.

A schematic of the outlet geometry is shown in Figure 5.13a: The PTFE supply tube from the aerosol generator ends in the outlet which is then expanding from a diameter of 0.8 cm to a diameter of 3 cm,

reducing the flow velocity. Afterwards, the aerosol has to pass a sieve with a mesh size of 8 – 10 μm , restraining bigger particles, and especially agglomerates, from reaching the chip surface. Finally, the particles come into the proximity of the chip surface.

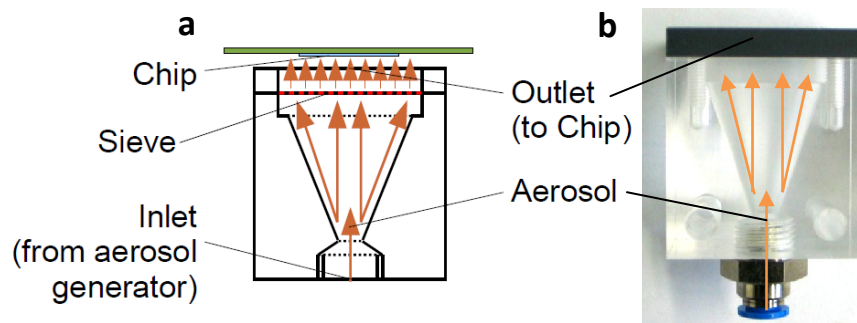


Figure 5.13: Geometry of the aerosol outlet and the CMOS chip position in the aerosol stream for particle deposition. Schematic construction drawing (a), original outlet (b) manufactured by the Kirchhoff Institute of physics workshop.

The construction drawing (Figure 5.13a) of this geometry was devised in Autodesk Inventor (Autodesk, Inc., USA) and manufactured accordingly by the workshop of the Kirchhoff Institute of Physics (Figure 5.13b).

In Figure 5.14, the actual aerosol generator is shown with the 20 ejectors, particle reservoirs, and outlets. A computer interface (EtherCAT hardware and TwinCAT software, Beckhoff GmbH, Germany) controls different 24 V outputs, which operate the electronic valves (SMC Pneumatik GmbH, Germany) connected to pressurized air. The 40 different valves control the two pressurized air inlets of each of the 20 ejectors. The electronic operation ensures reproducible air flow durations.

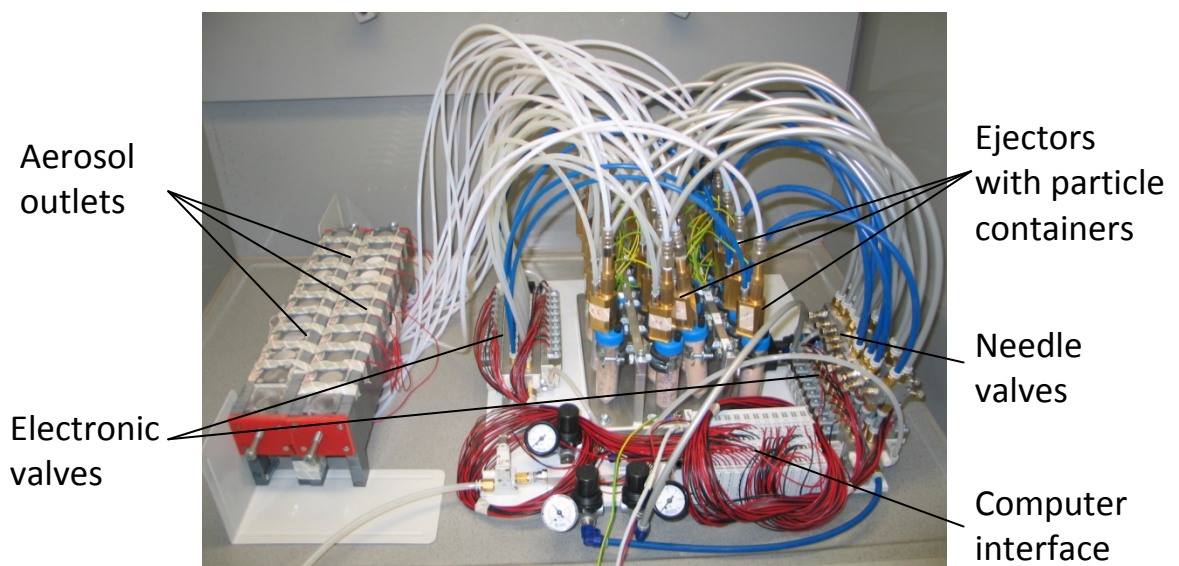


Figure 5.14: Device for aerosol generation, controlled through a computer interface. The CMOS chip is positioned in the aerosol stream near the outlets for particle deposition.

The pressurized air is controlled in two separate ways: The dosage air is switched on continuously for 1.4 s and the transport air is switched on for three pulses of 200 ms with a 200 ms break before each pulse and after the last pulse. The idea is to create short pulses of a rather dense aerosol and use the constant dosage air flow, to transport the particles through the PTFE tube to the outlet. This operation method ensures that the ejector is not clogged by particles, because a constant transport air flow with lower air pressure leads to clogging of the ejector nozzle. Additionally, the dosage air can also be used to clear the PTFE tube.

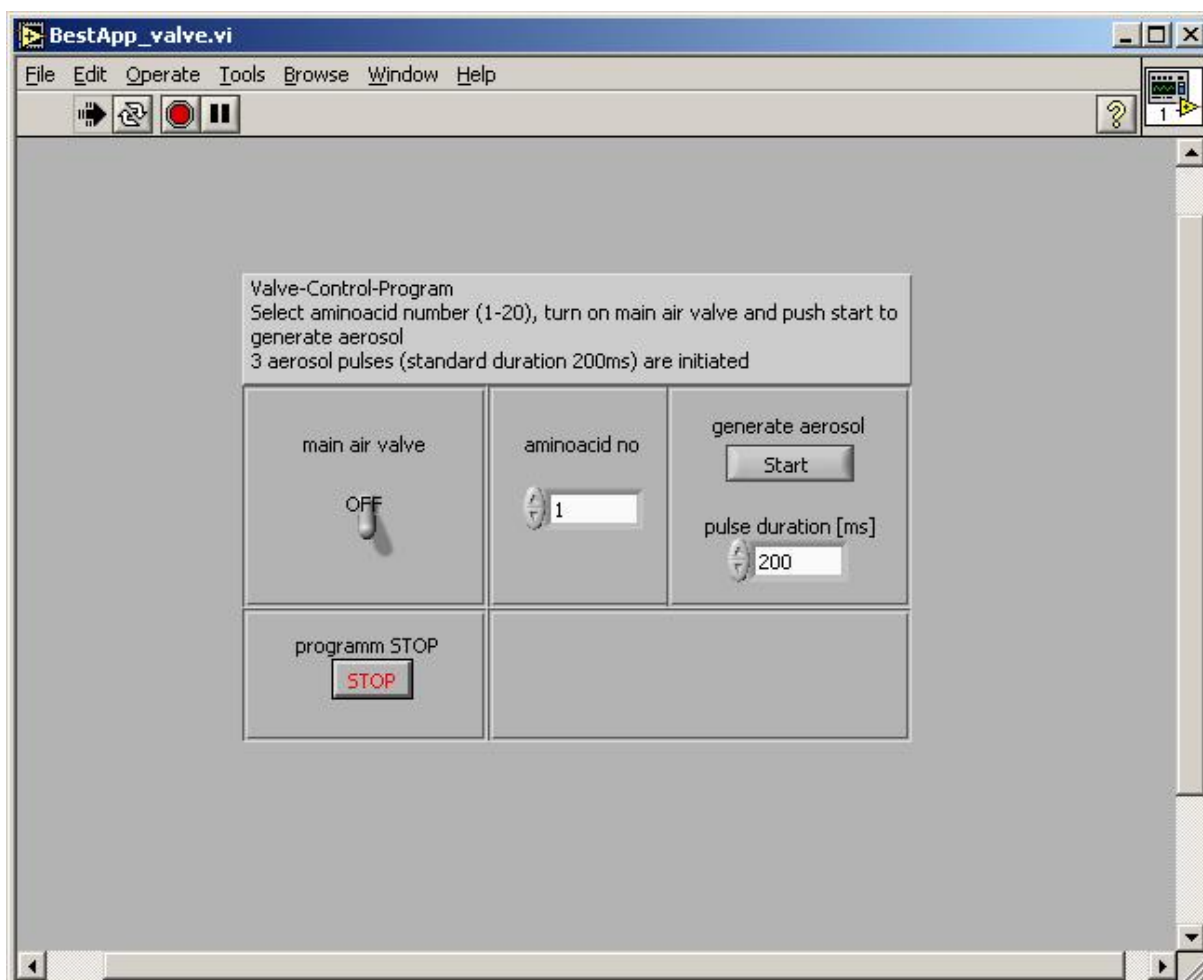


Figure 5.15: LabVIEW interface. Aerosol generation control program, written in LabVIEW (National Instruments, USA)

Figure 5.15 shows the interface, programmed in LabVIEW (National Instruments, USA). A switch for the main valve controls the vibration plate and the general air feed for the valves. The amino acid selector selects the valves for generating one certain type of aerosol. Additionally, a “start” button for aerosol generation is located above the selector for the pulse duration.

A drawback of this system is that the transport air inlet of each ejector requires an additional, individually, and manually adjusted needle valve, to control the aerosol density. The needle valve has to be adjusted to the particle type, because each particle type possesses its own flow characteristics, and has to be readjusted occasionally. Yet, the particle consumption of this system is much lower than the consumption of the former aerosol system (chapter 1, subsection 1.4.2.1) and the aerosol density is significantly improved and much more stable.

5.2.3 Improved experimental particle deposition on the chip

As shown in the preceding chapter, the simulations revealed that the particle size in

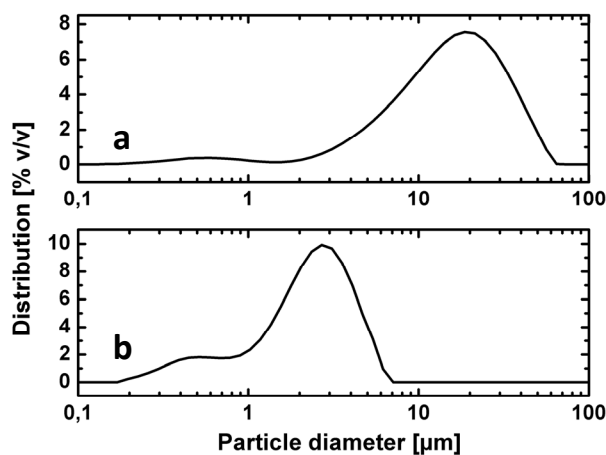


Figure 5.16: Particle distribution in volume percent (% v/v): (a) wide distribution of larger SAC particles with a mean diameter of 15.6 μm ; **(b)** narrow distribution of small SAC particles with a mean diameter of 2.3 μm

combination with its maximum charge is a decisive parameter for spatially selective particle deposition. Focusing on this parameter, the particle production was optimized according to the simulations: In Figure 5.16, the particle size distributions of two different particle fractions are shown, measured with a Malvern Mastersizer. Particle fraction (a) exhibits a wide distribution of larger particles (named *coarse fraction*) with a mean diameter of 15.6 μm whereas in (b) a narrow

distribution of small particles with a mean diameter of 2.3 μm (named *fine fraction*) is shown.

The fine particle fraction is a result of the aforementioned optimization process. As proposed in the simulations, a fine particle fraction with a narrow size distribution, a small mean diameter, and, most importantly, a small maximum diameter of about 7 μm is required. The undesired coarse particle fraction, in turn, has a wider size distribution with a larger mean and maximum diameter.

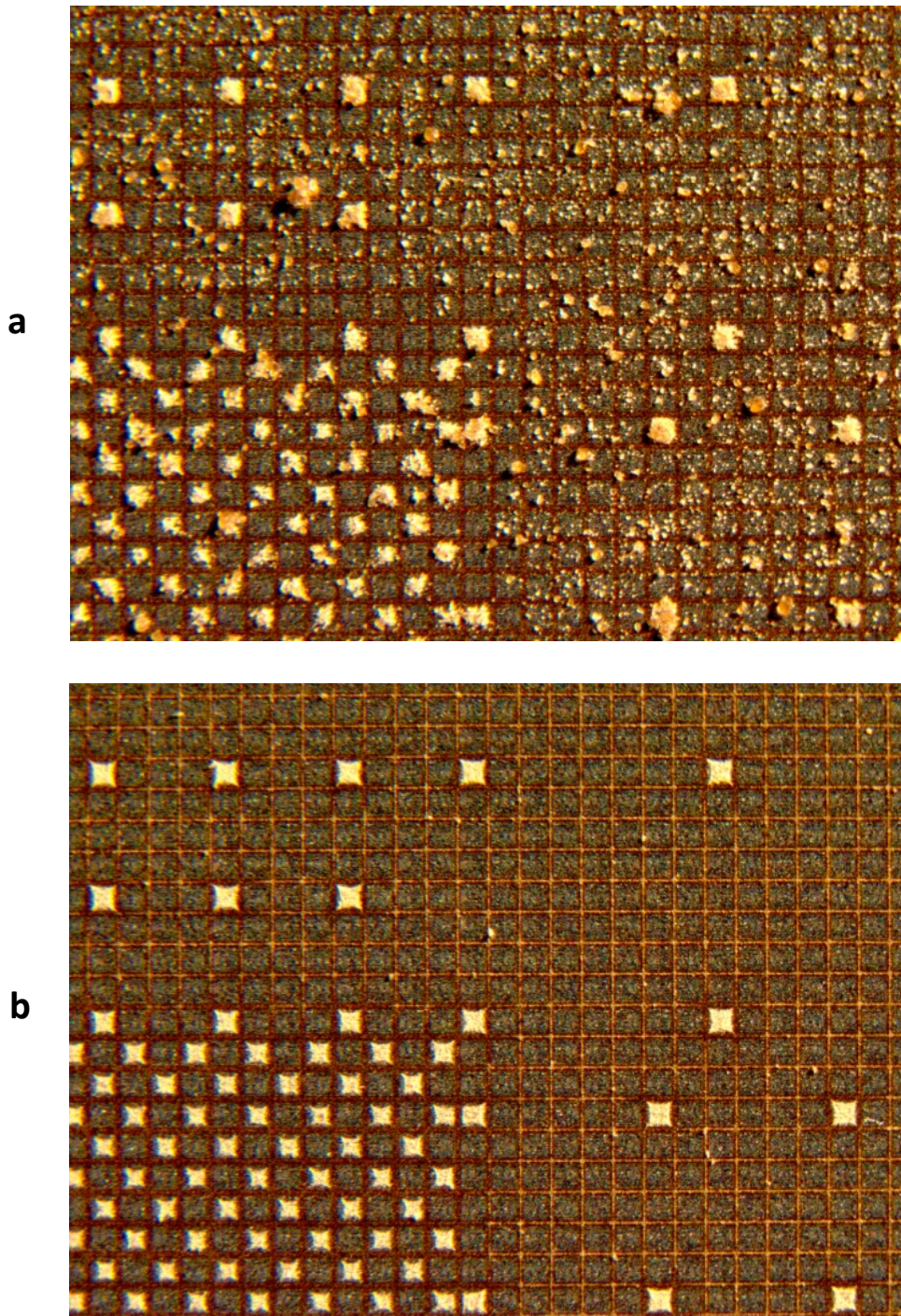


Figure 5.17: Four different deposition patterns of micro particles on each chip surface (checkerboard, 1 of 16, 1 of 36, 1 of 64): (a) high degree of contamination; particles with a wide size distribution and a mean diameter of $15.6\ \mu\text{m}$ were used; (b) almost free of contamination; particles with a narrow size distribution and a mean diameter of $2.3\ \mu\text{m}$ were used

Using this fine particle fraction, a powerful improvement in particle deposition quality can be achieved, as shown in Figure 5.17. In Figure 5.17a, the particle deposition shows a high degree of contamination, although the checkerboard pattern in the lower left part of the picture is clearly visible with an almost acceptable grade of contamination. The mean

diameter of particles used in this experiment was $15.6\ \mu\text{m}$. On the contrary, in Figure 5.17b, the deposition pattern is almost free of contamination, because theoretically achieved results were taken into account. The mean particle diameter here was $2.3\ \mu\text{m}$.

Thus, the results of the simulations could be verified in experiments, obtaining highly improved deposition results with the fine particle fraction. Furthermore, in Figure 5.17b, the grid electrode is covered with particles in regions with a high proportion of 0 V pixels, whereas in the region of the checkerboard pattern, no particles are deposited on the grid.

As considered theoretically in Figure 3.8, the grid electrode is very important for

contamination free deposition, because excess particles will always be part of particle deposition by means of an aerosol. Therefore, an adsorber for these excess particles was inevitable in our experiments.

With the grid electrode set to 30 V, experiments showed that at least ten consecutive particle depositions are possible without overloading the grid electrode with particles, which could yield notable contaminations. This will be further investigated in the next subsection. Due to the width of the grid electrode of only $15\ \mu\text{m}$, it is also important to use smaller particles. As shown in the simulations (Figure 3.9 and Figure 3.10), smaller particles provide a lesser total number of deposition events on the grid, thus, avoiding particle overload.

The effect, described in the simulations (Figure 3.12), is omnipresent in the

experiments: In Figure 5.18, particles with a mean diameter of $2.3\ \mu\text{m}$ were deposited on a

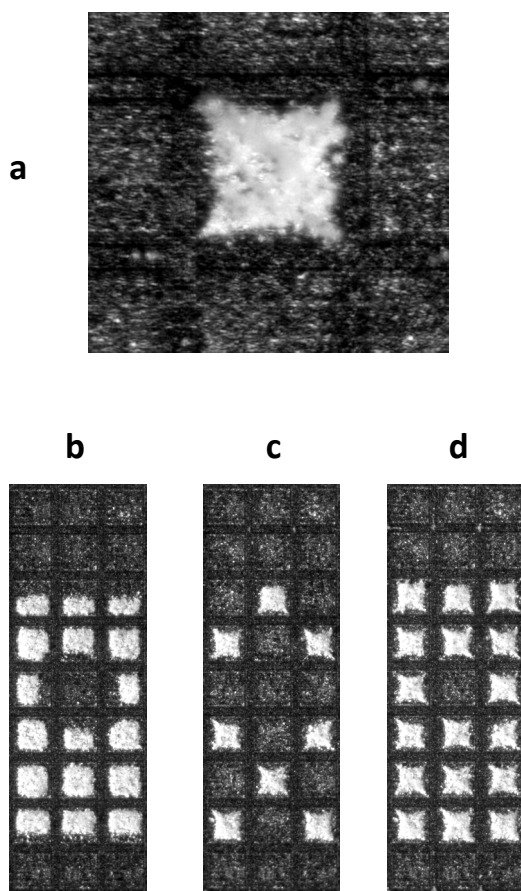


Figure 5.18: Deposition on a chip (mean particle diameter $2.3\ \mu\text{m}$) exhibiting the effect described in the simulations in Figure 3.12. (a) single pixel with the pincushion effect visible; (b) in dependence of the voltage of directly surrounding pixels, particles either tend to be deposited in the center or on the side of the pixel; to guarantee isotropic central coverage of pixels, the same deposition pattern is produced by two consecutive deposition steps (c) and (d)

chip surface. In Figure 5.18a, a magnification of a particle deposition pattern with one single 100 V pixel surrounded by grounded pixels is shown. The deposition shows the typical experimentally observed characteristics: The pixel is entirely covered with particles, except for the borders. The corners however, are covered, because the electric field of a peak is higher in comparison to the edges. As the shape resembles a cushion pinned at the edges, this effect was named the *pincushion-effect*. Although particles were only deposited on charged pixels in Figure 5.18b, some pixels are only half covered or particles are only deposited in the center of the pixel. This effect can be explained by the superposition of electrical fields, resulting in the depicted deposition pattern.

The pincushion effect (Figure 3.12a and Figure 5.18a) is still acceptable for spatially defined particle deposition because the center of the pixel is covered isotropically. In contrast to this, the effect shown in Figure 3.12b and Figure 5.18b impedes reliable particle deposition, as a reproducible deposition is required with homogeneous central coverage on each pixel. Being an intrinsic characteristic of the setup, as the simulations revealed, the effect only occurs when using smaller particle fractions, because of their precise deposition according to the electric fields. Bigger particles hide this effect due to their less accurate deposition behavior. In order to circumvent this in experiments, one possibility is to divide the deposition pattern into several sub-patterns, such that directly adjacent 100 V pixels are not simultaneously active in one pattern. For instance, an area with all pixels to be covered can be produced by two consecutive deposition steps with two complementary checkerboard patterns (Figure 5.18c, d). The disadvantage of this method is the increased number of necessary deposition steps. However, as simulations and experiments show, this guarantees isotropic central coverage while being simple to implement.

To illustrate the consistency of simulations and experiments, the electric potential of a detail of the chip surface was simulated. In Figure 5.19 left, a simulation of a 5 x 5 pixel checkerboard pattern on the CMOS chip surface is shown. Only the highest electric potential (between 99.8 V and 100 V) is depicted in yellow, pixels are colored in gray, the grid electrode is shown in brown. In Figure 5.19 right, the experimental result of particle deposition with a diameter of 2.3 μm on the CMOS chip is shown. The particle deposition clearly resembles the simulation of the highest electric potential, small particles tend to be

deposited in good agreement with the selective electrical field. Even the pincushion effect can be found in both cases.

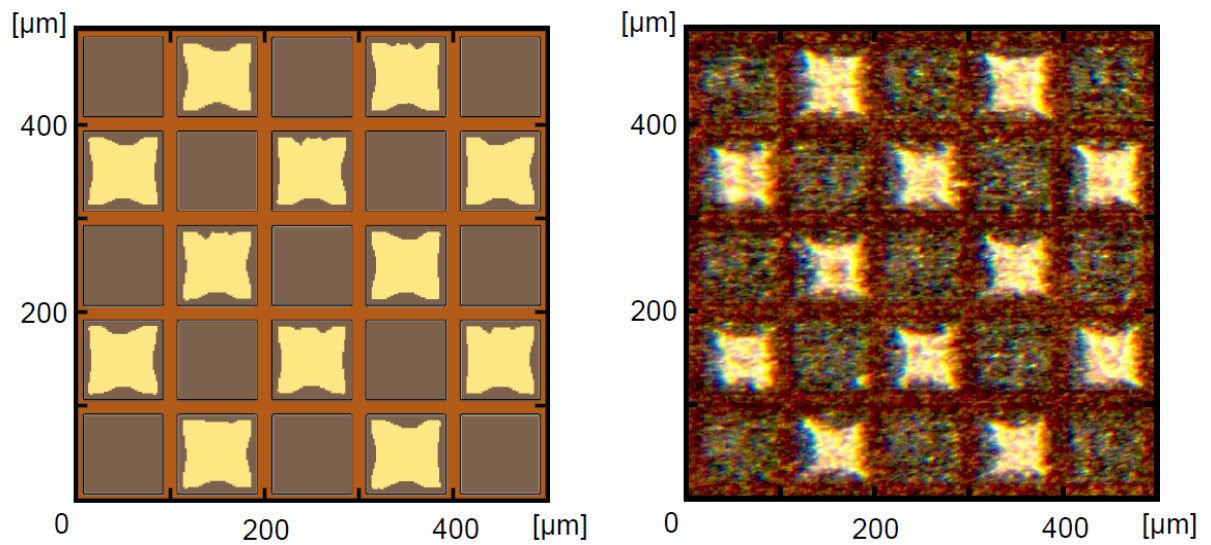


Figure 5.19: Simulation of a checkerboard pattern on the CMOS chip surface. Only the highest electric potential (99.8 - 100 V) is shown in yellow, pixels are gray, the grid electrode is shown in brown; (right) experimental result of particle deposition (mean diameter of 2.3 μm)(from [32])

Figure 5.20 shows a deposited particle pattern on the chip surface with very high quality and without any visible contaminating particles. Some pixels seem to exhibit single bright spots which are not caused by single mis-deposited particles, but by the roughness of the chip surface. The pattern was deposited in two steps, similar to Figure 5.18d, the pattern was divided into two complementary checkerboard patterns, deposited consecutively.

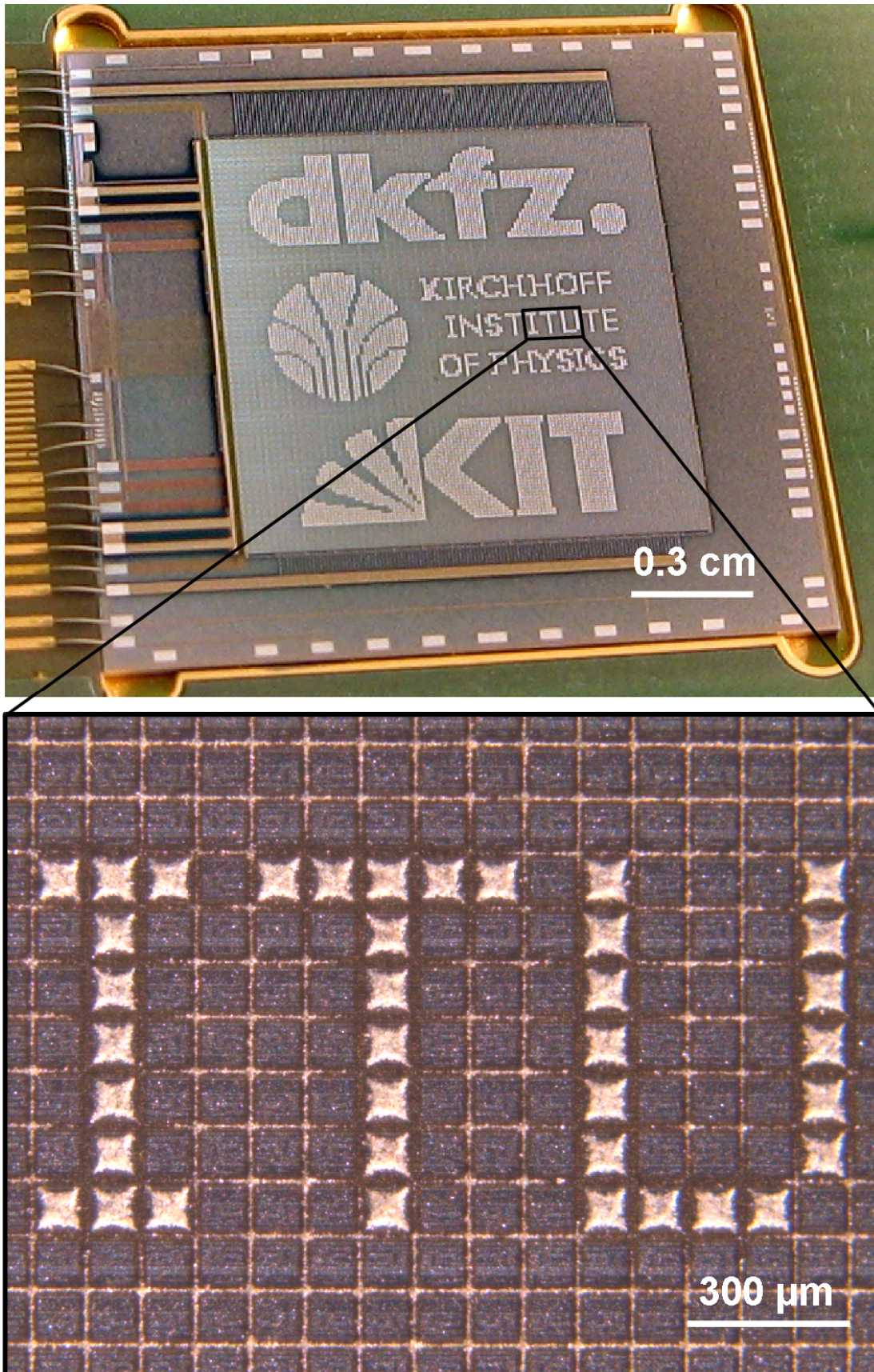


Figure 5.20: CMOS chip with particle deposition pattern with a total of 16,384 pixels on 1.28×1.28 cm^2 . Pattern (two consecutive deposition steps) on the chip (top) and 15 x magnification detail (bottom).

5.2.4 Deposition reproducibility

In this section, the repeated particle deposition on the CMOS chip is investigated. Using the image processing method from (and performed by) J. Wagner (see [61]), the pattern quality and especially the relative amount of contamination and the increase in contamination can be evaluated.

In the following experiment, 20 similar patterns were deposited subsequently onto the same

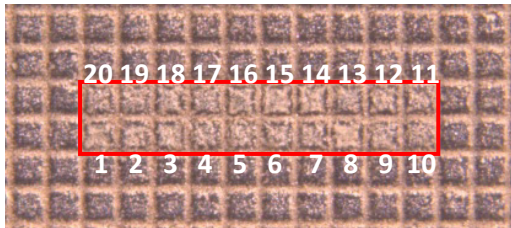


Figure 5.21: Deposition pattern of 20 adjacent and subsequently deposited patterns, covering 20 pixels (highlighted with red rectangle). Particle diameter 3.3 μm , pixel voltage 100 V, grid 25 V.

chip, using the same particle fraction (3.3 μm diameter, pixel voltage 100 V, grid 25 V). Figure 5.21 shows the final deposition pattern after 20 deposition steps: Each pattern consists of a single switched on pixel (numbered 1 – 20); the first one is located at the lower left, migrating in a row to the right until a line of ten adjacent pixels is accomplished. The eleventh pixel begins a new row just above the first, until 20 pixels are covered with particles.

Using this pattern, the amount of contamination was measured on the surrounding and supposedly uncovered pixels after 5, 10, 15, and 20 deposition steps. The evaluation was performed with the already mentioned tool.

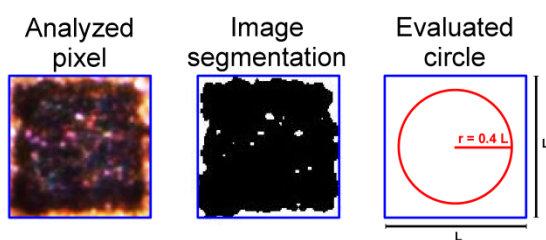


Figure 5.22: Pixel cell analysis. The pixel is analyzed, segmented, and the area of a circle with the radius of $0.4 \cdot L$ (L is the pixel length of 85 μm) is evaluated for the contamination statistic.

In Figure 5.22, the process of pixel analysis is explained: one pixel is analyzed, segmented, and the area of a circle with the radius of $0.4 \cdot L$ (L is the pixel length of 85 μm) is evaluated for the contamination statistic. In the following, only the contamination of the circle area of each pixel will be considered for the total percentage of contamination, because this is the most relevant area for combinatorial

synthesis. The higher the amount of contamination, the more white pixels are located inside the circle, and the higher is the pixel coverage. For more information about the segmentation process, see [61].

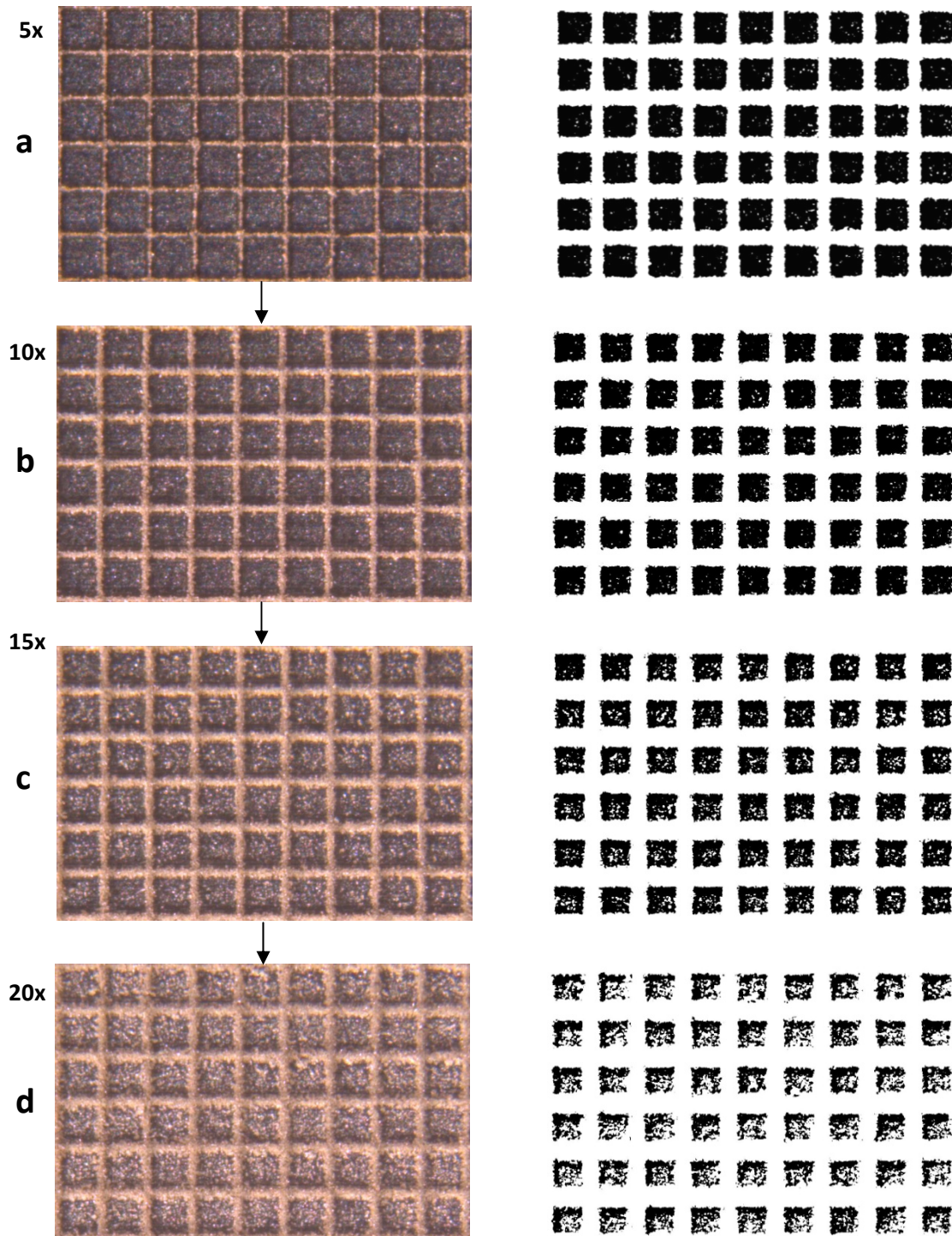


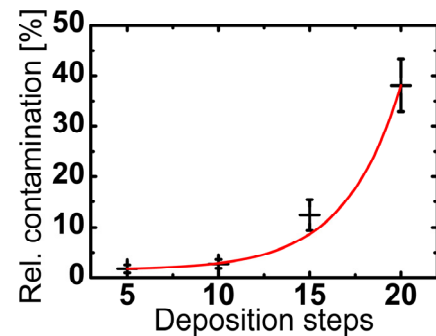
Figure 5.23: Repetitive particle deposition on the CMOS chip (left) and corresponding image segmentation (right). A selected area of supposedly uncovered pixels in sequential deposition after 5 (a), 10 (b), 15 (c), and 20 (d) deposition steps is shown with the corresponding image segmentation. All particles with a $3.3 \mu\text{m}$ median diameter were consecutively deposited, the pixel voltage was 100 V or 0 V, the grid voltage was 25 V (notice: each segmented pixel has to be flipped vertically in the pixel center, to correspond to the experimental deposition, due to the algorithm!)

Figure 5.23 shows a selected area of supposedly uncovered pixels in sequential particle deposition after 5, 10, 15, and 20 deposition steps (Ala particles with a median diameter of 3.3 μm) and the corresponding image segmentation.

As expected, the contamination gradually increases with the number of deposition steps. However, the statistical analysis in Table 5.2 shows that the contamination (i.e. the mean coverage of all 54 pixels with particles) increases in an exponential manner.

Table 5.2: Statistical contamination analysis of 54 pixels for the mean coverage in percent (see Figure 5.23). A graphical analysis of the results with an exponential fit is displayed in the right.

Deposition steps	Coverage	Std. dev.
5x	1.7 %	0.8 %
10x	2.7 %	0.9 %
15x	12.4 %	3.0 %
20x	38.1 %	5.2 %



This can be explained by the simulations performed in Figure 3.13, which introduced the idea of restriction of deposition layer thickness. The particle deposition on the grid electrode will at some point reach a certain maximum, where no particles will be deposited on the grid electrode (i.e. restriction) because the electric charge of the already deposited particles prevents further deposition. As a result, particles will contaminate switched off pixels. The simulations in Figure 3.8 (and corresponding experiments) have shown that the grid electrode is essential for a high quality particle deposition. Therefore, the width of the particle layer deposited on the grid electrode was investigated, assuming that the width can give a good estimation of the particle layer thickness. Table 5.3 shows the approximate mean width of the particle layer on the grid, exhibiting a supposedly logarithmic growth. This corresponds to the inverse function of the exponential increase in contamination.

Concluding from these results and the simulations, it was attempted to minimize the

Table 5.3: Analysis of width of the particle layer deposited on the grid electrode (see Figure 5.23), mean error $\pm 1.9 \mu\text{m}$

Deposition steps	Layer width [μm]
5x	5.8
10x	12.5
15x	17.3
20x	20.2

contamination by the following approach: After each cycle of 5 depositions, a picture of the deposition pattern was taken and afterwards the chip was heated for one minute, causing the particles to melt, but not yet inducing the coupling reaction.

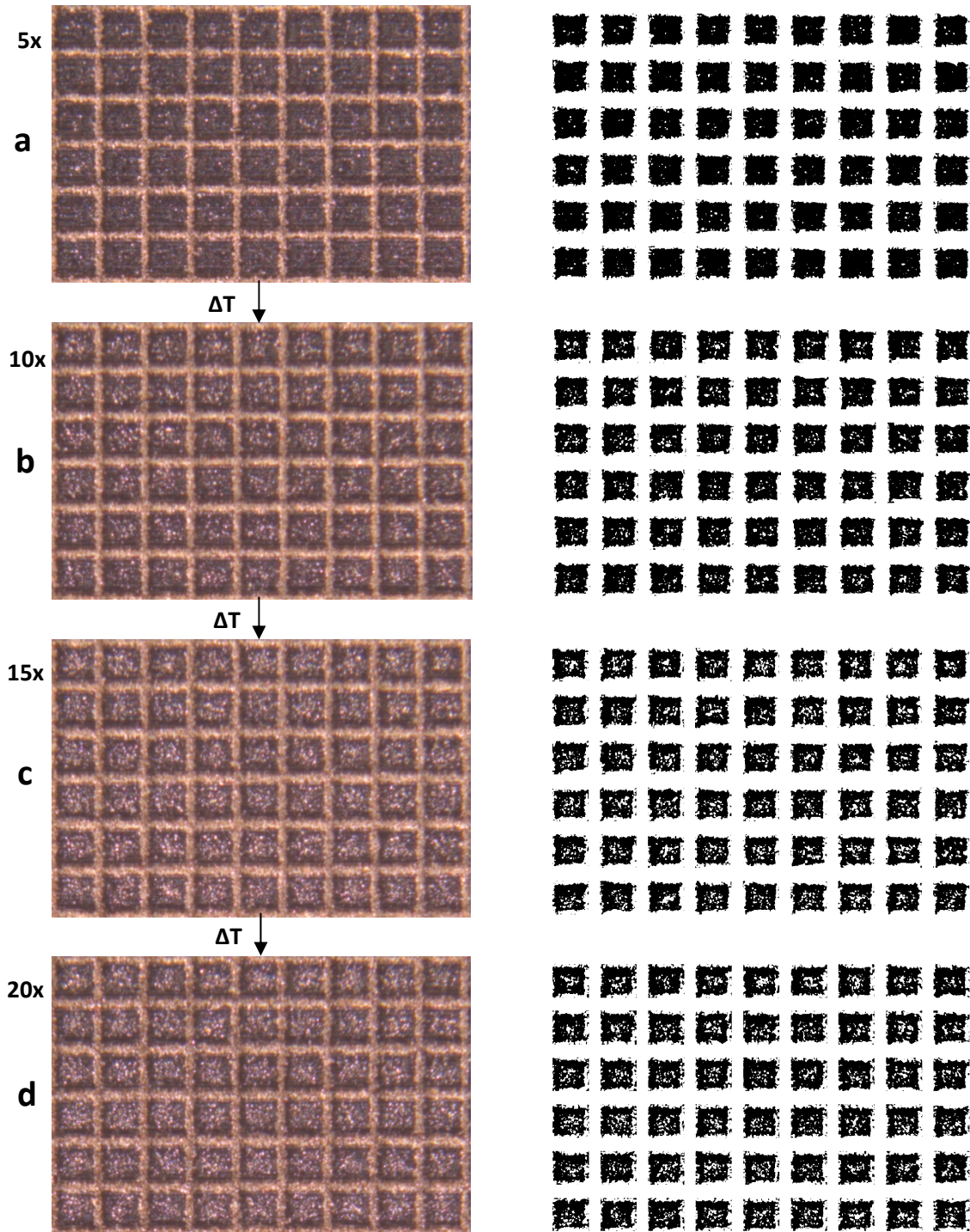


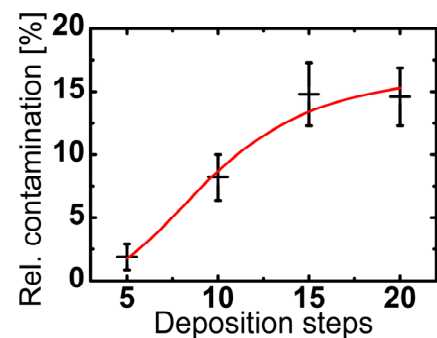
Figure 5.24: Repetitive particle deposition on the CMOS chip (left) and corresponding image segmentation (right). A selected area of supposedly uncovered pixels in sequential deposition after 5 (a), 10 (b), 15 (c), and 20 (d) deposition steps is shown with the corresponding image segmentation. After every five steps, the surface was heated to 90 °C for one minute. Lys particles with a 3.3 μm median diameter were consecutively deposited, the pixel voltage was 100 V or 0 V, the grid voltage was 25 V (notice: each segmented pixel has to be flipped vertically in the pixel center, to correspond to the experimental deposition!)

Following this approach, Figure 5.24 shows the deposition, where the chip surface was heated to 90 °C for one minute after every five deposition steps. In this case, the total amount of contamination seems to be reduced.

The most obvious result of the melting is that the particle layer shrinks. If one assumes that particles have a sphere like shape, the packing of the spheres in a particle layer can be estimated as roughly 20 % ([52]). Due to the low packing density in the unmelted state, the particle layer has a high extent. According to the simulations (see Figure 3.13), a higher extent of the particle layer causes a higher repulsive force. Hence, heating the chip and thereby melting the particles is a possible solution to this problem, which decreases the height of the particle layer by increasing the packing density.

Table 5.4: Statistical contamination analysis of 54 pixels for the mean coverage in percent (see Figure 5.24). A graphical analysis of the results with a sigmoidal fit is displayed in the right.

Deposition steps	Coverage	Std. dev.
5x	1.9 %	1.0 %
10x	8.2 %	1.8 %
15x	14.8 %	2.5 %
20x	14.6 %	2.3 %



In Table 5.4 the mean coverage of the pixels is shown. The coverage seems to reach a plateau at about 15 %, which is roughly half of the value reached without melting the particles.

Table 5.5: Analysis of width of the particle layer deposited on the grid electrode (see Figure 5.24), mean error $\pm 1.9 \mu\text{m}$

Deposition steps	Layer width [μm]
5x	11.5
10x	14.4
15x	14.4
20x	15.4

In this case, the width of the deposited particle layer on the grid electrode (Table 5.5) was also approximated, which also seems to reach a plateau at around 15 μm .

Thus, one can derive from the experiments that a carefully applied melting can significantly improve

the deposition quality. If the particles are melted, one creates more space for further particle deposition on the grid. Additionally, it can be assumed that the net charge of the particles might be redistributed or transferred to the metal of the chip by diffusion during the melting process, decreasing the overall charge of the particles.

However, the melting does also have a slightly negative effect on the image segmentation: Melted particles have the tendency to become less distinguishable (see Figure 5.25) for the camera and can be mistaken as uncovered chip surface. Thus, the total contamination is in fact slightly higher, yet, this was not analyzed in detail.

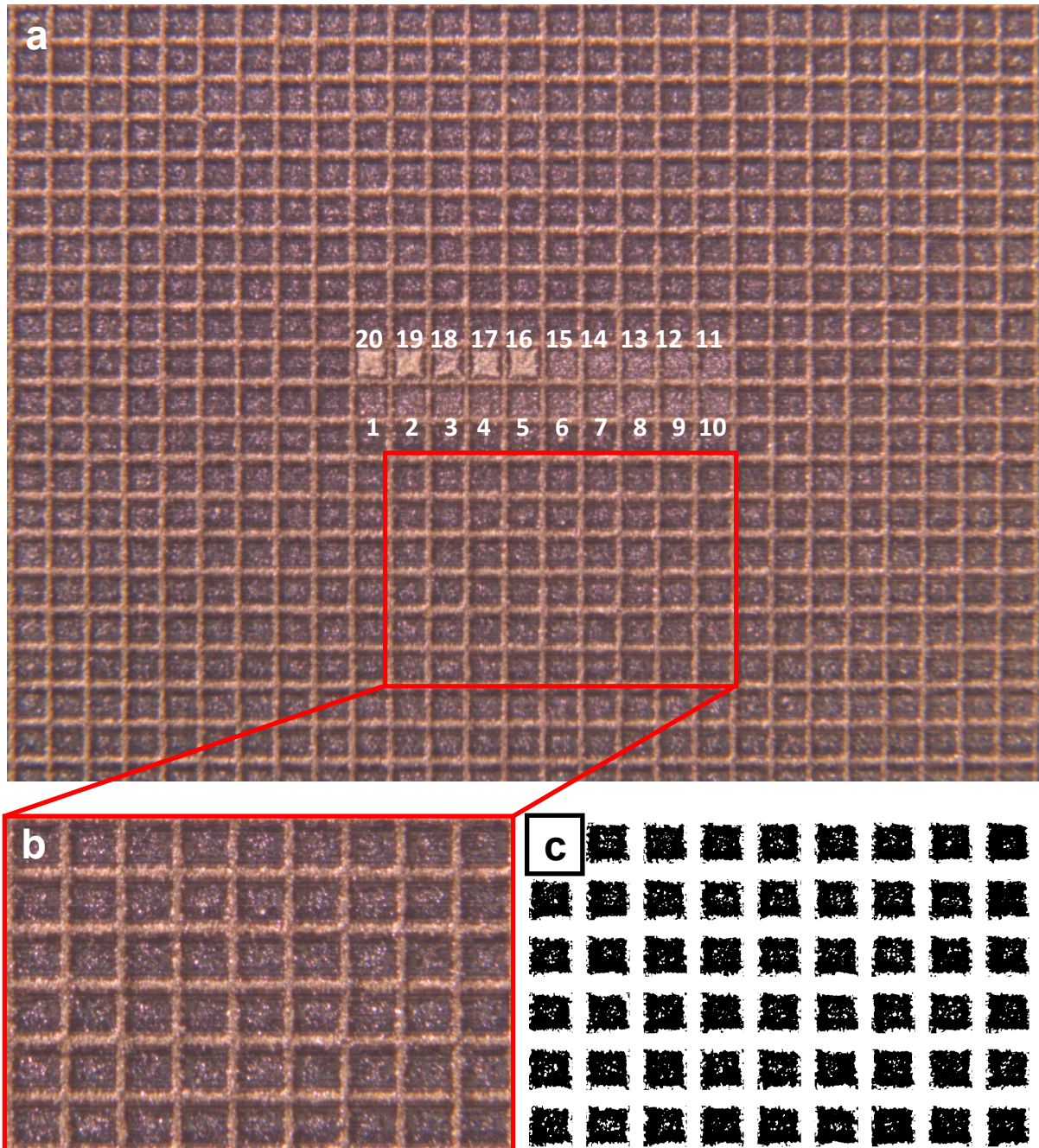


Figure 5.25: 20 repetitive particle deposition steps (numbered 1 - 20) on the CMOS chip with very low contamination (a). After every five deposition steps, the surface was heated to 90 °C for one minute, thus, particles on the pixels 1 – 15 are melted and have a different appearance. Lys particles with a 3.3 μm median diameter were consecutively deposited, the pixel voltage was 100 V or 0 V, the grid voltage was 25 V. The mean contamination after 20 steps is about 5 %. The magnification of the detail in (b) was analyzed with the image processing method (c).

In some areas of the chip, very good results with a total contamination of about 5 % (see Figure 5.25) were achieved. The highest contamination rate obtained with the heating after every five steps was about 18 %. To further improve the deposition pattern, the heating process can be repeated after 3 deposition steps or even after every single step.

These results lead to the conclusion that the generation of combinatorially synthesized peptide arrays on the CMOS chip is possible. Yet, the best possible particle fractions are required, i.e. a small median particle diameter with a narrow size distribution. This technical detail has to be tackled with new and better methods of milling, sieving, and winnowing, as well as improving flow characteristics with certain additives which are uncritical for the synthesis reaction.

5.2.5 Pixel miniaturization

In accordance to the simulations of miniaturized CMOS chip pixels, the particle deposition on a test chip was analyzed, which features different pixel electrode configurations. The following results have been published in [53].

The most interesting part of the test chip for our experiments are the different electrode matrices of 8 x 8 pixels with different pitches (see Figure 5.26). The fields of 44 μm , 30 μm , and 20 μm pitch were analyzed. A pitch of 44 μm would yield a spot density of about 50,000

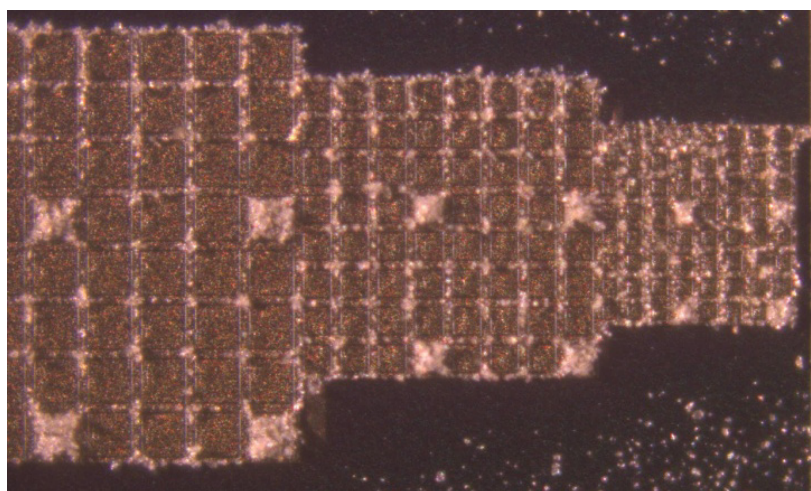


Figure 5.26: Particle deposition pattern on different electrode matrices of 8 x 8 pixels with a pitch of 44 μm , 30 μm , 20 μm (from left to right). Ala particles with a diameter of 3.3 μm were deposited (from [53]).

spots/ cm^2 , a pitch of 30 μm would be equal to 110,000 spots/ cm^2 , and a pitch of 20 μm would render 250,000 spots/ cm^2 . As one can observe in Figure 5.26, the quality of the deposition pattern is acceptable with low contamination. The applied pixel voltage

was 30 V and the grid voltage was set to 20 V, using Al₃ particles with a mean diameter of 3.3 μm. However, a smaller pixel pitch will require an even lower pixel voltage (below 30 V!), therefore, the only actually relevant deposition in Figure 5.26 is the 44 μm pitch.

Other, technologically more advanced high-voltage CMOS processes might allow for higher maximum pixel voltages. For these concerns, refer to [27].

Thus, only the experimental deposition on the 44 μm pixel pitch area was further investigated. Figure 5.27 shows the successful particle deposition of different particle patterns. The checkerboard pattern (Figure 5.27a) and the 1 of 16 pattern (Figure 5.27b) both exhibit a very low contamination and a good pixel coverage. In Figure 5.27 (c - f), a consecutive particle deposition is shown after 2 (c), 8 (d), 12 (e), and 15 (f) deposition steps. In this case, the before mentioned melting technique was not applied, thus, some pixels are not covered properly with particles. Yet, this shows, that a pixel pitch of 44 μm is in principle possible.

Due to the high costs, a new chip run for chips with 44 μm pitch (and more than 50,000 spots/cm²) was not yet affordable.

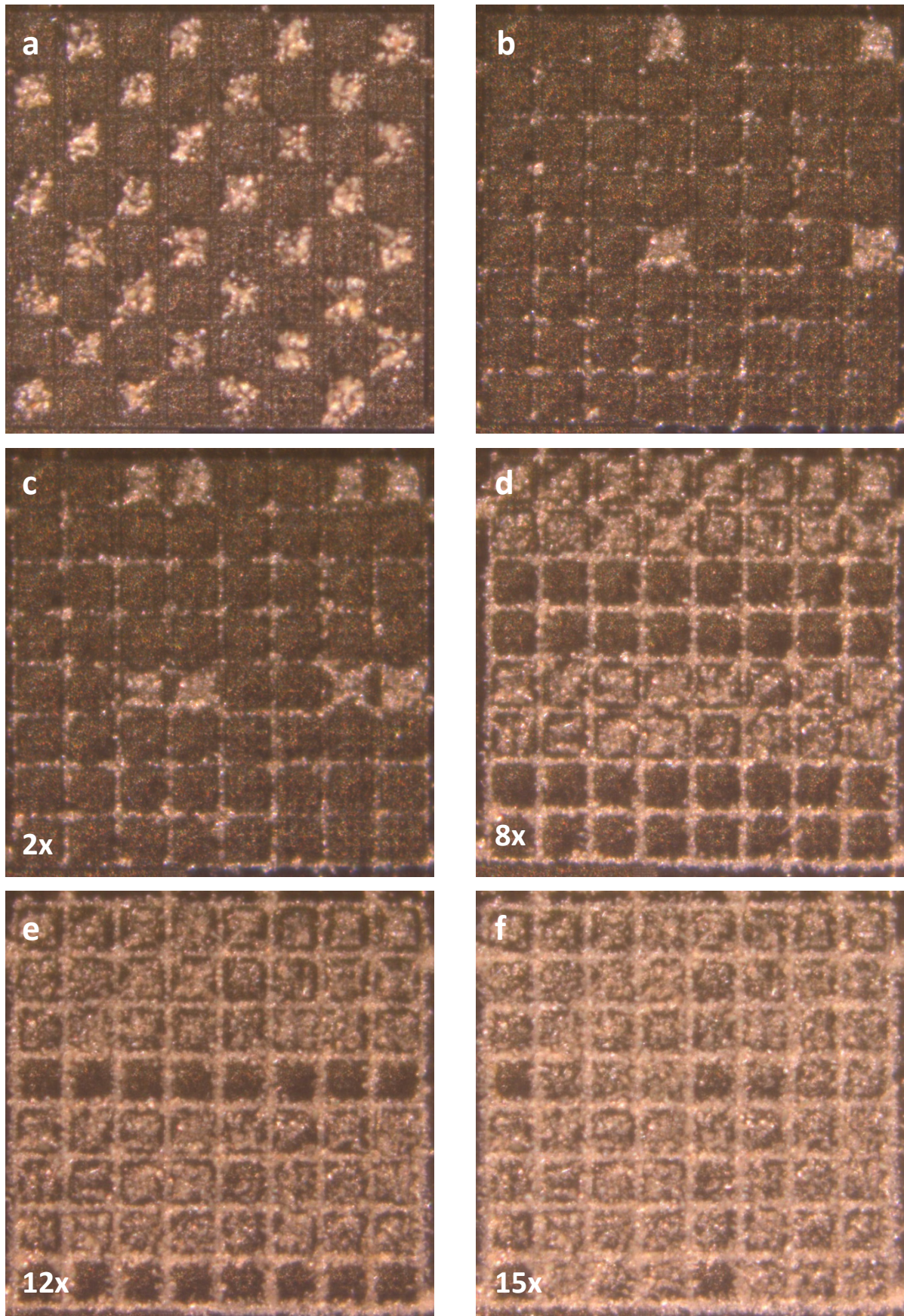


Figure 5.27: Different particle patterns on 44 μm pitch with 30 V pixel voltage and 20 V grid voltage. Checkerboard pattern (a), 1 of 16 (b), and 15x consecutive particle deposition (c - f). (from [53])

5.2.6 CMOS chip printing

As presented in the introduction, the CMOS chip can be used as a printing device (see Figure 1.15). According to the principle, a proof-of-principle experiment was conducted ([31]): A test pattern of Lys particles (4.0 μm mean diameter) was deposited onto the CMOS chip (Figure 5.28a), afterwards, the pattern was transferred to a glass slide (Figure 5.28b), heated (Figure 5.28c), and coupled. Finally, the coupled amino groups were stained with bromophenol blue (Figure 5.28d).

This experiment shows that the approach is feasible, however, the automated machine for a standard application of this process is subject of another thesis [30].

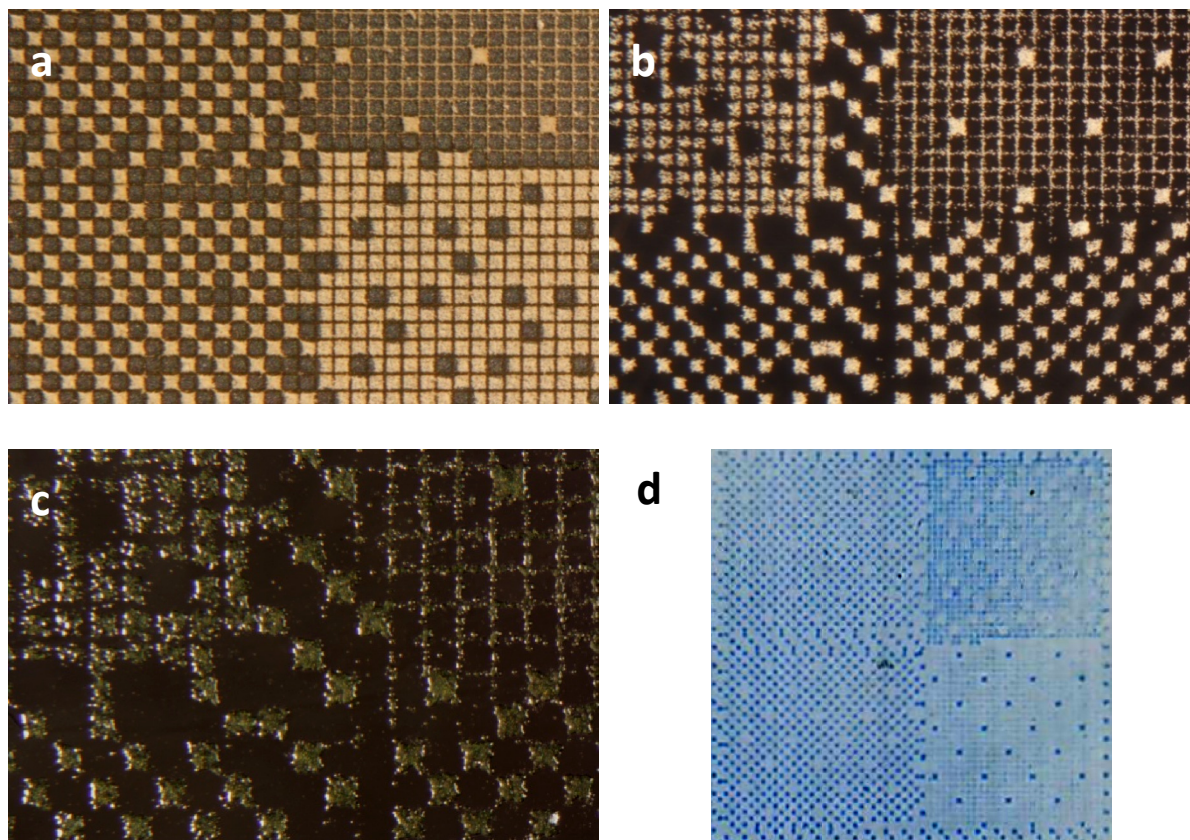


Figure 5.28: CMOS chip printer proof-of-principle. Lys particles deposited onto the CMOS chip (a) and transferred onto a glass slide (b). In (c), the pattern is shown after the melting/coupling process, the final bromophenol blue staining of the amino groups is shown in (d) (from [31]).

5.3 Peptide synthesis on a CMOS chip

Exploiting the improvements in high-precision particle deposition on the CMOS chip, as demonstrated in the previous section, a combinatorial peptide synthesis on the CMOS chip was performed.

It is well known that antibodies bind to several peptides at least with low- or medium-affinity because antibodies are quite promiscuous binders. Even if one can only find poor binders for certain antibodies in random peptide array screens, it is possible to systematically vary the sequences from these binders, and stain again with the same serum antibodies. This offers a straightforward way to find good peptide binders for these antibodies.

In a proof-of-principle experiment, this approach was adapted to two well known epitopes: the 9meric Flag-epitope (N-Tyr-Asp-Tyr-Lys-Asp-Asp-Asp-Asp-Lys-C) and the 9meric HA-epitope (N-Tyr-Pro-Tyr-Asp-Val-Pro-Asp-Tyr-Ala-C). Therefore, these epitopes were altered and different amino acids were substituted to investigate their importance in respective antibody binding. Two different array types were designed: Eight redundant smaller arrays with 34 x 31 (= 1,054) spots, offering 400 different Flag- and 400 different HA-epitope variants. Additionally, four redundant (bigger) arrays were designed with 31 x 63 (= 1,953) spots featuring 1,536 different HA- and Flag-epitope variants. The specific peptide array design and layout is discussed in chapter 4, section 4.3. For a complete list of the amino acid sequences, also see the Appendix (pp. 125 ff, Peptide array layout).

In the following, two different types of surface coatings were used for the CMOS chip peptide synthesis: A monomer coating (AEG₃) in subsection 5.3.1 and a polymer coating (PEGMA/MMA) in subsection 5.3.2. For further information on the coatings, see section 4.4.

The fluorescence images were obtained with a Molecular Devices GenePix 4000B microarray scanner (see subsection 4.6.1). The shown images were only adjusted in brightness and contrast.

After the completed synthesis, the peptide arrays were incubated with monoclonal mouse-Anti-HA IgG antibodies and polyclonal rabbit-Anti-Flag IgG antibodies and were detected with the corresponding secondary antibodies goat-Anti-mouse conjugated with the

fluorescent dye Alexa Fluor 546 and goat-Anti-rabbit conjugated with Alexa Fluor 647. Monoclonal antibodies are generally derived from one B-cell clone and are identical and monospecific. Thus, very few specific binding events are expected. Polyclonal antibodies are a mixture of antibodies, all directed against one antigen, which should result in a multitude of binding partners with various intensities.

5.3.1 Synthesis on AEG₃ coated CMOS chips

First, the monomer coating AEG₃ was used for a peptide synthesis. Due to the intrinsic character of a monomer surface, the total yield of peptides should be significantly lower

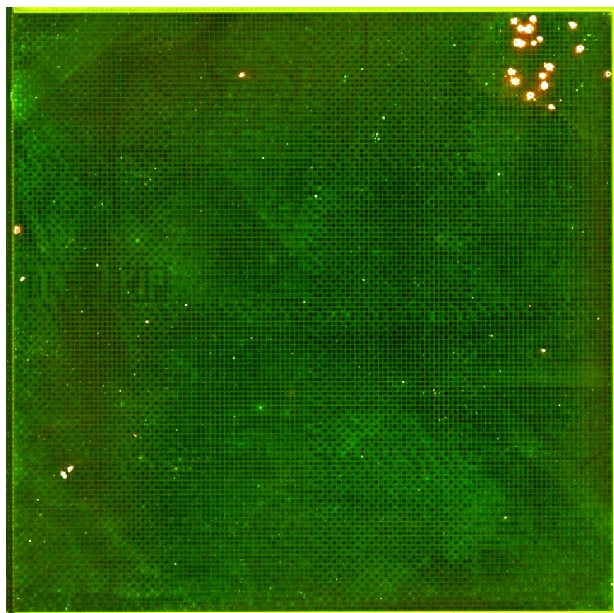


Figure 5.29: Fluorescence stained CMOS Chip with AEG₃ surface coating. The result is unacceptable due to indistinguishable intensities.

than on polymer surfaces. Yet, the accessibility of the peptides for the antibodies should be better (see [55]).

However, during the final side chain deprotection step with trifluoroacetic acid, the aluminum pixel surface seemed to be slightly unstable and showed some corrosive coloring.

Two chips have been prepared in parallel, but only one chip rendered a measurable fluorescence staining (shown in Figure 5.29). In this case, the chip had to be scanned with almost maximum sensitivity (green PMT 730, red PMT 900). The DKFZ and KIP letters can be recognized in fluorescence staining, yet, the staining result is still poor and, thus, it was refrained from analyzing the results for specific antibody binding.

These results are in line with similar approaches using laser printed arrays on AEG₃ coated glass substrates: The quality of the AEG₃ surface varies and research was still in progress at the time of the experiments. In the case of the CMOS chip, this surface seems to be (yet) unstable and unfeasible, also, because the SAM layer (in comparison to a polymer layer) seems to offer less protection to the topmost metal layer of the chip surface from the harsh chemical washing steps (e.g. trifluoroacetic acid).

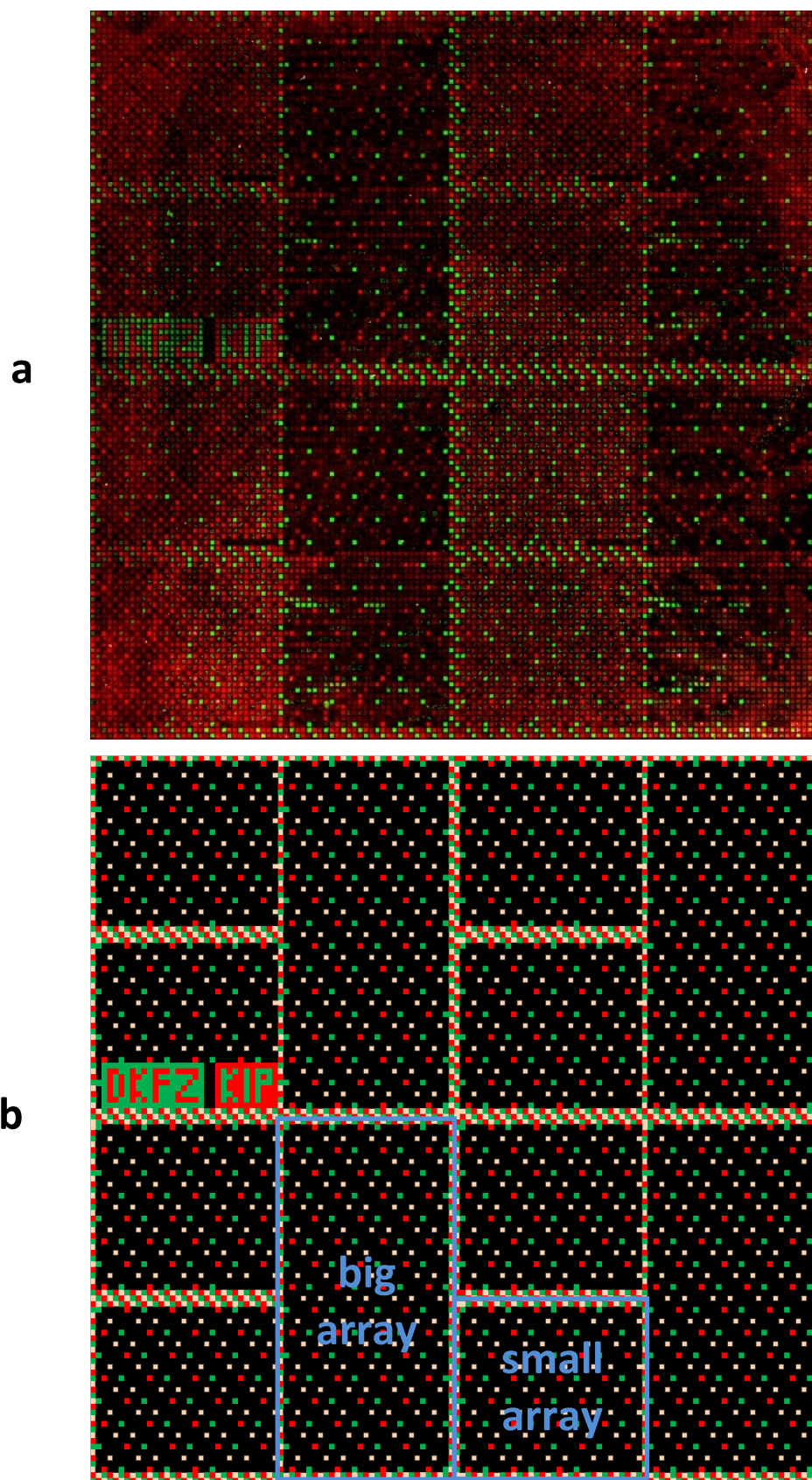


Figure 5.30: The fluorescence stained CMOS chip with PEGMA/MMA surface coating (a) and the chip layout for comparison (b). For the design of the layout, see chapter 4.

5.3.2 Synthesis on PEGMA/MMA coated CMOS chips

Similar to the previous subsection, the peptide synthesis was performed on PEGMA/MMA. The successful synthesis was stained and afterwards scanned. The results are shown in Figure 5.30.

Although several inhomogenously stained areas are visible, the overall result is acceptable, because distinct spot intensities are visible, comparable, and automatically evaluable. The quality issues, especially at the edges of the array, and drawbacks will be discussed at the end of this section.

In this context, it was possible to analyze the results in detail, especially one of the four arrays with 1536 different variants of the Flag-epitope and the HA-epitope. Figure 5.30b illustrates the two highlighted segments of the chip (blue rectangles), which were thoroughly analyzed, because these arrays (small, big) seemed to offer the best staining results with the lowest intensity variations in the control spots.

5.3.2.1 Analysis of the HA-epitope

In this section, the staining of the bigger and smaller array will be analyzed, regarding the results of the 532 nm channel of the fluorescence scan, which correlates with the monoclonal anti-HA antibody staining. Both arrays are framed by an alternation of HA-, Flag-, and the control peptide (N-Asp-Ala-Asp-Asp-Pro-Asp-Asp-Ala-C).

Figure 5.31 shows the big array with 31 x 63 (= 1,953) spots featuring 1,536 different HA- and Flag-epitope variants. The importance of substituted amino acids in specific antibody binding was investigated, using an automated intensity evaluation program: the GenePix Pro software (Molecular Devices, USA), included in the scanner software. The software measures the mean fluorescence intensity and the standard deviation of a circular spot (diameter of about 50 μm), based on a similar approach as the already mentioned image segmentation method (see subsection 5.2.4). Each one channel gray scale picture of a peptide spot was attributed with a mean intensity value of the measured spot. The spot intensity was divided by the maximum intensity to gain a relative value.

In Figure 5.31, several control spots are visible in a regular diagonal pattern, in accordance to the layout. Only 7 HA-epitope variants, highlighted with red rectangles, were intensively stained with a relative intensity > 99.6 % and a relative error < 1.9 % by the monoclonal antibody, indicating high affinity binding. Table 5.6 lists these top 7 binders according to Figure 5.31 (#1 is the wild type or standard HA-epitope, amino acid substitutions are highlighted in red). All other spots of the array were either wild type HA-epitope spots, or featured a relative fluorescence intensity of less than 30 %.

Table 5.6: The top 7 HA-epitope variants featuring a similar binding efficiency towards the monoclonal mouse-Anti-HA antibody (numbering according to Figure 5.31). #1 is the standard or wild type (wt) HA-epitope.

# in Figure	sequence	# in Figure	sequence
1 (wt HA)	YPYDVPDYA	5	YPYDD DPD WA
2	Y D YDVPDYA	6	Y D YD DPD WA
3	YP A DVPDYA	7	YP A DD DPD WA
4	Y D A D VPDYA	8	Y D A DD DPDWA

The mean intensity for all standard HA spots was 88.5 % with a standard deviation of 15.9 %. However, the measured minimum value was 1.2 %; the maximum value was 100 %. This big variation is a result of the inhomogenous staining, especially in the upper left corner. Due to this intensity variation, all spots with a significantly lower intensity (< 30 %) were neglected.

Interestingly, only peptide spots with two concurrent substitutions in the 5th position (Val -> Asp) and in the 8th position (Tyr -> Trp) seem to offer a binding efficiency similar to the wild type (i.e. standard) HA-epitope. Peptide spots with only one of these substitutions rendered very low signal intensities of about 30 %. This might be due to synthesis/surface errors or due to a relevant amino acid variation.

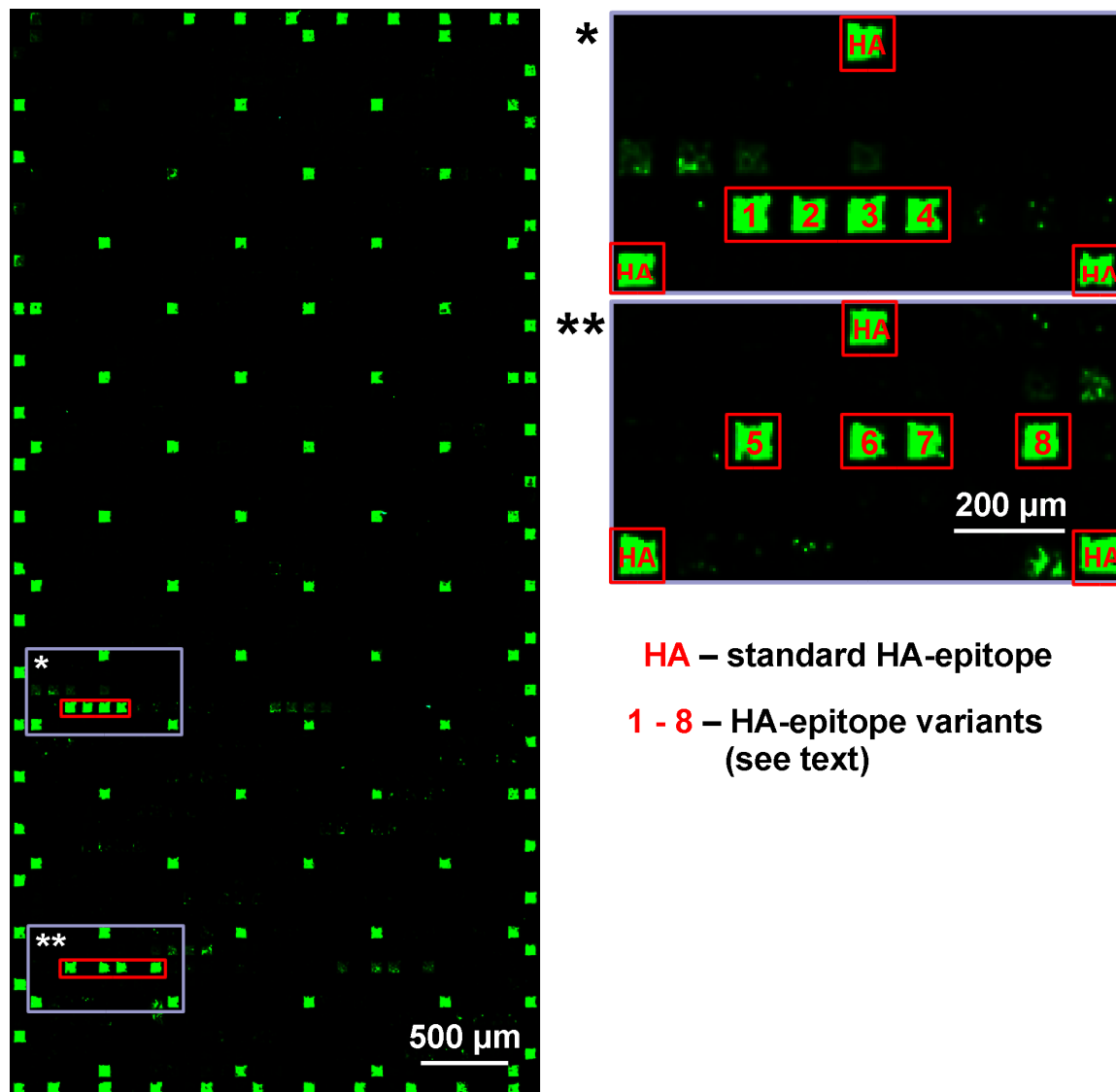


Figure 5.31: Peptide array of 31 x 63 = 1,953 spots with 1,536 different HA- and Flag-epitope variants. The array was incubated with monoclonal mouse-Anti-HA IgG antibodies and stained with the secondary IgG antibodies goat-Anti-mouse conjugated with Alexa Fluor 546. The array is framed by an alternation of HA-, Flag-, and another control peptide. Good binders (relative fluorescence intensity > 99 %) of the monoclonal mouse-Anti-HA antibody to altered HA-epitopes are highlighted with red rectangles. Figure (*) and (**) show magnified details of the array: only spots with relative fluorescence intensities of above 99 % are highlighted (HA standard epitope; 1 – 8 HA-epitope variants, see Table 5.7). All other visible spots, besides the standard HA epitope, exhibited relative fluorescence intensities between 10 - 30 %.

In the next step, the staining of the smaller array was analyzed. The smaller array offers 34 x 31 (= 1,054) spots with 400 different Flag- and 400 different HA-epitope variants. Figure 5.32 shows the staining result. The epitopes were only altered in the 3rd and 4th amino acid position, with all possible (20 x 20) amino acid types. The monoclonal anti-HA antibody only binds to peptides with Asp in the 4th position. Thus, the Asp residue in position 4 seems to be an essential binding mediator in this case.

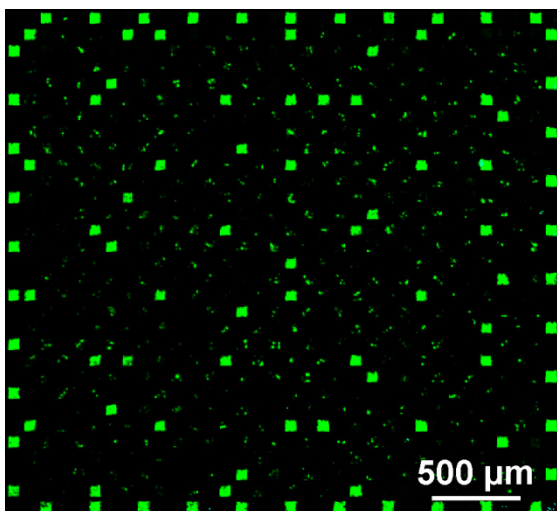


Figure 5.32: Peptide array of $34 \times 31 = 1,054$ spots, offering 400 different Flag- and 400 different HA-epitope variants. The epitopes were only altered in the 3rd and 4th amino acid, with all possible (20 x 20) amino acid types. The monoclonal Anti-HA antibody only binds to peptides with Asp in the 4th position, the 3rd position, however, seems unimportant for binding; any amino acid in position 3 is possible without significant change in affinity.

However, it might be possible that, due to contaminations during combinatorial particle deposition, some binding events are inhibited, because of incorrect peptide synthesis. Especially on this smaller type of array, all twenty amino acids were deposited, causing a higher contamination, in particular when using certain amino acid particle types, where only fractions with a greater mean diameter were available.

The 3rd position, however, seems to be unimportant for binding, the relative fluorescence intensities for all 19 variant spots (+ the wild type HA-epitope) were above 93 %, except for Ile (83.1 %) and Arg (75.6 %). Thus, any amino acid in position 3 seems to be possible without significant change in affinity. All other spots featured relative intensities below 50 %. On this type of array, the relative mean intensity of all wild type HA-epitopes was 97.9 % with a standard deviation of 2.9 % and a minimum intensity of 63.5 %. Thus, the overall staining is more homogenous than in the case of the bigger array.

The staining gave a rather clear result for the human beholder; yet, the automated analysis shows a similar but not so distinct result. This is owed to the higher contamination rate, because all 20 amino acid types were deposited in this type of array. Thus, the background noise (small green marks) can lead to some problems in the automated analysis of spot intensities.

Concluding, with this limited number of peptide variants and, therefore, a rather subjective approach, one can derive a sequence which seems to offer a similar binding efficiency as the wild type (standard) HA-epitope. The three most important amino acids in binding of the monoclonal anti-HA antibody are Asp in position 4 and 7 and Ala in position 9 (for position 9, see [24]). However, peptides containing an acidic residue (Asp) in the positions 5, 6, or 8 showed no measurable binding signal (see Table 5.7). In this instance the possibility of

insufficient synthesis or peptide quality is rather unlikely, since four adjacent Asp residues (positions 5 - 8) were successfully synthesized and stained in the Flag-epitope. On the contrary, a substitution in the 8th position with Trp instead of Tyr, which are two chemically rather similar amino acids (both aromatic), had no significantly decreasing effect on binding efficiency.

The qualitative binding efficiencies of the monoclonal mouse-Anti-HA antibody to amino acid substitutions in the HA-epitope are summarized in Table 5.7.

Table 5.7: Qualitative influence of amino acid substitutions in the wild type HA-epitope on the affinity of the monoclonal mouse-Anti-HA antibody.

amino acid #	1	2	3	4	5	6	7	8	9
HA-epitope	N- Tyr	Pro	Tyr	Asp	Val	Pro	Asp	Tyr	Ala -C
Substitutions resulting in good binding		Asp	Xxx					Trp	
Substitutions resulting in poor or no binding				Xxx	Asp	Asp	Glu/ Asn/ Gln	Asp/ Asn	Lys

5.3.2.2 Analysis of the Flag-epitope

In this section, the binding efficiency of the anti-Flag antibody is evaluated. The arrays were incubated with the polyclonal rabbit-Anti-Flag antibodies and stained with the secondary antibodies anti-rabbit conjugated with Alexa 647. The arrays are framed by an alternation of HA-, Flag-, and the control peptide (N-Asp-Ala-Asp-Asp-Pro-Asp-Asp-Ala-C) which was generally stained slightly red by the anti-Flag antibody.

An automated evaluation was performed with the GenePix software, as already discussed in the previous subsection, regarding the results of the 635 nm fluorescence scan, which correlates with the polyclonal anti-Flag antibody staining.

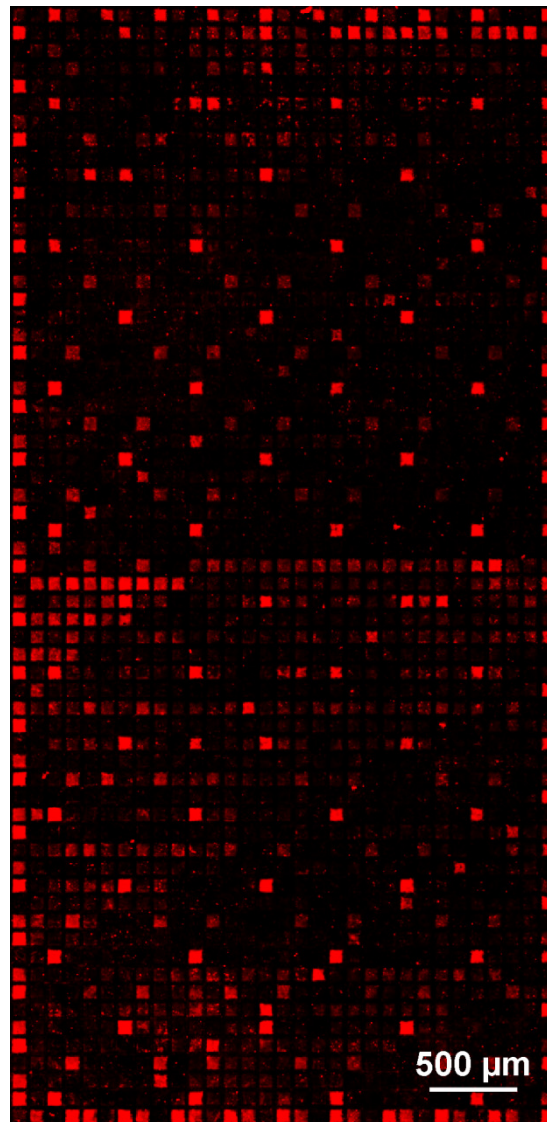


Figure 5.33: Peptide array of $31 \times 63 = 1,953$ spots with 1,536 different HA- and Flag-epitope variants. The array was incubated with polyclonal rabbit-Anti-Flag IgG antibodies and stained with the secondary IgG antibodies goat-Anti-rabbit conjugated with Alexa Fluor 647. The array is framed by an alternation of HA-, Flag-, and another control peptide. The staining shows abundant binders with various distinct binding efficiencies.

First, the bigger array is analyzed: Figure 5.33 shows the array with $31 \times 63 (= 1,953)$ spots featuring 1,536 different HA- and Flag-epitope variants. As expected, and in contrast to the monoclonal HA antibody, the polyclonal Flag serum shows very promiscuous binding towards epitope variants.

In Table 5.8, the results of the automated evaluation are shown, regarding the top 45 binders, amino acid substitutions are highlighted in red. On the one hand, a preference for poly-Asp can be identified: especially four and five (more or less) adjacent Asp residues, resembling the C-terminus of the Flag-epitope. On the other hand, one can observe strong binding of peptides with the amino acid sequence N-Tyr-Asp-Tyr-Lys-Asp-Asp-Xxx-Xxx-Xxx-C (and similar variants thereof), which corresponds to the five N-terminal amino acids of the Flag-epitope.

Table 5.8: The top 45 Flag-epitope variant binders of the bigger array with relative intensities between 40 – 100 %. Lower intensities were neglected, due to the test-epitope intensity variation of 20.3 ± 14.4 %, which reaches about 40 %. Thus, the relevancy of < 40 % is assumed as low.

Sequence	Intensity	Error	Sequence	Intensity	Error
YDYKDD N DK	95.4 %	6.5 %	YD A DDDDDA	67.9 %	12.1 %
YDY E DDDDA	94.7 %	2.9 %	YD A EDDDDA	61.1 %	10.8 %
YDYKDDDD A	94.2 %	4.4 %	YD A KDDDDK	60.1 %	16.8 %
YDYKDD E DA	93.0 %	3.8 %	YDYKDD Q YA	59.0 %	8.2 %
YDY D DDDDA	92.1 %	3.9 %	YDYKDD D WK	58.2 %	17.6 %
YDYKDD D WA	91.9 %	5.6 %	Y PE D EDA	58.1 %	12.2 %
YDYKDD E WA	91.4 %	5.8 %	YDYKDD N DA	57.8 %	14.1 %
Y PE D DDDA	89.6 %	3.8 %	YD A KDDDDA	57.7 %	9.9 %
YDYKDD D YK	88.6 %	5.5 %	YDYKDD N YA	57.1 %	16.8 %
YDYKDD N WA	85.3 %	6.8 %	YD A DD E DA	57.0 %	18.7 %
YDY E DDDDK	81.8 %	7.6 %	YDYKDD E NA	54.6 %	17.7 %
YDYKDD D YA	81.6 %	7.1 %	YDYKDD E WK	51.8 %	14.9 %
YDYKDD E DK	80.8 %	13.6 %	Y P A DDDDDA	51.4 %	12.4 %
Y PKDDDDK	79.7 %	8.1 %	YDY E DD N DA	50.8 %	16.2 %
YDYKDD E YA	78.9 %	11.3 %	Y P A E D DDDA	49.8 %	9.1 %
YD A DDDDDK	78.5 %	12.7 %	YDYKDD N WK	48.1 %	15.8 %
Y PKDDDDA	76.8 %	11.0 %	YDYK V D E YA	46.6 %	42.6 %
YDY E DD E DA	73.2 %	15.0 %	YDYKDD Q DA	46.4 %	20.6 %
YDYKDD Q WA	71.2 %	13.8 %	Y PKDD E DA	43.2 %	14.2 %
Y PYDDDDDA	70.4 %	8.4 %	YD A E D D Q DA	43.2 %	25.2 %
Y PE D DDDK	70.4 %	9.5 %	YDYKDD D NA	42.7 %	14.3 %
YDY D DDDDK	69.8 %	9.3 %	YD A E D D N DA	41.3 %	15.0 %
YD A E D DEDA	67.9 %	15.4 %			

Additionally, some species of the polyclonal antibodies seem to bind weakly (mean intensity: 20.3 %) to the control peptide N-Asp-Ala-Asp-Asp-Pro-Asp-Asp-Ala-C, which is located in the array frame, being a repeated alternation of HA- (bright red), Flag- (bright green, see Figure 5.30), and control epitope (light red).

The relative mean intensity of all wild type Flag-epitopes was 92.8 % with a standard deviation of 5.7 % and a minimum intensity of 66.1 %. In comparison to this, the relative mean intensity of the test-epitope (initially expected as almost zero) was 20.3 % with a

standard deviation of 14.4 %, a maximum of 91.2 % and a minimum of 2.4 %. Thus, considering the rather large 1-sigma region between about 5 – 35 %, all spots with intensities below 40 % were considered as neglectable, because experimental errors become highly relevant.

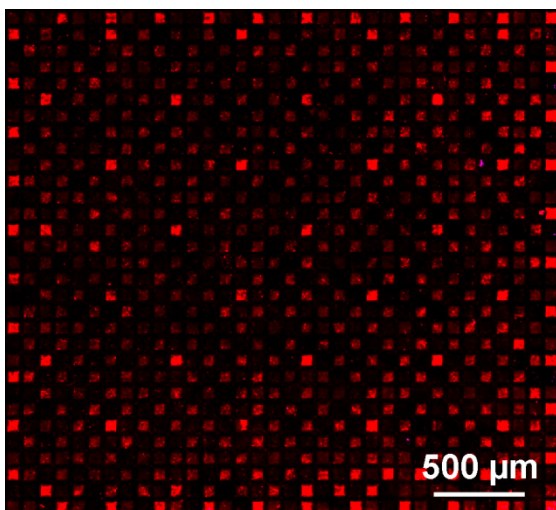


Figure 5.34: Peptide array of 34 x 31 = 1,054 spots, offering 400 different Flag- and 400 different HA-epitope variants. The array was incubated with polyclonal rabbit-Anti-Flag antibodies and stained with the secondary antibodies anti-rabbit conjugated with Alexa 647. observed.

The intensity variation of the Flag-epitope is rather low, the intensity variation of the test-epitope, however, is rather large. This is probably again owed to the surface quality and the inhomogenous staining. Secondly, the smaller array was analyzed in respect to the polyclonal Flag staining. In Figure 5.34, the red channel of the staining of the smaller array is shown, featuring 34 x 31 (= 1,054 spots) with 400 different Flag- and 400 different HA-epitope variants. This experiment was focused on the substitution of position 3 and 4 of both epitopes. Again, a multitude of binders can be

The relative mean intensity of all wild type Flag-epitopes was 89.7 % with a standard deviation of 9.7 % and a minimum intensity of 50.3 %. A tendency for a better binding seems to be a Tyr in the 3rd or 4th position. However, because the polyclonal anti-Flag antibodies tend to bind to four adjacent Asp residues, a specific binding pattern in this type of array cannot be derived, because all peptides include at least the four adjacent Asp residues. In Table 5.9, only the top 22 binding partners are listed with relative intensities between 60 and 100 %. Due to the rather high standard deviation of the mean intensity of the Flag-epitope and its low minimum intensity, spots with intensities below 60 % were neglected.

Table 5.9: The top 22 Flag-epitope variant binders of the smaller array with relative intensities between 60 – 100 %. A specific binding pattern in this type of array cannot be derived. Thus, and due to the high standard deviation of the mean intensity of the Flag-epitope, all spots below 60 % intensity were neglected.

Sequence	Intensity	Error	Sequence	Intensity	Error
-DYI ^I DDDDK	97.6 %	1.7 %	-DY ^Y DDDDK	74.4 %	23.3 %
-DY ^M DDDDK	96.3 %	6.1 %	-DF ^F DDDDK	73.3 %	21.5 %
-DY ^Y DDDDK	95.9 %	5.2 %	-DE ^E DDDDK	72.7 %	19.9 %
-DQ ^Y DDDDK	94.1 %	12.2 %	-DL ^L DDDDK	69.9 %	18.8 %
-DY ^H DDDDK	88.9 %	13.5 %	-DW ^W DDDDK	69.8 %	24.7 %
-DS ^Y DDDDK	88.8 %	10.8 %	-DY ^V DDDDK	69.6 %	26.2 %
-DY ^L DDDDK	85.2 %	21.8 %	-DF ^E DDDDK	64.1 %	19.2 %
-DY ^E DDDDK	79.2 %	20.5 %	-DW ^E DDDDK	63.3 %	19.8 %
-DG ^N DDDDK	78.7 %	20.5 %	-DY ^G DDDDK	62.8 %	19.8 %
-DM ^I DDDDK	78.4 %	18.4 %	-DV ^S DDDDK	61.6 %	23.7 %
-DY ^N DDDDK	78.4 %	17.3 %	-DQ ^D DDDDK	60.5 %	18.9 %

Additionally, it is noted that these arrays were subsequently incubated with a monoclonal anti-Flag serum and afterwards stained with a secondary antibody system conjugated with Alexa Fluor 546 (results not shown). Here, only a qualitative binding study was performed, because the staining result was rather poor and the previous staining of the monoclonal anti-HA antibody had to be subtracted from the fluorescence pattern. Yet, this monoclonal antibody almost exclusively bound to variants of Flag with the sequence N-Tyr-Asp-Tyr-Lys-Asp-Xxx-Xxx-Xxx-Xxx-C, which corresponds to the four N-terminal amino acids of the Flag-epitope. Variations in the 3rd and 4th position completely prohibited the binding.

5.3.2.3 Intensity variations of fluorescence staining

Concluding from the staining results, some peptide spots exhibit background noise in fluorescence imaging and also a slight intensity fluctuation over the array surface can be

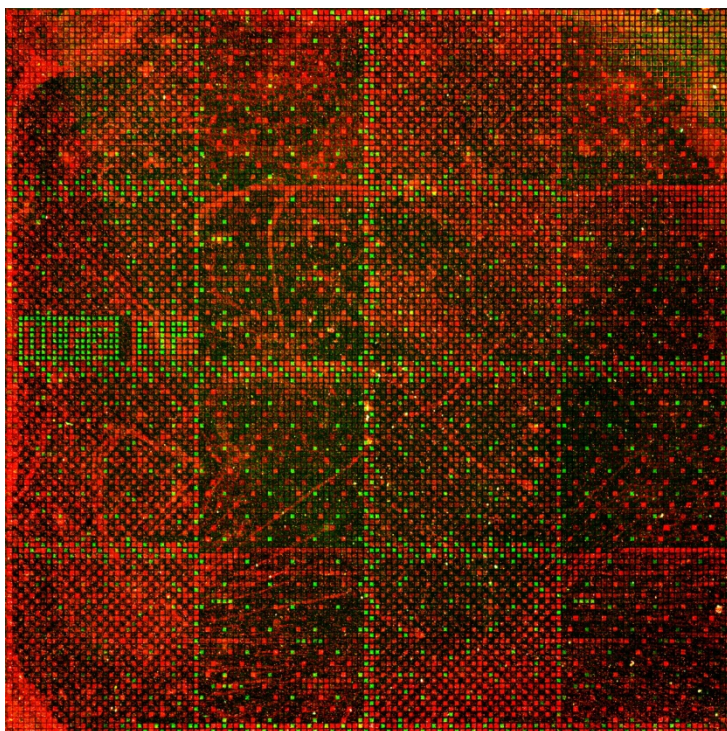


Figure 5.35: Another fluorescence stained CMOS chip with PEGMA/MMA surface coating. The staining shows many inhomogeneities with high background noise, which is probably caused by an inhomogenous surface coating.

observed. This may be owed to the sometimes insufficient particle pattern quality, the inhomogenous surface coating and the staining process which so far has to be done manually with all typical shortcomings in preparing micro techniques by hand. Further improvements of the peptide micro chip should therefore mainly comprise the optimization of surface coating and particle quality reproducibility, the latter being the critical factor in high-precision particle deposition.

Another evidence for the surface inhomogeneity is the staining of an in parallel performed peptide synthesis on a similar PEGMA/MMA coated chip surface, which should feature similar results as in subsection 5.3.2. Although the particle deposition in this case was qualitatively better, Figure 5.35 shows that the staining result exhibits many inhomogeneities and high background noise, which made an evaluation impossible.

The deposition quality issues will be further discussed in the following subsection.

5.3.3 Deposition quality on CMOS chips during synthesis

A layer by layer quality analysis of a detail of the pattern of the peptide synthesis, illustrated in the previous section, has been performed by J. Wagner in ([47], pp. 98-106). The analysis pinpointed to certain layers, which had a higher amount of only medium (satisfactory) or

bad pixel coverage. Especially in deposition layer 6 (Figure 5.36b), the deposition pattern was assumed to be problematic (note: the deposition layer number is counted from the C-terminus and corresponds to the reverse counting of the amino acid number, which starts at the N-terminus). This is on the one hand caused by the high amount of deposition steps (all 20 amino acids needed to be deposited in this layer) and also by insufficient particle quality (particle fractions with a greater mean diameter and, thus, a bad deposition behavior). On the other hand, technical errors e.g. malfunction during chip programming (Figure 5.36c) or human error might have led to some poorer deposition results, due to the still semi-automated aerosol deposition.

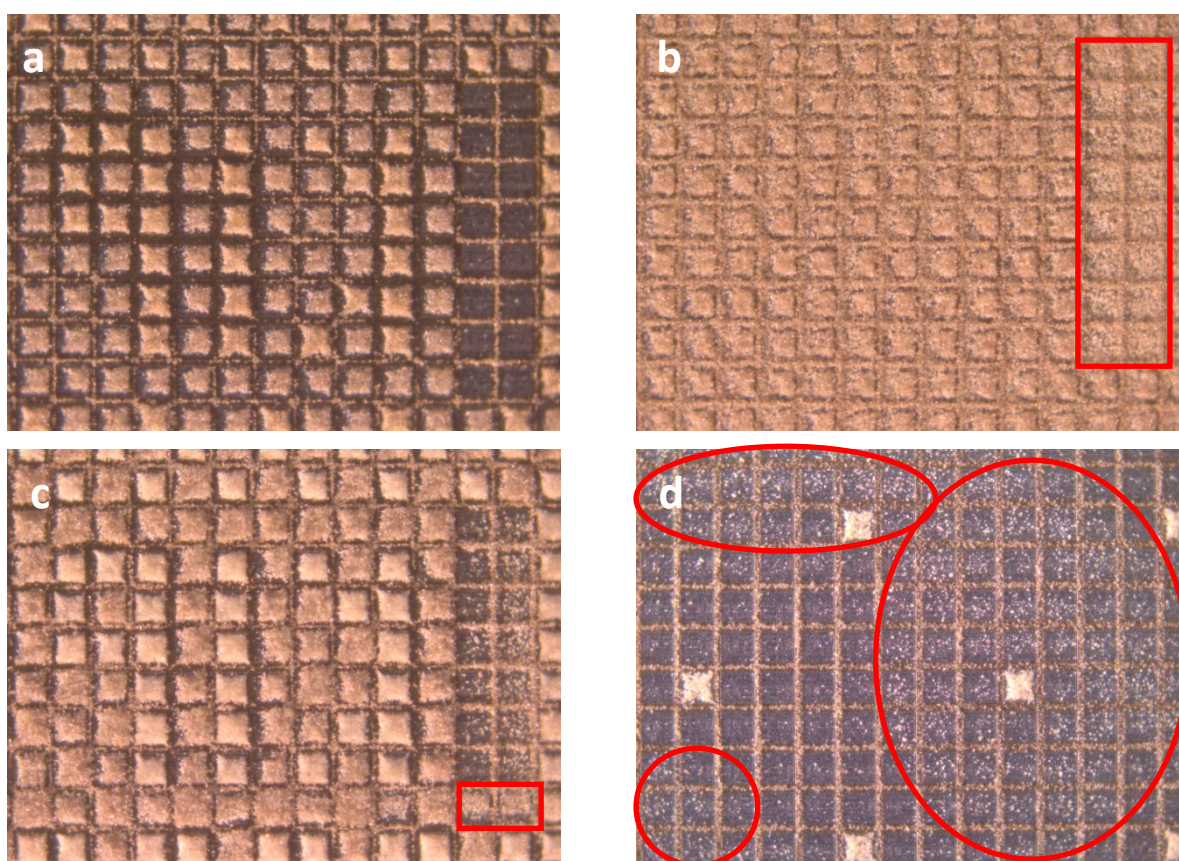


Figure 5.36: Different aspects and effects observed during the CMOS chip peptide synthesis. In deposition layer 5 (a) with Asp and Val particles deposited, the pattern quality is very good and almost no contamination is visible. In layer 6 (b), the deposition quality is poor, because all twenty amino acids (including some particle types with insufficient particle diameter) were deposited onto the chip surface. An acceptable deposition quality in (c) features a malfunction during chip programming, two pixels were falsely covered. Another notable effect is shown in (d): The shielding of electric fields emanating from the grid electrode causes contaminations (also see text).

Another artifact (Figure 5.36d), which was also investigated in [27], seemed to point to a shielding of the electric fields of the chips by the PEGMA/MMA coating. However, chip surface analysis with a time of flight secondary ion mass spectrometry (TOF-SIMS) in [47]

indicated the incidence of high amounts of potassium in the silicon nitrite layer, which covers the grid electrode. The potassium ions together with water might cause conductivity, shielding the electric fields emanating from the grid electrode. This shielding effect also appears on uncoated chips at high relative humidity of above 50 %, thorough washing steps with dimethylformamide and methanol eliminate the water and restore the desired insulating surface properties.

Yet, the staining results were still acceptable, despite the possible error sources shown in Figure 5.36. The probably most important factor, which was also assumed in [47], is the inhomogeneity of the polymer surface, causing variations in amino acid coupling. This seems to be the main cause for the observed intensity variations in the fluorescence pattern of the chip.

5.4 Epitope mapping using laser printed arrays

The human adaptive immune system reacts to a specific pathogen by evolving antibodies directed against it. Meanwhile, it is well known that immunodominant epitopes are prevalent in many pathogens. Those cause the adaptive immune system of different individuals to react in similar ways, evolving antibodies, which are directed against the same immunodominant epitope (e.g. in viruses: [62], [63]). The question arises, whether it is possible to find immunodominant regions of a specific pathogen with our peptide-based approach. Therefore, a proof-of-principle peptide microarray experiment was devised, in order to assess this question.

A very common pathogen is *Clostridium tetani*, which elicits the tetanus disease. This pathogen produces a toxic protein, which is called tetanus toxin or tetanospasmin. In infected patients, this toxin blocks inhibitory neuron action, which leads to chronic muscle contraction and untreated eventually to death ([6]). Fortunately, in respect to this disease, a very common vaccination is available. It is a standard procedure and almost every person in western countries has had such a vaccination at least once in his/her life. Thus, tetanus seems to be an appropriate proof-of-principle target.

5.4.1 Tetanus toxin/toxoid mapping

The tetanus toxin is composed of two domains, a heavy and a light chain. The heavy chain is required for the cell binding and subsequent internalization into the cell, but only the light chain causes the intracellular toxic effect in neurons. Fortunately, it was possible to design a potent vaccine: The toxic light chain is denatured, whereas the heavy chain stays intact. The conformation (three-dimensional folding) of the light chain is changed to an inactive form, but the amino acid sequence remains unmodified. This partly denatured protein is called tetanus toxoid and has no neurotoxic effect, but it is a very potent vaccine. If injected, the body can create antibodies directed against this protein, without suffering from the toxic effect. Eventually, this makes the human organism “immune” to the (active) tetanus toxin.

In our case, the task of finding a dominant immunogenic region was approached with the mapping of the tetanus toxin on a peptide microarray. The amino acid sequence of the tetanus toxin (1315 amino acids + 18 amino acids in total from initial and final linker) is

shown in Table 5.10 and was taken from [64]. This sequence was divided in 2638 coherent duplicate 15mer spots (40 x 66 – 2), with an overlap of 14 amino acids in the following spot. The array is framed by an alternation of the already mentioned Flag and HA epitopes. The arrays were designed, produced, and finalized by Pepperprint GmbH ([25]).

Table 5.10: Amino acid sequence of the tetanus toxin/toxoid (1315 amino acids) amended with an initial and final linker of nine amino acids each (GSGSGSGSG). The light chain is located between the amino acids 2 – 457, the heavy chain begins at the amino acid number 458. Note: the initial and the final linker were omitted.

```
GSGSGSGSG
MPITINNFYSDPVNNDTIIMMEPPYCKGLDIYYKAFKITDRIWIVPERYEFGTKEPEDFN      60
PPSSLIEGASEYYDPNYLRTDSDKDRFLQTMVKLFNRIKNNVAGEALLDKIINAI P YLGN      120
SYSLLDKFDTNSNSVSFNLLLEQDPSGATTKSAMLTNLIIFGPGPVLNKNEVRGIVLRVDN      180
KNYFPCRDGFGSIMQMAFCPEYVPTFDNVIENITSLTIGKSKYFQDPALLLMHELIVLH      240
GLYGMQVSSHEIIPSKQEIYMQHTYPI SAEELFTFGGQDANLISIDIKNDLYEKTLDNDYK      300
AIANKLSQVTSCNDPNIDIDSYKQIYQKQYQFDKDSNGQYIVNEDKFQILYNSIMYGFTE      360
IELGKKFNIKTRLSYFSMNHDPVKIPNLLDDTIYNDTEGFNIESKDLKSEYKQNMVRNT      420
NAFRNVDGSGLVSKLIGLCKKIIPPTNIRENLYNRTASLTDLGGELCIKIKNEDLTFIAE      480
KNSFSEEPFQDEIVSYNTKNKPLNFNYSLDKIIDVYNLQSKITLPNDRTPVTKGIPYAP      540
EYKSNAASTIEIHNIDDNTIYQYLYAQKSP TTLQRITMTNSVDDALINSTKIYSYFPSVI      600
SKVNQGAQGILFLQWVRDIIDDFTNES SQKTTIDKISDVSTIVPYIGPALNIVKQGYEGN      660
FIGALETTGVVLLLEIPEITLPVIAALSIAESSTQKEKIIKTIDNFLEKRYEKWIEVYK      720
LVKAKWLGTVNTQFQKRSYQMYRSLEYQVDAIKKIIDYEYKIYSGPDKEQIAD EINN LKN      780
KLEEKANKAMININIFMRESSRSFLVNQMINEAKKQLLEFDTQSKNILMQYIKANSKFIG      840
ITELKKLESKINKVFSTPIPFSSYKNLDCWVDNEEDIDVILKKSTILNLDINNDIISDIS      900
GFNSSVITYPDAQLVPGINGKAIHLVN NESSEVIVHKAMDIEYNDMFNNFTVSFWLRVPK      960
VSASHLEQYGTNEYSIISSMKKHSLSIGSGWSVSLKGNLIWTLKDSAGEVRQITFRDLP      1020
DKFNAYLAN KWVFITITNDRLSSANLYINGVLMGSAEITGLGA IREDNNITLKLDR C N N N      1080
NQYVSIDKFRIFCKALNPKEIEKLYTSYLSITFLRDFWGNPLRYDTEYYLIPVASSSKDV      1140
QLKNITDYMYLTNAPS YTNGLNIIYRRLYNGLKFI IKRYTPNNEIDSFVKSGDFIKLYV      1200
SYNNNEHIVGYPKDGNAFNNDRLILRVGYNAPGIPLYKKMEAVKLRDLKTYSVQLKLYDD      1260
KNASLGLVGTHNGQIGNDPNRDILIASNWYFNHLKDKILGCDWYFVPTDEGWTND      1315
GSGSGSGSG
```

To gain a first insight into this problem, three sera were acquired from individuals with a tetanus vaccination within the last 2 years, but at least 8 weeks ago to assure that the immune system has had enough time for a response. In addition, one serum (see Figure 5.37a) was positively tested (from [65]) for a sufficient titer of anti-tetanus antibodies, which indicates a sufficient immunity.

Although an approach with 3 sera is rather subjective, a first screen might pinpoint to those candidate peptides, which are often targeted by the immune system. Furthermore, this may lead to simplified and smaller arrays with selected candidates, making more screens with frugal consumption of serum possible.

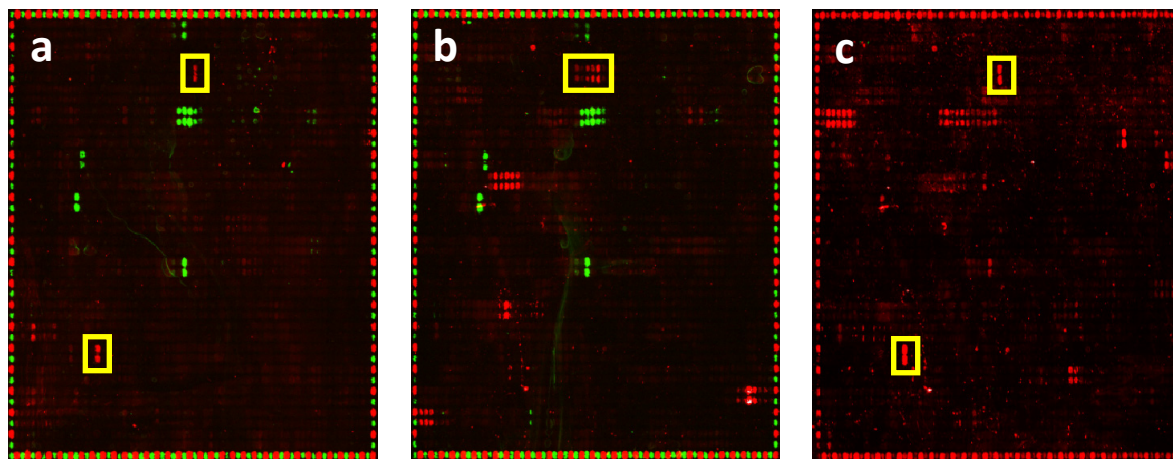


Figure 5.37: Peptide arrays featuring an epitope mapping of the tetanus toxin (1315 amino acids + 18 amino acids poly-GS), offering 1319 spot duplicates of 15meric peptides. Two arrays with identical peptide composition were stained with two sera from individuals immunized with tetanus toxoid (a, b). The array shown in (b) was then stripped from all antibodies in a stripping buffer and afterwards incubated (and detected) with a third serum from an immunized individual (c). The array frame (a, b) was stained with anti-Flag (in green) and anti-HA (only red frame) antibodies. Array (c) only shows the red anti-HA staining.

Figure 5.37 shows the staining of the arrays with three different sera. Note that the peptide spots are in the shape of a rectangle, in contrast to the CMOS chip spots, which are quadratic. The staining results feature low background noise and a homogenous control spot staining. The assay was performed as follows: First, the array was incubated with the secondary goat-anti-human antibodies, to distinguish the binding events from binding of the secondary antibodies (data not shown). The results showed no evidence for a significant binding of the secondary antibodies to any peptide spots. In a subsequent step, the array was incubated with the serum and afterwards detected with the secondary antibodies. Finally, the anti-Flag (in green) and the anti-HA staining (also in red) was performed. The anti-Flag antibodies, which are known to be rather promiscuous binders, seem to bind to some peptides within the array, but are, due to their green color, easy to distinguish. In the case of the red anti-HA staining, only the HA epitope spots in the array frame were stained and, thus, the red staining results on the array do only originate from the serum interaction (data not shown).

Arrays (a) and (b) were stained with anti-Flag (in green) and anti-HA (only red frame) antibodies. Array (c) is in fact array (b), which was stripped from all antibodies (30 min in stripping buffer: 1 % SDS, 200 mM glycine, pH 2) and afterwards incubated (and detected) with a serum from another patient. In this case, the HA binding is so persistent, that the washing could not remove these antibodies, which is why the red frame is still visible in array (c). However, with a previous secondary anti-human staining, it was tested that all serum antibodies were efficiently washed away by the stripping buffer (data not shown).

Comparing the results from the three stainings, peptide spots with coinciding amino acid sequences could be found, which are highlighted with yellow boxes in Figure 5.37. In particular, all three arrays exhibit a staining of the sequence LIIFGPGPVLNKNEV (upper yellow box). This sequence is part of the light chain and is located between the 156th and 171st amino acid in the tetanus toxin sequence. A second coinciding spot, which is only found on the arrays (a) and (c), is GNNLIWTLKDSAGEV. It is located on the heavy chain (996-1011).

A remarkable result is that the coinciding spots on arrays (a) and (c) seem to exhibit no stained neighboring spots. Regarding these two sera, this might indicate that all 15 amino acids in the sequence are required for an efficient binding of the epitope, or that a steric hinderance of the surface coating inhibits the binding of antibodies to similar sequences. Further experiments with longer peptides (e.g. 17meric) might elucidate this phenomenon. Interestingly, the amino acid sequence of peptides stained on all three arrays, only features stained neighboring spots on array (b), which pinpoints to a shorter epitope of the corresponding antibody.

Concluding from these results, a dominating antibody species in the case of tetanus vaccination might be the amino acid sequence LIIFGPGPVLNKNEV. However, due to the limited approach of only 3 sera, further experiments with additional sera need to be performed, to confirm this result. In this case, several smaller arrays with only a few sequences, selected from these results, might give a faster and cheaper possibility to assess this problem with more patient sera.

6 Conclusion and outlook

In the scope of this thesis, two related techniques, enabling full combinatorial bioparticle deposition for the synthesis of peptide microarrays, were investigated: the laser printer and the CMOS chip.

Regarding the laser printing process, which is meanwhile commercialized in the Pepperprint GmbH ([25]), the problem of homogenous particle deposition on glass slides was analyzed. In this context, the gaps in the printing pattern (gap phenomenon) were experimentally observed, which could be theoretically explained by a series of numerical simulations. Emerging from those, the occurrence of electric air breakdown could explain and confirm the experimental results. In a subsequent analysis of surface conductivity of different glass substrates, using a specially devised measurement technique (particle charge electrometer), the optimal glass material could be determined. It turned out that the higher the surface conductivity of a glass substrate, the better was the printing result. In this context, the amount of iron oxide in the glass material pointed out to be the critical parameter, being on the one hand responsible for the higher surface conductivity and, on the other hand, being responsible for the higher autofluorescence. Finally, an optimal glass substrate could be found, which offers the best results in homogenous printing together with a low autofluorescence in infrared fluorescence scanning. This result is now in routine application of the laser printing process.

Applying the laser printed peptide arrays to the biological question, whether the adaptive immune system of different individuals reacts in similar ways regarding a certain pathogen, it was possible to pinpoint a peptide candidate. Using a mapping of the tetanus toxin, a small set of three different sera was analyzed. A qualitative comparison of these staining results indicates that a certain region in the light chain of the tetanus toxoid (i.e. the tetanus vaccine, nontoxic, inactivated tetanus toxin) seems to be a frequent target for an immune response. However, due to the limited statistical relevance, further experiments have to be performed, in order to validate these results. Yet, selected peptide candidates of these first results may already be applied to generate smaller and more cost-effective arrays to screen additional sera.

In a second project, the CMOS chip technique was investigated. In this case, the state-of-the-art technology was lacking behind the laser printer, due to the yet high background contamination, making a full combinatorial approach practically impossible. However, the chip technology offers certain advantages over the laser printer, due to the much higher spot density, the intrinsic alignment, and the comfortable pattern generation.

In order to overcome the problems of contamination, a thorough analysis of particle dynamics was performed. Similar to the laser printing, a series of numerical simulations were performed to elucidate these dynamics in detail. First, an analytical model was defined which is based on the drag force and the electrical force acting on the particles in the aerosol. The particle dynamics and flow in the presence of these fields was then investigated in simulations implemented in COMSOL, which numerically evaluates the equations of motion and calculates the particle trajectories by means of a finite element method.

Conducting simulations, the influence of particle diameter, the q/m value, the long-range fields, and the field superposition on the selective particle deposition process was studied. The importance of the grid electrode as an adsorber for excess particles and thus preventing contaminations could be theoretically affirmed.

Concluding from the simulations, aerosols feature a wide charge distribution, especially particles with a high charge and a larger diameter will lead to contaminations. The results obtained also led to experimental optimization in particle production. Using particles with a small mean ($2 - 3 \mu\text{m}$) and maximum diameter ($< 7 \mu\text{m}$) reproducibly yields deposition patterns with very high precision. This can be explained by the lower inertia of small-sized particles which are therefore easier to manipulate by electrical fields.

Additionally, long-range fields of particle clouds significantly influence the deposition. A constant long-range electrical field can be generated by applying high voltage to a metallic sieve located parallel to the chip surface. The sieve allows for the selection of particles smaller than the mesh size and, furthermore, the selection of particles with equal charge signs. This reduces contaminations by restraining positively charged particles and particle agglomerations from entering the deposition region. Thus, the sieve provides an important tool in particle manipulation.

The experimentally observed pincushion-effect could be simulated, which restricts particle deposition to certain areas of a pixel in dependence of the surrounding voltage pattern applied to the chip. The simplest way to guarantee isotropic central pixel coverage is to divide a deposition pattern into two complementary checkerboard patterns, applied in consecutive deposition steps.

The simulated deposition patterns exhibit strong compliance with the experiments. Investigating this, one should keep in mind that the results of the simulations also have their limits concerning the lowest bound of the particle diameter, as for particles smaller than 1 μm , molecular effects like Brownian motion become relevant. The latter then cause deviations from the equations of motion as currently simulated so that nano particles cannot be modeled using the COMSOL implementation presented here.

Applying the results from the simulations, which favor the application of fine particle fractions, several drawbacks of the former aerosol chambers made it necessary to devise a new aerosol generation system, especially when using fine particle fractions. Hence, a compact system was built in cooperation with R.O.T GmbH, consisting of 20 different particle containers, mounted on a vibrating plate. The principle is based on an air ejector, which was especially designed to allow for very small amounts of aerosol to be ejected. This system allows for a reproducible generation of the different aerosols with frugal consumption of particles.

In addition, a deposition geometry was devised, to achieve the best possible results in deposition. The geometry was designed to decelerate the aerosol particles and to offer a homogenous particle distribution in the aerosol.

Yet, the aerosol generation system has still a drawback, which needs to be improved in the future: Because small particles are difficult to handle due to their high adhesion forces, they tend to clog the metal sieve in the deposition geometry. Thus, the sieve has to be cleaned manually with an air stream after several repetitive aerosol generation steps, but this also highly depends on the particle quality. Regarding a good quality and good flow characteristics, particles need to be dry, i.e. the solvents during particle production need to be thoroughly removed from the matrix. Particles with minor solvent residues cause rapid clogging of the sieve. (The amount of remaining solvent can be measured by weighing the particle components before adding the solvent and after distillation of the final particle

matrix.) The clogging of the sieve might be circumvented with an automated cleaning step, using the dosage air inlet. However, before implementation of such a step, all particle types should offer the same quality and this requires a thorough analysis of particle production techniques, which will be performed in future work. Additionally, the particle reservoirs in the aerosol generator were designed to connect an extra air inlet, which allows for the introduction of a controlled atmosphere with e.g. dry air or nitrogen. This might further improve particle flow characteristics, but could not be implemented so far due to the lack of laboratory space.

Applying this new aerosol generator, an automated analysis of the pattern quality could confirm that a twenty times repeated deposition with very low contamination (about 5 %) on the same chip is in fact possible. Again, it is important to use the best possible (dry) particles with a small mean and maximum diameter, to acquire the lowest amounts of contamination.

Exploiting the now available high-precision deposition of amino acid particles, a fully combinatorial peptide array was successfully facilitated on a microelectronic chip, showing the feasibility of the approach. The presented method offers an (until today) unprecedented spot density for *in situ* combinatorial peptide arrays. The fluorescence staining was analyzed with an automated routine and offered an overall sensible result in respect to the monoclonal anti-HA and the polyclonal anti-Flag antibodies. Yet, the results also expose the requirement for a better and more reliable surface coating technique and further automated handling (e.g. automated washing), which will improve the array quality.

Today's CMOS technique is mature and advanced, providing cost-efficient micro chips and, thus, making this process feasible for microarray production. The experimental results showed that the particle patterning with this technique has the potential to become a powerful method for combinatorial chemistry applications. By means of further miniaturization, the spot count and density can be easily increased, which is shown in additional simulations and experiments, offering pixel densities of over 50,000 spots/cm². However, this was not yet feasible in large scale, because a new chip run would be required, which is highly expensive.

Future developments should be also devised in the scope of automation: Robotics, used in particle deposition, chip handling, and "wet" chemical coupling steps will improve the

robustness of the procedure for routine applications. The complete process should be associated by automatic quality control as already described for the particle pattern. Furthermore, a particle recycling system, which recycles particles that were not deposited on the chip surface, is in the planning phase. This might further reduce the costs and make the process even more efficient. Successful tackling of all these process steps will finally allow for an automated routine application of this research tool.

Concluding, this method can be very interesting for future applications. The method is easily extendable to D-amino acids, which makes it applicable in synthetic peptide generation and synthetic drug discovery. Additionally, the technique is not only applicable in the field of peptide synthesis, but also has the potential for a wide application in general combinatorial approaches, e.g. peptidomimetics (compounds mimicking peptides), which might be used in chemical screenings for catalysts or for new organic electronics. Other possible molecules for a combinatorial approach might be (poly)saccharides and DNA/RNA, which could be compatible with a slightly altered chemical approach.

However, the most straightforward approach is the peptide generation. This can enable applications, such as the already shown epitope mapping, which allows finding continuous epitopes in protein-protein interaction. Exploiting this technique producing many thousands of random peptides, it might be also possible to find mimicking or cross-reaction partners.

Another, much more ambitious approach would be to perform population-wide serum screenings with many arrays, to perform immune system profiling, i.e. searching for correlations of staining patterns to certain diseases or disease states. This would require many high-density peptide arrays together with a systems biology approach, in order to draw statistically relevant conclusions. Thus, a population-wide study still requires a massive improvement and cost-reduction of the here presented methods, but might be an emerging field in the future.

Realistic applications in the near future would be to facilitate assays for proteases, kinases, and other enzymatic reactions. Additionally, a screening for inhibitory peptides can be easily facilitated: Using random peptides, it is possible to detect peptidic inhibitors for a specific protein, which might be directly used for new therapeutics.

The presented improvements of the now feasible highly precise CMOS chip method allow for high-density peptide microarrays, with the possibility of further miniaturization. Such arrays are favorable due to cost issues and frugal consumption of expensive analyte. Furthermore, the possibility for a wide variety of different peptides is favored, because this e.g. increases the success rate of any random peptide approach.

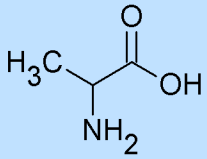

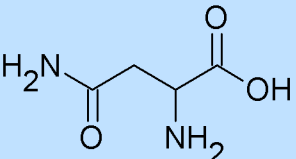
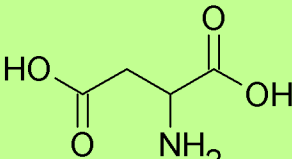
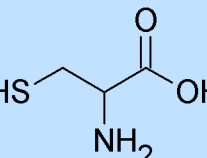
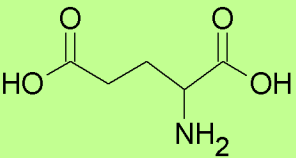

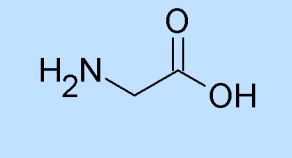
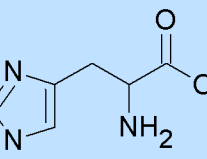

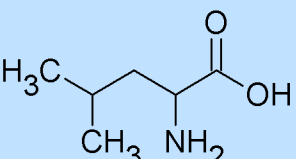
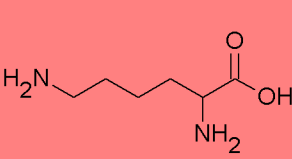
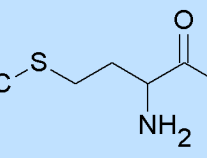
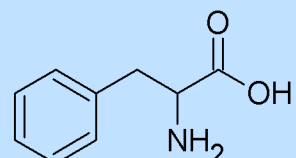
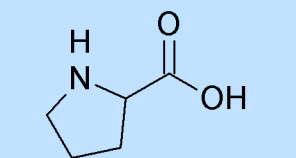
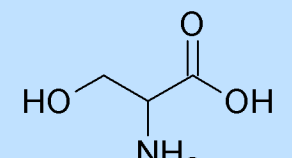

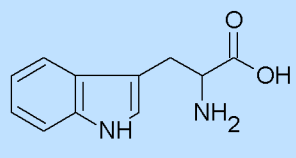
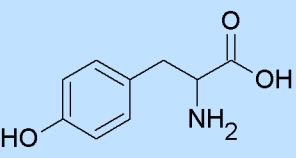

Yet, there are many further experiments for future research required, to give a more decisive statement about protein interactions. Nevertheless, the here presented methodology is in fact an important tool which can deliver the possibility of thorough investigation of protein interactions on a new and unprecedented scientific basis.

Appendix

ABBREVIATIONS AND SIDE CHAIN RESIDUES OF AMINO ACIDS

Amino acid	3-let. abbr.	1-let. abbr.	Side chain residue (R)	Acidic/basic/neutral
Alanine	Ala	A	—CH ₃	Neutral
Arginine	Arg	R	—CH ₂ CH ₂ CH ₂ NH C(NH)NH ₂	Basic (strong)
Asparagine	Asn	N	—CH ₂ CONH ₂	Neutral
Aspartic acid	Asp	D	—CH ₂ COOH	Acidic
Cysteine	Cys	C	—CH ₂ SH	Neutral
Glutamine	Gln	Q	—CH ₂ CH ₂ CONH ₂	Neutral
Glutamic acid	Glu	E	—CH ₂ CH ₂ COOH	Acidic
Glycine	Gly	G	—H	Neutral
Histidine	His	H	—CH ₂ (C ₃ H ₃ N ₂)	Basic (weak)
Isoleucine	Ile	I	—CH(CH ₃)CH ₂ CH ₃	Neutral
Leucine	Leu	L	—CH ₂ CH(CH ₃) ₂	Neutral
Lysine	Lys	K	—CH ₂ CH ₂ CH ₂ CH ₂ NH ₂	Basic
Methionine	Met	M	—CH ₂ CH ₂ SCH ₃	Neutral
Phenylalanine	Phe	F	—CH ₂ (C ₆ H ₅)	Neutral
Proline	Pro	P	—CH ₂ CH ₂ CH ₂ —	Neutral
Serine	Ser	S	—CH ₂ OH	Neutral
Threonine	Thr	T	—CH(OH)CH ₃	Neutral
Tryptophan	Trp	W	—CH ₂ (C ₈ H ₆ N)	Neutral
Tyrosine	Tyr	Y	—CH ₂ (C ₆ H ₄)OH	Neutral
Valine	Val	V	—CH(CH ₃) ₂	Neutral

STRUCTURES OF AMINO ACIDS

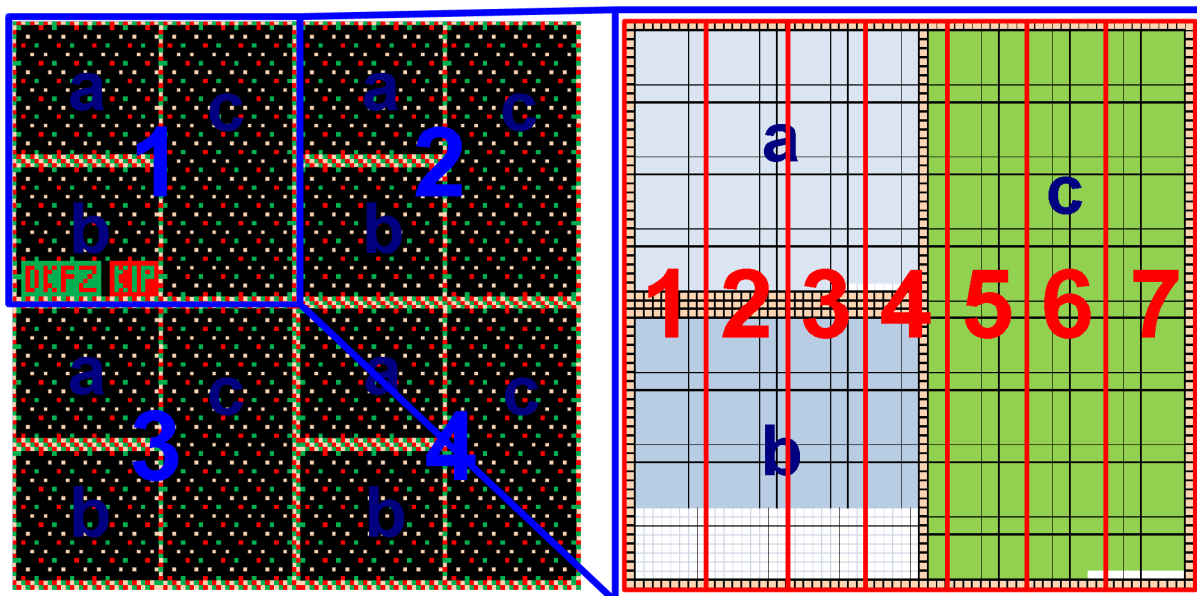
 <p>Ala</p>	 <p>Arg</p>	 <p>Asn</p>	 <p>Asp</p>
 <p>Cys</p>	 <p>Glu</p>	 <p>Gln</p>	 <p>Gly</p>
 <p>His</p>	 <p>Ile</p>	 <p>Leu</p>	 <p>Lys</p>
 <p>Met</p>	 <p>Phe</p>	 <p>Pro</p>	 <p>Ser</p>
 <p>Thr</p>	 <p>Trp</p>	 <p>Tyr</p>	 <p>Val</p>

Neutral amino acids are shown in blue, basic in red, and acidic in green.

PEPTIDE ARRAY LAYOUT

The peptides, which were generated on the CMOS chip, are shown in the following tables. The chip pattern is divided into four repetitive regions (1 - 4, see Supplementary Figure 1 left). Except for the control peptides (HA, Flag, Test) at the borders, which might differ slightly in the arrangement, all 4 regions resemble each other in terms of the amino acid sequences (except for region 1).

One region consists of three arrays (a, b, c): two smaller arrays (a: upper left, b: lower left) and one bigger array (c: right). The two smaller arrays (a, b) possess the same sequences, except for region 1, where the lower left array (b) is cut off by the letters “DKFZ” and “KIP”.



Supplementary Figure 1: The CMOS chip pattern. The pattern is divided into 4 repetitive regions (left). One region consists of two smaller arrays (a: upper left, b: lower left), which possess the same amino acid sequences, except for region 1, where the lower left array is cut off by the letters “DKFZ” and “KIP”.

Each of the following pages displays one of seven tables (table numeration 1 - 7 in Supplementary Figure 1 right), showing the different generated amino acid sequences. The numeration of the areas is shown in Supplementary Figure 1 right (1 – 7).

Area 1

YPYDVPDYA	-DYKDDDDK	-DADDPDDA	YPYDVPDYA	-DYKDDDDK	-DADDPDDA	YPYDVPDYA	-DYKDDDDK	-DADDPDDA
-DADDPDDA	YPYDVPDYA	-DAADDDDK	YPAAVPDYA	-DACDDDDK	YPACVPDYA	-DYKDDDDK	YPADVPDYA	-DADDDDDK
-DYKDDDDK	-DAPDDDDK	YPAVPDYA	-DAQDDDDK	YPAQVPDYA	-DARDDDDK	YPARVPDYA	-DASDDDDK	YPASVPDYA
YPYDVPDYA	YPCKVPDYA	-DCKDDDDK	-DADDPDDA	-DCLDDDDK	YPCLVPDYA	-DCMDDDDK	YPCMVDPYA	-DADDPDDA
-DADDPDDA	-DDADDDDK	YPDAVPDYA	-DDCDDDDK	YPCVDPYA	-DDDDDDDK	YPDDVPDYA	-DDEDDDDK	YPDEVDPYA
-DYKDDDDK	YDTPVPDYA	-DYKDDDDK	YDTPVPDYA	-DDVDDDDK	YPYDVPDYA	-DDVDDDDK	YPDWVPDYA	-DDWDDDDK
YPYDVPDYA	-DEKDDDDK	YPEKVPDYA	-DELDDDDK	YPELVPDYA	-DEMDDDDK	YPEMVDPYA	-DENDDDDK	YPENVDPYA
-DADDPDDA	YFFFVPDYA	-DFFDDDDK	YFVGVPDYA	-DADDPDDA	YFVGVPDYA	-DFHDDDDK	-DADDPDDA	-DFHDDDDK
-DYKDDDDK	-DFTDDDDK	YFVTVPDYA	-DFVDDDDK	YFVVVPDYA	-DFWDDDDK	YFVWVPDYA	-DFYDDDDK	YFFVVPDYA
YPYDVPDYA	YDHFDDDDK	-DGFDDDDK	YDHFDDDDK	-DGHDDDDK	YDHFDDDDK	-DGHDDDDK	YDHFDDDDK	-DGHDDDDK
-DADDPDDA	-DHFDDDDK	YPHFVPDYA	-DHGDDDDK	YPHGVPDYA	-DHHDDDDK	YPHHVPDYA	-DHIDDDDK	YPHIVDPYA
-DYKDDDDK	YPIAVPDYA	-DIADDDDK	-DADDPDDA	-DICDDDDK	YPICVPDYA	-DIDDDDDK	YPIDVPDYA	-DADDPDDA
YPYDVPDYA	-DIPDDDDK	YPIVVPDYA	-DIQDDDDK	YPIQVPDYA	-DIRDDDDK	YPIRVPDYA	-DISDDDDK	YPIVVPDYA
-DADDPDDA	YPKKVPDYA	-DYKDDDDK	YPKKVPDYA	-DKLDDDDK	YPYDVPDYA	-DKLDDDDK	YPKMVDPYA	-DKMDDDDK
-DYKDDDDK	-DLADDDDK	YPLAVPDYA	-DLCDDDDK	YPLCVPDYA	-DLDDDDDK	YPLDVPDYA	-DLEDDDDK	YPLEVPDYA
YPYDVPDYA	YPLTVPDYA	-DLTDDDDK	YPLVVPDYA	-DADDPDDA	YPLVVPDYA	-DLWDDDDK	-DADDPDDA	-DLWDDDDK
-DADDPDDA	-DMKDDDDK	YPMKVPDYA	-DMLDDDDK	YPMLVDPYA	-DMMDDDDK	YPMMVDPYA	-DMNDDDDK	YPMNVDPYA
-DYKDDDDK	YPYDVPDYA	-DNFDDDDK	YPNFVPDYA	-DNGDDDDK	YPNGVPDYA	-DYKDDDDK	YPNHVPDYA	-DNHDDDDK
YPYDVPDYA	-DNTDDDDK	YDNTVPDYA	-DNVDDDDK	YDNTVPDYA	-DNWDDDDK	YDNTVPDYA	-DNYDDDDK	YDNTVPDYA
-DADDPDDA	YPPVPDYA	-DPPDDDDK	-DADDPDDA	-DPQDDDDK	YPPQVPDYA	-DPRDDDDK	YPPRVPDYA	-DADDPDDA
-DYKDDDDK	-DQFDDDDK	YDQFVPDYA	-DQGDDDDK	YDQGVPDYA	-DQHDDDDK	YDQHVPDYA	-DQIDDDDK	YDQIVDPYA
YPYDVPDYA	YDRAVPDYA	-DYKDDDDK	YDRAVPDYA	-DRCDDDDK	YPYDVPDYA	-DRCDDDDK	YDRAVPDYA	-DRDDDDDK
-DADDPDDA	-DRAPDDDK	YDRAVPDYA	-DRQDDDDK	YDRAVPDYA	-DRRDDDDK	YDRAVPDYA	-DRSDDDDK	YDRAVPDYA
-DYKDDDDK	YPSKVPDYA	-DSKDDDDK	YPSLVPDYA	-DADDPDDA	YPSLVPDYA	-DSMDDDDK	-DADDPDDA	-DSMDDDDK
YPYDVPDYA	-DTADDDDK	YDTAVPDYA	-DTCDDDDK	YDTCVPDYA	-DTEDDDDK	YDTEVPDYA	-DTEDDDDK	YDTEVPDYA
-DADDPDDA	YPYDVPDYA	-DTTDDDDK	YDTPVPDYA	-DTEDDDDK	YDTPVPDYA	-DYKDDDDK	YDTPVPDYA	-DTEDDDDK
-DYKDDDDK	-DVKDDDDK	YDVKVPDYA	-DVLDDDDK	YDVLVPDYA	-DVMDDDDK	YDVMVPDYA	-DVNDDDDK	YDVMVPDYA
YPYDVPDYA	YDWFVPDYA	-DWFDDDDK	-DADDPDDA	-DWGDDDDK	YDWFVPDYA	-DWHDDDDK	YDWHVPDYA	-DADDPDDA
-DADDPDDA	-DWTDDDDK	YDWTVPDYA	-DWVDDDDK	YDWTVPDYA	-DWWDDDDK	YDWTVPDYA	-DXYDDDDK	YDWTVPDYA
-DYKDDDDK	YDYPVPDYA	-DYKDDDDK	YDYPVPDYA	-DYQDDDDK	YPYDVPDYA	-DYQDDDDK	YDYPVPDYA	-DYQDDDDK
YPYDVPDYA	-DYKDDDDK	-DADDPDDA	YPYDVPDYA	-DYKDDDDK	-DADDPDDA	YPYDVPDYA	-DYKDDDDK	-DADDPDDA
-DADDPDDA	YPYDVPDYA	-DYKDDDDK	-DADDPDDA	YPYDVPDYA	-DYKDDDDK	-DADDPDDA	YPYDVPDYA	-DYKDDDDK
-DYKDDDDK	-DADDPDDA	YPYDVPDYA	-DYKDDDDK	-DADDPDDA	YPYDVPDYA	-DYKDDDDK	-DADDPDDA	YPYDVPDYA
YPYDVPDYA	YPYDVPDYA	-DAADDDDK	YPAAVPDYA	-DACDDDDK	YPACVPDYA	-DYKDDDDK	YPADVPDYA	-DADDDDDK
-DADDPDDA	-DAPDDDDK	YPAVPDYA	-DAQDDDDK	YPAQVPDYA	-DARDDDDK	YPARVPDYA	-DASDDDDK	YPASVPDYA
-DYKDDDDK	YPCKVPDYA	-DCKDDDDK	-DADDPDDA	-DCLDDDDK	YPCLVPDYA	-DCMDDDDK	YPCMVDPYA	-DADDPDDA
YPYDVPDYA	-DDADDDDK	YPDAVPDYA	-DDCDDDDK	YPCVDPYA	-DDDDDDDK	YPDDVPDYA	-DDEDDDDK	YPDEVDPYA
-DADDPDDA	YDTPVPDYA	-DYKDDDDK	YDTPVPDYA	-DDVDDDDK	YPYDVPDYA	-DDVDDDDK	YPDWVPDYA	-DDWDDDDK
-DYKDDDDK	-DEKDDDDK	YPEKVPDYA	-DELDDDDK	YPELVPDYA	-DEMDDDDK	YPEMVDPYA	-DENDDDDK	YPENVDPYA
YPYDVPDYA	YFFFVPDYA	-DFFDDDDK	YFVGVPDYA	-DADDPDDA	YFVGVPDYA	-DFHDDDDK	-DADDPDDA	-DFHDDDDK
-DADDPDDA	-DFTDDDDK	YFVTVPDYA	-DFVDDDDK	YFVVVPDYA	-DFWDDDDK	YFVWVPDYA	-DFYDDDDK	YFFVVPDYA
-DYKDDDDK	YPYDVPDYA	-DGFDDDDK	YDHFDDDDK	-DGHDDDDK	YDHFDDDDK	-DGHDDDDK	YDHFDDDDK	-DGHDDDDK
-DADDPDDA	YPIAVPDYA	-DIADDDDK	-DADDPDDA	-DICDDDDK	YPICVPDYA	-DIDDDDDK	YPIDVPDYA	-DADDPDDA
-DYKDDDDK	-DIPDDDDK	YPIVVPDYA	-DIQDDDDK	YPIQVPDYA	-DIRDDDDK	YPIRVPDYA	-DISDDDDK	YPIVVPDYA
YPYDVPDYA	YPKKVPDYA	-DYKDDDDK	YPKKVPDYA	-DKLDDDDK	YPYDVPDYA	-DKLDDDDK	YPKMVDPYA	-DKMDDDDK
-DADDPDDA	-DLADDDDK	YPLAVPDYA	-DLCDDDDK	YPLCVPDYA	-DLDDDDDK	YPLDVPDYA	-DLEDDDDK	YPLEVPDYA
-DYKDDDDK	YPLTVPDYA	-DLTDDDDK	YPLVVPDYA	-DADDPDDA	YPLVVPDYA	-DLWDDDDK	-DADDPDDA	-DLWDDDDK
YPYDVPDYA	-DMKDDDDK	YPMKVPDYA	-DMLDDDDK	YPMLVDPYA	-DMMDDDDK	YPMMVDPYA	-DMNDDDDK	YPMNVDPYA
-DADDPDDA	YPYDVPDYA	-DNFDDDDK	YPNFVPDYA	-DNGDDDDK	YPNGVPDYA	-DYKDDDDK	YPNHVPDYA	-DNHDDDDK
-DYKDDDDK	-DNTDDDDK	YDNTVPDYA	-DNVDDDDK	YDNTVPDYA	-DNWDDDDK	YDNTVPDYA	-DNYDDDDK	YDNTVPDYA
YPYDVPDYA	YPPVPDYA	-DPPDDDDK	-DADDPDDA	-DPQDDDDK	YPPQVPDYA	-DPRDDDDK	YPPRVPDYA	-DADDPDDA
-DADDPDDA	-DQFDDDDK	YDQFVPDYA	-DQGDDDDK	YDQGVPDYA	-DQHDDDDK	YDQHVPDYA	-DQIDDDDK	YDQIVDPYA
-DYKDDDDK	YDRAVPDYA	-DYKDDDDK	YDRAVPDYA	-DRCDDDDK	YPYDVPDYA	-DRCDDDDK	YDRAVPDYA	-DRDDDDDK
YPYDVPDYA	YPAAVPDYA	YPYDVPDYA	YPYDVPDYA	YPYDVPDYA	YPYDVPDYA	YPYDVPDYA	YPYDVPDYA	YPYDVPDYA
-DADDPDDA	YPAAVPDYA	YPYDVPDYA	-DYKDDDDK	-DYKDDDDK	YPYDVPDYA	YPYDVPDYA	-DYKDDDDK	YPYDVPDYA
-DYKDDDDK	YPAAVPDYA	YPYDVPDYA	-DYKDDDDK	YPYDVPDYA	-DYKDDDDK	YPYDVPDYA	-DYKDDDDK	-DYKDDDDK
YPYDVPDYA	YPYDVPDYA	YPYDVPDYA	-DYKDDDDK	YPYDVPDYA	-DYKDDDDK	YPYDVPDYA	-DYKDDDDK	YPYDVPDYA
-DADDPDDA	YPAAVPDYA	YPYDVPDYA	-DYKDDDDK	YPYDVPDYA	-DYKDDDDK	YPYDVPDYA	-DYKDDDDK	YPYDVPDYA
-DYKDDDDK	YPAAVPDYA	YPYDVPDYA	-DYKDDDDK	YPYDVPDYA	-DYKDDDDK	YPYDVPDYA	-DYKDDDDK	-DYKDDDDK
YPYDVPDYA	YPAAVPDYA	YPYDVPDYA	-DYKDDDDK	-DYKDDDDK	YPYDVPDYA	YPYDVPDYA	-DYKDDDDK	YPYDVPDYA
-DADDPDDA	YPAAVPDYA	YPYDVPDYA	YPYDVPDYA	YPYDVPDYA	YPYDVPDYA	YPYDVPDYA	YPYDVPDYA	YPYDVPDYA
-DYKDDDDK	-DADDPDDA	YPYDVPDYA	-DYKDDDDK	-DADDPDDA	YPYDVPDYA	-DYKDDDDK	-DADDPDDA	YPYDVPDYA

Area 2

YPYDVPDYA	-DYKDDDDK	-DADDPDDA	YPYDVPDYA	-DYKDDDDK	-DADDPDDA	YPYDVPDYA	-DYKDDDDK	-DADDPDDA
YPYDVPDYA	-DAEDDDDK	YPAEVPDYA	-DAFDDDDK	YPAFVPDYA	-DYKDDDDK	YPAGVPDYA	-DAGDDDDK	YPYDVPDYA
-DATDDDDK	YPATVPDYA	-DAVDDDDK	YPAVVPDYA	-DAWDDDDK	YPAWVPDYA	-DAYDDDDK	YPAVVPDYA	-DCADDDDK
YPCNVDPYA	-DCNDDDDK	-DADDPDDA	-DCPDDDDK	YPCVPDYA	-DCQDDDDK	YPCQVPDYA	-DADDPDDA	YPCRVDPYA
-DDFDDDDK	YPDFVPDYA	-DDGDDDDK	YPDGVPDYA	-DDHDDDDK	YPDHVPDYA	-DDIDDDDK	YPDIVDPYA	-DDKDDDDK
YPDYVPDYA	-DYKDDDDK	YPDYVPDYA	-DEADDDDK	YPYDVPDYA	-DDADDDDK	YPECVPDYA	-DECDDDDK	YPEDVPDYA
-DEPDDDDK	YPEPVPDYA	-DEQDDDDK	YPEQVPDYA	-DERDDDDK	YPERVPDYA	-DESDDDDK	YPEVVPDYA	-DETDDDDK
YPFIVDPYA	-DFIDDDDK	YPFKVPDYA	-DADDPDDA	YPFKVPDYA	-DFLDDDDK	-DADDPDDA	-DFLDDDDK	YPFMVPDYA
-DGADDDDK	YPGAVPDYA	-DGCDDDDK	YPGCVPDYA	-DGDDDDDK	YPGDVPDYA	-DGEDDDDK	YPGVVPDYA	-DGFDDDDK
YPYDVPDYA	-DGSDDDDK	YPGSVPDYA	-DGTDDDDK	YPGTVPDYA	-DYKDDDDK	YPGVVPDYA	-DGVDDDDK	YPYDVPDYA
-DHKDDDDK	YPHKVPDYA	-DHLDDDDK	YPHLVPDYA	-DHMDDDDK	YPHMVPDYA	-DHNDDDDK	YPHNVPDYA	-DHPDDDDK
YPIEVPDYA	-DIEDDDDK	-DADDPDDA	-DIFDDDDK	YPIFVPDYA	-DIGDDDDK	YPIGVPDYA	-DADDPDDA	YPIHVPDYA
-DITDDDDK	YPIVVPDYA	-DIVDDDDK	YPIVVPDYA	-DIWDDDDK	YPIWVPDYA	-DIYDDDDK	YPIYVPDYA	-DKADDDDK
YPKNVDPYA	-DYKDDDDK	YPKNVDPYA	-DKPDDDDK	YPYDVPDYA	-DKPDDDDK	YPKQVPDYA	-DKQDDDDK	YPKRVDPYA
-DLFDDDDK	YPLFVPDYA	-DLGDDDDK	YPLGVPDYA	-DLHDDDDK	YPLHVPDYA	-DLIDDDDK	YPLIVDPYA	-DLKDDDDK
YPLYVPDYA	-DLYDDDDK	YPMVVPDYA	-DADDPDDA	YPMVVPDYA	-DMCDDDDK	-DADDPDDA	-DMCDDDDK	YPMVVPDYA
-DMPDDDDK	YPMVVPDYA	-DMQDDDDK	YPMQVPDYA	-DMRDDDDK	YPMRVPDYA	-DMSDDDDK	YPMVVPDYA	-DMTDDDDK
YPYDVPDYA	-DNIDDDDK	YPNIVDPYA	-DNKDDDDK	YPNKVPDYA	-DYKDDDDK	YPNLVPDYA	-DNLDDDDK	YPYDVPDYA
-DPADDDDK	YPPAVDPYA	-DPCDDDDK	YPPCVPDYA	-DPDDDDDK	YPPDVPDYA	-DPEDDDDK	YPPVVPDYA	-DPFDDDDK
YPPSVPDYA	-DPSDDDDK	-DADDPDDA	-DPTDDDDK	YPTVVPDYA	-DPVDDDDK	YPPVVPDYA	-DADDPDDA	YPPWVPDYA
-DQKDDDDK	YQKVPDYA	-DQLDDDDK	YQLVDPYA	-DQMDDDDK	YQMVVPDYA	-DQNDDDDK	YQNVVPDYA	-DQPDDDDK
YPREVPDYA	-DYKDDDDK	YPREVPDYA	-DRFDDDDK	YPYDVPDYA	-DRFDDDDK	YPRGVPDYA	-DRGDDDDK	YPRHVPDYA
-DRTDDDDK	YPRVVPDYA	-DRVDDDDK	YPRVVPDYA	-DRWDDDDK	YPRWVPDYA	-DRYDDDDK	YPRYVPDYA	-DSADDDDK
YPSNVDPYA	-DSNDDDDK	YPSVVPDYA	-DADDPDDA	YPSVVPDYA	-DSQDDDDK	-DADDPDDA	-DSQDDDDK	YPSRVDPYA
-DTFDDDDK	YPTFVPDYA	-DTGDDDDK	YPTGVPDYA	-DTHDDDDK	YPTHVPDYA	-DTIDDDDK	YPTIVDPYA	-DTKDDDDK
YPYDVPDYA	-DTYDDDDK	YPTYVPDYA	-DVADDDDK	YPAVVPDYA	-DYKDDDDK	YPCVVPDYA	-DVCDDDDK	YPYDVPDYA
-DVPDDDDK	YVPVVPDYA	-DVQDDDDK	YVPQVPDYA	-DVRDDDDK	YVVRVPDYA	-DVSDDDDK	YVSVVPDYA	-DVTDDDDK
YPWIVDPYA	-DWIDDDDK	-DADDPDDA	-DWKDDDDK	YPWKVPDYA	-DWLDDDDK	YPLWVPDYA	-DADDPDDA	YPMVVPDYA
-DYADDDDK	YPAVVPDYA	-DYCDDDDK	YPCVVPDYA	-DYDDDDDK	YPDVVPDYA	-DYEDDDDK	YPEVVPDYA	-DYFDDDDK
YPSVVPDYA	-DYKDDDDK	YPSVVPDYA	-DYTDDDDK	YPYDVPDYA	-DYTDDDDK	YPYVVPDYA	-DYVDDDDK	YPYVVPDYA
YPYDVPDYA	-DYKDDDDK	-DADDPDDA	YPYDVPDYA	-DYKDDDDK	-DADDPDDA	YPYDVPDYA	-DYKDDDDK	-DADDPDDA
-DADDPDDA	YPYDVPDYA	-DYKDDDDK	-DADDPDDA	YPYDVPDYA	-DYKDDDDK	-DADDPDDA	YPYDVPDYA	-DYKDDDDK
-DYKDDDDK	-DADDPDDA	YPYDVPDYA	-DYKDDDDK	-DADDPDDA	YPYDVPDYA	-DYKDDDDK	-DADDPDDA	YPYDVPDYA
YPYDVPDYA	-DAEDDDDK	YPAEVPDYA	-DAFDDDDK	YPAFVPDYA	-DYKDDDDK	YPAGVPDYA	-DAGDDDDK	YPYDVPDYA
-DATDDDDK	YPATVPDYA	-DAVDDDDK	YPAVVPDYA	-DAWDDDDK	YPAWVPDYA	-DAYDDDDK	YPAVVPDYA	-DCADDDDK
YPCNVDPYA	-DCNDDDDK	-DADDPDDA	-DCPDDDDK	YPCVPDYA	-DCQDDDDK	YPCQVPDYA	-DADDPDDA	YPCRVDPYA
-DDFDDDDK	YPDFVPDYA	-DDGDDDDK	YPDGVPDYA	-DDHDDDDK	YPDHVPDYA	-DDIDDDDK	YPDIVDPYA	-DDKDDDDK
YPDYVPDYA	-DYKDDDDK	YPDYVPDYA	-DEADDDDK	YPYDVPDYA	-DDADDDDK	YPECVPDYA	-DECDDDDK	YPEDVPDYA
-DEPDDDDK	YPEPVPDYA	-DEQDDDDK	YPEQVPDYA	-DERDDDDK	YPERVPDYA	-DESDDDDK	YPEVVPDYA	-DETDDDDK
YPFIVDPYA	-DFIDDDDK	YPFKVPDYA	-DADDPDDA	YPFKVPDYA	-DFLDDDDK	-DADDPDDA	-DFLDDDDK	YPFMVPDYA
-DGADDDDK	YPGAVPDYA	-DGCDDDDK	YPGCVPDYA	-DGDDDDDK	YPGDVPDYA	-DGEDDDDK	YPGVVPDYA	-DGFDDDDK
YPYDVPDYA	-DGSDDDDK	YPGSVPDYA	-DGTDDDDK	YPGTVPDYA	-DYKDDDDK	YPGVVPDYA	-DGVDDDDK	YPYDVPDYA
-DHKDDDDK	YPHKVPDYA	-DHLDDDDK	YPHLVPDYA	-DHMDDDDK	YPHMVPDYA	-DHNDDDDK	YPHNVPDYA	-DHPDDDDK
YPIEVPDYA	-DIEDDDDK	-DADDPDDA	-DIFDDDDK	YPIFVPDYA	-DIGDDDDK	YPIGVPDYA	-DADDPDDA	YPIHVPDYA
-DITDDDDK	YPIVVPDYA	-DIVDDDDK	YPIVVPDYA	-DIWDDDDK	YPIWVPDYA	-DIYDDDDK	YPIYVPDYA	-DKADDDDK
YPKNVDPYA	-DYKDDDDK	YPKNVDPYA	-DKPDDDDK	YPYDVPDYA	-DKPDDDDK	YPKQVPDYA	-DKQDDDDK	YPKRVDPYA
-DLFDDDDK	YPLFVPDYA	-DLGDDDDK	YPLGVPDYA	-DLHDDDDK	YPLHVPDYA	-DLIDDDDK	YPLIVDPYA	-DLKDDDDK
YPLYVPDYA	-DLYDDDDK	YPMVVPDYA	-DADDPDDA	YPMVVPDYA	-DMCDDDDK	-DADDPDDA	-DMCDDDDK	YPMVVPDYA
-DMPDDDDK	YPMVVPDYA	-DMQDDDDK	YPMQVPDYA	-DMRDDDDK	YPMRVPDYA	-DMSDDDDK	YPMVVPDYA	-DMTDDDDK
YPYDVPDYA	-DNIDDDDK	YPNIVDPYA	-DNKDDDDK	YPNKVPDYA	-DYKDDDDK	YPNLVPDYA	-DNLDDDDK	YPYDVPDYA
-DPADDDDK	YPPAVDPYA	-DPCDDDDK	YPPCVPDYA	-DPDDDDDK	YPPDVPDYA	-DPEDDDDK	YPPVVPDYA	-DPFDDDDK
YPPSVPDYA	-DPSDDDDK	-DADDPDDA	-DPTDDDDK	YPTVVPDYA	-DPVDDDDK	YPPVVPDYA	-DADDPDDA	YPPWVPDYA
-DQKDDDDK	YQKVPDYA	-DQLDDDDK	YQLVDPYA	-DQMDDDDK	YQMVVPDYA	-DQNDDDDK	YQNVVPDYA	-DQPDDDDK
YPREVPDYA	-DYKDDDDK	YPREVPDYA	-DRFDDDDK	YPYDVPDYA	-DRFDDDDK	YPRGVPDYA	-DRGDDDDK	YPRHVPDYA
YPYDVPDYA	YPYDVPDYA	YPYDVPDYA	YPYDVPDYA	YPYDVPDYA	YPYDVPDYA	YPYDVPDYA	YPYDVPDYA	YPYDVPDYA
-DYKDDDDK	YPYDVPDYA	-DYKDDDDK	-DYKDDDDK	-DYKDDDDK	YPYDVPDYA	-DYKDDDDK	-DYKDDDDK	-DYKDDDDK
YPYDVPDYA	YPYDVPDYA	-DYKDDDDK	YPYDVPDYA	YPYDVPDYA	YPYDVPDYA	YPYDVPDYA	YPYDVPDYA	YPYDVPDYA
YPYDVPDYA	YPYDVPDYA	-DYKDDDDK	-DYKDDDDK	-DYKDDDDK	YPYDVPDYA	YPYDVPDYA	YPYDVPDYA	-DYKDDDDK
YPYDVPDYA	YPYDVPDYA	-DYKDDDDK	YPYDVPDYA	YPYDVPDYA	YPYDVPDYA	YPYDVPDYA	-DYKDDDDK	YPYDVPDYA
YPYDVPDYA	YPYDVPDYA	-DYKDDDDK	YPYDVPDYA	YPYDVPDYA	YPYDVPDYA	-DYKDDDDK	YPYDVPDYA	YPYDVPDYA
-DYKDDDDK	YPYDVPDYA	-DYKDDDDK	YPYDVPDYA	YPYDVPDYA	YPYDVPDYA	-DYKDDDDK	-DYKDDDDK	-DYKDDDDK
YPYDVPDYA	YPYDVPDYA	YPYDVPDYA	YPYDVPDYA	YPYDVPDYA	YPYDVPDYA	YPYDVPDYA	YPYDVPDYA	YPYDVPDYA
-DYKDDDDK	-DADDPDDA	YPYDVPDYA	-DYKDDDDK	-DADDPDDA	YPYDVPDYA	-DYKDDDDK	-DADDPDDA	YPYDVPDYA

Area 3

YPYDVPDYA	-DYKDDDDK	-DADDPDDA	YPYDVPDYA	-DYKDDDDK	-DADDPDDA	YPYDVPDYA	-DYKDDDDK	-DADDPDDA
-DAHDDDDK	YPAHVDPYA	-DAIDDDDK	YPAIVDPYA	-DYKDDDDK	YPAKVDPYA	-DAKDDDDK	YPYDVPDYA	-DALDDDDK
YPCAVPDYA	-DCCDDDDK	YPCCVPDYA	-DCDDDDDK	YPCDVDPYA	-DCEDDDDK	YPCFVDPYA	-DCFDDDDK	YPCFVDPYA
-DCRDDDDK	-DADDPDDA	-DCSDDDDK	YPCSVPDYA	-DCTDDDDK	YPCTVPDYA	-DADDPDDA	YPCVVPDYA	-DCVDDDDK
YPKVVPDYA	-DDLDDDDK	YPLVVPDYA	-DDMDDDDK	YPLMVPDYA	-DDNDDDDK	YPLNVPDYA	-DDPDDDDK	YPLPVPDYA
-DYKDDDDK	YPEDVPDYA	-DEEDDDDK	YPYDVPDYA	-DEEDDDDK	YPEFVPDYA	-DEFDDDDK	YPEGVPDYA	-DYKDDDDK
YPETVPDYA	-DEVDDDDK	YPEVVPDYA	-DEWDDDDK	YPEWVPDYA	-DEYDDDDK	YPEYVPDYA	-DFADDDDK	YFAVVPDYA
-DFMDDDDK	YPFNVDPYA	-DADDPDDA	YPFNVDPYA	-DFPDDDDK	-DADDPDDA	-DFPDDDDK	YPFQVPDYA	-DFQDDDDK
YPGFVPDYA	-DGGDDDDK	YGGVVPDYA	-DGHDDDDK	YGHVVPDYA	-DGIDDDDK	YGGVVPDYA	-DGKDDDDK	YPGKVPDYA
-DGWDDDDK	YGVWVPDYA	-DGYDDDDK	YGYVVPDYA	-DYKDDDDK	YHAVVPDYA	-DHADDDDK	YPYDVPDYA	-DHCDDDDK
YPHPVPDYA	-DHQDDDDK	YPHQVPDYA	-DHRDDDDK	YPHRVPDYA	-DHSDDDDK	YPHSVPDYA	-DHTDDDDK	YHTVVPDYA
-DIHDDDDK	-DADDPDDA	-DIIDDDDK	YPIVVPDYA	-DIKDDDDK	YPIKVPDYA	-DADDPDDA	YPIVVPDYA	-DILDDDDK
YPAVVPDYA	-DKCDDDDK	YKCVVPDYA	-DKDDDDDK	YKDVVPDYA	-DKEDDDDK	YKEVVPDYA	-DKFDDDDK	YKFVVPDYA
-DYKDDDDK	YKRVVPDYA	-KSDDDDK	YPYDVPDYA	-KSDDDDDK	YKTVVPDYA	-KTDDDDDK	YKVVPDYA	-DYKDDDDK
YPLKVPDYA	-DLLDDDDK	YPLLVPDYA	-DLMDDDDK	YPLMVPDYA	-DLNDDDDK	YPLNVPDYA	-DLPDDDDK	YPLPVPDYA
-DMDDDDDK	YMEVVPDYA	-DADDPDDA	YMEVVPDYA	-DMFDDDDK	-DADDPDDA	-DMFDDDDK	YPMGVPDYA	-DMGDDDDK
YPMVVPDYA	-DMVDDDDK	YPMVVPDYA	-DMWDDDDK	YPMWVPDYA	-DMYDDDDK	YPMYVPDYA	-DNADDDDK	YNAVVPDYA
-DNMDDDDK	YPNMVPDYA	-DNNDDDDK	YPNVVPDYA	-DYKDDDDK	YPNVVPDYA	-DNPDDDDK	YPYDVPDYA	-DNQDDDDK
YPPFVPDYA	-DPGDDDDK	YPPGVPDYA	-DPHDDDDK	YPPHVPDYA	-DPIDDDDK	YPPVVPDYA	-DPKDDDDK	YPPKVPDYA
-DPWDDDDK	-DADDPDDA	-DPYDDDDK	YPPYVPDYA	-DQADDDDK	YQAVVPDYA	-DADDPDDA	YQCVVPDYA	-DQCDDDDK
YQPVPDYA	-DQQDDDDK	YQQVVPDYA	-DQRDDDDK	YQRVVPDYA	-DQSDDDDK	YQSVVPDYA	-DQTDDDDK	YQTVVPDYA
-DYKDDDDK	YRHPVPDYA	-DRIDDDDK	YPYDVPDYA	-DRIDDDDK	YPRKVPDYA	-DRKDDDDK	YRNVVPDYA	-DYKDDDDK
YSAVVPDYA	-DSCDDDDK	YSCVVPDYA	-DSDDDDDK	YSDVVPDYA	-DSEDDDDK	YSEVVPDYA	-DSFDDDDK	YSFVVPDYA
-DSRDDDDK	YSSVVPDYA	-DADDPDDA	YSSVVPDYA	-DSTDDDDK	-DADDPDDA	-DSTDDDDK	YSSVVPDYA	-DSVDDDDK
YPTKVPDYA	-DTLDDDDK	YPTLVPDYA	-DTMDDDDK	YPTMVPDYA	-DTNDDDDK	YPTNVPDYA	-DTPDDDDK	YPTVVPDYA
-DVDDDDDK	YPVVVPDYA	-DVEDDDDK	YPEVVPDYA	-DYKDDDDK	YPVVVPDYA	-DVFDDDDK	YPYDVPDYA	-DVGDDDDK
YPTVVPDYA	-DVVDDDDK	YVVVVPDYA	-DVWDDDDK	YVWVVPDYA	-DVIYDDDDK	YVYVVPDYA	-DWADDDDK	YWAVVPDYA
-DWMDDDDK	-DADDPDDA	-DWNDDDDK	YWNVVPDYA	-DWPDDDDK	YWPVVPDYA	-DADDPDDA	YWPVVPDYA	-DWQDDDDK
YPIVVPDYA	-DYGDDDDK	YPIVVPDYA	-DYHDDDDK	YPIVVPDYA	-DYIDDDDK	YPIVVPDYA	-DYKDDDDK	YPIVVPDYA
-DYKDDDDK	YPIVVPDYA	-DYYDDDDK	YPYDVPDYA	-DYYDDDDK	-----	-----	-----	-----
YPYDVPDYA	-DYKDDDDK	-DADDPDDA	YPYDVPDYA	-DYKDDDDK	-DADDPDDA	YPYDVPDYA	-DYKDDDDK	-DADDPDDA
-DADDPDDA	YPYDVPDYA	-DYKDDDDK	-DADDPDDA	YPYDVPDYA	-DYKDDDDK	-DADDPDDA	YPYDVPDYA	-DYKDDDDK
-DYKDDDDK	-DADDPDDA	YPYDVPDYA	-DYKDDDDK	-DADDPDDA	YPYDVPDYA	-DYKDDDDK	-DADDPDDA	YPYDVPDYA
-DAHDDDDK	YPAHVDPYA	-DAIDDDDK	YPAIVDPYA	-DYKDDDDK	YPAKVDPYA	-DAKDDDDK	YPYDVPDYA	-DALDDDDK
YPCAVPDYA	-DCCDDDDK	YPCCVPDYA	-DCDDDDDK	YPCDVDPYA	-DCEDDDDK	YPCFVDPYA	-DCFDDDDK	YPCFVDPYA
-DCRDDDDK	-DADDPDDA	-DCSDDDDK	YPCSVPDYA	-DCTDDDDK	YPCTVPDYA	-DADDPDDA	YPCVVPDYA	-DCVDDDDK
YPKVVPDYA	-DDLDDDDK	YPLVVPDYA	-DDMDDDDK	YPLMVPDYA	-DDNDDDDK	YPLNVPDYA	-DDPDDDDK	YPLPVPDYA
-DYKDDDDK	YPEDVPDYA	-DEEDDDDK	YPYDVPDYA	-DEEDDDDK	YPEFVPDYA	-DEFDDDDK	YPEGVPDYA	-DYKDDDDK
YPETVPDYA	-DEVDDDDK	YPEVVPDYA	-DEWDDDDK	YPEWVPDYA	-DEYDDDDK	YPEYVPDYA	-DFADDDDK	YFAVVPDYA
-DFMDDDDK	YPFNVDPYA	-DADDPDDA	YPFNVDPYA	-DFPDDDDK	-DADDPDDA	-DFPDDDDK	YPFQVPDYA	-DFQDDDDK
YPGFVPDYA	-DGGDDDDK	YGGVVPDYA	-DGHDDDDK	YGHVVPDYA	-DGIDDDDK	YGGVVPDYA	-DGKDDDDK	YPGKVPDYA
-DGWDDDDK	YGVWVPDYA	-DGYDDDDK	YGYVVPDYA	-DYKDDDDK	YHAVVPDYA	-DHADDDDK	YPYDVPDYA	-DHCDDDDK
YPHPVPDYA	-DHQDDDDK	YPHQVPDYA	-DHRDDDDK	YPHRVPDYA	-DHSDDDDK	YPHSVPDYA	-DHTDDDDK	YHTVVPDYA
-DIHDDDDK	-DADDPDDA	-DIIDDDDK	YPIVVPDYA	-DIKDDDDK	YPIKVPDYA	-DADDPDDA	YPIVVPDYA	-DILDDDDK
YPAVVPDYA	-DKCDDDDK	YKCVVPDYA	-DKDDDDDK	YKDVVPDYA	-DKEDDDDK	YKEVVPDYA	-DKFDDDDK	YKFVVPDYA
-DYKDDDDK	YKRVVPDYA	-KSDDDDK	YPYDVPDYA	-KSDDDDDK	YKTVVPDYA	-KTDDDDDK	YKVVPDYA	-DYKDDDDK
YPLKVPDYA	-DLLDDDDK	YPLLVPDYA	-DLMDDDDK	YPLMVPDYA	-DLNDDDDK	YPLNVPDYA	-DLPDDDDK	YPLPVPDYA
-DMDDDDDK	YMEVVPDYA	-DADDPDDA	YMEVVPDYA	-DMFDDDDK	-DADDPDDA	-DMFDDDDK	YPMGVPDYA	-DMGDDDDK
YPMVVPDYA	-DMVDDDDK	YPMVVPDYA	-DMWDDDDK	YPMWVPDYA	-DMYDDDDK	YPMYVPDYA	-DNADDDDK	YNAVVPDYA
-DNMDDDDK	YPNMVPDYA	-DNNDDDDK	YPNVVPDYA	-DYKDDDDK	YPNVVPDYA	-DNPDDDDK	YPYDVPDYA	-DNQDDDDK
YPPFVPDYA	-DPGDDDDK	YPPGVPDYA	-DPHDDDDK	YPPHVPDYA	-DPIIDDDK	YPPVVPDYA	-DPKDDDDK	YPPKVPDYA
-DPWDDDDK	-DADDPDDA	-DPYDDDDK	YPPYVPDYA	-DQADDDDK	YQAVVPDYA	-DADDPDDA	YQCVVPDYA	-DQCDDDDK
YQPVPDYA	-DQQDDDDK	YQQVVPDYA	-DQRDDDDK	YQRVVPDYA	-DQSDDDDK	YQSVVPDYA	-DQTDDDDK	YQTVVPDYA
-DYKDDDDK	YRHPVPDYA	-DRIDDDDK	YPYDVPDYA	-DRIDDDDK	YPRKVPDYA	-DRKDDDDK	YRNVVPDYA	-DYKDDDDK
YPYDVPDYA	YPYDVPDYA	-----	-----	-DYKDDDDK	-DYKDDDDK	-DYKDDDDK	-DYKDDDDK	-DYKDDDDK
-DYKDDDDK	YPYDVPDYA	-----	-----	-DYKDDDDK	YPYDVPDYA	-DYKDDDDK	YPYDVPDYA	-DYKDDDDK
-DYKDDDDK	YPYDVPDYA	-----	-----	-DYKDDDDK	YPYDVPDYA	-DYKDDDDK	-DYKDDDDK	-DYKDDDDK
YPYDVPDYA	YPYDVPDYA	-----	-----	-DYKDDDDK	YPYDVPDYA	-DYKDDDDK	-DYKDDDDK	-DYKDDDDK
YPYDVPDYA	YPYDVPDYA	-----	-----	-DYKDDDDK	YPYDVPDYA	-DYKDDDDK	-DYKDDDDK	-DYKDDDDK
-DYKDDDDK	YPYDVPDYA	-----	-----	-DYKDDDDK	YPYDVPDYA	-DYKDDDDK	YPYDVPDYA	-DYKDDDDK
YPYDVPDYA	YPYDVPDYA	-----	-----	-DYKDDDDK	-DYKDDDDK	-DYKDDDDK	-DYKDDDDK	-DYKDDDDK
-DYKDDDDK	-DADDPDDA	YPYDVPDYA	-DYKDDDDK	-DADDPDDA	YPYDVPDYA	-DYKDDDDK	-DADDPDDA	YPYDVPDYA

Area 4

YPYDVPDYA	-DYKDDDDK	-DADDPDDA	YPYDVPDYA	-DYKDDDDK	-DADDPDDA	YPYDVPDYA	-DYKDDDDK	-DADDPDDA	
YPALVPDYA	-DAMDDDDK	YPAMVPDYA	-DYKDDDDK	YPANVPDYA	-DANDDDDK	-DADDPDDA	YPYDVPDYA	YPYKVDKDK	
-DCGDDDDK	YPCGVDPYA	-DCHDDDDK	YPCHVPDYA	-DCIDDDDK	YPCIVDPYA	-DADDPDDA	-DYKDDDDK	YPAEDDDDK	YDAEDDDDK
-DADDPDDA	-DCWDDDDK	YPCWVPDYA	-DCYDDDDK	YPCYVPDYA	-DADDPDDA	YPYDVPDYA	YPYDVPDYA	YDAKVDEDK	YPYDVEDDK
-DDQDDDDK	YPDQVPDYA	-DDRDDDDK	YPRVVPDYA	-DDSDDDDK	YPSVVPDYA	-DADDPDDA	YDYKVPEDK	YPAKVPEDK	
YPEGVPDYA	-DEHDDDDK	YPYDVPDYA	-DEHDDDDK	YPEIVDPYA	-DEIDDDDK	-DYKDDDDK	YPADVNDK	-DYKDDDDK	
-DFCDDDDK	YPCVVPDYA	-DFDDDDDK	YPDFVPDYA	-DFEDDDDK	YPFVVPDYA	YPYDVPDYA	YDAKVPNDK	YPYDVPNDK	
YPRVVPDYA	-DADDPDDA	YPRVVPDYA	-DFSDDDDK	-DADDPDDA	-DFSDDDDK	-DADDPDDA	YPYEVQDK	YDYEVDQDK	
-DGLDDDDK	YPLVVPDYA	-DGMDDDDK	YPMVVPDYA	-DGNDDDDK	YPMVVPDYA	-DYKDDDDK	YPADVQDK	YDADVQDK	
YPHCVDPYA	-DHDDDDDK	YPHDVPDYA	-DYKDDDDK	YPHEVPDYA	-DHEDDDDK	YPYDVPDYA	YPYDVPDYA	YDAEVDYK	
-DHVDDDDK	YPHVVPDYA	-DHWDDDDK	YPHWVPDYA	-DHYDDDDK	YPHYVPDYA	-DADDPDDA	YDYEVPDYK	YPAEVPDYK	
-DADDPDDA	-DIMDDDDK	YIMVVPDYA	-DINDDDDK	YINVPDYA	-DADDPDDA	-DYKDDDDK	YPAKDEYK	YDAKDEYK	
-DKGDDDDK	YKGVVPDYA	-DKHDDDDK	YKHVPDYA	-DKIDDDDK	YKIVVPDYA	YPYDVPDYA	YPYKDEYK	YDYKDEYK	
YKVVVPDYA	-DKWDDDDK	YPYDVPDYA	-DKWDDDDK	YKYVVPDYA	-DKYDDDDK	-DADDPDDA	YDYDDNYK	-DYKDDDDK	
-DLQDDDDK	YPLQVPDYA	-DLRDDDDK	YPLRVPDYA	-DLSDDDDK	YPLVVPDYA	-DYKDDDDK	YPAKDPNYK	YDAKDPNYK	
YPMHVPDYA	-DADDPDDA	YPMHVPDYA	-DMIDDDDK	-DADDPDDA	-DMIDDDDK	YPYDVPDYA	YDADDQYK	YPYEDDQYK	
-DNCDDDDK	YPCVVPDYA	-DNDDDDDK	YPCVVPDYA	-DNEDDDDK	YPCVVPDYA	-DADDPDDA	YDYDDPQYK	YPADDPQYK	
YPCVVPDYA	-DNRDDDDK	YPCVVPDYA	-DYKDDDDK	YPCVVPDYA	-DNSDDDDK	-DYKDDDDK	YPYDVPDYA	YPAEDDDNK	
-DPLDDDDK	YPLVVPDYA	-DPMDDDDK	YPMVVPDYA	-DPNDDDDK	YPMVVPDYA	YPYDVPDYA	YPYEDPDK	YDYEVPDK	
-DADDPDDA	-DQDQDDDK	YQDQVPDYA	-DQEDDDDK	YQEVVPDYA	-DADDPDDA	-DADDPDDA	YDYKVPENK	YPAKVPENK	
-DQVDDDDK	YQVVPDYA	-DQWDDDDK	YQWVVPDYA	-DQYDDDDK	YQYVVPDYA	-DYKDDDDK	YDAEDPENK	YPYKVDNNK	
YRVLVPDYA	-DRMDDDDK	YPYDVPDYA	-DRMDDDDK	YRNVVPDYA	-DRNDDDDK	YPYDVPDYA	YPYDVPNDK	-DYKDDDDK	
-DSGDDDDK	YSGVVPDYA	-DSHDDDDK	YSHVVPDYA	-DSIDDDDK	YSHVVPDYA	-DADDPDDA	YDYDVPQNK	YPAKVPQNK	
YSHVVPDYA	-DADDPDDA	YSHVVPDYA	-DSYDDDDK	-DADDPDDA	-DSYDDDDK	-DYKDDDDK	YPADVQNK	YDADVQNK	
-DTQDDDDK	YPTQVPDYA	-DTRDDDDK	YPTRVPDYA	-DTSDDDDK	YPTVVPDYA	YPYDVPDYA	YPYDVPNDK	YDYDVPNDK	
YPVGVPDYA	-DVHDDDDK	YPVHVPDYA	-DYKDDDDK	YPIVVPDYA	-DVIDDDDK	-DADDPDDA	YPYDVPDYA	YDYEVPDK	
-DWCDDDDK	YWCVVPDYA	-DWDDDDDK	YWDVVPDYA	-DWEDDDDK	YWEVVPDYA	-DYKDDDDK	YDADVDEWK	YPYEVDEWK	
-DADDPDDA	-DWRDDDDK	YWRVVPDYA	-DWSDDDDK	YWSVVPDYA	-DADDPDDA	YPYDVPDYA	YPYKDEWK	YDYKDEWK	
-DYLDDDDK	YPLVVPDYA	-DYMDDDDK	YPMVVPDYA	-DYNDDDDK	YPMVVPDYA	-DADDPDDA	YPAEVDNWK	YDAEVDNWK	
-----	-----	-----	-----	-----	-----	-DYKDDDDK	YDAKDPNWK	-DYKDDDDK	
YPYDVPDYA	-DYKDDDDK	-DADDPDDA	YPYDVPDYA	-DYKDDDDK	-DADDPDDA	YPYDVPDYA	YPYKDDQWK	YDYKDDQWK	
-DADDPDDA	YPYDVPDYA	-DYKDDDDK	-DADDPDDA	YPYDVPDYA	-DYKDDDDK	-DADDPDDA	YDYDDPQWK	YPADDPQWK	
-DYKDDDDK	-DADDPDDA	YPYDVPDYA	-DYKDDDDK	-DADDPDDA	YPYDVPDYA	-DYKDDDDK	YDAKDDDDA	YPYDDDDA	
YPALVPDYA	-DAMDDDDK	YPAMVPDYA	-DYKDDDDK	YPANVPDYA	-DANDDDDK	YPYDVPDYA	YPYDVPDYA	YPYEDPDDA	
-DCGDDDDK	YPCGVDPYA	-DCHDDDDK	YPCHVPDYA	-DCIDDDDK	YPCIVDPYA	-DADDPDDA	YPADDDEDA	YDADDDEDA	
-DADDPDDA	-DCWDDDDK	YPCWVPDYA	-DCYDDDDK	YPCYVPDYA	-DADDPDDA	-DYKDDDDK	YDAEDPEDA	YPYKVDNDA	
-DDQDDDDK	YPDQVPDYA	-DDRDDDDK	YPRVVPDYA	-DDSDDDDK	YPSVVPDYA	YPYDVPDYA	YDYEDDNDK	YPAEDDNDK	
YPEGVPDYA	-DEHDDDDK	YPYDVPDYA	-DEHDDDDK	YPEIVDPYA	-DEIDDDDK	-DADDPDDA	YPAKVDQDA	-DYKDDDDK	
-DFCDDDDK	YPCVVPDYA	-DFDDDDDK	YPDFVPDYA	-DFEDDDDK	YPFVVPDYA	-DYKDDDDK	YDAEDDQDA	YPYKVPQDA	
YPRVVPDYA	-DADDPDDA	YPRVVPDYA	-DFSDDDDK	-DADDPDDA	-DFSDDDDK	YPYDVPDYA	YPYDVPDYA	YDYDVPDYA	
-DGLDDDDK	YPLVVPDYA	-DGMDDDDK	YPMVVPDYA	-DGNDDDDK	YPMVVPDYA	-DADDPDDA	YPAKVPDYA	YDAKVPDYA	
YPHCVDPYA	-DHDDDDDK	YPHDVPDYA	-DYKDDDDK	YPHEVPDYA	-DHEDDDDK	-DYKDDDDK	YPYDVPDYA	YDADVDEYA	
-DHVDDDDK	YPHVVPDYA	-DHWDDDDK	YPHWVPDYA	-DHYDDDDK	YPHYVPDYA	YPYDVPDYA	YDYDVEYA	YPADVPEYA	
-DADDPDDA	-DIMDDDDK	YIMVVPDYA	-DINDDDDK	YINVPDYA	-DADDPDDA	-DADDPDDA	YPAEVDNYA	YDAEVDNYA	
-DKGDDDDK	YKGVVPDYA	-DKHDDDDK	YKHVPDYA	-DKIDDDDK	YKIVVPDYA	-DYKDDDDK	YPYEVPNYA	YDYEVPNYA	
YKVVVPDYA	-DKWDDDDK	YPYDVPDYA	-DKWDDDDK	YKYVVPDYA	-DKYDDDDK	YPYDVPDYA	YDYKDDQYA	-DYKDDDDK	
-DLQDDDDK	YPLQVPDYA	-DLRDDDDK	YPLRVPDYA	-DLSDDDDK	YPLVVPDYA	-DADDPDDA	YPAEVPQYA	YDAEVPQYA	
YPMHVPDYA	-DADDPDDA	YPMHVPDYA	-DMIDDDDK	-DADDPDDA	-DMIDDDDK	-DYKDDDDK	YDAKDDDNA	YPYDDDNA	
-DNCDDDDK	YPCVVPDYA	-DNDDDDDK	YPCVVPDYA	-DNEDDDDK	YPCVVPDYA	YPYDVPDYA	YDYKDPNA	YPAKDPNA	
YPCVVPDYA	-DNRDDDDK	YPCVVPDYA	-DYKDDDDK	YPCVVPDYA	-DNSDDDDK	-DADDPDDA	YPYDVPDYA	YPADDDENA	
-DPLDDDDK	YPLVVPDYA	-DPMDDDDK	YPMVVPDYA	-DPNDDDDK	YPMVVPDYA	-DYKDDDDK	YPYDDPENA	YDYDDPENA	
-DADDPDDA	-DQDQDDDK	YQDQVPDYA	-DQEDDDDK	YQEVVPDYA	-DADDPDDA	YPYDVPDYA	YDYEDDNNK	YPAEDDNNK	
-DQVDDDDK	YQVVPDYA	-DQWDDDDK	YQWVVPDYA	-DQYDDDDK	YQYVVPDYA	-DADDPDDA	YDADDPNNA	YPYEDPNNA	
YRVLVPDYA	-DRMDDDDK	YPYDVPDYA	-DRMDDDDK	YRNVVPDYA	-DRNDDDDK	-DYKDDDDK	YPYKVPQNA	-DYKDDDDK	
-DYKDDDDK	-DYKDDDDK	-DYKDDDDK	-DYKDDDDK	-DYKDDDDK	-DYKDDDDK	YPYDVPDYA	YDYEDPQNA	YPAEDPQNA	
YPYDVPDYA	-DYKDDDDK	YPYDVPDYA	YPYDVPDYA	YPYDVPDYA	-DYKDDDDK	-DADDPDDA	YPAKVPDWA	YDAKVPDWA	
YPYDVPDYA	-DYKDDDDK	YPYDVPDYA	YPYDVPDYA	YPYDVPDYA	-DYKDDDDK	YPYDVPDYA	YPYKVEWA	YDYKVEWA	
YPYDVPDYA	-DYKDDDDK	YPYDVPDYA	YPYDVPDYA	YPYDVPDYA	-DYKDDDDK	YPYDVPDYA	YPYDVPDYA	YDYDVEWA	
YPYDVPDYA	-DYKDDDDK	YPYDVPDYA	-DYKDDDDK	-DYKDDDDK	-DYKDDDDK	-DADDPDDA	YDAKVDNWA	YPYDVDNWA	
YPYDVPDYA	-DYKDDDDK	YPYDVPDYA	-DYKDDDDK	-DYKDDDDK	-DYKDDDDK	-DYKDDDDK	YPYEVPNWA	YDYEVPNWA	
YPYDVPDYA	-DYKDDDDK	YPYDVPDYA	-DYKDDDDK	-DYKDDDDK	-DYKDDDDK	YPYDVPDYA	YPADVQWA	YDADVQWA	
-DYKDDDDK	-DYKDDDDK	-DYKDDDDK	-DYKDDDDK	-DYKDDDDK	-DYKDDDDK	-DADDPDDA	YDAEVPQWA	-DYKDDDDK	
-DYKDDDDK	-DADDPDDA	YPYDVPDYA	-DYKDDDDK	-DADDPDDA	YPYDVPDYA	-DYKDDDDK	-DADDPDDA	YPYDVPDYA	

Area 5

YPYDVPDYA	-DYKDDDDK	-DADDPDDA	YPYDVPDYA	-DYKDDDDK	-DADDPDDA	YPYDVPDYA	-DYKDDDDK	-DADDPDDA
YDYKVDDDK	YPAKVDDDK	YDAKVDDDK	-DYKDDDDK	YPYDVDDDK	YDYDVDDDK	YPYDVPDYA	YPADVDDDK	YDADVDDDK
YPYKVPDDK	YDYKVPDDK	YPAKVPDDK	YDAKVPDDK	YPYDVPDDK	YDYDVPDDK	YPYDVPDYA	YDADVDDDK	YPYDVPDDK
-DADDPDDA	YDYDVDEDK	YPADVDEDK	YDADVDEDK	YPYEVDEDK	-DADDPDDA	YDYEVDEDK	YPAEVDEDK	-DADDPDDA
YDAKVPEDK	YPYDVPEDK	YDYDVPEDK	YPADVPEDEK	YDADVPEDEK	YPYEVPEDEK	YDYEVPEDEK	YPAEVPEDEK	YDAEVPEDEK
YDADVNDK	YPYEVNDK	YPYDVPDYA	YDYEVNDK	YPAEVNDK	YDAEVNDK	YPYKDDNDK	-DYKDDDDK	YDYKDDNDK
YDYDVPNDK	YPADVPNDK	YDADVPNDK	YPYEVPNDK	YDYEVPNDK	YPAEVPNDK	YDAEVPNDK	YPYKDPNDK	YDYKDPNDK
YPAEVDQDK	-DADDPDDA	YDAEVDQDK	YPYKDDQDK	-DADDPDDA	YDYKDDQDK	YPAKDDQDK	YDAKDDQDK	YPYDDQDK
YPYEVQDK	YDYEVQDK	YPAEVQDK	YDAEVQDK	YPYKDPQDK	YDYKDPQDK	YPAKDPQDK	YDAKDPQDK	YPYDDPQDK
YPYKDDDYK	YDYKDDDYK	YPAKDDDYK	-DYKDDDDK	YDAKDDDYK	YPYDDDDYK	YPYDVPDYA	YDYDDDDYK	YPADDDDYK
YDAEVPDYK	YPYKDPDYK	YDYKDPDYK	YPAKDPDYK	YDAKDPDYK	YPYDDPDYK	YDYDDPDYK	YPADDPDYK	YDADDPDYK
-DADDPDDA	YPYDDDEYK	YDYDDDEYK	YPADDDDEYK	YDADDDDEYK	-DADDPDDA	YPYEDDEYK	YDYEDDEYK	-DADDPDDA
YPAKDPEYK	YDAKDPEYK	YPYDDPEYK	YDYDDPEYK	YPADDPPEYK	YDADDPPEYK	YPYEDPEYK	YDYEDPEYK	YPAEDPEYK
YPADDDNYK	YDADDDNYK	YPYDVPDYA	YPYEDDNYK	YDYEDDNYK	YPAEDDNYK	YDAEDDNYK	-DYKDDDDK	YPYKVPNYK
YPYDDPNYK	YDYDDPNYK	YPADDPNYK	YDADDPNYK	YPYEDPNYK	YDYEDPNYK	YPAEDPNYK	YDAEDPNYK	YPYKVDQYK
YDYEDDQYK	-DADDPDDA	YPAEDDQYK	YDAEDDQYK	-DADDPDDA	YPYKVPQYK	YDYKVPQYK	YPAKVPQYK	YDAKVPQYK
YDADDPQYK	YDYEDDPQYK	YDYEDDPQYK	YPAEDDPQYK	YDADDPQYK	YPYKVDNKN	YDYKVDNKN	YPAKVDNKN	YDAKVDNKN
YDAEDDDNK	YPYKVPDNK	YDYKVPDNK	-DYKDDDDK	YPAKVPDNK	YDAKVPDNK	YPYDVPDYA	YPYDVPDNK	YDYDVPDNK
YPAEDPDNK	YDAEDPDNK	YPYKVDENK	YDYKVDENK	YPAKV DENK	YDAKV DENK	YPYDVENK	YDYDVENK	YPADV DENK
-DADDPDDA	YDAKVPENK	YPYDVPENK	YDYDVPENK	YPADV PENK	-DADDPDDA	YDADV PENK	YPYEV PENK	-DADDPDDA
YDYKVDNKN	YPAKV DNNK	YDAKV DNNK	YPYDVPDNNK	YDYDVPDNNK	YPADV DNNK	YDADV DNNK	YPYEV DNNK	YDYEV DNNK
YDYDVPNNK	YPADV PNNK	YPYDVPDYA	YDADV PNNK	YPYEV PNNK	YDYEV PNNK	YPAEVPNNK	-DYKDDDDK	YDAEVPNNK
YDAKVDQNK	YPYDVPQNK	YDYDVPQNK	YPADV DQNK	YPYEV DQNK	YDYEV DQNK	YPAEVDQNK	YDYEVDQNK	YDAEVDQNK
YPYEVQNK	-DADDPDDA	YDYEVQNK	YPAEVPQNK	-DADDPDDA	YDAEVPQNK	YPYKDPQNK	YDYKDPQNK	YPAKDPQNK
YPADVDDWK	YDADVDDW	YPYEVDDWK	YDYEVDDWK	YPAEVDWK	YDAEVDWK	YPYKDDWK	YDYKDDWK	YPAKDDWK
YPAEVPDWK	YDAEVPDWK	YPYKDPDWK	-DYKDDDDK	YDYKDPDWK	YPAKDPDWK	YPYDVPDYA	YDAKDPDWK	YPYDDPDWK
YDYEVDEWK	YPAEVDEWK	YDAEVDEWK	YPYKDDDEWK	YDYKDDDEWK	YPAKDDDEWK	YDAKDDDEWK	YPYDDDEWK	YDYDDDEWK
-DADDPDDA	YPAKDPEWK	YDAKDPEWK	YPYDDPEWK	YDYDDPEWK	-DADDPDDA	YPADDPPEWK	YDADDPPEWK	-DADDPDDA
YPYKDDNWK	YDYKDDNWK	YPAKDDNWK	YDAKDDNWK	YPYDDDNWK	YDYDDDNWK	YPADDDNWK	YDADDDNWK	YPYEDDNWK
YPYDDPNWK	YDYDDPNWK	YPYDVPDYA	YPADDPNWK	YDADDPNWK	YPYEDPNWK	YDYEDPNWK	-DYKDDDDK	YPYEDPNWK
YPAKDDQWK	YDAKDDQW	YPYDDDQWK	YDYDDDQW	YPADDDQW	YDADDDQW	YPYEDDQWK	YDYEDDQWK	YPAEDDQWK
YDADDPQW	-DADDPDDA	YPYEDPQWK	YDYEDPQWK	-DADDPDDA	YPAEDPQWK	YDAEDPQWK	YPYKVDQDA	YDYKVDQDA
YDYDDDDDA	YPADDDDDA	YDADDDDDA	YPYEDDDDA	YDYEDDDDA	YPAEDDDDA	YDAEDDDDA	YPYKVPDDA	YDYKVPDDA
YDYEDPDDA	YPAEDPDDA	YDAEDPDDA	-DYKDDDDK	YPYKVEDA	YDYKVEDA	YPYDVPDYA	YPAKVEDA	YDAKVEDA
YPYEDDEDA	YDYEDDEDA	YPAEDDEDA	YDAEDDEDA	YPYKVPEDA	YDYKVPEDA	YPAKVPEDA	YDAKVPEDA	YPYDVPEDA
-DADDPDDA	YDYKVDNDA	YPAKVDNDA	YDAKVDNDA	YPYDVPDND	-DADDPDDA	YDYDVPDND	YPADV DND	-DADDPDDA
YDAEDDND	YPYKVPNDA	YDYKVPNDA	YPAKVPNDA	YDAKVPNDA	YPYDVPNDA	YDYDVPNDA	YPADV DND	YDADV DND
YDAKVDQDA	YPYDVPQDA	YPYDVPDYA	YDYDVPQDA	YPADV DQDA	YDADV DQDA	YPYEV DQDA	-DYKDDDDK	YDYEV DQDA
YDYKVPQDA	YPAKVPQDA	YDAKVPQDA	YPYDVPQDA	YDYDVPQDA	YPADV DQDA	YDADV DQDA	YPYEV DQDA	YDYEV DQDA
YPADVDDYA	-DADDPDDA	YDADVDDYA	YPYEVDDYA	-DADDPDDA	YDYEVDDYA	YPAEVDDYA	YDAEVDDYA	YPYKDDDYA
YPYDVPDYA	YDYDVPDYA	YPADV DYA	YDADV DYA	YPYEV DYA	YDYEV DYA	YPAEV DYA	YDAEV DYA	YPYKDPDYA
YPYEVDEYA	YDYEVDEYA	YPAEVDEYA	-DYKDDDDK	YDAEVDEYA	YPYKDDDEYA	YPYDVPDYA	YDYKDDDEYA	YPAKDDDEYA
YDADVPEYA	YPYEVPEYA	YDYEVPEYA	YPAEVPEYA	YDAEVPEYA	YPYKDPPEYA	YDYKDPPEYA	YPAKDPPEYA	YDAKDPPEYA
-DADDPDDA	YPYKDDNYA	YDYKDDNYA	YPAKDDNYA	YDAKDDNYA	-DADDPDDA	YPYDDDNYA	YDYDDDNYA	-DADDPDDA
YPAEVPNYA	YDAEVPNYA	YPYKDPNYA	YDYKDPNYA	YPAKDPNYA	YDAKDPNYA	YPYDDPNYA	YDYDDPNYA	YPADDPNYA
YPAKDDQYA	YDAKDDQYA	YPYDVPDYA	YPYDDDQYA	YDYDDDQYA	YPADDDQYA	YDADDDQYA	-DYKDDDDK	YPYEDDQYA
YPYKDPQYA	YDYKDPQYA	YPAKDPQYA	YDAKDPQYA	YPYDDPQYA	YDYDDPQYA	YPADDPQYA	YDADDPQYA	YPYEDPQYA
YDYDDDDNA	-DADDPDDA	YPADDDDNA	YDADDDDNA	-DADDPDDA	YPYEDDDNA	YDYEDDDNA	YPAEDDDNA	YDAEDDDNA
YDAKDPDNA	YPYDDPDNA	YDYDDPDNA	YPADDPDNA	YDADDPDNA	YPYEDPDNA	YDYEDPDNA	YPAEDPDNA	YDAEDPDNA
YDADDDENA	YPYEDDENA	YDYEDDENA	-DYKDDDDK	YPAEDDENA	YDAEDDENA	YPYDVPDYA	YPYKVPENA	YDYKVPENA
YPADDPENA	YDADDPENA	YPYEDPENA	YDYEDPENA	YPAEDPENA	YDAEDPENA	YPYKVDNNA	YDYKVDNNA	YPAKVDNNA
-DADDPDDA	YDAEDDNN	YPYKVPNNA	YDYKVPNNA	YPAKVPNNA	-DADDPDDA	YDAKVPNNA	YPYDVPNNA	-DADDPDDA
YDYEDPNNA	YPAEDPNNA	YDAEDPNNA	YPYKVDQNA	YDYKVDQNA	YPAKVDQNA	YDAKVDQNA	YPYDVPQNA	YDYDVPQNA
YDYKVPQNA	YPAKVPQNA	YPYDVPDYA	YDAKVPQNA	YPYDVPQNA	YDYDVPQNA	YPADV DQNA	-DYKDDDDK	YDADV DQNA
YDAEDPQNA	YPYKVDQNA	YDYKVDQNA	YPAKVDQNA	YDAKVDQNA	YPYDQNA	YDYDQNA	YPYDQNA	YDADV DQNA
YPYDVPDWA	-DADDPDDA	YDYDVPDWA	YPADV DWA	-DADDPDDA	YDADV DWA	YPYEV DWA	YDAEV DWA	YPYDVPDWA
YPAKVEWA	YDAKVEWA	YPYDVEWA	YDYDVEWA	YPADV DWA	YDADV DWA	YPYEV DWA	YDYEV DWA	YPAEV DWA
YPADVPEWA	YDADVPEWA	YPYEVPEWA	-DYKDDDDK	YDYEVPEWA	YPAEVPEWA	YPYDVPDYA	YDAEVPEWA	YPYKDPPEWA
YDYDNDW	YPADV DNDW	YDADV DNDW	YPYEV DNDW	YDYEV DNDW	YPAEV DNDW	YDAEV DNDW	YPYKDDNWA	YDYKDDNWA
-DADDPDDA	YPAEVPNWA	YDAEVPNWA	YPYKDPNWA	YDYKDPNWA	-DADDPDDA	YPAKDPNWA	YDAKDPNWA	-DADDPDDA
YPYEV DQWA	YDYEV DQWA	YPAEV DQWA	YDAEV DQW	YPYKDDQWA	YDYKDDQWA	YPAKDDQW	YDAKDDQW	YPYDDQWA
YPYKDPQWA	YDYKDPQWA	YPYDVPDYA	YPAKDPQWA	YDAKDPQW	YPYDDPQWA	YDYDDPQWA	-DYKDDDDK	YPADDPQWA
-DYKDDDDK	-DADDPDDA	YPYDVPDYA	-DYKDDDDK	-DADDPDDA	YPYDVPDYA	-DYKDDDDK	-DADDPDDA	YPYDVPDYA

Area 7

YPYDVPDYA	-DYKDDDDK	-DADDPDDA	YPYDVPDYA	-DYKDDDDK	-DADDPDDA	YPYDVPDYA	-DYKDDDDK	-DADDPDDA	HA*
YDAKDDDDK	-DYKDDDDK	YPYDDDDK	YDYDDDDK	YPYDVPDYA	YPADDDDK	YDADDDDK	YPYEDDDK	YDYEDDDK	Cont*
YPADDPDDK	YDADDPDDK	YPYEDPDDK	YDYEDPDDK	YPAEDPDDK	YDAEDPDDK	YPYKVDDEK	YDYKVDDEK	YPAKVDDEK	Flag*
YPADDDDEK	YDADDDDEK	YPYEDDEK	-DADDPDDA	YDYEDDEK	YPAEDDEK	-DADDPDDA	YDAEDDEK	YPYKVPDEK	HA*
YDYEDPEDK	YPAEDPEDK	YDAEDPEDK	YPYKVDNDK	YDYKVDNDK	YPAKVDNDK	YDAKVDNDK	YPYDVDNDK	YDYDVDNDK	Cont*
YPYDVPDYA	YDYEDDNDK	YPAEDDNDK	YDAEDDNDK	YPYKVPNDK	-DYKDDDDK	YDYKVPNDK	YPAKVPNDK	YPYDVPDYA	Flag*
YDAEDPNDK	YPYKVDQDK	YDYKVDQDK	YPAKVDQDK	YDAKVDQDK	YPYDVPQDK	YDYDVPQDK	YPADVPQDK	YDADVPQDK	HA*
YDAEDDQDK	YPYKVPQDK	-DADDPDDA	YDYKVPQDK	YPAKVPQDK	YDAKVPQDK	YPYDVPQDK	-DADDPDDA	YDYDVPQDK	Cont*
YPAKVVDDYK	YDAKVVDDYK	YPYDVVDDYK	YDYDVVDDYK	YPADVVDDYK	YDADVDDYK	YPYEVDDYK	YDYEVDDYK	YPAEVDDYK	Flag*
YPAKVPDYK	-DYKDDDDK	YDAKVPDYK	YPYDVPDYK	YPYDVPDYA	YPYDVPDYK	YPADVPDYK	YDADVPDYK	YPYEVDPYK	HA*
YDYDVDEYK	YPADVDEYK	YDADVDEYK	YPYEVDEYK	YDYEVDEYK	YPAEVDEYK	YDAEVDEYK	YPYKDDYK	YDYKDDYK	Cont*
YDYDVPEYK	YPADVPEYK	YDADVPEYK	-DADDPDDA	YPYEVPEYK	YDYEVPEYK	-DADDPDDA	YPAEVPEYK	YDAEVPEYK	Flag*
YPYEVDPYK	YDYEVDPYK	YPAEVDPYK	YDAEVDPYK	YPYKDDNYK	YDYKDDNYK	YPAKDDNYK	YDAKDDNYK	YPYDDDPYK	HA*
YPYDVPDYA	YPYEVPNYK	YDYEVPNYK	YPAEVPNYK	YDAEVPNYK	-DYKDDDDK	YPYKDPNYK	YDYKDPNYK	YPYDVPDYA	Cont*
YPAEVDPYK	YDAEVDPYK	YPYKDDQYK	YDYKDDQYK	YPAKDDQYK	YDAKDDQYK	YPYDDDPYK	YDYDDDPYK	YPADDDQYK	Flag*
YPAEVQYK	YDAEVQYK	-DADDPDDA	YPYKDPQYK	YDYKDPQYK	YPAKDPQYK	YDAKDPQYK	-DADDPDDA	YPYDDPQYK	HA*
YDYKDDDNK	YPAKDDDNK	YDAKDDDNK	YPYDDDDNK	YDYDDDDNK	YPADDDDNK	YDADDDDNK	YPYEDDDNK	YDYEDDDNK	Cont*
YDYKDPDNK	-DYKDDDDK	YPAKDPDNK	YDAKDPDNK	YPYDVPDYA	YPYDDPDNK	YDYDDPDNK	YPADDPDNK	YDADDPDNK	Flag*
YPYDDDENK	YDYDDDENK	YPADDDENK	YDADDDENK	YPYEDDENK	YDYEDDENK	YPAEDDENK	YDAEDDENK	YPYKVPENK	HA*
YPYDDPENK	YDYDDPENK	YPADDPENK	-DADDPDDA	YDADDPENK	YPYEDPENK	-DADDPDDA	YDYEDPENK	YPAEDPENK	Cont*
YDADDDNNK	YPYEDDNNK	YDYEDDNNK	YPAEDDNNK	YDAEDDNNK	YPYKVPNNK	YDYKVPNNK	YPAKVPNNK	YDAKVPNNK	Flag*
YPYDVPDYA	YDADDPNNK	YPYEDPNNK	YDYEDPNNK	YPAEDPNNK	-DYKDDDDK	YDAEDPNNK	YPYKVDQNK	YPYDVPDYA	HA*
YDYEDDQNK	YPAEDDQNK	YDAEDDQNK	YPYKVPQNK	YDYKVPQNK	YPAKVPQNK	YDAKVPQNK	YPYDVPQNK	YDYDVPQNK	Cont*
YDYEDPQNK	YPAEDPQNK	-DADDPDDA	YDAEDPQNK	YPYKVDQNK	YDYKVDQNK	YPAKVDQNK	-DADDPDDA	YDAKVDQNK	Flag*
YPYKVPDWK	YDYKVPDWK	YPAKVPDWK	YDAKVPDWK	YPYDVPDWK	YDYDVPDWK	YPADVPDWK	YDADVPDWK	YPYEVDPWK	HA*
YPYKVDDEWK	-DYKDDDDK	YDYKVDDEWK	YPAKVDDEWK	YPYDVPDEWK	YDYDVPDEWK	YPADVPDEWK	YDADVPDEWK	YPYEVDEWK	Cont*
YDAKVPDEWK	YPYDVPDEWK	YDYDVPDEWK	YPADVPDEWK	YDADVPDEWK	YPYEVPEWK	YDYEVPEWK	YPAEVPEWK	YDAEVPEWK	Flag*
YDAKVDNWK	YPYDVDNWK	YDYDVDNWK	-DADDPDDA	YPADVDNWK	YDADVDNWK	-DADDPDDA	YPYEVDNWK	YDYEVDNWK	HA*
YPADVPNWK	YDADVPNWK	YPYEVNWK	YDYEVNWK	YPAEVNWK	YPYKDPNWK	YDYKDPNWK	YPAKDPNWK	YDAKDPNWK	Cont*
YPYDVPDYA	YPADVPQWK	YDADVPQWK	YPYEVQWK	YDYEVQWK	-DYKDDDDK	YPAEVQWK	YDAEVQWK	YPYDVPDYA	Flag*
YPYEVQWK	YDYEVQWK	YPAEVQWK	YDAEVQWK	YPYKDPQWK	YDYKDPQWK	YPAKDPQWK	YDAKDPQWK	YPYDDPQWK	HA*
YPYEVDDA	YDYEVDDA	-DADDPDDA	YPAEVDDA	YDAEVDDA	YPYKDDDA	YDYKDDDA	-DADDPDDA	YPAKDDDA	Cont*
YDAEVPDDA	YPYKDPDDA	YDYKDPDDA	YPAKDPDDA	YDAKDPDDA	YPYDDPDDA	YDYDDPDDA	YPADDPDDA	YDADDPDDA	Flag*
YDAEVDADA	-DYKDDDDK	YPYKDDADA	YDYKDDADA	YPYDVPDYA	YPAKDDADA	YDAKDDADA	YPYDDDDA	YDYDDDDA	HA*
YPAKDPEDA	YDAKDPEDA	YPYDDPEDA	YDYDDPEDA	YPADDPEDA	YDADDPEDA	YPYEDPEDA	YDYEDPEDA	YPAEDPEDA	Cont*
YPAKDDNDA	YDAKDDNDA	YPYDDNDNA	-DADDPDDA	YDADDDNDA	YPADDDNDA	-DADDPDDA	YDADDDND	YPYEDDND	Flag*
YDYDDPNDA	YPADDPNDA	YDADDPNDA	YPYEDPNDA	YDYEDPNDA	YPAEDPNDA	YDAEDPNDA	YPYKVDQDA	YDYKVDQDA	HA*
YPYDVPDYA	YDYDDQDA	YPADDDQDA	YDADDDQDA	YPYEDDQDA	-DYKDDDDK	YDYEDDQDA	YPAEDDQDA	YPYDVPDYA	Cont*
YDADDPQDA	YPYEDPQDA	YDYEDPQDA	YPAEDPQDA	YDAEDPQDA	YPYKVDQDA	YDYKVDQDA	YPAKVDQDA	YDAKVDQDA	Flag*
YDADDDDYA	YPYEDDDYA	-DADDPDDA	YDYEDDDYA	YPAEDDDYA	YDAEDDDYA	YPYKVPDYA	-DADDPDDA	YDYKVPDYA	HA*
YPAEDPDYA	YDAEDPDYA	YPYKVDYA	YDYKVDYA	YPAKVDYA	YDAKVDYA	YPYDVPDYA	YDYDVPDYA	YPADVPDYA	Cont*
YPAEDDEYA	-DYKDDDDK	YDAEDDEYA	YPYKVPDYA	YPYDVPDYA	YDYKVPDYA	YPAKVPDYA	YDAKVPDYA	YPYDVPDYA	Flag*
YDYKVDNYA	YPAKVDNYA	YDAKVDNYA	YPYDVDNYA	YDYDVDNYA	YPADVDNYA	YDADVDNYA	YPYEVDPYA	YDYEVDPYA	HA*
YDYKVPNYA	YPAKVPNYA	YDAKVPNYA	-DADDPDDA	YPYDVPNYA	YDYDVPNYA	-DADDPDDA	YPADVPNYA	YDADVPNYA	Cont*
YPYDVPDYA	YDYDVPQYA	YPADVPQYA	YDADVPQYA	YPYEVDPYA	YDYEVDPYA	YPAEVDPYA	YDAEVDPYA	YPYKDDQYA	Flag*
YPYDVPDYA	YPYDVPQYA	YDYDVPQYA	YPADVPQYA	YDADVPQYA	-DYKDDDDK	YPYEVQYA	YDYEVQYA	YPYDVPDYA	HA*
YPADVDNA	YDADVDNA	YPYEVDDNA	YDYEVDDNA	YPAEVDDNA	YDAEVDDNA	YPYKDDNA	YDYKDDNA	YPAKDDNA	Cont*
YPADVPDNA	YDADVPDNA	-DADDPDDA	YPYEVDPNA	YDYEVDPNA	YPAEVDPNA	YDAEVDPNA	-DADDPDDA	YPYKDPDNA	Flag*
YDYEVDDNA	YPAEVDDNA	YDAEVDDNA	YPYKDDENA	YDYKDDENA	YPAKDDENA	YDAKDDENA	YPYDDENA	YDYDDENA	HA*
YDYEVDPNA	-DYKDDDDK	YPAEVDPNA	YDAEVDPNA	YPYDVPDYA	YPYKDPENA	YDYKDPENA	YPAKDPENA	YDAKDPENA	Cont*
YPYKDDNNA	YDYKDDNNA	YPAKDDNNA	YDAKDDNNA	YPYDDNNA	YDYDDNNA	YPADDDNNA	YDADDDNNA	YPYEDDNN	Flag*
YPYKDPNNA	YDYKDPNNA	YPAKDPNNA	-DADDPDDA	YDAKDPNNA	YPYDDPNN	-DADDPDDA	YDYDDPNN	YPADDPNNA	HA*
YDAKDDQNA	YPYDDQNA	YDYDDQNA	YPADDDQNA	YDADDDQNA	YPYEDDQNA	YDYEDDQNA	YPAEDDQNA	YDAEDDQNA	Cont*
YPYDVPDYA	YDAKDDQNA	YPYDDPQNA	YDYDDPQNA	YPADDPQNA	-DYKDDDDK	YDADDPQNA	YPYEDPQNA	YPYDVPDYA	Flag*
YDYDDDDW	YDADDDW	YDADDDW	YPYEDDDW	YDYEDDDW	YPAEDDDW	YDAEDDDW	YPYKVPDWA	YDYKVPDWA	HA*
YDYDDPDW	YPADDPDWA	-DADDPDDA	YDADDPDWA	YPYEDPDWA	YDYEDPDWA	YPAEDPDWA	-DADDPDDA	YDADDPDWA	Cont*
YPYEDDEWA	YDYEDDEWA	YPAEDDEWA	YDAEDDEWA	YPYKVPDWA	YDYKVPDWA	YPAKVPDWA	YDAKVPDWA	YPYDVPDWA	Flag*
YPYEDPEWA	-DYKDDDDK	YDYEDPEWA	YPAEDPEWA	YPYDVPDYA	YDAEDPEWA	YPYKVDNWA	YDYKVDNWA	YPAKVDNWA	HA*
YDAEDDNW	YPYKVPNWA	YDYKVPNWA	YPAKVPNWA	YDAKVPNWA	YPYDVPNWA	YDYDVPNWA	YPADVPNWA	YDADVPNWA	Cont*
YDAEDPNWA	YPYKVDQWA	YDYKVDQWA	-DADDPDDA	YPAKVDQW	YDAKVDQW	-DADDPDDA	YPYDVPQW	YDYDVPQW	Flag*
YPAKVPQWA	YDAKVPQW	YPYDVPQWA	YDYDVPQW	YPADVPQW	YDADVPQW	YPYEVQWA	YDYEVQWA	YPAEVQWA	HA*
YPYDVPDYA	-----	-----	-----	-----	-DYKDDDDK	-----	-----	YPYDVPDYA	Cont*
-DYKDDDDK	-DADDPDDA	YPYDVPDYA	-DYKDDDDK	-DADDPDDA	YPYDVPDYA	-DYKDDDDK	-DADDPDDA	YPYDVPDYA	Flag*

*Cont = -DADDPDDA, Flag = -DYKDDDDK, HA = YPYDVPDYA; abbreviated due to spatial issues

Acknowledgments

I am very grateful to **Prof. Dr. Michael Hausmann** for his support throughout my academic studies, for introducing me to this project, for his advice, and especially for the supervision of this thesis.

I am very thankful to **Prof. Dr. Reiner Dahint** for accepting the position of second adviser for this thesis.

I am indebted to **PD Dr. Alexander Nesterov-Müller**, who has supported and advised me throughout my scientific career, for his patience, the interesting discussions, and teaching me the physics behind particles.

I am equally indebted to **PD Dr. F. Ralf Bischoff**, who has supervised, supported, and advised me, especially in the fields of biology and biochemistry, teaching me the basics of microarrays, proteomics, and the catalytic triade.

I am very grateful to **Dr. Gerhard Moldenhauer** for granting me the position in his group and for his advice and support throughout the project.

I thank **PD Dr. Frank Breitling** for his support and the very helpful discussions. Also, I thank **Dr. Volker Stadler**, **Dr. Thomas Felgenhauer**, and **Jochen Stortz** for their support and cooperation.

I am very thankful to **Christopher Schirwitz** for his good cooperation, helpful discussion, the proofreading of the chemical sections, and the generation of surface coatings on the CMOS chips.

I thank **Dr. Kai König**, especially for his initial work and the chip design, and **Dr. Jennifer Wagner**, for the automated image analysis, and for their general work and good cooperation.

I am very grateful to **Klaus Leibe** for teaching me the basics in engineering and construction, and supporting me in all mechanical and technical problems, as well as in laser printing issues. Additionally, I thank **Siegfried Spiegel**, teaching me to use the tools in the mechanical workshop of the Kirchhoff-Institute of physics and supporting me in the construction of the aerosol generator.

I thank the Kirchhoff-Institute of physics and its workshop, especially **Werner Lamade**, for producing the outlet geometry of the aerosol generation system.

I am very thankful to **Dr. Simon Fernandez**, **Daniela Rambow**, and **Sebastian Heß**, for the good cooperation, supporting me, and supplying me with the required toner particles.

I thank **Tobias Förtsch** for his work on the simulations in his bachelor thesis and his helpful discussions.

I thank **Jürgen Kretschmer** for his support and teaching me the practical basics in biological laboratory work. Also, I would like to thank **Ralf Achenbach** for his support in chip bonding.

I thank **Michael Deininger**, **Dr. Gloria Torralba**, and **Dr. Eberhard Schmitt**, for their support and the helpful discussions.

I thank the DKFZ PhD program for the financial support.

I am thankful to all members of Pepperprint, supporting me and for the supply of the laser printed arrays.

I thank **Prof. Dr. Stefan Güttler** and **Ilia Fedoseev** from the IPA Fraunhofer Institute for their cooperation and their supporting experiments in laser printing.

I thank my friends and colleagues **Matthias Henrich**, **Frieder Märkle**, and **Sebastian Schillo** for the final proofreading.

I thank my father **Prof. Dr. Peter Löffler** and his friend **Dr. Wolfgang Pilz** for their support and active participation in this work.

I thank my mother **Katharina Löffler** and my father for their support and the final proofreading.

I am very grateful to **Christina Lehrer** for her sacrificing support, the very helpful discussions and explanations of biological and chemical questions, and for the critical proof reading.

I thank my family and my friends for their support.

References

1. Collins, F.S., et al., *Finishing the euchromatic sequence of the human genome*. Nature, 2004. **431**(7011): p. 931-945.
 2. Humphery-Smith, I., *A human proteome project with a beginning and an end*. Proteomics, 2004. **4**(9): p. 2519-2521.
 3. Berg, J.M., J.L. Tymoczko, and L. Stryer, *Biochemistry*. 6th ed. 2007, New York: W.H. Freeman.
 4. <http://structure.ncbi.nlm.nih.gov/>.
 5. Burkhardt A., et al., *High-pressure cooling of protein crystals directly in their mother liquor*. To be published, 2011.
 6. Janeway, C., *Immunobiology: the immune system in health and disease*. 6th ed. 2005, New York: Garland Science. 823 p.
 7. Soloviev, M., C. Shaw, and P. Andr n, *Peptidomics : methods and applications*. 2008, Hoboken, N.J.: Wiley-Interscience. 401 p., 8 p. of plates.
 8. Carr, P.A. and G.M. Church, *Genome engineering*. Nature Biotechnology, 2009. **27**(12): p. 1151-1162.
 9. Hoheisel, J.D., *Microarray technology: beyond transcript profiling and genotype analysis*. Nature Reviews Genetics, 2006. **7**(3): p. 200-210.
 10. Tian, J.D., et al., *Parallel on-chip gene synthesis and application to optimization of protein expression*. Nature Biotechnology, 2011. **29**(5): p. 449-452.
 11. Kosuri, S., et al., *Scalable gene synthesis by selective amplification of DNA pools from high-fidelity microchips*. Nature Biotechnology, 2010. **28**(12): p. 1295-1299.
 12. Uttamchandani, M. and S.Q. Yao, *Peptide microarrays: Next generation biochips for detection, diagnostics and high-throughput screening*. Current Pharmaceutical Design, 2008. **14**(24): p. 2428-2438.
 13. Cipolla, L., et al., *Carbohydrate scaffolds for the production of bioactive compounds*. Current Organic Synthesis, 2005. **2**(2): p. 153-173.
 14. Merrifield, R.B., *Solid Phase Peptide Synthesis .1. Synthesis of a Tetrapeptide*. Journal of the American Chemical Society, 1963. **85**(14): p. 2149-2154.
 15. Merrifield, R.B., *Automated synthesis of peptides*. Science, 1965. **150**(3693): p. 178-85.
 16. Merrifield, R.B. and J.M. Stewart, *Automated peptide synthesis*. Nature, 1965. **207**(996): p. 522-3.
-

17. Frank, R., *Spot-Synthesis - an Easy Technique for the Positionally Addressable, Parallel Chemical Synthesis on a Membrane Support*. Tetrahedron, 1992. **48**(42): p. 9217-9232.
 18. Stadler, V., et al., *Multifunctional CMOS microchip coatings for protein and peptide Arrays*. Journal of Proteome Research, 2007. **6**(8): p. 3197-3202.
 19. Stadler, V., et al., *PEGMA/MMA copolymer graftings: Generation, protein resistance, and a hydrophobic domain*. Langmuir, 2008. **24**(15): p. 8151-8157.
 20. Nesterov, A., et al., *Peptide Arrays with a Chip*, in *Small Molecule Microarrays: Methods and Protocols*, M.U.a.S.Q.Q. Yao, Editor. 2010, Springer. p. 109-124.
 21. Beyer, M., *Entwicklung und Anwendung neuartiger Trägeroberflächen zur kombinatorischen Peptidsynthese mit Aminosäure-Tonerpartikeln*, in *Physical-Chemical Institute*. 2005, Ruperto-Carola University: Heidelberg.
 22. Fodor, S.P.A., et al., *Light-Directed, Spatially Addressable Parallel Chemical Synthesis*. Science, 1991. **251**(4995): p. 767-773.
 23. Schein, L.B., *Electrophotography and development physics*. 1988: Springer.
 24. Stadler, V., et al., *Combinatorial synthesis of peptide arrays with a laser printer*. Angewandte Chemie-International Edition, 2008. **47**(37): p. 7132-7135.
 25. <http://www.pepperprint.com/>.
 26. Beyer, M., et al., *Combinatorial synthesis of peptide arrays onto a microchip*. Science, 2007. **318**(5858): p. 1888-1888.
 27. König, K., *CMOS-Based Peptide Arrays*, in *Kirchhoff Institute of Physics*. 2010, Ruperto-Carola University: Heidelberg.
 28. Koenig, K., et al., *Programmable high voltage CMOS chips for particle-based high-density combinatorial peptide synthesis*. Sensors and Actuators B-Chemical, 2010. **147**(2): p. 418-427.
 29. Nesterov, A., *Ortsgenaue Ablagerung von Aminosäurepartikeln für die kombinatorische Synthese von Peptidarrays of einem Chip*, in *Kirchhoff Institute of Physics*. 2006, Ruperto-Carola University: Heidelberg.
 30. Cheng, Y.C., *in preparation*. 2012, Darmstadt University of Technology.
 31. Cheng, Y.C., et al. *Chip printer*. in *WSEAS International Conference on Nanotechnology*. 2010.
 32. Loffler, F., et al., *Biofunctional Xerography*, in *Biotechnology of Biopolymers*, M. Elnashar, Editor. 2011, InTech.
 33. Nesterov, A., et al., *Noncontact charge measurement of moving microparticles contacting dielectric surfaces*. Review of Scientific Instruments, 2007. **78**(7): p. 075111.
-

-
34. Nesterov, A., et al., *Measurement of triboelectric charging of moving micro particles by means of an inductive cylindrical probe*. Journal of Physics D-Applied Physics, 2007. **40**(19): p. 6115-6120.
 35. Löffler, F., *Physikalische Charakterisierung von Biopartikeln und deren Ablagerungsverhalten auf CMOS-Chips*, in *Kirchhoff Institute of Physics*. 2009, Ruperto-Carola University: Heidelberg.
 36. Charlson, E.M., et al., *Study of the Contact Electrification of Polymers Using Contact and Separation Current*. Ieee Transactions on Electrical Insulation, 1992. **27**(6): p. 1144-1151.
 37. Diaz, A.F., *Contact electrification of materials: The chemistry of ions on polymer surfaces*. Journal of Adhesion, 1998. **67**(1-4): p. 111-122.
 38. Manouchehri, H.R., K.H. Rao, and K.S.E. Forsberg, *Triboelectric charge characteristics and donor-acceptor, acid-base properties of minerals - Are they related?* Particulate Science and Technology, 2001. **19**(1): p. 23-43.
 39. Hughes, J.F., *Electrostatic powder coating*. Electronic & electrical engineering research studies Electrostatics and electrostatic applications series. 1984, Letchworth, Herts., England: Research Studies Press; Wiley. 121 p.
 40. Nesterov, A., et al., *Characterization of triboelectrically charged particles deposited on dielectric surfaces*. Journal of Physics D-Applied Physics, 2010. **43**(16): p. 0022-3727.
 41. Hermstein, W., *Die Stromfaden-Entladung und ihr Übergang in das Glimmen*. Electrical Engineering (Archiv für Elektrotechnik), 1960. **45**(3): p. 209-224.
 42. Schmid, J., *Influence of Absolute-Humidity on the Electrical Breakdown in Air*. European Transactions on Electrical Power Engineering, 1992. **2**(5): p. 327-331.
 43. Löffler, F., et al., *High-Precision Combinatorial Deposition of Micro Particle Patterns on a Microelectronic Chip*. Aerosol Science and Technology, 2010. **45**(1): p. 65-74.
 44. Hinds, W.C., *Aerosol technology : properties, behavior, and measurement of airborne particles*. 2nd ed. 1999, New York: Wiley. 483 p.
 45. Baron, P.A., P. Kulkarni, and K. Willeke, *Aerosol measurement : principles, techniques, and applications*. 3rd ed. 2011, Hoboken, N.J.: Wiley.
 46. Coulson, J.M. and J.F. Richardson, *Coulson & Richardson's chemical engineering*. Vol. 3. 1996, Oxford ; Boston: Butterworth-Heinemann.
 47. Wagner, J., *Quality control for peptide chip array production*. 2011, Ruperto-Carola University: Heidelberg.
 48. Nesterov, A., et al., *Precise selective deposition of microparticles on electrodes of microelectronic chips*. Review of Scientific Instruments, 2008. **79**(3): p. 035106.
 49. Cooper, K., A. Gupta, and S. Beaudoin, *Simulation of the Adhesion of Particles to Surfaces*. Journal of Colloid and Interface Science, 2001. **234**(2): p. 284-292.
-

50. Bailey, A.G., *Charging of Solids and Powders*. Journal of Electrostatics, 1993. **30**: p. 167-180.
 51. Harper, W.R., *Contact and frictional electrification*. Monographs on the physics and chemistry of materials. 1967, Oxford: Clarendon P. 369 p.
 52. Foertsch, T., *Ortsgenaue Partikeldeposition mit dem CMOS Peptid Chip und durch Selective Laser Fusing*. 2011, Ruperto-Carola University: Heidelberg.
 53. Wagner, J., et al., *Microparticle Transfer onto Pixel Electrodes of 45 μm Pitch on HV-CMOS Chips - Simulation and Experiment*. Sensor Actuat A-Phys, 2011. **172**(2): p. 533-545.
 54. Kawagishi, Y., Y. Ishida, and K. Ishikawa, *Metal complexes for use in developers for electrostatic images, charge control function*, L.J. Orient Chemical Industries, Editor. 1983: United States.
 55. Schirwitz, C., *in preparation*, in *Physical-Chemical Institute*. 2012, Ruperto-Carola University: Heidelberg.
 56. Schirwitz, C., et al., *Combinatorial Peptide Synthesis on a Microchip*, in *Current Protocols in Protein Science*. 2009, John Wiley & Sons, Inc.
 57. Ulman, A., *Formation and structure of self-assembled monolayers*. Chemical Reviews, 1996. **96**(4): p. 1533-1554.
 58. Love, J.C., et al., *Self-assembled monolayers of thiolates on metals as a form of nanotechnology*. Chemical Reviews, 2005. **105**(4): p. 1103-1169.
 59. Herrwerth, S., et al., *Factors that determine the protein resistance of oligoether self-assembled monolayers - Internal hydrophilicity, terminal hydrophilicity, and lateral packing density*. Journal of the American Chemical Society, 2003. **125**(31): p. 9359-9366.
 60. Baytekin, H.T., et al., *The Mosaic of Surface Charge in Contact Electrification*. Science, 2011. **333**(6040): p. 308-312.
 61. Wagner, J., et al., *Quality analysis of selective microparticle deposition on electrically programmable surfaces*. Review of Scientific Instruments, 2010. **81**(7): p. 073703.
 62. Ferguson, N.M., A.P. Galvani, and R.M. Bush, *Ecological and immunological determinants of influenza evolution*. Nature, 2003. **422**(6930): p. 428-433.
 63. Tobin, G.J., et al., *Deceptive imprinting and immune refocusing in vaccine design*. Vaccine, 2008. **26**(49): p. 6189-6199.
 64. Fairweather, N.F. and V.A. Lyness, *The Complete Nucleotide-Sequence of Tetanus Toxin*. Nucleic Acids Research, 1986. **14**(19): p. 7809-7812.
 65. <http://www.praxis-ockstadt.de/>.
-

Eidesstattliche Erklärung

Hiermit versichere ich, dass ich diese Arbeit selbstständig verfasst habe und keine anderen als die ausdrücklich bezeichneten Quellen und Hilfsmittel verwendet habe. Die direkte oder indirekte Übernahme von Methoden, Proben oder Ergebnissen Dritter wurden als solche spezifiziert.

Des Weiteren erkläre ich, dass ich an keiner anderen Stelle ein Prüfungsverfahren beantragt bzw. die Dissertation in dieser oder anderer Form bereits anderweitig als Prüfungsarbeit verwendet oder einer anderen Fakultät als Dissertation vorgelegt habe.

Heidelberg, den 06.02.2012

Felix Löffler